Surface Charge Density and its Influence on Insulator Flashover

A thesis submitted to the University of Manchester Institute of Science and Technology
for the degree of Doctor of Philosophy

Daniel Charles Faircloth, B.Eng. M.Sc.

2000

“A smell of burning fills the startled air -

The electrician is no longer there”

From Newdigate Poem

Hilaire Belloc 1870-1953

Declaration

No portion of the work referred to in this thesis has been submitted in support of an application for another degree or qualification of the University of Manchester Institute of Science and Technology or any other university, or other institute of learning.

Abstract

A technique is developed to measure high-resolution surface charge density distributions on high voltage insulators. This technique is developed into a piece of laboratory equipment and used to investigate the surface charging of practical axi-symmetric insulators by high voltage discharges and its influence on insulator flashover.

The different techniques available for surface charge measurement are discussed and the electrostatic probe is chosen for development. The process of calculating surface charge density distributions from probe voltage measurements is detailed.

The probe and the mechanism designed to move it over a range of different sized and contoured axi-symmetric insulators is detailed.

The software that automates the entire technique is then described. The Software controls the actual measurement process; calculates the charge density distributions; and allows the user to view and analyse the results.

The measurement system is evaluated and tested thoroughly and then used for a series of experiments. The experimental work is based around cylindrical PTFE insulators positioned in a rod-plane gap. Various techniques for neutralising surface charge are evaluated.

An impulse generator is used to produce single positive discharge events in the rod-plane gap. Each discharge event is recorded using three photomultipliers and current shunts discharge current measurements. Charge density distributions are also recorded. Three different rod diameters and rod surface separations are investigated.

The effect of flashover on surface charge is studied and the charge distributions left by negative impulse, DC and AC test voltages on the rod are recorded.

The surface charging of several other materials is then briefly studied along with the decay of surface charge and the surface charging of a contoured insulator with a single shed.

A full analysis using three-dimensional finite modelling is undertaken of the electrostatic probe, the electrode arrangement, and of the field produced by surface charge.

Contents

Acknowledgements

I would like to start by thanking Dr. Norman Allen who has helped and encouraged me throughout my research work and the writing of this thesis and who kindly stepped in to act as my Supervisor. I would also like to thank Dr. Keith Cornick who first inspired me to go into High Voltage Engineering and who initially supervised me until he left for sunnier climes. Len Warren also deserves note for acting as my Nominal Supervisor.

Special thanks should go to Derek Greaves and Steve Hill whose expert knowledge and practical skills were essential in the High Voltage Laboratory work.

I am indebted to Malcolm Walker for his expert mechanical knowledge and great skill in fabricating the parts for the scanning platform.

Malcolm Bailey should also be thanked for his in-depth knowledge on stepper motors and their drive boards as should all his colleagues in the Electronics Workshop.

I would like to thank Geoff Rubner for his knowledge of UNIX through the years and the staff of UMIST MCC for their help with the Galaxy.

All the rest of the support staff in the Electrical Engineering Department including Mike in Stores.

I would like to thank Bill Hall from VATech for his support.

I thank EPSRC for provided funding for this work.

I would also like to thank all my friends and family who helped keep me sane during the work on this thesis.

Chapter 1: INTRODUCTION

1.1 General

In any high voltage system the high voltage conductor must be mechanically supported by some means. The only practical solution is to use solid insulation. This introduces an insulating surface between the high voltage conductor and earth.

Insulating surfaces are not introduced only for mechanical support. They occur in circuit breaker nozzles where the insulation surrounds the electrodes some distance away and is used to pressurise the arc-extinguishing medium. A large complex insulator surface area also exists inside cast epoxy resin transformers between the cast insulation and the windings.

As insulator design progresses and new demands are placed on materials, a physical knowledge of the surface insulating properties of solid insulation is crucial. The insulator surface is intrinsically the weakest part of the solid-gas insulation system and it is remarkable that the surface flashover of insulators is poorly understood.

This research project investigates experimentally the interaction of discharges with insulating surfaces on practical insulator geometries used in high voltage engineering.

1.2 Approach

When discharges propagate over insulating surfaces they often deposit charge, this is an important factor in the surface flashover of insulators because:

- The localised electric field produced by this surface charge could affect the propagation of further discharges.
- The surface charge deposited may provide a source/sink for further ions.
- The pattern of deposited charge provides ideas about the nature of the propagation of discharges.

A study of the surface charge deposited on an insulator surface would thus be very helpful in understanding surface flashover phenomenon.

1.3 Charge Measurement

1.3.1 Techniques Available

Dust or Lichtenburg Figures

The earliest investigations of insulator surface charging under electrical stress were not quantitative in nature but relied mainly on recording the distributions of charge deposited in non-uniform field geometries as revealed from the dust figures obtained when insulating powder was sprinkled on a charged surface.

Early studies used lycopodium powder and then progressed to the combined use of sulphur and lead oxide, where sulphur adheres preferentially to positive charge and lead oxide to negative, thus revealing any bipolar charging. An excellent, readily available modern-day alternative is photocopier toner, the type used in this thesis adheres to positive charge.

One major problem with this method of charge detection is the contamination of the sample being investigated; the other is that it is in no way quantitative. However the major advantage of this technique is that very precise patterns of charging may be obtained relatively easily.

Liquid crystals

The self-field of surface charge on a liquid crystal aligns the domains in the crystal so that colour or contrast changes develop between the charged and un-charged areas. This technique has been applied by only a few researchers (Sone et al, 1974). The main problem with this method is that it can only be used to measure surface charge on a liquid crystal, and again it is not quantitative.

Electro-optical Measurements

Modifications to the electric fields at the insulator gas interface can be measured electro-optically using either the Pockels (Iizuka et al, 1997) or Kerr (Mahajan, 1994) effects.

The Pockels cell is constructed using a potassium dihydrogen phosphate (KDP) crystal as the insulator. The measurable response relies on the fact that linearly polarised light components, parallel and perpendicular to the surface, travel with different phase velocities through the crystal. The phase velocity difference is proportional to the applied electric field so that orthogonal light components are not in phase and the magnitude of the phase difference can be related to the electric field in the insulator. Phase differences are measured using a polarisation analyser. This method is limited by the fact that the choice of insulator material is restricted to those in which the Pockels effect can be measured. A variation of the Pockels Cell is the Pockels Probe, in which a Pockels Cell is held very near to the insulating surface, this allows the technique to be employed to different insulator surfaces. Unwieldy and complex apparatus is required to implement a scanning technique using a Pockels Cell.

A similar electro-optic principal is employed in the Kerr cell (Connolly, 1984). Here the insulating surface of interest is in the form of a hollow, cylindrical cell bounded at either end by uniform field electrodes. The interface of interest is on the inner surface of the cylinder, and the cell is filled with the gas concerned. The outer wall of the insulator is surrounded by nitrobenzene. Orthogonal polarisation components of light passing through the nitrobenzene near the insulator surface also experience relative phase shifts which are dependent on the fields present in the device. The Kerr cell would allow for different materials to be substituted as the insulator but elaborate experimental techniques would be involved if a complete surface would be scanned and high

resolution in the overall measurement were to be achieved. Mahajan, 1994 has used the Kerr effect to measure space charge in transformer oil.

These two types of cell do have the advantage in so far as they allow changes in the overall field to be measured while a voltage is applied to the test electrodes, they also have very fast response times. It therefore becomes possible to measure the temporal development of surface charge.

Probes

Electrostatic probes are one of the most practical ways of measuring the charge density present on a surface. Several types of probe can be employed for scanning the surfaces of charged specimens and the presence of charge is detected by the voltage or current induced upon them. These probes fall into three main groups:

- Field mills
- Vibrating probes
- Capacitive probes

Field mills and vibrating probes operate in a similar manner by having a sensing electrode to which an electrostatic field may couple and a second electrode which is used to modulate the field at the sensing electrode thus generating a varying voltage signal which can be detected by an amplifier. In the case of the field mill the modulating electrode is a rotating earthed vane which passes in front of the sensing electrode. Chubb, 1999 has made several improvements to the field mill technique by using a floating, rather than an earthed rotating chopper vane. A floating vane removes the need for earthing brushes, which greatly simplifies construction of the field mill and eliminates many frictional problems.

For the vibrating probe the movement of the probe itself provides the modulation.

A number of complications arise when interpreting the signal from probes with a modulated electrode:

1. It is hard to calculate an exact surface charge density from the probe signal.
2. The modulating electrode introduces varying capacitances that are hard to account for.

3. There are inherent noise and vibration problems in the use of probes with moving parts, which can significantly increase measurement error.

In contrast, the capacitive probe removes the need for modulation of sensing electrode, by having a much greater time constant than the other two probes. This is achieved by the use of very high input impedance amplifiers in the voltage measurement circuit of the probe (typically $>10^{13}\Omega$).

The simplest type of electrostatic probe is just a sensing electrode held stationary in the vicinity of the charged region. The resolution of the probe can be greatly improved if:

- The sensing electrode is surrounded by an earthed guard screen.
- The sensing electrode is made as small as possible.
- The sensing electrode is brought as close as possible to the surface.

As the probe is now stationary the last two problems with modulated probes stated previously are removed, and the first problem of how to calculate a surface charge density is simplified: a constant, quasi-uniform, electrostatic field is set up between the probe and the charged surface located beneath it. This allows a more complete field analysis and evaluation to be carried out.

A general difficulty arises in that any probe will affect the quantity it is designed to measure. This is a fundamental law of instrumentation. The quantity being measured (the measurand) is always changed slightly by the measurement process itself. A well designed measurement system aims to reduce the effect on the measureand to an amount below the resolution of the measurement system itself. In this way the measurement system has no discernible effect on the measurement.

1.3.2 Choice of Measurement Method

Discharge activity does not produce uniform surface charging; the exact structure of the charge deposited will have microscopic features as has been shown with work using the electro-optic techniques (Iizuka et al, 1997).

The major drawback of measurement techniques with a sub-micron resolution is the size and shape of the test object. The test surface is flat and has an area in the order of $1cm^2$, whereas insulators that are used in everyday high-voltage engineering situations

are much larger, invariably have axial symmetry, and are often contoured. It would be highly impractical to measure surface charge distributions to a sub-micron resolution over the entire surface of one of these insulators, mainly because of the vast number of measurements involved.

Instead a macroscopic measurement technique is required, where the surface is divided up into a large number of surface elements and the net charge contained within each element is measured. This approach will provide a picture of the overall charge distribution for the entire insulator surface, and still allow the total charge on the surface to be calculated.

The ideal candidate is the capacitive electrostatic probe, it is simple to construct and a full analysis of its operation can be undertaken on commercially available electrostatic field solvers.

1.3.3 Simple Capacitative Model of Electrostatic Probe Operation

Thin Insulators

The basic operation of the electrostatic probe is best explained using a simple capacitative model. This argument was first put forward by D.K.Davies, 1967. Consider the arrangement shown in figure 1.3.1(b). A thin insulator specimen is mounted on a grounded back-plate. A charge Q is on the surface over a small area A, the central axis of the probe is positioned directly above the charged region, this sets up the circuit shown in figure 1.3.1(b) and the equivalent circuit shown in figure 1.3.1(c). The capacitance between the area on the insulator surface and all earthed surfaces is referred to as C_{sg}. It is mainly comprised of two capacitances: C_{sg1}, the capacitance between the insulator surface and the grounded screen of the probe and C_{sg2}, the capacitance between the grounded back-plate. It is across this lumped capacitance that a voltage, V_s is developed by the surface charge Q. This voltage is then divided by the voltage divider created by the two capacitances: C_{sp} and C_{pg} as shown in figure 1.3.1(c), where C_{sp} is the capacitance between the insulator surface and the probe, and C_{pg} is the capacitance between the probe and ground.

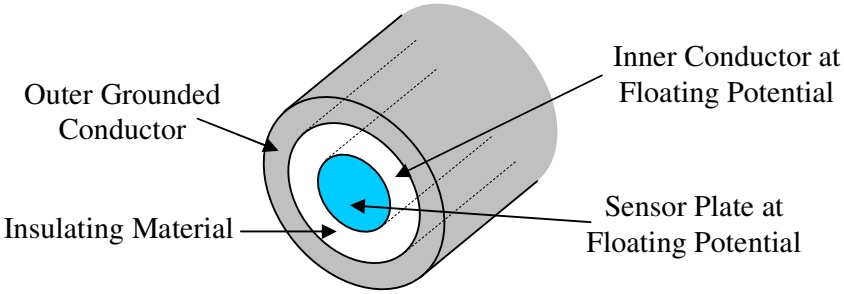

(a) Basic construction of the electrostatic probe

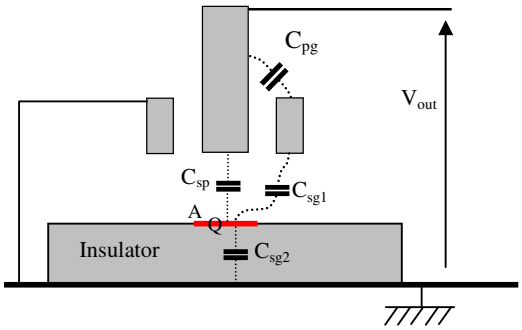

(b) The circuit set up by the probe

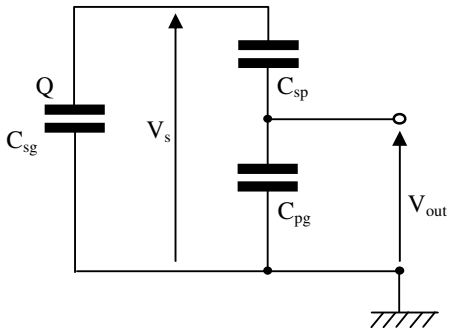

(c) The equivalent circuit

Figure 1.3.1: Diagram showing the principal of the capacitive probe operation.

By solving the circuit equations, it is possible to find Q in terms of V_{out}, and by estimating the effective area, the charge density can be found. The equations that follow show the derivation of the charge density.

Using a standard capacitor divider equation:

$$V_{out} = V_s \frac{C_{sp}}{C_{pg} + C_{sp}}$$ where V_s is the voltage across C_{sg}

also: $V_s = \frac{Q}{C_{TOTAL}}$ where $C_{TOTAL} = C_{sg} + \frac{C_{pg}C_{sp}}{C_{pg} + C_{sp}}$ (total capacitance)

thus: $V_s = \frac{A\sigma}{C_{sg} + \frac{C_{pg}C_{sp}}{C_{pg} + C_{sp}}}$

Substituting gives:

$$V_{out} = \frac{A\sigma}{\left(C_{sg} + \frac{C_{pg}C_{sp}}{C_{pg}+C_{sp}}\right)} \cdot \frac{C_{sp}}{C_{pg}+C_{sp}} = \frac{A\sigma C_{sp}}{C_{sg}\left(C_{pg}+C_{sp}\right)+C_{pg}C_{sp}}$$

And rearranging:

$$\sigma = V_{out}\left(\frac{C_{sg}\left(C_{pg}+C_{sp}\right)+C_{pg}C_{sp}}{AC_{sp}}\right)$$

Hence: $\sigma = kV_{out}$ where: $k = \frac{C_{sg}\left(C_{pg}+C_{sp}\right)+C_{pg}C_{sp}}{AC_{sp}}$

Probe voltage is linearly related to surface charge density. So to generate a surface charge density map each measured probe voltage is simply multiplied by a constant, k.

Many researchers have successfully applied this technique. Earlier researchers, before large quantities of computing power were available, had a problem handling and displaying the measured results. Connolly, 1984 used a spiral scanning technique; scanning a flat circular insulator surface like a record on a turntable. The results were then displayed as a single line on a two-dimensional graph, as if the scanning path had been unrolled. This technique has obvious limitations in the interpretation of the results. Abdul-Hussain and Cornick, 1987 and Vasconcelos, 1994 used a similar scanning technique but displayed the results as three-dimensional surfaces, allowing a clearer picture of the overall distribution. Davidson and Bailey, 1999 also measured charge distributions on thin insulators against a grounded back plane. They employed a similar concentric circle scanning technique.

The resolution of the charge distributions obtained by all these previous researchers was limited by the size of the probe employed and the limited screening offered by the outer grounded conductor of the probe (see next section on probe response).

The simple capacitive model of probe operation is useful for comparing different insulating materials, but it is limited to thin insulating specimens on grounded back-planes.

Thick Insulators

Varying Capacitance to Ground

When the simple capacitive technique is applied to thick insulator specimens a number of problems occur with interpreting the probe signal. The voltage induced on the probe depends on both the surface charge density and the capacitances in the circuit set up by the probe as shown in figure 1.3.2.

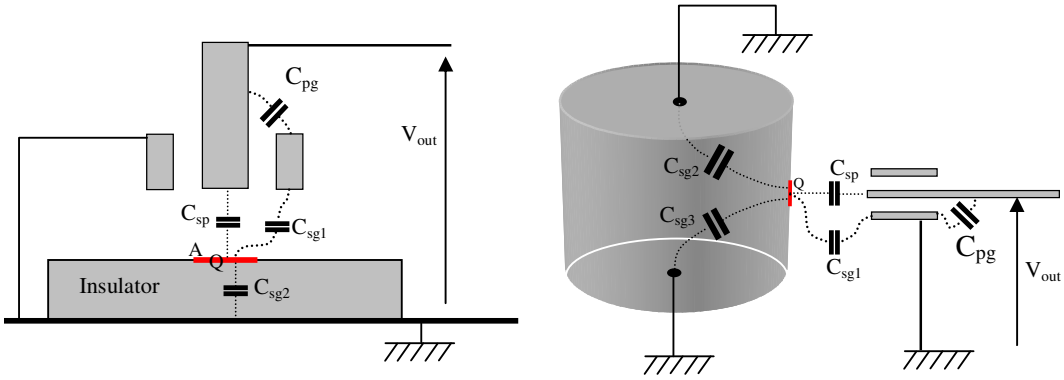

(a) Thin insulator specimen circuit. *(b) Thick insulator specimen circuit.*

Figure 1.3.2: The two circuits set up by the probe, surface charge, and insulator with thick and thin insulator specimens.

As the probe moves over a thin surface as shown in figure 1.3.2(a) the capacitances that make up the equivalent circuit shown in figure 1.3.1(c) do not change. For a thick insulator specimen the surface element to ground capacitance is comprised of a parallel combination of several capacitances as shown in figure 1.3.2(b). C_{sg1}, the capacitance between the element and the grounded outer screen of the probe will not change significantly, however C_{sg2} and C_{sg3} the capacitance between the element and any other grounded object will vary as the probe nears them. Hence simple calibration of the probe is invalid.

Probe Response

However the main problem with the simple capacitive analysis when applied to thick insulators is that it assumes that only the charge directly beneath the probe influences the probe voltage.

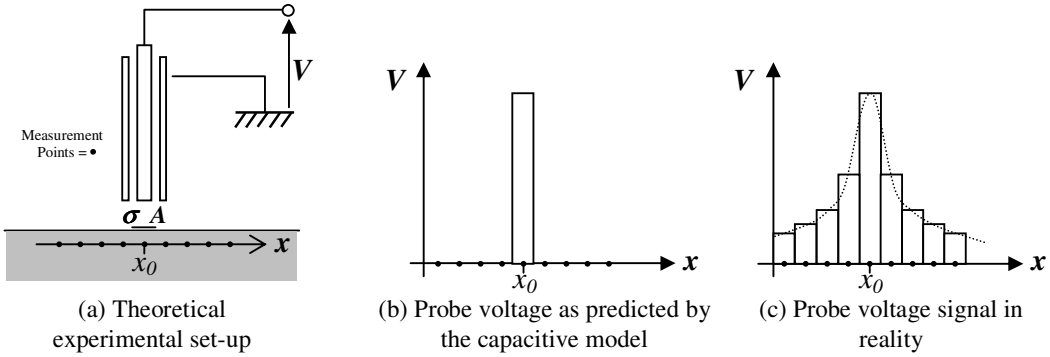

(a) Theoretical experimental set-up

(b) Probe voltage as predicted by the capacitive model

(c) Probe voltage signal in reality

Figure 1.3.3: A simple experiment to illustrate the deficiencies of the simple capacitive model.

Consider the simple thought experiment shown in figure 1.3.3(a). An element with area A, and charge density σ, is placed on an insulator surface and an electrostatic probe is scanned across it in the direction of arrow x taking measurements at regular intervals. A voltage signal is induced on the probe when it is above the charged element. The simple capacitive model assumes the probe only responds to charge directly beneath the central axis of the probe. This is shown in figure 1.3.3(b), where the probe voltage is zero until the charged element is directly under the probe, when it will assume a voltage directly proportional to the charge density, and then drop back to zero when the probe has passed.

In reality this will obviously not be the case, areas of surface charge some distance away from the central axis of the probe can still induce a significant voltage on the probe. This is illustrated in figure 1.3.3(c), where the single element of charge at x_0 induces a voltage on the probe at measurement points some distance from the charge itself.

This problem also manifests itself for thin insulators though not as seriously. The grounded back plane electrode combined with the grounded outer electrode around the probe effectively screens the influence of distant charges.

The problem of varying capacitance to ground combined with the problems of probe response effectively limits the simple capacitive analysis of the electrostatic probe to thin insulators on a grounded back plane.
Some researchers have however used the capacitive approach for thick insulators. The charge density maps of Al-Bawy and Farish, 1991 clearly lack any sort of spatial resolution because their probe responds to charges some distance away.

1.3.4 Probe Response Theory Of Operation

It is clear that for accurate and quantitative electrostatic probe surface charge density measurements on thick insulators, a detailed analysis involving the probe's response function is required. Takuma et al, 1998 came to the same conclusion in a recent review paper on surface charge measurements with the electrostatic probe.

Previous researchers have, with varying degrees of success, attempted a number of different analysis techniques.
Bier et al 1991 used a transfer function and Fourier-transform technique to remove the probe's response function from probe measurements above a thin insulator. Their calculated charge distribution was low resolution and the distribution appeared very similar before and after analysis. No significant detail could be observed in their published charge distribution.

A successful technique for calculating charge densities on thick insulators was described by Pedersen, 1987. By modelling the probe, insulator and surface charge the probe's response to distant charges could be found. Pedersen's λ-function relates the Gaussian charge induced on the probe to the surface charge density at the dielectric interface. The surface charge density distribution can then be calculated from the probe measurements using a matrix inversion technique required to solve the simultaneous equations. A recent discussion paper by Wintle et al, 1997 on the λ-function technique illustrated that the 2-dimensional modelling, to find the probe's response function, employed by Rerup et al, 1996 led to errors in the calculated charge distributions. It concluded that an accurate 3-dimensional model of the probe-insulator-surface charge

geometry was required to obtain accurate charge density distributions on thick insulator specimens.

Ootera and Nakanishi, 1988 used the electrostatic probe to measure charge distributions on DC-GIS cone spacers. This work provides a significant advantage in that it studies the charge on a practical high voltage insulator arrangement. They also undertook a 3-dimensional analysis of the operation of the electrostatic probe. The technique used to calculate surface charge density measurements is a combination of a probe response to nearby charges and a voltage offset. The calculated charge distributions compared favourably with the dust figures obtained by the researchers. However the resolution of their technique was limited by the size of their probe (1cm diameter) and they could only pick out regions of different surface charge density. Concerns are also raised by the poor discretisation of their 3-dimensional probe model, this will affect the accuracy of their results, however they were limited by the computing power of the day.

Sudhakar and Srivastava, 1987 studied charge distributions on a cylindrical spacer. They used a similar technique to Ootera and Nakanishi, 1988 to calculate the surface charge distribution from multiple probe voltage measurements. To find the values required for the calculation they assumed the probe responded to the field present at the sensor plate. However, they calculated this field using an axi-symmetric model, neglecting the probe because it would spoil the axial symmetry of the model. The presence of the probe is fundamental to the whole arrangement so it is not realistic to neglect its effect on the induced probe voltage. Their calculation is hence invalid, Takuma et al, 1998 make the same comment.

1.3.5 Requirements for Further Work

To enhance the knowledge of the surface charging of insulators a system to measure surface charge requires the following characteristics:

- *High-Resolution:* To allow a detailed study into the pattern of surface charging and allow the resolution of the charge deposited by individual streamer channels.
- *Thick and Contoured Insulators*: The system must be capable of measuring charge distributions on a range of practical high voltage insulators.

- *Calibration Technique:* A technique is required that accounts both for the probe's response to distant charges and the varying capacitance to ground as the probe moves over the surface.
- *Probe Response Analysis:* A full detailed and accurate 3-Dimensional analysis of the probe is required.

This research project aims to develop a surface charge scanning system with the above characteristics. This will provide an advance in surface charge measurement techniques.

1.4 Theory

1.4.1 Introduction

Discharges in a Gas

The basic theory of discharge growth in a gas in a uniform field as first put forward by Townsend, 1910 is as follows:

As the discharge propagates different processes act to change the number of free electrons present, these basic processes are described in section 1.4.2. The cumulative effect of these processes can be simply represented by two quantities: α the ionisation coefficient, and η the attachment coefficient. Where: α is defined as the number of extra free electrons produced in a unit propagation distance for each initial electron, and η is the number of free electrons removed (by attachment processes) for each initial electron.

These processes act in proportion to the number of electrons present; the relationship can be formalised thus:

At a distance x from the start point there will be n electrons

The change in the number of electrons present in a finite element of distance, dx is:

$dn = (\alpha - \eta)ndx$

by assuming there are N_0 initial electrons at $x = 0$ this equation can be solved as:

$n = N_0 e^{(\alpha - \eta)x}$

This equation describes the number of electrons present in a single electron avalanche. The discharge as a whole will be comprised of a large number of avalanches, each of which will have been started by a free electron.

At higher applied voltages as discharges begin to cover the entire gap between the electrodes, secondary ionisation processes become significant. Secondary ionisation processes can produce extra free electrons that result in additional avalanches. The main secondary process is positive ions (or large metastable molecules) drifting back to the cathode, causing secondary electrons to be emitted from the electrode. Photons reaching the cathode can also cause secondary emission of electrons. Townsend, 1910 described the extra production of electrons by a second ionisation coefficient γ, which he defined as the mean number of electrons released per positive ion incident on the cathode. Values for γ depend on the gas and the electrode material and electrode surface condition.

Many formulas can be derived from α, η and γ, such as external circuit current and breakdown criteria. However all the coefficients vary depending on field strength and so can only be applied in uniform fields.

The Townsend mechanism of discharge growth was adapted by Meek and Craggs, 1953 to include streamers. A streamer is a highly conducting, luminous, filamentary, fast propagating discharge. It is effectively a plasma channel that propagates by connecting and engulfing individual avalanches. The principle features of streamer propagation theories are a large amount of photo-ionisation of gas molecules in the space ahead of the streamer and the large local enhancement of the electric field by the ion space charge at the tip of the streamer. During streamer propagation the positive ions may be assumed to be stationary in comparison to the more rapidly moving electrons, and the streamer develops as a cloud of electrons behind which is left a positive ion space charge.

Discharges in the Presence of an Insulating Surface

The simple attachment/ionisation model works for discharges in gases but when an insulator is present the process becomes more complicated. However it is possible to assume the same model but the attachment and ionisation coefficients are changed to surface enhanced ones. The surface enhanced ionisation coefficient, α_e is the surface

ionisation coefficient, α_s plus the ionisation coefficient for the surrounding air, α_o. The surface enhanced attachment coefficient is defined in a similar way $\eta_e = \eta_s + \eta_o$, where η_o is the attachment coefficient for the surrounding air.

The charge deposited on the surface by a discharge is the proposed measurand so it is important to try to understand the basic mechanisms involved in depositing surface charge.

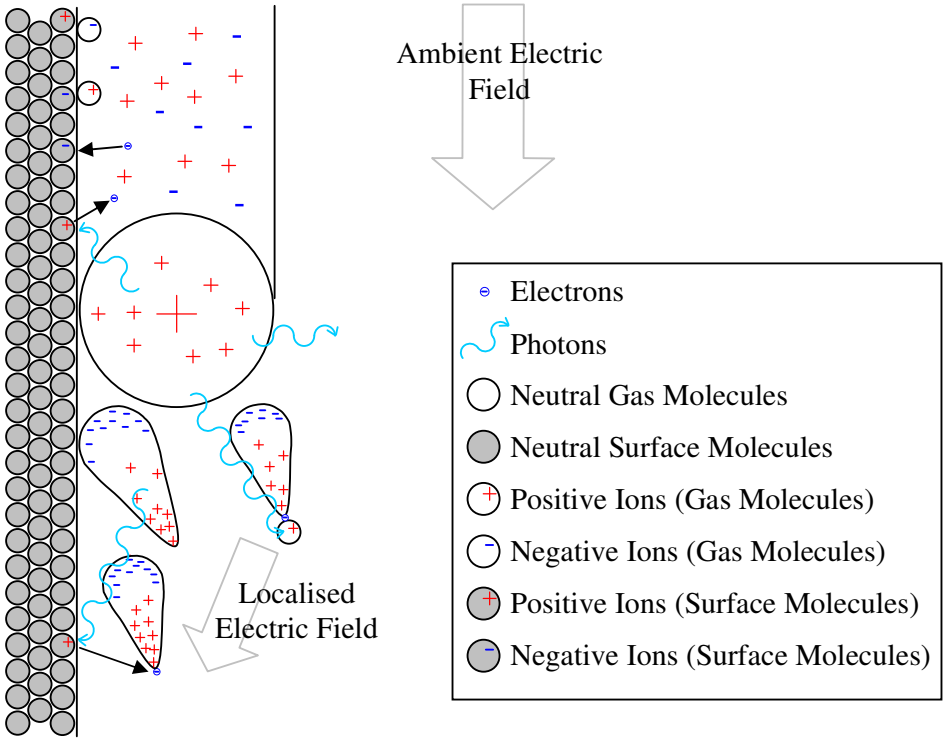

Figure 1.4.1: A representation of the different processes involved in the propagation of streamers and the deposition of surface charge.

Streamers propagate in the air-insulator interface so basic processes in air and on the surface should both be considered. Figure 1.4.1 shows a representation of the different processes involved in streamer propagation and the deposition of surface charge. The localised electric field is distorted towards the insulator surface by the presence of the insulator. Each of these basic processes is described in the next section. The surface discharge is a complex interaction of many processes and the surface enhanced coefficient model may not realistically describe discharges propagating along surfaces.

1.4.2 Basic processes

Ionisation Processes

Electron Ionisation

Accelerated electrons of sufficient energy hit neutral gas molecules creating a secondary free electron and a free positive ion, figure 1.4.2(a). This is the basic process in the development of avalanches and is quantified in the discharge growth model as α_0, the ionisation coefficient of air.

In a similar way electrons hit neutral surface molecules creating a secondary free electron and a fixed positive surface ion, figure 1.4.2(b). This process is quantified by α_s the surface ionisation coefficient.

Photon Ionisation

Most excited molecules (or atoms) have a lifetime in the region of 10^{-8}s before they return to their ground state with the consequent emission of a photon. These low-energy photons may strip off an outer electron from another neutral gas molecule creating a free electron and a free positive ion, figure 1.4.2(c). Photon ionisation is an important factor in streamer propagation (Allen, 1995).

In a similar way photons can ionise neutral surface molecules creating a free electron and a fixed positive surface ion, figure 1.4.2(d).

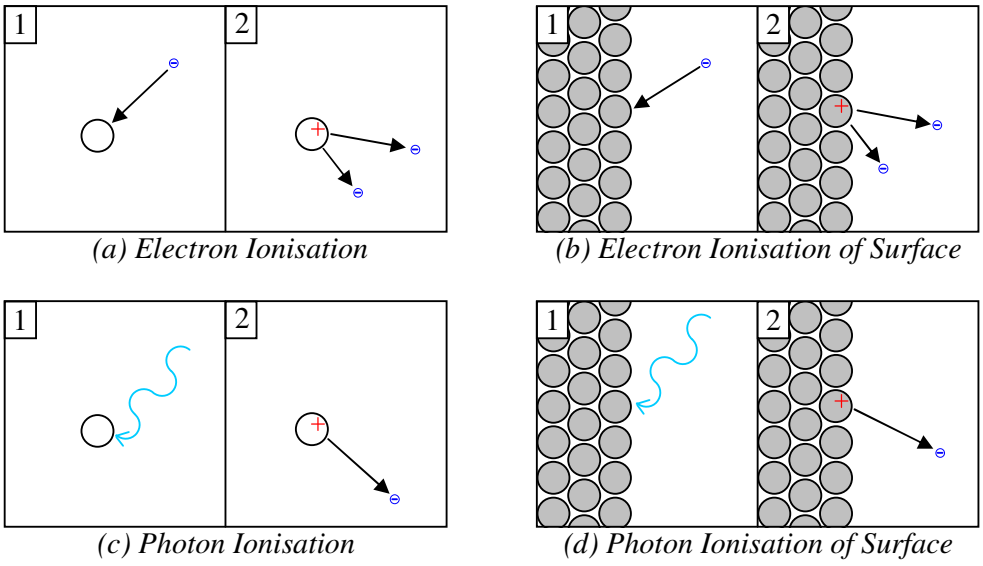

(a) Electron Ionisation *(b) Electron Ionisation of Surface*

(c) Photon Ionisation *(d) Photon Ionisation of Surface*

Figure 1.4.2: Ionisation processes resulting in production of free electrons and positive ions.

Detachment Processes

Ionisation processes are not the only way to produce extra free electrons; detachment of an electron from a negative ion is also possible.

A negative gas ion, a molecule with an extra electron, can be hit by a free electron, resulting in a neutral molecule and two free electrons as shown in figure 1.4.3(a).

In a similar way a free electron can hit a negative surface ion, releasing an extra free electron, figure 1.4.3(b).

Photons can also cause electron detachment as illustrated in figures 1.4.3(c) and (d). This process is referred to as Photo-Detachment.

Spontaneous detachment is also possible where a negative ion loses its extra electron, figures 1.4.3(e) and (f), however this process is rare. A similar process can occur when a negative ion gains enough energy from the applied electric field and collides with a neutral gas molecule, resulting in detachment. For example, this process is usually regarded as the mechanism by which free electrons are initially created in the field near the tip of a pointed rod, so leading to corona.

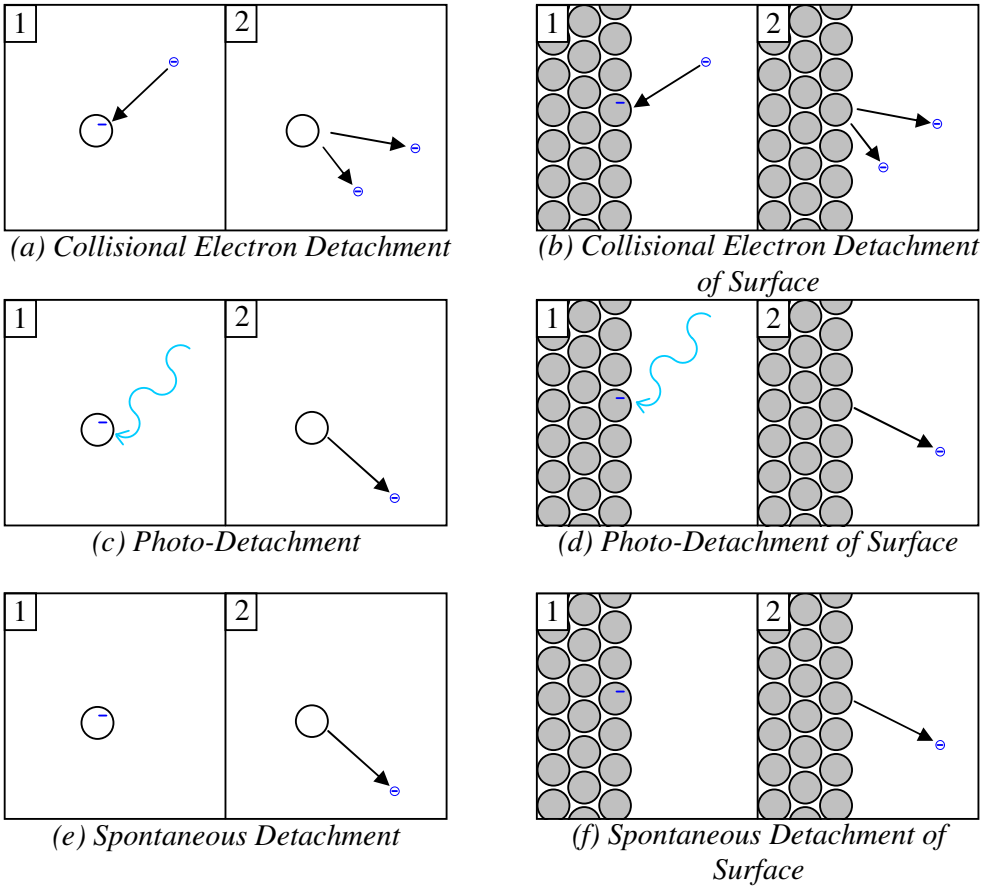

(a) Collisional Electron Detachment

(b) Collisional Electron Detachment of Surface

(c) Photo-Detachment

(d) Photo-Detachment of Surface

(e) Spontaneous Detachment

(f) Spontaneous Detachment of Surface

Figure 1.4.3: Detachment processes resulting in production of free electrons.

Electron Attachment Processes

Electron attachment processes act to reduce the number of free electrons present and are quantified in the avalanche development model by the attachment coefficient, η.

Neutral molecules can attach free electrons resulting in a negative ion as illustrated in figures 1.4.4(a) and (b). In a material or gas the degree of this attachment is referred to as its electronegativity. Most insulating surfaces are located in an electronegative gas, such as air or SF_6. In atmospheric air, the electronegativity is due to the presence of oxygen and water vapour. PTFE is an electronegative insulator material.

By removing free electrons from the discharge process, which would have otherwise contributed to avalanche development, an elevated breakdown voltage is achieved.

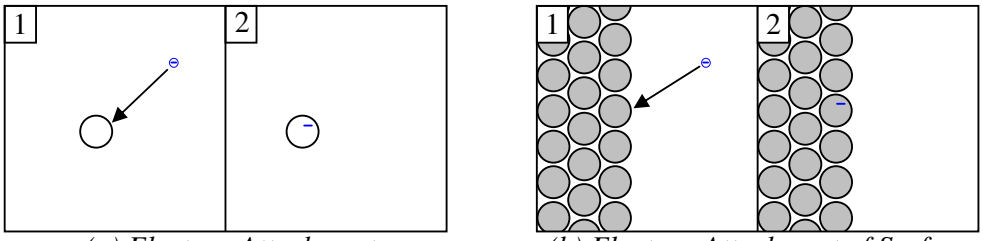

(a) Electron Attachment *(b) Electron Attachment of Surface*

Figure 1.4.4: Electron attachment processes resulting in the absorption of free electrons.

Electron attachment can occur by one of two mechanisms (Gallagher, 1984). Firstly, dissociative attachment can take place where a molecule captures a free electron, becoming an unstable ion, which then disassociates to two stable particles, one negatively charged and one neutral, the excess energy is taken away as the kinetic energy of the two particles. Secondly, a three-body collision may occur between two neutral molecules and an electron resulting in a stable negative molecular ion and a neutral molecule. The additional neutral molecule is thought to stabilise the attachment process by helping to remove excess energy.

Combination Processes

Other processes not covered by the simple ionisation and attachment process are combination processes involving electron transfer. Figure 1.4.5(a) illustrates this process for the combination of a free positive ion and a free negative ion. An electron is transferred between the two resulting in two neutral free molecules. Similar processes can occur between free ions and oppositely charged surface ions as indicated by figures 1.4.5(b) and (c).

The number of free electrons can also be reduced by the recombination of electrons with positive ions (figures 1.4.4(c) and (d)) however this is a comparatively rare occurrence.

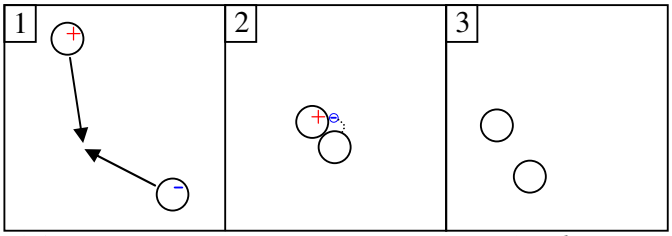

(a) Free Positive Ion-Free Negative Ion Combination

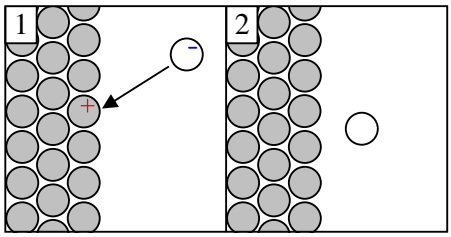

(b) Surface Positive Ion-Free Negative Ion Combination

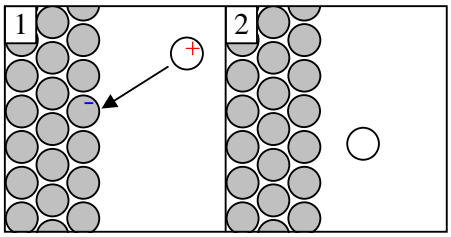

(c) Surface Negative Ion-Free Positive Ion Combination

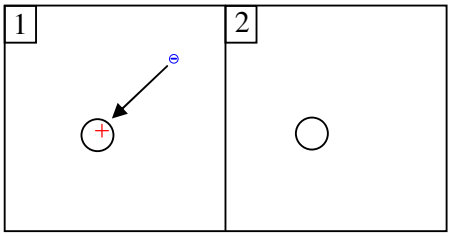

(d) Electron-Positive Ion Recombination

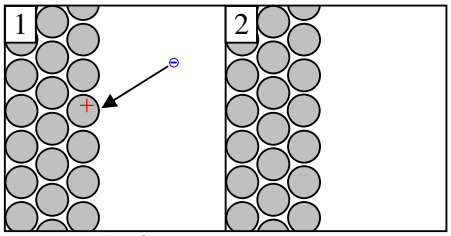

(e) Electron-Positive Ion Recombination

Figure 1.4.5: Electron transfer processes during ion combination.

Molecular Attraction and Other Processes

In addition to the all the mechanisms already listed a number of other processes are present.

As stated previously, the electronegativity of atmospheric air is due to the presence of oxygen and water vapour, which together form complexes of the form $O_2(H_2O)_n$ and it is known that in addition to the propensity of molecular oxygen to pick up free electrons to form O^-_2 ions, the complexes are also efficient in retaining negative charge to form $O^-_2(H_2O)_n$ ions.

There are other types of complexes that could form such as free negative-positive ion complexes. Similarly fixed positive surface ions can attract and trap free negative ions and visa versa. It is also possible that charged molecules and even low velocity electrons can attach to a neutral surface by dipole attraction.

It is clear that the surface propagation of streamers and their deposition of surface charge are complex phenomena involving a large number of interacting processes. The processes involved depend on material permittivity, electronegativity, surface and volume resistivity, and may other physical properties. It is also clear that different materials will interact with surface discharges in different ways.

1.4.3 Deposited Surface Charge

The charge deposited on the surface by a discharge is the proposed measurand so it is important to try to understand the basic mechanisms involved in depositing surface charge.

The surface enhanced ionisation and attachment coefficient model of avalanche propagation suggests that the surface charge will be deposited in thin channels as the streamers propagate. It also suggests that the distribution of surface charge in these surface streamer channels whilst the streamer is propagating will be exponential because of the exponential nature of the attachment process. Given the surface

attachment coefficient, the surface charge deposited by the streamer channel whilst propagating is: $q_{sp} = N_o e^{-\eta_s x}$ where η_s is the surface attachment coefficient.

However the charge measured on the insulator surface shows the state of the insulator surface *long after* the discharge has *finished* propagating; it is effectively the charge '*footprint*' left by the discharge.

So the charge measured on the surface is a combination of fixed surface ions and trapped gaseous ions that have been attached to these fixed surface ions. Charged molecules and even low velocity electrons can also attach to a neutral surface by inducing dipoles in neutral surface molecules (electrostatic image forces), thus adding to or reducing the net surface charge.

The electric field (or self-field) of charge in the streamer channel itself may also play an important part in the deposition of surface charge.

The underlying attached distribution of surface charge in the streamer channel during propagation is exponential, so it is not an unreasonable assumption that the final measured distribution of surface charge in the surface streamer channels, just as they stop propagating, will also be exponential. Using this assumption an overall surface attachment coefficient, which covers both propagation and charge deposition after propagation has finished, can be defined. This overall surface attachment coefficient is referred to as A, and is defined as:

$q_s = N_o e^{-Ax}$ where q_s is the measured surface charge in the surface streamer channel.

It can only be obtained by direct measurement of the surface charge distribution along charged paths deposited by individual streamers where they stopped propagating.

1.4.4 Field Enhancement

Introduction

The electric fields in which streamers are initiated and propagate, depend not only on the electrode arrangement but also the effect of any insulation present. Insulators have a higher permittivity than air, and in certain circumstances high field strengths can occur in localised regions where the permittivity abruptly changes. This is commonly known as the Triple Junction Effect. It occurs at the intersection of three materials with different permittivities and manifests itself most strongly when the permittivities of the three materials are vastly different and their intersection is grossly non-orthogonal. The highest field strength is always in the material of the lowest permittivity.

The Triple Junction Effect and its consequences are best illustrated by the example shown in figure 1.4.2.

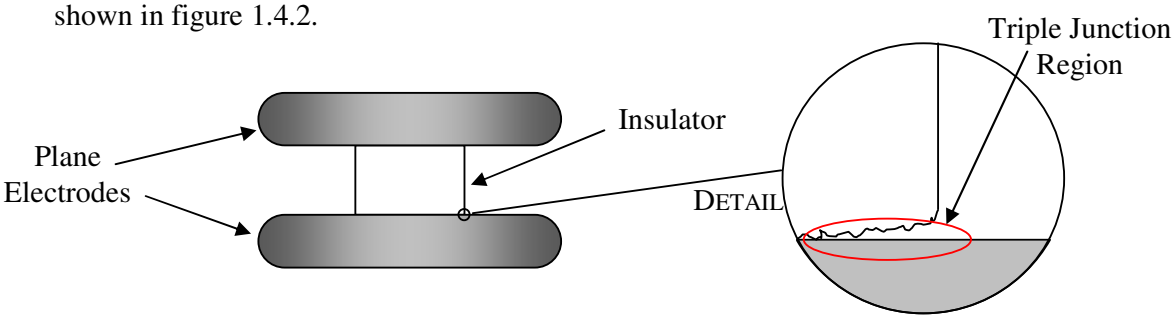

Figure 1.4.2: Example insulator-electrode arrangement to illustrate location of triple junction.

A real insulator between two plane electrodes should be in a perfectly uniform field, however it is impossible to have the insulator make perfect contact with the electrode all the way round. Thus at a small enough scale, a triple junction will exist somewhere on the electrode-insulator-air boundary as illustrated in figure 1.4.2.

Model

The effect a triple junction like this has on the electric field strength is shown in figure 1.4.3. The figure shows the results from a 2-dimensional model of an idealised PTFE insulator-air-electrode triple junction. Removing a rectangular slice from the bottom of the insulator forms the triple junction. By applying a voltage to the line at the top of the model and grounding the bottom planes of the model a uniform field of $500kVm^{-1}$ is set up.

Effect of Triple Junction Size

The equipotentials in figure 1.4.3 clearly show how the step change in permitivity causes a distortion in the electric field. A 4mm high triple junction can cause the localised electric field strength in the air to rise from the ambient 500kVm^{-1} to almost 750kVm^{-1}. As the height of the triple junction is reduced the field strength increases and becomes even more localised. A 0.5mm high triple junction contains field strengths double the ambient.

As the height of the triple junction is reduced further even greater field strengths arise and it is obvious that the triple junction region will be the initiation site for any discharges.

This triple junction induced discharge initiation site is a fundamental problem in the design of high voltage solid-gas insulation systems. It is overcome by the use of screening electrodes designed to minimise the ambient field surrounding the triple junction.

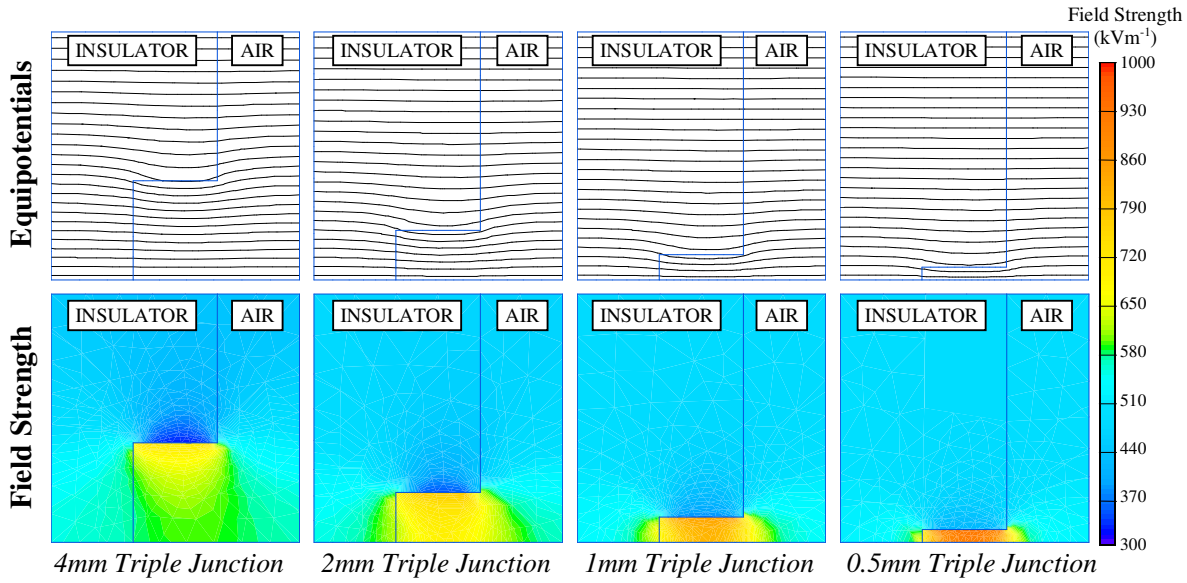

Figure 1.4.3: The electric field in PTFE (ε_r = 2.2) with a triple junction of different heights in an ambient field of 500kVm^{-1}.

Effect of Insulator Permittivity

Another important factor determining the exact amount of field enhancement is the permittivity of the insulator. Figure 1.4.4 shows the same model used as before but with the triple junction height held constant at 1mm and the relative permittivity of the insulator material increased from 1.0 (air) to 7.0 (porcelain).

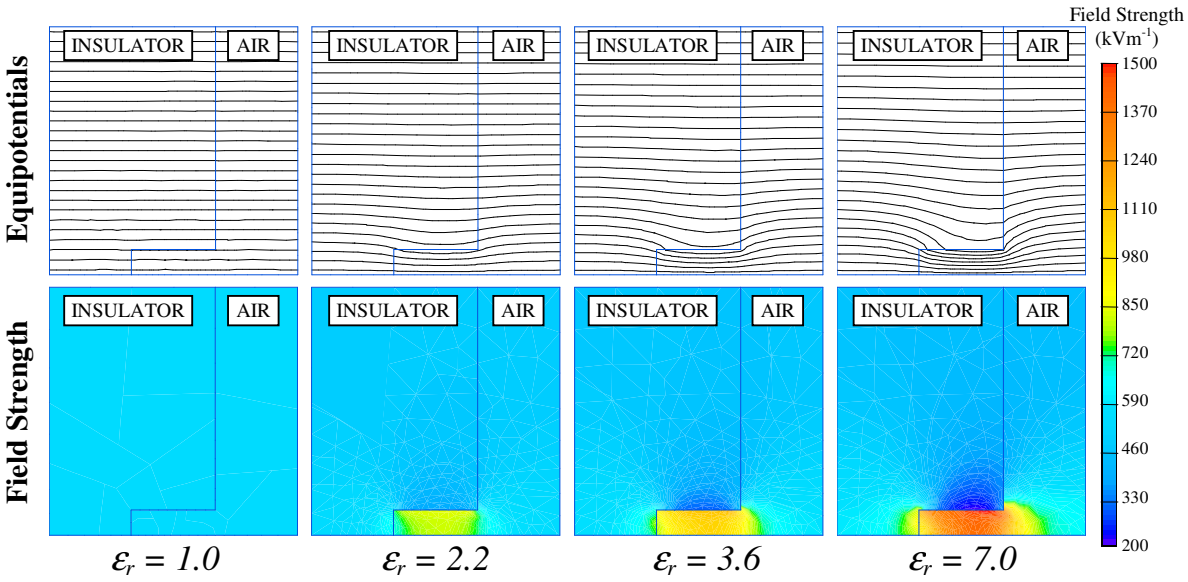

Figure 1.4.4: The electric field in a 1mm triple junction in materials of different permittivities in an ambient field of 500kVm^{-1}.

When the insulator has the same permittivity as air there is no field enhancement. As the insulator material permittivity is increased the electric field strength in the air in the triple junction region increases rapidly. For a material with a high permittivity such as porcelain the localised field strength can reach values three times the ambient.

Other Triple Junction Locations

The triple junction effect can also manifest itself when an electrode touches an insulator at one point. A typical example of this is shown in figure 1.4.5 where an insulator is positioned in a rod-plane gap. The triple junction is formed in the air between the rounded rod electrode and the insulator. The effect does not depend on small material irregularities like the previous example and will occur in even a 'perfect' theoretical model. The rod-plane gap with an insulator cannot be reduced to a two-dimensional

problem so a study of its triple junction can only be undertaken with a three-dimensional field solver. An investigation into the electric field in this type of arrangement is undertaken in chapter 4.

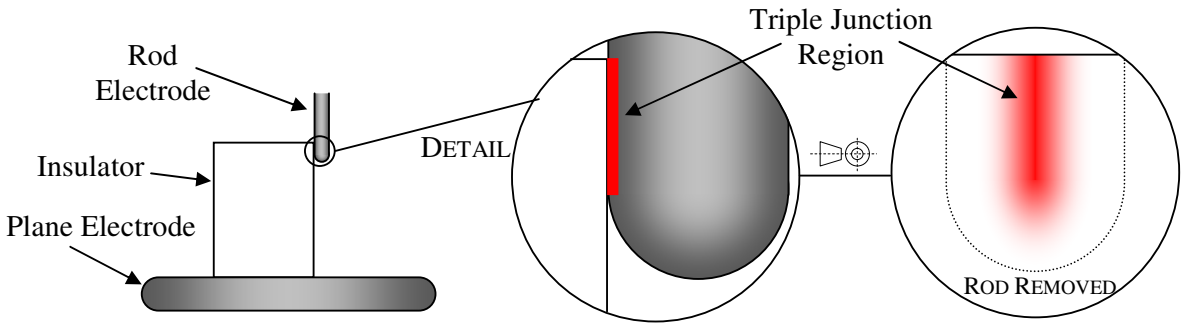

Figure 1.4.5: Location of triple junction in a rod-plane gap with an insulator.

1.5 Thesis Plan

1.5.1 Introduction

This thesis covers three different areas of study; the system developed to measure surface charge; the practical experimental work; and the theoretical simulations and analysis.

1.5.2 Charge Measurement

Chapter 2 details the surface charge scanning system developed for this project. The system comprises of the hardware required to physically measure the charge using the electrostatic probe principle; the software required to control the scanning hardware; the software required to calculate the surface charge density distribution; and the software required to view and analyse the calculated charge density distributions. The complete scanning system is designed to be simple and easy to use with the complexity of the task hidden from the operator.

1.5.3 Experiments

Chapter 3 covers the high voltage testing conducted to evaluate the effectiveness of the surface charge scanning system and to improve our understanding of the charging of insulators. The experimental work is based around the rod-plane electrode configuration. This configuration is a standard electrode arrangement in high voltage testing. It also offers a representation of the practical situation in high voltage plant where a discharge begins in a region of high field and propagates into a diverging field. Impulse voltages are applied to the rod to produce a controllable discharge in the gap. Three photo-multipliers are used to observe the propagation of the discharge. The current in the gap is measured using a resistive shunt connected to the grounded plane electrode. Insulator test objects are placed in the gap and the surface charge density distributions produced by discharges are measured using the scanning system. The main insulator material studied is PTFE; this is because of its common place usage in modern high voltage engineering applications, and its ability to store surface charge. A few other materials are briefly studied. The DC and AC charging of PTFE is touched on along with the decay of charge from the surface.

1.5.4 Simulations and Analysis

Chapter 4 covers the theoretical work undertaken. The theoretical work mainly consists of 3-dimensional finite element modelling studies. The electrostatic probe arrangement is modelled to allow a deeper understanding of its operation and to obtain calibration values required to convert probe measurements into surface charge density measurements. The effect of this conversion procedure is analysed in detail. The electrode arrangement is modelled to evaluate the fields present in the gap. Finally important observations are made about the electric field produced by the surface charge density measurements obtained in the experimental work.

1.5.5 Discussions and Conclusions

The work conducted during this research project is discussed and commented upon and conclusions drawn.

Chapter 2: CHARGE MEASUREMENT

2.1 Introduction

2.1.1 Overview

This chapter describes the surface charge measurement system developed for this project based upon the electrostatic probe. This first introductory section covers general points involving taking measurements over surfaces. The next section details the technique required to calculate surface charge density measurements from the probe voltage measurements and provides an example to illustrate the technique. The probe, and the mechanism required to move it over the surface, make up the scanning system hardware part of this chapter. This is followed by a description of the software required to control the scanning procedure. Finally the software used to implement the probe voltage to surface charge density conversion is described and the software designed to view and analyse the results is detailed.

2.1.2 Recording Surface Charge Density Maps

A charge density map is made from a collection of surface charge density measurements at points on the insulator's surface. Each measurement is of the net surface charge density over each element of the insulator's surface.

The optimum size for the surface elements and hence the limit of resolution is a compromise between a number of factors, which are discussed in this thesis. However it is important to take a sensible number of measurements for a particular measurement resolution, this fact is illustrated in figure 2.1.1.

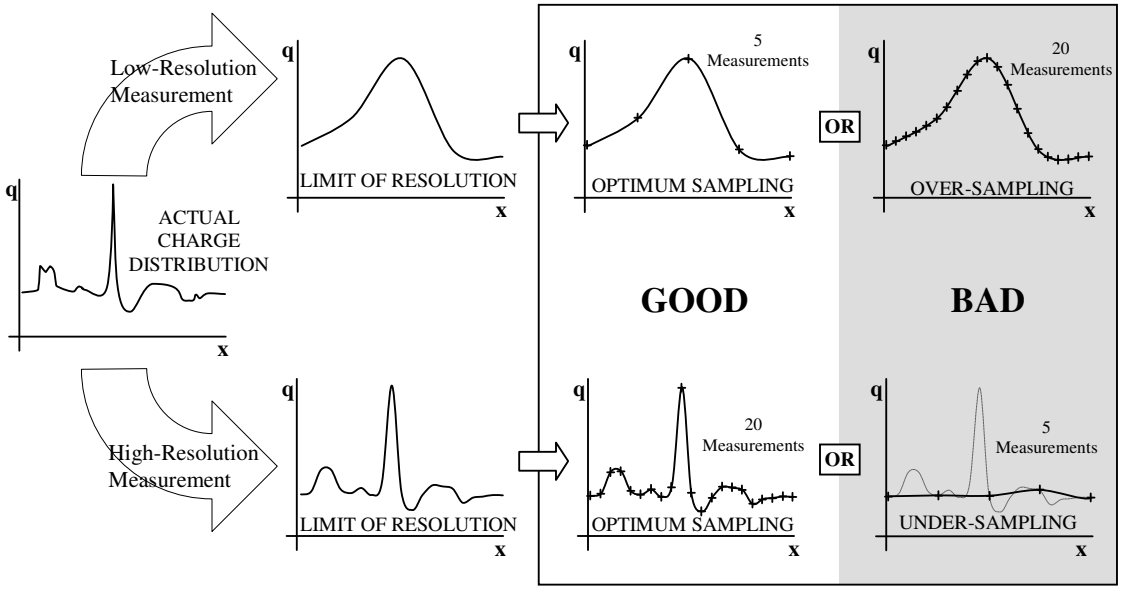

Figure 2.1.1: The number of measurements required depends on the measurement resolution.

Over-sampling occurs when too many measurements are taken for a particular resolution, this results in a waste of data storage resources. Conversely under-sampling occurs when too few measurements are taken for a particular resolution, and this could result in loss of features in the distribution.

The example shown in figure 2.1.1 is in 2-dimensions: a charge density axis and a single distance axis. To map a surface a second distance axis, y is required. This greatly increases the number of measurements required to define the distribution. So when considering a surface, increases in the resolution of measurement has an even larger effect on the number of measurements required.

If the example shown in figure 2.1.1 is expanded on to a regular surface grid:

Low-Resolution Measurement = $5 \times 5 = 25$ measurements

High-Resolution Measurement = $20 \times 20 = 400$ measurements

A four-fold increase in resolution results in a sixteen-fold increase in the number of measurements required.

It is therefore very important when recording high-resolution surface charge distributions to optimise the number of measurements taken.

2.2 V to σ

2.2.1 Introduction

As discussed in Chapter 1, the probe voltage measurements require further analysis to convert them to surface charge density values. The probe's response must be removed, or de-convoluted, from the probe voltage measurements to calculate the charge density distribution.

The technique used here is an adaptation of Pedersen's λ-function (Pedersen, 1987). He related the Poissonian charge (q) induced on the probe sensor plate to the surface charge density (σ) on a surface element: $q = \lambda\sigma$. The technique employed here uses the probe response function or *ϕ-function* to relate the contribution to the total probe voltage (v) to the surface charge density (σ) on a surface element: $v = \phi\sigma$. The total probe voltage (V) is the sum of the contributions from all the elements of surface charge: $V = \Sigma v = \Sigma\phi\sigma$. This relationship can then be used to calculate surface charge density distributions from the multiple probe measurements above each element of the surface.

This technique requires three prerequisites to work:

1. The probe response function must be known
2. The probe must have a linear response
3. The Principle of Superposition must hold

These are covered in the following section.

2.2.2 Model of Probe Operation

The ϕ-Function

The ϕ-function or probe response function is the probe's response to charge at different distances away from it. For the technique to work the ϕ-function of the probe must be accurately known.

Consider the screened probe is kept stationary in the centre of the insulator and a unit charge is moved in turn to each element of the insulator surface. The voltages induced on the probe by the unity charge in each element position give the probe response function or ϕ-function.

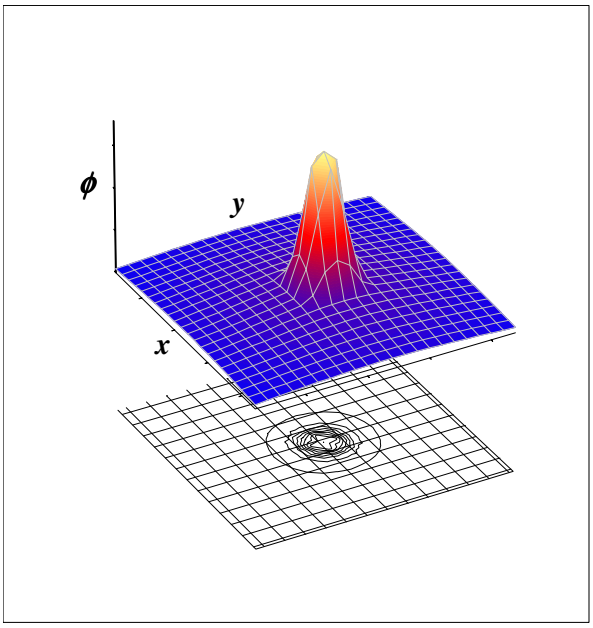

Figure 2.2.2: The probe response function ϕ.

An example ϕ-function is shown in figure 2.2.2, finite element modelling is used to obtain the ϕ-function. The smooth shape of the ϕ-function shows that the probe's resolution cannot be simply stated as a definite area, instead it must be given as the area within which the ϕ-function is above a certain value.

The exact shape of the function will depend on a number of factors including the dimensions of the probe, the distance of the probe from the surface and the size of the elements. The general rule for a ϕ-function is: charge close to the probe axis will induce a much larger voltage on the probe than charge further away.

ϕ-Function and Probe Position

The position of the probe and the position of surface elements should be defined on the same set of axes; this greatly simplifies element definition when trying to calculate charge distributions. When the surface is scanned measurements are taken above every element so if common axes are used a unique ϕ-function exists for every probe position. A few examples are shown in figure 2.2.3, the probe response is represented as contours with the black circle representing the position of the probe.

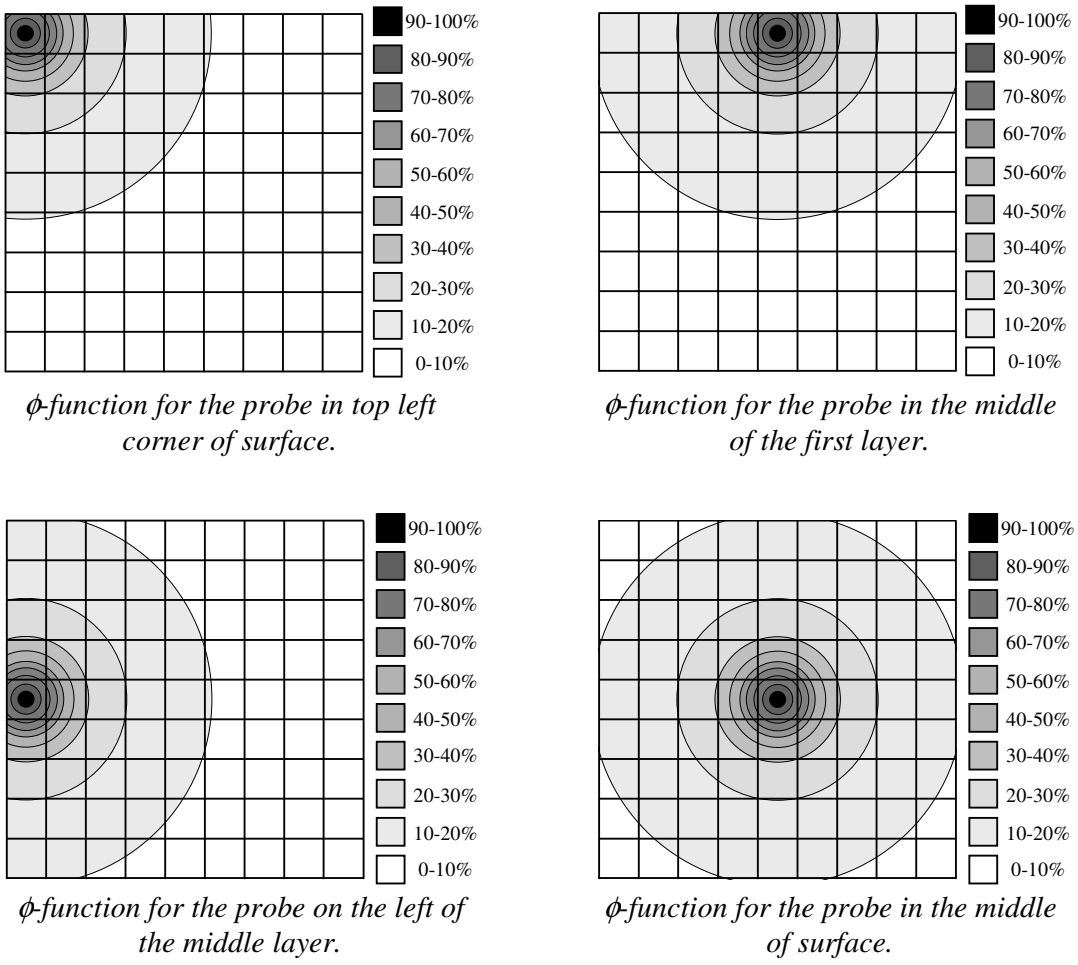

Figure 2.2.3: For each probe position a unique probe response function ϕ must be generated.

In general for each probe position the corresponding ϕ-function is simply linear translation of the same function. However the probe response does vary slightly as the probe moves over the surface. As the probe nears a ground plane the contributions from distant elements of charge reduce. If the test object surface is contoured the probe response will also be distorted slightly.

The probe response function is accurately found using three-dimensional finite element modelling as detailed in Chapter 4.

Linear response

The value of the ϕ-function for a particular element is the constant of proportionality between the net charge density on that element and the voltage induced on the probe.

$$v = \phi\sigma \qquad \text{and similarly:} \qquad \sigma = \frac{1}{\phi}v$$

Units of ϕ: Volts unit area per unit charge

The linear relationship is effectively the same result as derived using the simple capacitive model. The idea of a linear response is true for all surface elements, not just ones directly underneath the axis of the probe. This is confirmed by finite element modelling.

Principal of Superposition

The charges from a number of elements on the surface make contributions to the probe voltage. The total probe voltage is equal to the sum of the individual induced voltages from each of the elements on their own. This is illustrated by the results from a finite element modelling experiment shown in figure 2.2.4.

Three elements of surface charge each 1mm^2 with a charge density of 1μCm^{-2}.

Probe voltage for each element on its own:

A	10mV
B	6mV
C	3mV

Combinations of elements:

A and B	16mV	(=10+6)
B and C	9mV	(=6+3)
A and C	13mV	(=10+3)
A and B and C	19mV	(=10+6+3)

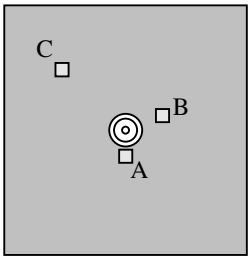

Figure 2.2.4: A simple theoretical experiment to demonstrate the principle of superposition.

When the probe is above a surface with an unknown charge distribution the probe voltage is the sum of each element of charge on the surface multiplied by its relevant ϕ-value obtained from the ϕ-function for the probe.

2.2.3 The Φ-Matrix Technique

Given the prerequisites are confirmed a surface charge density distribution can be calculated from a probe voltage distribution.

The first step is to formalise the definition of probe and element position on the surface, this is shown in figure 2.2.5.

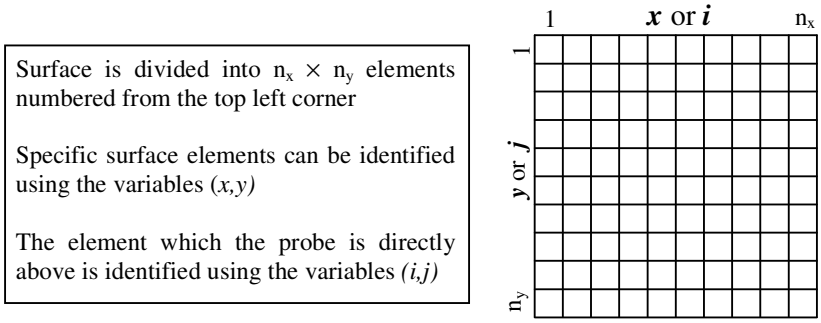

Figure 2.2.5: The generalised division of the insulator surface into elements.

This allows us to formulate a general equation for the induced voltage. With the probe above element (i,j) the probe voltage is given by:

$$v_{ij} = \sum_{n_y}^{y=1}\left[\sum_{n_x}^{x=1}\phi_{ij}(xy)\,\sigma_{xy}\right]$$

Where, $\phi_{ij}(xy)$ is the probe's response function to charge at position (x,y) for the probe at position (i,j) and, σ_{xy} is the surface charge density on the surface element at position (x,y).

This expands to:

$$\begin{aligned} v_{i,j} = {} & \phi_{i,j}(1,1)\,\sigma_{1,1} + \phi_{i,j}(2,1)\,\sigma_{2,1} + \cdots + \phi_{i,j}(n_x,1)\,\sigma_{n_x,1} \\ & + \phi_{i,j}(1,2)\,\sigma_{1,2} + \phi_{i,j}(2,2)\,\sigma_{2,2} + \cdots + \phi_{i,j}(n_x,2)\,\sigma_{n_x,2} \\ & \quad\vdots \qquad\qquad \vdots \qquad\qquad \vdots \\ & + \phi_{i,j}(n_y,2)\sigma_{n_y,2} + \phi_{i,j}(n_y,2)\,\sigma_{n_y,2} + \cdots + \phi_{i,j}(n_x,n_y)\,\sigma_{n_x,n_y} \end{aligned}$$

which is a first order function of the $n_x n_y$ surface charge densities.

There are $n_x n_y$ probe voltage measurements in total and each of these voltages is a function of $n_x n_y$ surface charge densities. The problem is reduced to the solution of $n_x n_y$ simultaneous equations. The matrix inversion technique lends itself ideally to the solution of large numbers of simultaneous equations. The application of this technique to this problem will now be detailed.

Define a voltage vector V, which is made up of all the probe voltage measurements:

$$\overline{V} = \begin{bmatrix} v_{1,1} & v_{2,1} & v_{3,1} & \cdots & v_{1,2} & v_{2,2} & v_{3,2} & \cdots & v_{1,n_y} & v_{2,n_y} & v_{3,n_y} & \cdots & v_{(n_x-2),n_y} & v_{(n_x-1),n_y} & v_{n_x,n_y} \end{bmatrix}$$

and a charge density vector σ, which is made up of the unknown surface charge densities:

$$\overline{\sigma} = \begin{bmatrix} \sigma_{1,1} & \sigma_{2,1} & \sigma_{3,1} & \cdots & \sigma_{1,2} & \sigma_{2,2} & \sigma_{3,2} & \cdots & \sigma_{1,n_y} & \sigma_{2,n_y} & \sigma_{3,n_y} & \cdots & \sigma_{(n_x-2),n_y} & \sigma_{(n_x-1),n_y} & \sigma_{n_x,n_y} \end{bmatrix}$$

They are related by the following matrix equation: $\overline{\sigma}\,\Phi = \overline{V}$

Where, Φ is a matrix containing all the ϕ-function values that are coefficients of the simultaneous equations:

$$\Phi = \begin{bmatrix}
\phi_{1,1}(1,1) & \phi_{2,1}(1,1) & \cdots & \phi_{1,2}(1,1) & \phi_{2,2}(1,1) & \cdots & \phi_{1,n_y}(1,1) & \phi_{2,n_y}(1,1) & \cdots & \phi_{(n_x-1),n_y}(1,1) & \phi_{n_x,n_y}(1,1) \\
\phi_{1,1}(2,1) & \phi_{2,1}(2,1) & \cdots & \phi_{1,2}(2,1) & \phi_{2,2}(2,1) & \cdots & \phi_{1,n_y}(2,1) & \phi_{2,n_y}(2,1) & \cdots & \phi_{(n_x-1),n_y}(2,1) & \phi_{n_x,n_y}(2,1) \\
\vdots & \vdots & \ddots & & & & & & & \vdots & \vdots \\
\phi_{1,1}(1,2) & \phi_{2,1}(1,2) & & \phi_{1,2}(1,2) & & & & & & \phi_{(n_x-1),n_y}(1,2) & \phi_{n_x,n_y}(1,2) \\
\phi_{1,1}(2,2) & \phi_{2,1}(2,2) & & & \phi_{2,2}(2,2) & & & & & \phi_{(n_x-1),n_y}(2,2) & \phi_{n_x,n_y}(2,2) \\
\vdots & \vdots & & & & \ddots & & & & \vdots & \vdots \\
\phi_{1,1}(1,n_y) & \phi_{2,1}(1,n_y) & & & & & \phi_{1,n_y}(1,n_y) & & & \phi_{(n_x-1),n_y}(1,n_y) & \phi_{n_x,n_y}(1,n_y) \\
\phi_{1,1}(2,n_y) & \phi_{2,1}(2,n_y) & & & & & & \phi_{2,n_y}(2,n_y) & & \phi_{(n_x-1),n_y}(2,n_y) & \phi_{n_x,n_y}(2,n_y) \\
\vdots & \vdots & & & & & & & \ddots & \vdots & \vdots \\
\phi_{1,1}(n_x-1,n_y) & \phi_{2,1}(n_x-1,n_y) & \cdots & \phi_{1,2}(n_x-1,n_y) & \phi_{2,2}(n_x-1,n_y) & \cdots & \phi_{1,n_y}(n_x-1,n_y) & \phi_{2,n_y}(n_x-1,n_y) & \cdots & \phi_{(n_x-1),n_y}(n_x-1,n_y) & \phi_{n_x,n_y}(n_x-1,n_y) \\
\phi_{1,1}(n_x,n_y) & \phi_{2,1}(n_x,n_y) & \cdots & \phi_{1,2}(n_x,n_y) & \phi_{2,2}(n_x,n_y) & \cdots & \phi_{1,n_y}(n_x,n_y) & \phi_{2,n_y}(n_x,n_y) & \cdots & \phi_{n_x-1,n_y}(n_x,n_y) & \phi_{n_x,n_y}(n_x,n_y)
\end{bmatrix}$$

Hence the unknown charge density's can be found by multiplying the probe voltage vector by the inverted Φ-Matrix thus:

$$\overline{\sigma} = \overline{V}\,\Phi^{-1}$$

2.2.4 Example Problem

In order to illustrate the application of the Φ-matrix technique to find charge distributions an example problem will now be worked through.

Consider a flat test object measuring 10mm by 10mm. The surface is divided into 10×10 square elements making a total of 100 elements numbered as shown in figure 2.2.6, where *x* and *y* are the co-ordinates of surface elements and *i* and *j* are the co-ordinates of the probe position above each element

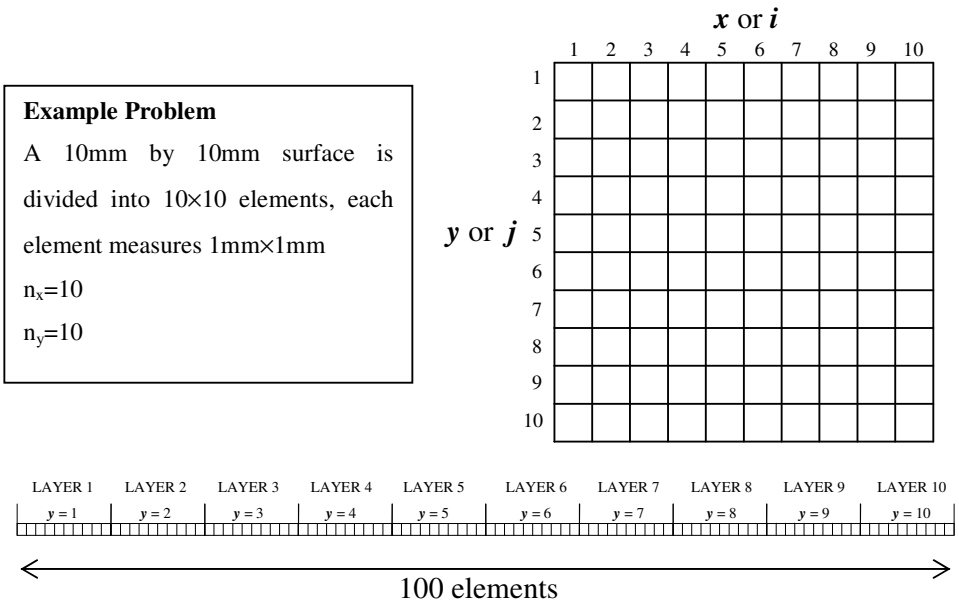

Figure 2.2.6: An example scanning problem, the division of the surface and the resultant voltage vector.

The surface will be scanned in horizontal layers, the probe will move horizontally across the surface starting from the top left-hand corner of the surface and the probe voltage will be recorded above each of the elements. The probe voltages are stored as a voltage vector as shown in figure 2.2.6.

The Φ-Matrix containing all the ϕ-values for the measurement test object is shown in figure 2.2.7. This matrix must be inverted, and then charge distributions can easily be found simply by multiplying the voltage vector by the inverted matrix. Other distributions measured using the same surface division can be solved using the same inverted matrix.

The Φ-Matrix shown in figure 2.2.7 is quite large, it contains 10,000 values. To solve a low-resolution charge distribution, 10×10 elements in this example, a 100×100 matrix must be inverted. The full implications of this size will be discussed in the Solver Software section.

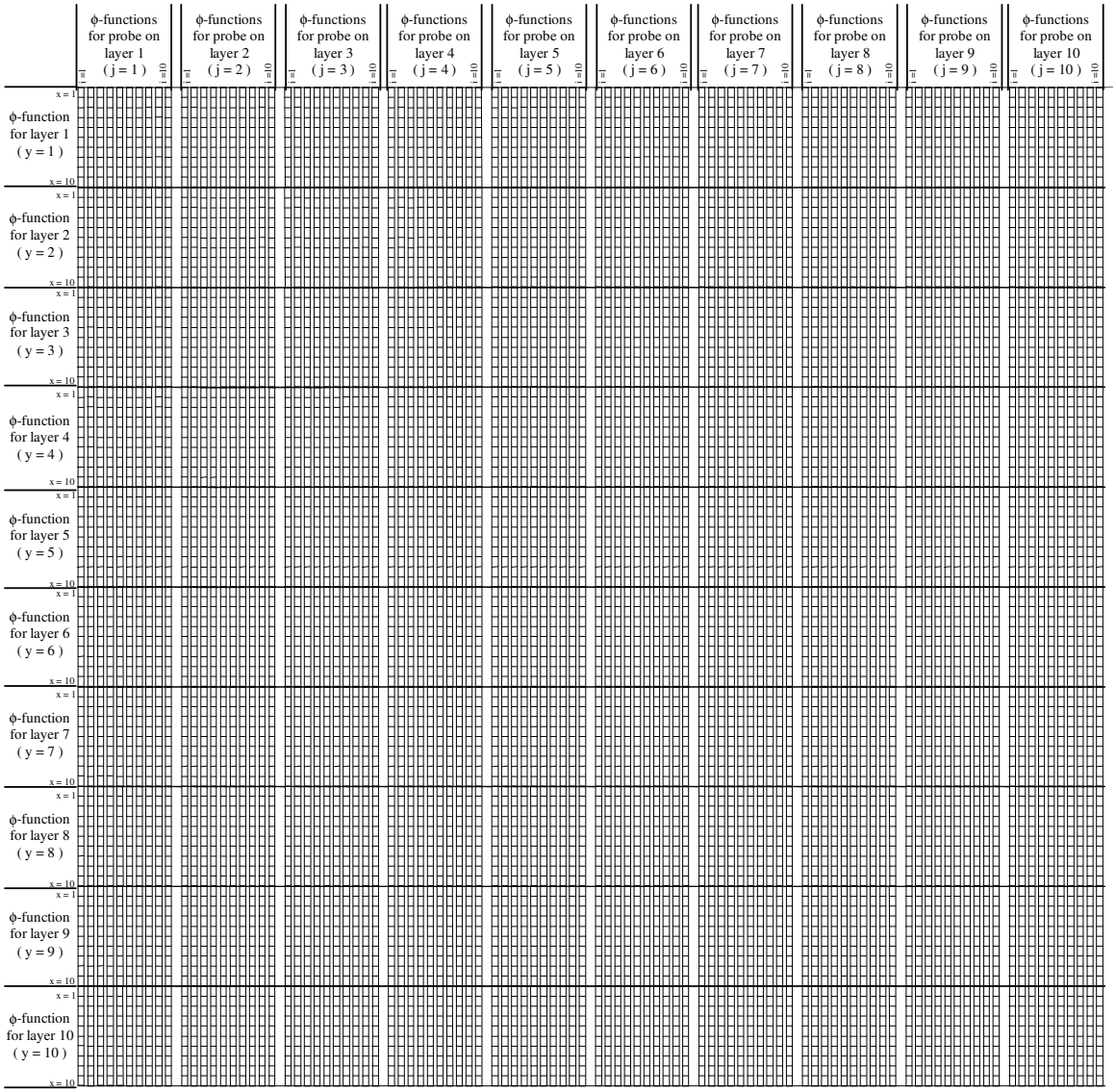

Figure 2.2.7: The size and layout of a Φ-Matrix to solve a 10×10 surface charge distribution.

2.3 Scanning System Hardware

2.3.1 Probe Design

Detailed Construction

The electrostatic probe is constructed from an inner conductor, surrounded by a PTFE insulating sleeve, and a grounded outer tube. Figure 2.3.1, shows the detailed construction.

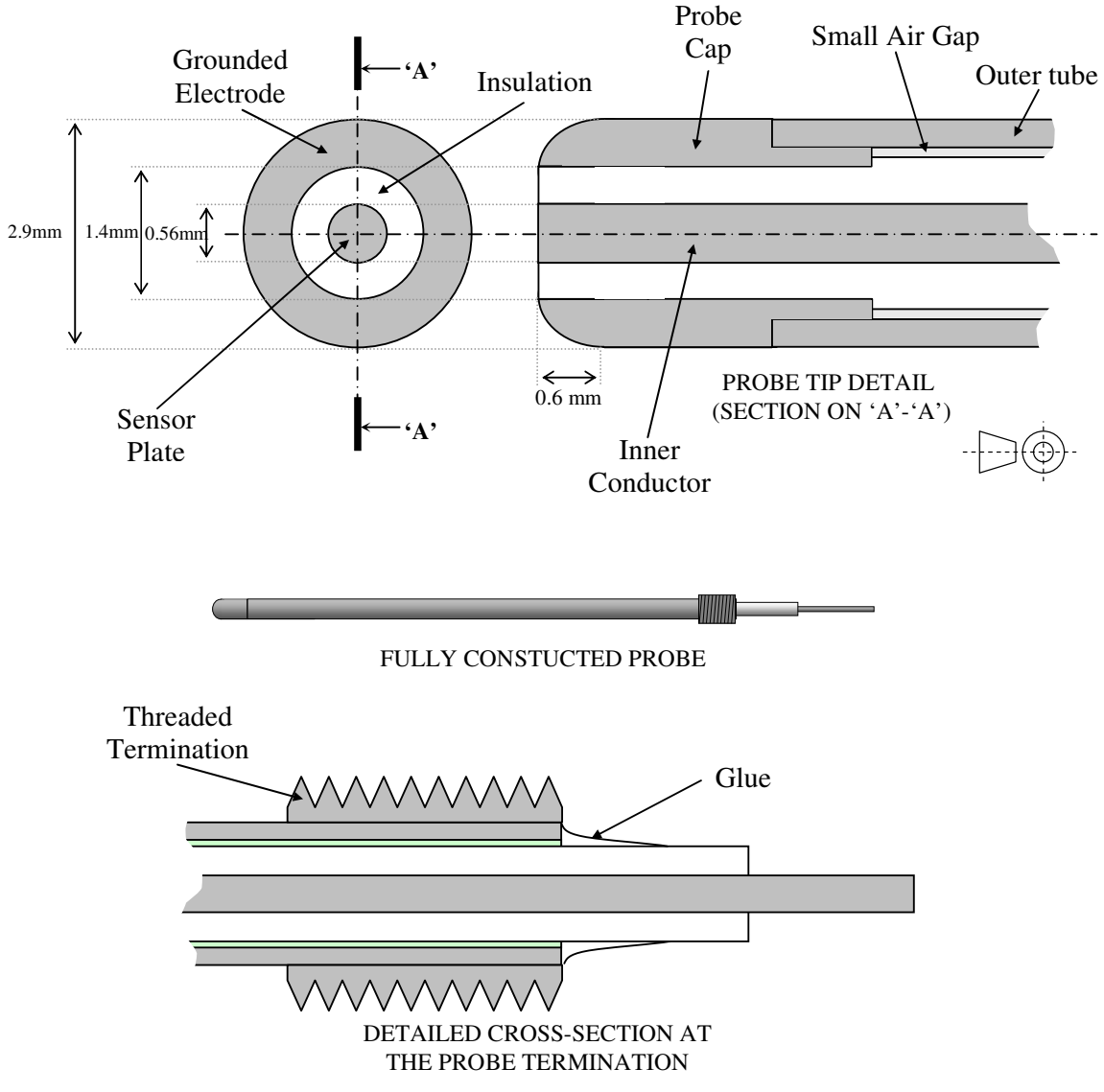

Figure 2.3.1: Detailed construction of the probe.

The probe is approximately 50mm long. The insulation is held in place at the probe termination by a small amount of glue. Care was taken to ensure the glue does not contact between the inner and outer conductors because this will increase the leakage current.

The outer tube is threaded at the probe termination to allow it to be mounted in a box. The grounded electrode on the probe cap is rounded to reduce field enhancements in the vicinity of the probe tip. This is done in an attempt to avoid discharges between the probe and the surface.

Capacitance to ground

Referring to figure 1.3.1, the probe-ground capacitance acts as the low voltage arm of the voltage divider set up by the probe, insulator specimen and surface and charge. The high voltage arm is the probe-insulator surface capacitance, which for the probe 1mm away from the surface is in the order of a few femtofarads.

The probe-ground capacitance was measured using an LCR bridge and found to be 10.8pF, this gives a divider ratio in the order of 1:10,000. Surface to ground voltages will be in the range of a few kV; hence probe voltages will be in the order of 1V. This is comfortably in the input voltage range for digital measurement systems.

Leakage resistance to ground

The product of the probe's resistance and capacitance to ground gives the measurement circuit RC time constant. The probe's resistance to ground is made up of the probe leakage resistance in parallel with the input resistance of the measurement circuit. The probe's capacitance is fixed by its geometry, so to achieve as large an RC time constant as possible, the probe's resistance to ground must be maximised. This will prevent charge loss as the probe scans across the surface. The probe is above each element of the surface for only a fraction of a second so provided the RC time constant is much greater than this, then the effect on the surface charge density will be minimal.

To give a time constant of around 100 seconds the resistance to ground needs to be at least 10,000GΩ. To achieve such a high value a good insulation material is required combined with a very high input impedance measuring system. Being one of the best insulating materials available, PTFE is the ideal candidate. It has a bulk resistivity of

over $10^{18}\Omega cm^{-1}$. The insulator surface is also an important factor; surface water films and dirt drastically reduce surface resistivity. PTFE has a good resistance to surface water absorption and the insulator surface at the probe tip was cleaned with ethanol to remove any grease. Before the probe was installed its insulation was tested with a Megger and the leakage resistance was found to be in excess of 100GΩ.

Probe buffering

Most voltage-measuring instruments (such as oscilloscopes) do not have a high enough input impedance to prevent a significant current being drawn from the probe and hence the charge on the surface of the insulator affected. To effectively isolate the probe voltage signal a buffer circuit is required. The ideal solution is an op-amp configured as a buffer amplifier. The op-amp must have a very low input bias current; a specialised device is available from Analog Devices. The AD549 is a monolithic electrometer operational amplifier with very low input bias current. "Topgate" JFET technology, a process exclusive to Analog Devices, allows the fabrication of extremely low input current JFETs, compatible with a standard junction-isolated bipolar process. The $10^{15}\Omega$ common-mode impedance, a result of the bootstrapped input stage, ensures that the input current is essentially independent of common-mode voltage. The probe buffer circuit diagram is shown in figure 2.3.2.

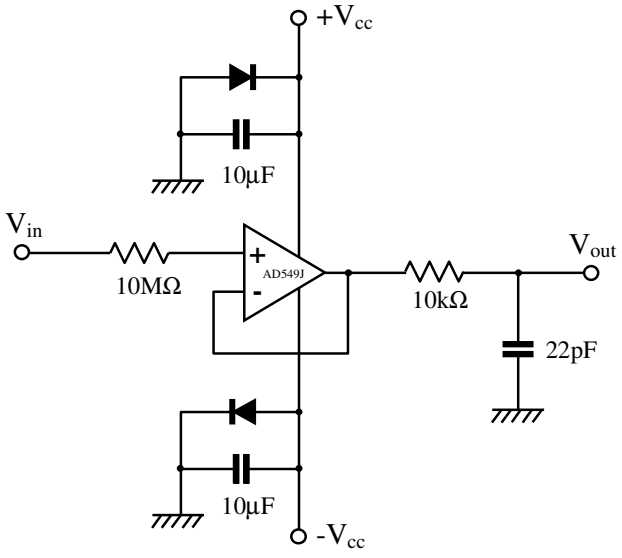

Notes

The diodes and 10µF capacitors on the power supply lines provide additional voltage stabilisation. The 10MΩ resistor offers input protection from 'accidents' with the probe. The 10kΩ resistor and 22pF capacitor make up a low pass filter on the output of the circuit.

Figure 2.3.2: Circuit diagram of probe buffer amplifier.

Probe Voltage Drift

The input bias current, besides possibly affecting the charge on the surface, also acts to charge the probe capacitance. This results in the probe voltage slowly drifting with time. The very low input bias-current required for the AD549 minimises this problem but cannot completely remove it. Grounding the probe will discharge the probe capacitance but the current drawn will act to slowly charge it again. Figure 2.3.3 shows this effect for the probe held stationary away from any surfaces. The first 4-minute run is different from the later three because the op-amp is still warming up; the manufacturers give the warm up time as 2 minutes. After the op-amp has settled a repeatable output voltage drift is obtained (runs 3 and 4 are almost identical).

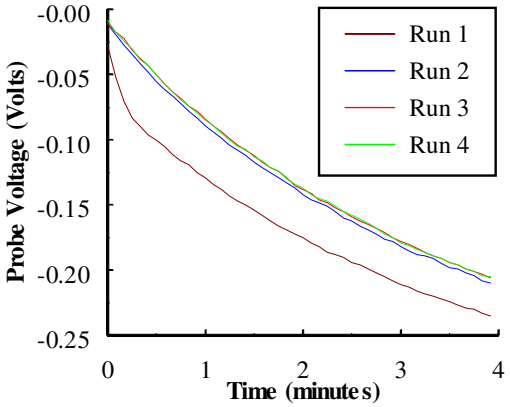

Figure 2.3.3: The probe drift and warm-up characteristics.

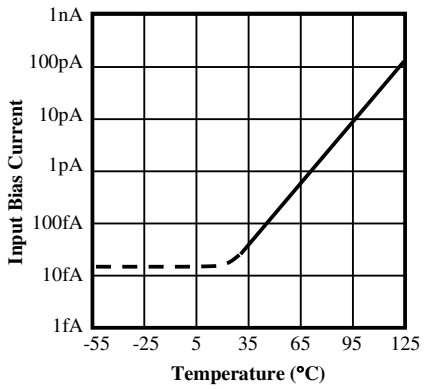

Figure 2.3.4: Manufacturer's Input bias current vs. Ambient Temperature data.

The repeatability of the drift rate means that the probe drift component can be removed from the measured probe voltage distribution after it has been recorded. This technique is described in the later section on the scanning software.

An important point to note is that the input bias current does vary with temperature, the manufacturer's response characteristics are shown in figure 2.3.4. On chip power dissipation will raise chip-operating temperature causing an increase in input bias current. Due to the AD549's low quiescent supply current, chip temperature is usually less than 3°C higher than ambient. The difference in input bias current will be small, but external temperature variations will affect the probe drift rate on a day to day basis. Hence the probe drift rate should be measured each day measurements are conducted; a utility for simply doing this is described in the scanning software section.

Buffer Circuit Construction

There are various physical phenomena that become important factors when designing circuit board layouts for very high input impedance amplifiers. Parasitic leakages and capacitances become significant; for this circuit application the leakage paths are of primary interest. The parasitic capacitances to ground are only of real importance when high frequencies are involved and in any case the parasitic capacitance at the buffer circuit input will be insignificant compared to the probe-ground capacitance in parallel with it. Various techniques have been applied to minimise leakage, figure 2.3.5 shows the printed circuit board layout for the probe buffer amplifier.

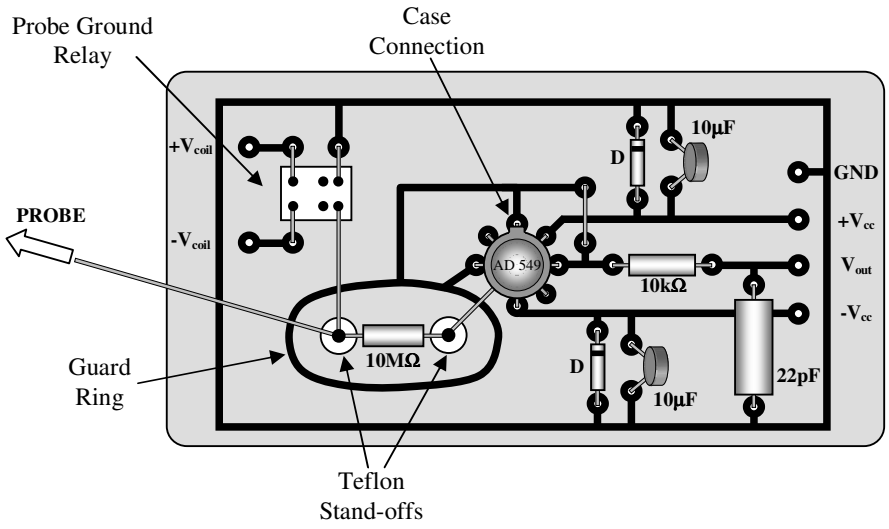

Figure 2.3.5: Printed Circuit Board layout for the probe buffer circuit.

Insulation resistance of over $10^{15}\Omega$ is required between the amplifier's signal and supply lines in order to capitalise on the AD549's very low input current. Standard PCB material does not have high enough insulation resistance, so the input line is connected to PTFE stand-offs. PTFE has a high enough volume resistivity to provide adequate isolation. The surface of the stand-offs is also an important factor; surface water films and dirt drastically reduce surface resistivity. PTFE has a good resistance to surface water absorption and the stand-offs were cleaned with ethanol to remove any grease.

By surrounding the input line with a metal conductor at the same potential, the leakage is further reduced. This is achieved by use of guarding techniques such as a guard ring and a case connection. The ring and case are bootstrapped to the same potential as the

input by connecting them to the output of the amplifier. Guard rings also reduce parasitic ground capacitances and case bootstrapping reduces parasitic capacitances between the input and other legs on the chip.

The miniature relay for grounding the probe is mounted with its legs sticking in the air so as to avoid the PCB. The open circuit resistance of the relay was found to be greater than 100GΩ using a Megger.

Other construction considerations include keeping the input line as short as possible, this is achieved by mounting the probe on the same box as the circuit board so it can connect directly to the circuit. The circuit assembly is kept rigid to reduce triboelectric, piezoelectric and microphonic charging of the insulating stand-offs. The box is well screened to provide good shielding from interference noise. Screened cable is used to take the external connections for the circuit and low noise coax takes the probe signal to the measurement apparatus. The fully constructed probe is shown in figure 2.3.6.

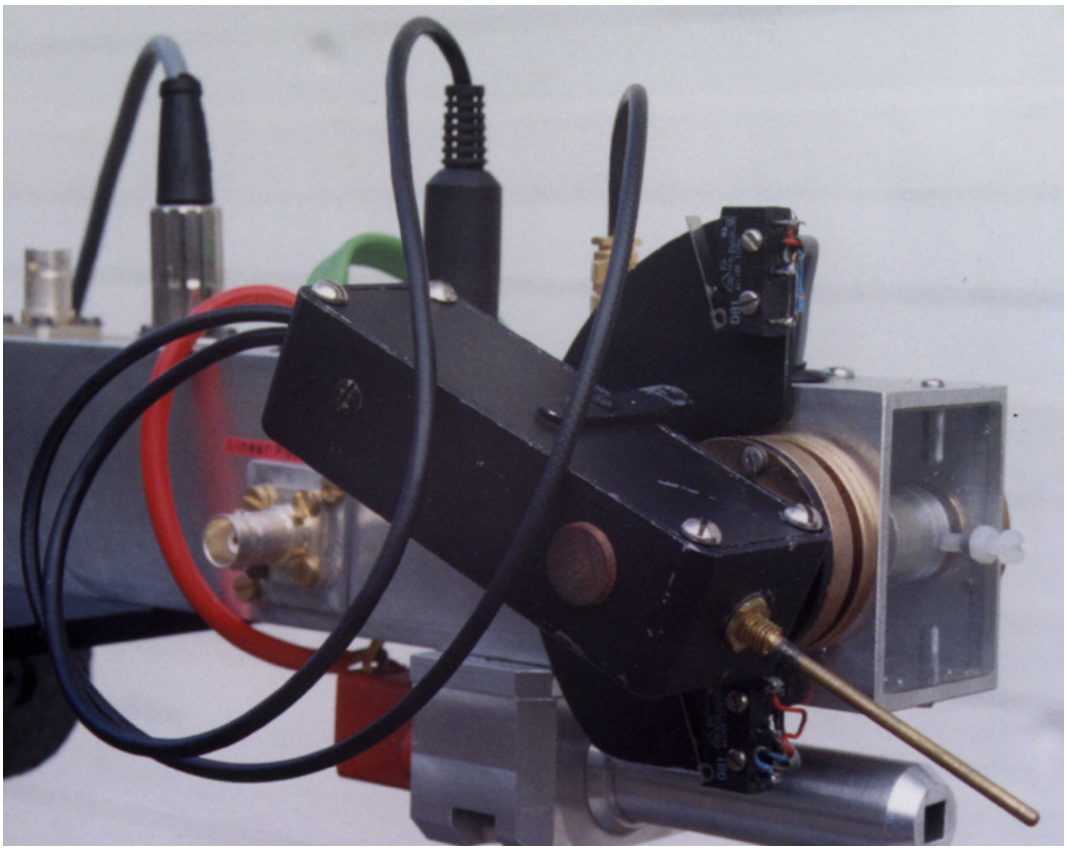

Figure 2.3.6: The fully constructed probe mounted on the scanning platform.

2.3.2 The Scanning Platform

Requirements

The measuring probe must move over the entire region of the insulator surface to be scanned taking probe voltage measurements from above each element of the surface. This means the probe has to take a certain path across the surface; like a television picture which is made up of a number of lines, each line made up of a number of points. The probe sensor plate must also be positioned parallel to and at a specific distance from each surface element. This will keep the calibration as simple as possible. Different insulator shapes call for different scanning techniques.

Scanning Techniques

Flat Surfaces

The simplest way to scan a flat surface to in either in either rows or columns as shown in figure 2.3.7. Bier et al, 1991 applied this technique. Abdul-Hussain and Cornick, 1987 employed an arc shaped scanning path. However this led to complications involving element size and interpolation onto a regular grid. The only reason for choosing a more exotic scanning technique is to simplify another part of the apparatus.

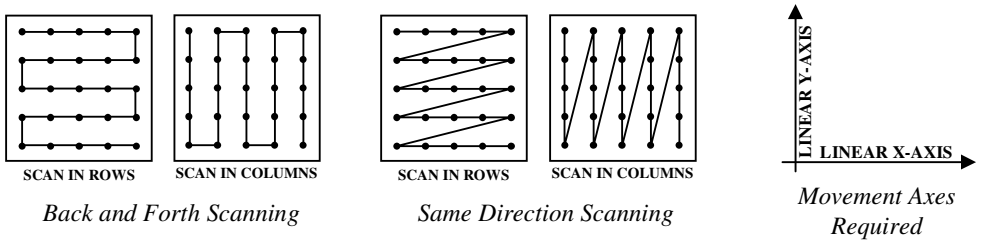

Figure 2.3.7: Simple scanning paths and scanning axes for a flat insulator surface.

Only two axes are required to move a probe over a flat surface. It is advisable to scan each layer in the same direction as opposed to back and forth for two reasons:

1. The probe will move at a constant velocity along each layer and may have a small time response, if the layers are scanned in alternate directions then when the distribution is reconstructed there will be slight visible discontinuities between each layer.

2. Due to slack in mechanical systems it is hard to position the probe exactly at a specific location, however relative positioning is no problem because when the probe moves to one position then back again the slack error is removed. If the probe is following a same-direction scanning path then it will always have the same relative start position for each layer. However back and forth scanning means that only alternate layers will have exactly the same start position. If the slack is large enough this will be visible as discontinuities between the layers in the reconstructed distribution.

The only advantage of back and forth scanning is that the distance the probe has to move is almost halved, which will translate to a saving in scanning time.

Cylindrical Surfaces

There are several options open when considering a cylindrical specimen as shown in figure 2.3.8. In the same way as with a flat surface only two axes are required to move the probe over the surface.

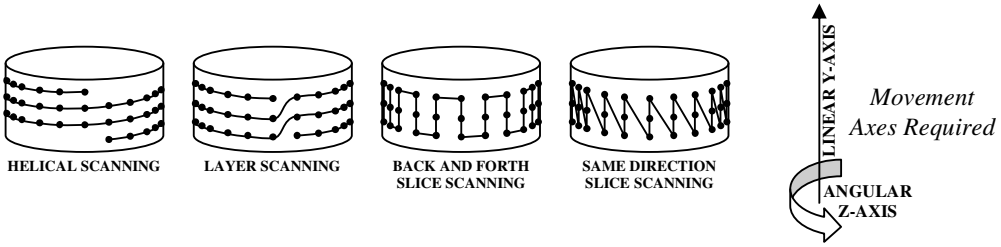

Figure 2.3.8: Scanning path and scanning axis for a cylindrical insulator surface.

One approach is to continuously rotate the insulator specimen and move the probe slowly down, thus creating a helical scanning path. The problem with this technique is that it makes reconstructing the distribution accurately rather difficult. Al-Bawy, 1991 used this technique in work on cylindrical insulators and made the simplification of taking each helical revolution as a circular revolution of the cylinder. This introduces a small amount of distortion to the element shapes; an effect that increases as the pitch of the helical path increases (i.e. the distance the probe has moved down for each revolution of the sample).

The major advantage of helical scanning is that the scanning apparatus can be very simple; two motors set to run at constant specific speeds.

The element shape distortion problem associated with helical scanning is not a factor when considering the other scanning paths shown in figure 2.3.8. The two simplest scanning paths are either in circular layers or in vertical slices moving around the circumference of cylinder. The advantage of scanning in circular layers is that the probe always returns to the start position for the next layer so the need to go back and forth is removed. Although the scanning apparatus required is more complicated than for the helical case, scanning in circular layers is the best technique for cylindrical insulators.

Simple Contoured Surfaces

A contoured surface is much more difficult to scan than a flat or cylindrical one. The additional complication is caused by the need to keep the probe sensor plate parallel to each surface element. Simple contoured surfaces are only curved in one dimension, the example shown in figure 2.3.9 is only curved in the Y-axis dimension, paths on the surface in the Z-axis dimension are straight lines. Simple surface contouring means that two additional movement axes are required to position the probe: a linear axis and an angular probe yaw axis.

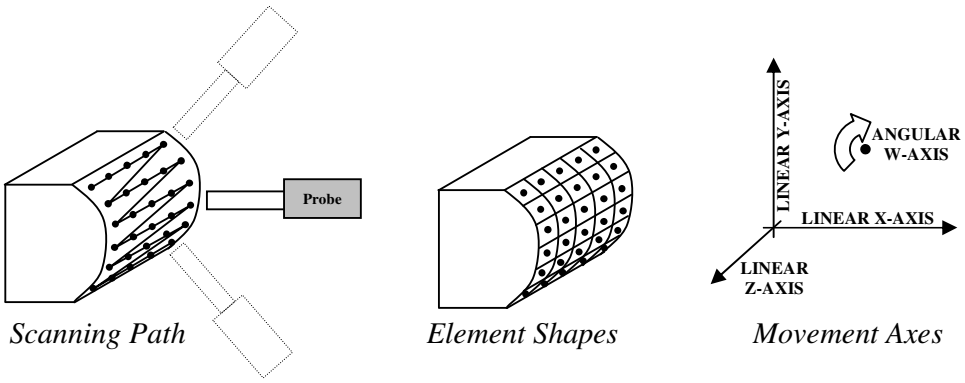

Figure 2.3.9: Scanning path and scanning axis for a simple contoured insulator surface.

Contoured Axi-Symmetric Surfaces

Contoured axi-symmetric insulators are almost exactly the same as simple contoured surfaces except the Z-axis is angular rather than linear as is shown in figure 2.3.10. The difference is that the elements change shape as the radius of the surface (X-axis) varies.

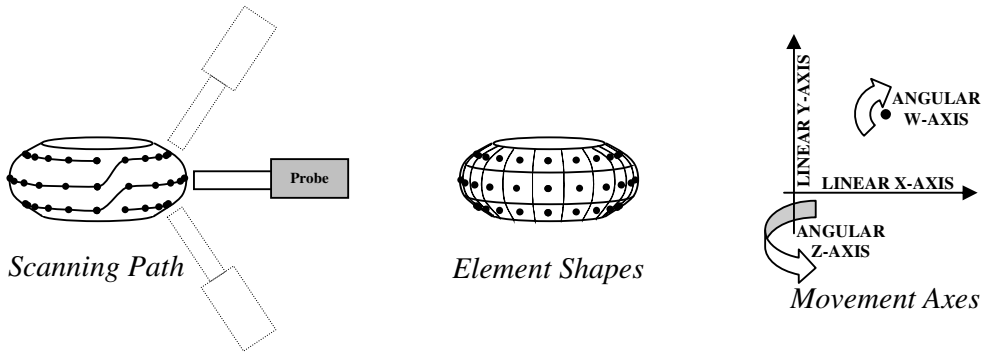

Figure 2.3.10: Scanning path and scanning axis for an axi-symmetric contoured insulator surface.

Contoured axi-symmetric surfaces are visible in the shape of many practical high-voltage insulators, which makes their study very attractive. The complication of varying element area can be dealt with during the calibration procedure.

Other Contoured Surfaces

More complex geometries, such as surfaces contoured in two dimensions require an additional probe movement axis: angular probe yawl. For a system with 5-degrees of freedom the mechanics and control software become increasingly complicated.

Some geometries could be scanned using a specifically designed rig, however a dedicated scanning system would remove almost all flexibility. Other complex test objects may be reducible to simpler compound objects of which one or some could be scanned using the other scanning techniques.

An example of a previous scanning system for dedicated geometries was that of Ootera and Nakanishi, 1988 to measure charge distributions on DC-GIS cone shaped spacers.

Implementing The Scanning Technique

To build a generalised scanning platform capable of scanning any contoured test object would raise too many technical difficulties; one has to weigh-up the benefits of any possible discoveries with the additional effort involved in developing such apparatus. Contoured axi-symmetric surfaces offer the best geometry for the study of practical high voltage insulators. In order to implement such a scanning technique for a general surface the probe must be mounted on a unit that can yaw about a horizontal axis, and move vertically and horizontally along linear shafts. The insulation sample must be mounted so that it can be rotated on a vertical axis. A diagram of the scanning platform is shown in figure 2.3.11.

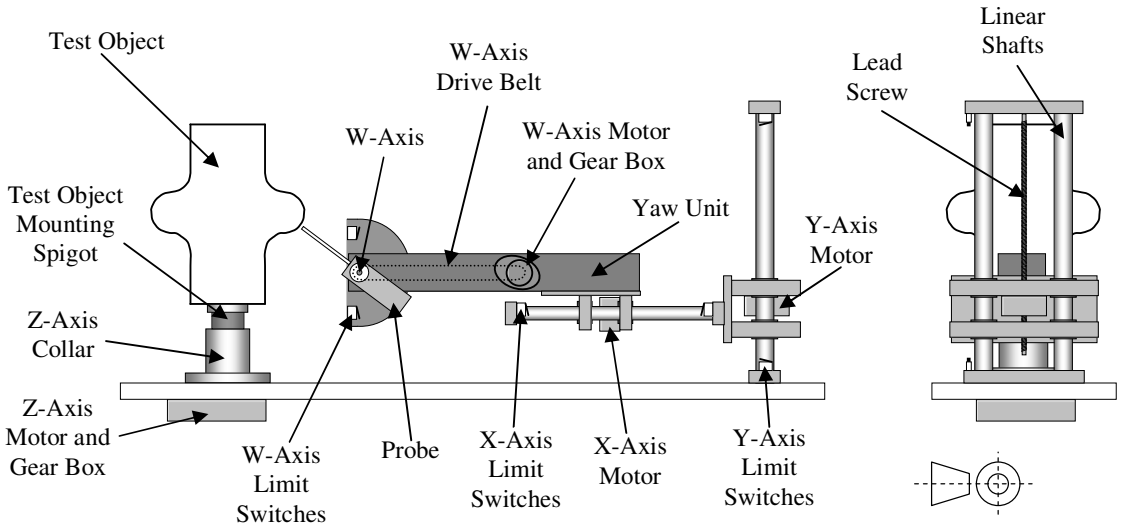

Figure 2.3.11: A detailed Schematic of the Scanning Platform.

The positioning of the axes is obviously critical, so the choice of actuation method is of importance. Movements along the main load bearing axes (X and Y) are made by means of linear actuators with lead screws, thus providing high torque and fine control over positioning. The distance between the end of the yaw unit and the W-axis must be minimised to optimise the potential scanning locus. To achieve this the axis is driven from a motor with a gearbox via a non-stretch drive belt (syncroflex timing), allowing the W-axis to be mounted at the very end of the yaw unit. The Z-axis is driven by a motor via a gearbox to give fine positional control. A load-bearing collar takes the weight of the test object, which is mounted on the Z-axis by a spigot.

The scanning platform was manufactured in the Mechanical Workshop in the Ferranti Building at UMIST.

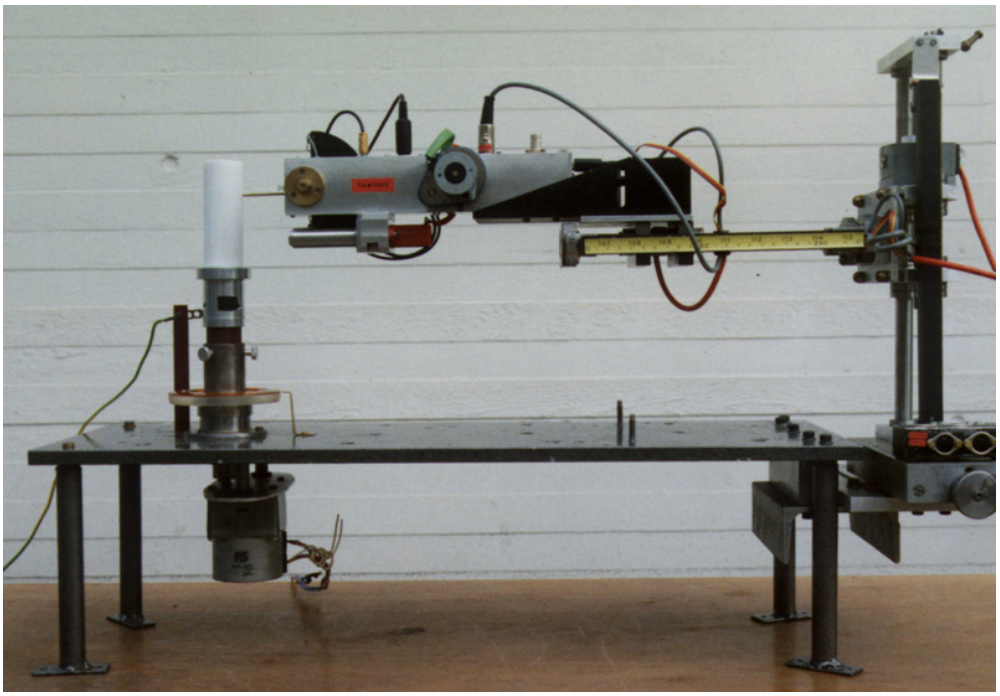

Figure 2.3.12: The scanning platform and a cylindrical test object.

Stepper motors

Stepper motors were chosen to drive the scanning platform because of their excellent controllability and positional accuracy. They are also ideally suited to digital control systems.

The stepper motor translates a pulsed square-wave excitation into a precisely defined angular increment in shaft position. Each pulse moves the motor through a fixed angle, so when a given number of drive pulses have been supplied to the motor, the shaft will have turned through a known angle. This allows the use of an open-loop position control system.

The angle through which the shaft moves for each pulse is termed the step angle, and is expressed in degrees. The smaller the step angle, the greater the number of steps per revolution, and the finer the resolution of the positioning can be. This resolution can also be improved further by the use of gearboxes.

Figure 2.3.13 illustrates the basic method of controlling stepper motors.

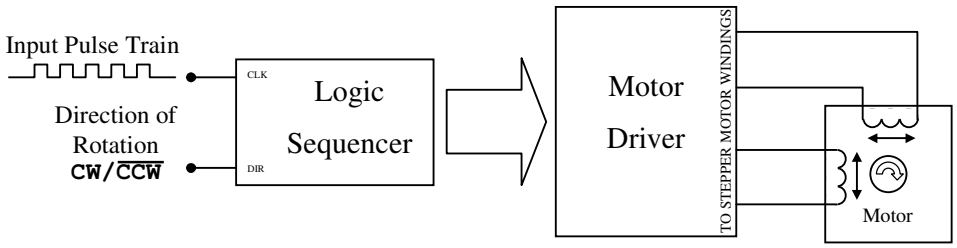

Figure 2.3.13: Basic principal of stepper motor control

A train of pulses is sent to a logic sequencer together with a logic signal representing the desired direction of rotation. This sequencer produces a set of logic signals that drive the power output stage (the motor driver), feeding the phases of the stepper motor. The number of pulses in the input pulse train determines the total angle turned through, and the 'input pulse rate' sets the motor speed.

When the motor is energised and stationary, it will resist rotation; the holding torque is defined as the maximum steady torque that can be applied to the shaft of an energised motor without causing continuous rotation.

If the motor has a permanent magnet rotor it will have a braking torque even when not energised. This is the detent (residual) torque which is a useful feature for positional integrity.

Note that the dynamic performance is limited because the motor may lose synchronisation, particularly with high-inertia loads. Also the rotor movement becomes oscillatory and unstable in certain speed ranges. However the control software ensures neither of these things happen.

The Stepper Motors used in the scanning platform have the following specifications:
X and Y-axis are driven by the same type of stepping linear actuator.

Step Size (Full Step)	0.025mm
Starting Force	125N
Rated Voltage	12V
Rated Current/phase	0.48A
Step accuracy	±0.005mm
Accuracy of repetition	±0.01mm

Table 2.3.1: X and Y-axis linear actuator specifications.

The Z and W axis are driven by 4-phase unipolar permanent magnet stepper motors. The two motors used are from the same range, but the Z-axis motor is the highest rated motor in the series and the W-axis motor is the lowest.

Axis	Z	W
Step Angle (full step)	7.5°	7.5°
Holding Torque	240mNm	20mNm
Detent Torque	16mNm	3mNm
Rated Voltage	12.7V	12.7V
Rated Current/phase	0.48A	0.19A

Table 2.3.2: Z and W-axis linear actuator specifications.

The Z and W axis motors are used in conjunction with gearboxes to improve torque ratings and provide finer positional control.

Axis	Z	W
Gear Ratio	5:1	12.5:1
Max Output Torque Capability	4Nm	0.8Nm

Table 2.3.3: Z and W-axis gearbox specifications.

The use of gearboxes introduces backlash into the system which has consequences for the positional accuracy; this effect is accounted for by the control software (see backlash compensation in the scanning system control software section). The manufacturers give typical gearbox backlash as 2°.

The overall technical specification for the scanning platform actuation system is:

Axis	X	Y	Z	W
Step size (full step)	0.025mm	0.025mm	1.5°	0.6°
Max Torque/Force	125N	125N	1.2Nm	0.25Nm

Table 2.3.4: Overall specifications.

If half-stepping is used the step size can be halved; this is discussed in the section on the scanning system interface unit.

Limit Switches

In order that the control software can align itself and know when the scanning platform has hit its end-stops limit switches are required. These are simply lever arm micro-switches positioned at the limits of travel for each of the axes, which are triggered when the platform runs into them. The positions of the limit switches for the X,Y and W axis are shown in figure 2.3.11. The Z-axis, used for test object rotation, does not need limit switches because it is free to rotate continuously. The position of the Z-axis is measured relative to an arbitrary start point.

Scanning Locus

The lengths of the axes define the range of test object geometries that can be scanned. The overall scanning platform locus is shown figure 2.3.14.

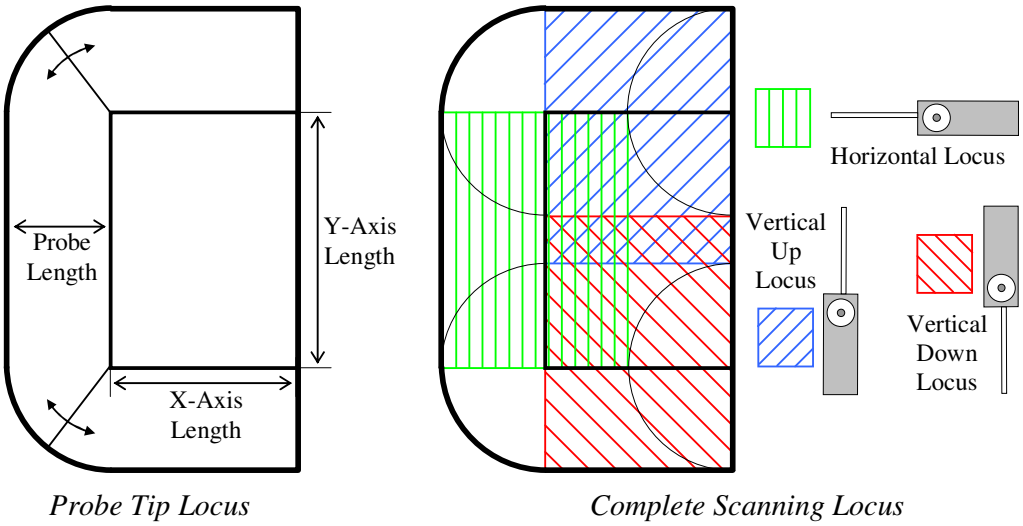

Axis Lengths:

X = 125mm Y = 171.75mm

Z = 360° continuous W = 180°

Probe Length = 69.5mm

Figure 2.3.14: The movement locus of the scanning platform.

Platform Offset

To allow a range of different size insulators to be scanned the scanning platform locus can be offset. The yaw unit can be moved backwards on its support and the test object mounting spigot can be height adjusted to allow for different sized insulator specimens.

Position Sensor

A sprung loaded variable resistor is mounted on the bottom of the yaw unit, this can be seen in figure 2.3.15. The purpose of this device is to automate the process of inputting the surface geometry to be scanned. A square cross-sectioned rod with a small wheel mounted on its end can be slotted into the variable resistor housing. Under the control of the scanning software the platform moves in until the wheel hits the surface and depresses the sprung loaded variable resistor. The platform then tracks down the insulator surface recording its profile by the corresponding movements of the rod.

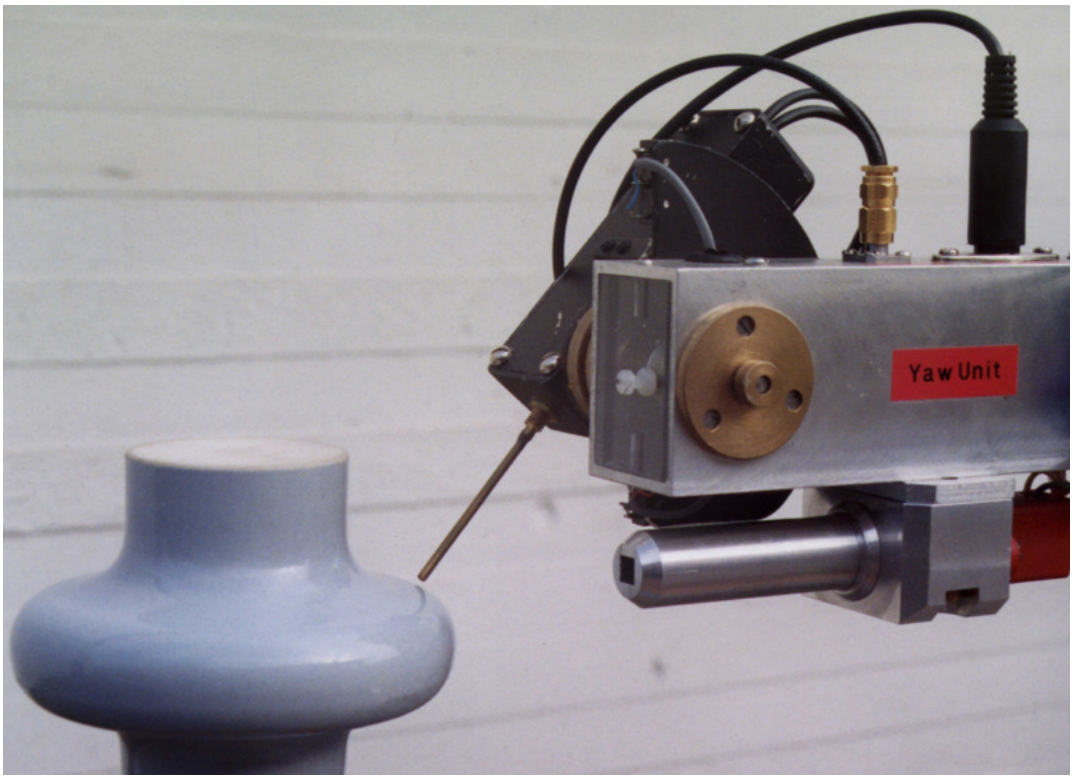

Figure 2.3.15: The scanning system in action, scanning a contoured insulator specimen.

2.3.3 Scanning System Interface Unit

Purpose

The scanning system interface unit is required to provide the connection between the scanning platform and the control hardware. It contains the logic sequencing and power electronics for driving the stepper motors, the circuitry to control and monitor the electrostatic probe, and provides electrical isolation between the scanning platform and the control hardware.

Drive boards

Introduction

The drive boards convert the low voltage pulse train and control signals from the control hardware into voltages and currents high enough to drive the stepper motors. There was no need to design new driver boards for the motors. An undergraduate laboratory in the Electrical and Electronic Engineering Department at UMIST involves designing and writing a program to control an X-Y plotter. The drive boards used here are simply modified versions of these. The drive circuitry for a single motor is shown in figure 2.3.16.

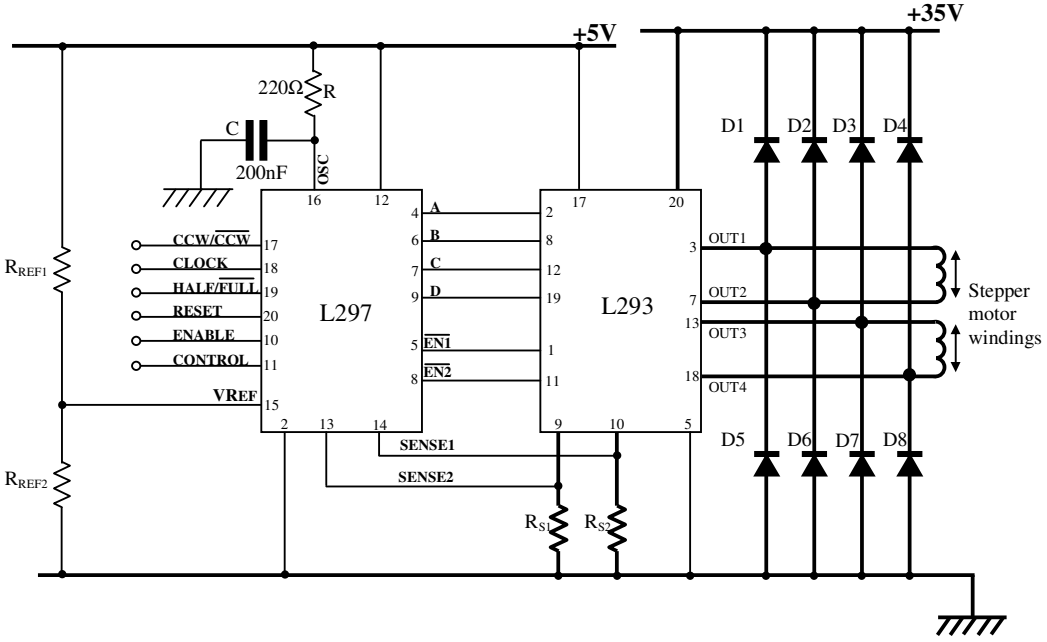

Figure 2.3.16: Stepper motor drive circuit.

Logic Control

The drive circuitry consists of a logic sequencer, the L297 Controller, and a power electronics chip, the L293 Full Bridge Driver. The logic sequencer is used to generate the required control signals (labelled A,B,C and D in figure 2.3.16) and enable lines ($\overline{EN1}$ and $\overline{EN2}$) to control the power electronics stage.

The equilibrium positions for stepper motors are different depending on whether one phase alone is energised or whether two phases are energised together. It is hence possible to operate the motors in two different modes: full or half-stepping. The logic sequences for the two different modes of operation are shown in figure 2.3.17.

STEPPING SEQUENCE

	A	B	C	D
1	ON	OFF	OFF	ON
2	ON	OFF	ON	OFF
3	OFF	ON	ON	OFF
4	OFF	ON	OFF	ON
Repeat	ON	OFF	OFF	ON

Full Stepping

STEPPING SEQUENCE

	A	B	C	D
1	ON	OFF	ON	OFF
2	ON	OFF	OFF	OFF
3	ON	OFF	OFF	ON
4	OFF	OFF	OFF	ON
5	OFF	ON	OFF	ON
6	OFF	ON	OFF	OFF
7	OFF	ON	ON	OFF
8	OFF	OFF	ON	OFF
Repeat	ON	OFF	ON	OFF

Half Stepping

Figure 2.3.17: The two modes of stepper motor operation.

In full stepping mode two phases are energised at each step, however in half stepping mode first two phases then one phase are energised on alternate steps. Half-stepping effectively adds another step half way between each of the full steps.

The advantage of half stepping is that it doubles the positional resolution obtainable and increases dynamic stability by reducing the susceptibility of the motor to resonance. However there is a price to pay for these benefits in that the maximum torque obtainable is almost halved when operating in half stepping mode.

In this application fine control over positioning is the important factor so half-stepping is used on all the motors. By using overrated stepper motors the problems of reduced torque are removed.

The current drive pulses that are applied to the stepper motor coils should have a fast rise time to allow the motors to be driven as fast as possible. This is achieved by over-volting the motors with a high frequency chopped drive pulse. The higher voltage allows a fast build up of current in the coils. To prevent damage to the motors the current through the coils is monitored by the sensing resistors R_{S1} and R_{S2} and limited by the L297 chip.

Referring back to Figure 2.3.16 the chopping frequency is set by R and C connected to OSC on the L297 chip. The frequency is given by 1/0.69RC, which for the values used gives: f = 1/0.69×220Ω×200nF = 33kHz. This frequency was chosen because it is slow enough to allow complete current build up in the inductive coils, yet high enough to remain inaudible.

The coil current is limited when the voltage across the sensing resistors becomes greater than V_{REF}, as set by the voltage divider made up by R_{REF1} and R_{REF2}. For each of the motors the current is limited to its rated value.

Power Output Stage

The motor control signals from the logic chip are connected to the power output stage that drives the stepper motor coils. The L293 is a quad push-pull driver capable of delivering output currents up to 1A per channel. Each channel is controlled by a TTL-compatible logic input and each pair of drivers (a full bridge) is equipped with an enable line which turns off the transistors. A block diagram for the L293 is shown in Figure 2.3.18.

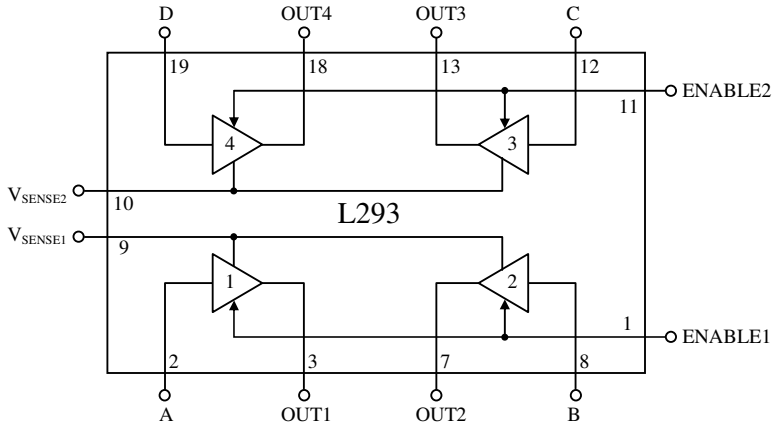

Figure 2.3.18: Block diagram showing operation of the L293 quad push-pull driver.

Interface Boards

The primary function of these boards is to isolate optically the power electronics components from the control hardware circuitry. They connect the signal lines from the control hardware to the motor driver boards, limit switches, and probe control relays. The drive boards are mounted on the interface board by means of a multi-way connector. Each interface board can take two drive boards and hence only two stepper motors. This is because the interface board was originally designed for an x-y plotter. Hence to control four motors, two interface boards are required.

Power Supply

In order to mount the drive and interface boards inside a single case, power must be supplied to them both. Power for a cooling fan is also required because the bridge driver chips can get quite hot especially if they are in an enclosed space.

It is desirable to have a single power input into the case, thus reducing the number of external connections required. In order to do this additional internal power supply circuitry is needed to provide the three different DC voltage levels required:

- 5V Supply voltage required for the controller and interface chips
- 12V Rated voltage of cooling fan
- 35V Supply voltage for bridge driver chips

Of these three voltages only the 5V supply is critical and therefore requires a voltage regulator. The internal power supply circuit for the interface unit is shown in Figure 2.3.19.

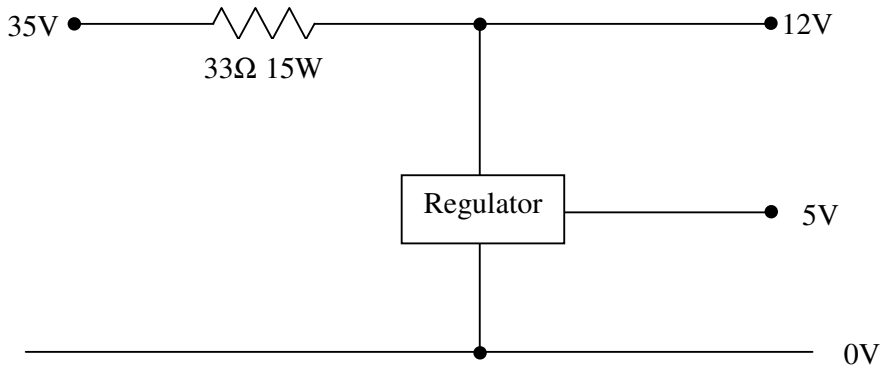

Figure 2.3.19: Circuit diagram of power supply for the scanning system interface unit.

The circuit is powered by a 35V supply that is dropped down to 12V by a crude divider arrangement consisting of a 33Ω power resistor and the internal impedance of the regulator in parallel with the fan. The circuit is mounted on a small piece of strip-board inside the case and the power resistor is solidly bonded to the case to provide good thermal dissipation.

Probe Control

The interface unit also contains the probe power relay and supply monitoring circuitry. The probe supply voltage is provided by a laboratory power supply connected to the interface unit. The power to the probe can be turned on and off by a relay which is controlled by one of the interface boards. The probe supply voltage is stepped down by a simple resistive voltage divider to allow the scanning system to monitor the probe supply voltage. The other interface board is used to provide the power to the grounding relay contained within the probe housing itself.

External Connections

Case Construction

The case for the interface unit was constructed from thin sheet steel in the mechanical workshop at UMIST. The circuit boards are mounted inside on supports. The fully constructed interface unit is shown in figure 2.3.20. The unit has a power switch and a grille for the cooling fan. All connections for the boards and cards must be brought out of the case; this is done using a number of connectors described next.

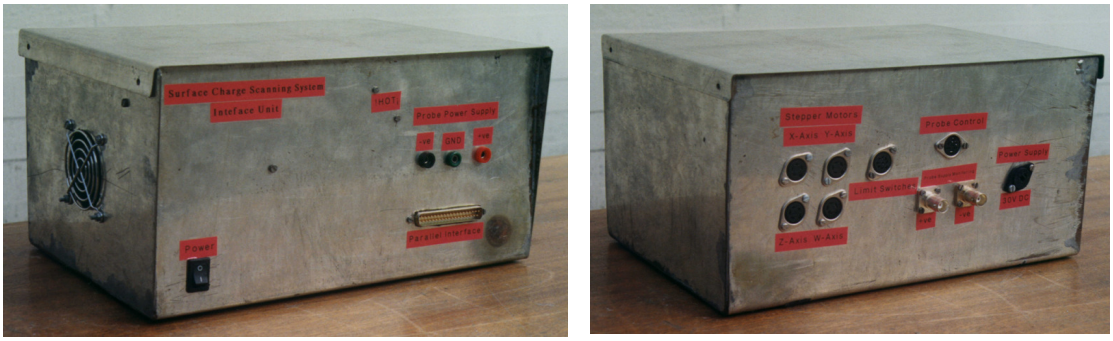

Front *Back*

Figure 2.3.20: The fully constructed scanning interface unit.

Power Supplies

The pin-out for the main power supply to the unit is shown in figure 2.3.21(a). The connector is mounted on the back of the unit and a +35V, 10A DC power supply is used. The power supply for the probe is provided by a laboratory power supply connected to the interface unit using three coloured banana sockets on the front of the unit as shown in figure 2.3.21(b).

(a) Interface Unit Supply *(b) Probe Supply*

Figure 2.3.21: The power supply connections to the interface unit.

Probe Control

The pin-out for the connections to the electrostatic probe is shown in figure 2.3.22. A 5-pin DIN connector is provided on the back of the unit, which connects via a 5-core cable to the scanning platform. The cable carries the probe power supply lines and the 12V probe ground relay signal.

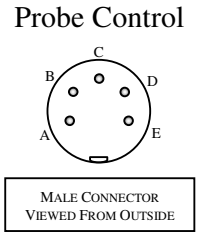

A. Negative Power Supply
B. Positive Power Supply
C. Ground
D. Probe Ground Relay Coil
E. Probe Ground Relay Coil

Figure 2.3.22: Pin-out for the Probe Control Connector.

Probe Power Supply Monitoring

Two stepped down signals from the positive and negative probe power supplies are provided on the back of the unit via two BNC connectors. They are monitored by the scanning hardware.

Stepper Motors

Each motor has its own 4-pin din connector labelled, X-Axis, Y-Axis, Z-Axis and W-Axis. The pin-out for the connectors is shown in figure 2.3.23. 4-core cable with a suitable current carrying capability is used between the interface unit and the scanning platform.

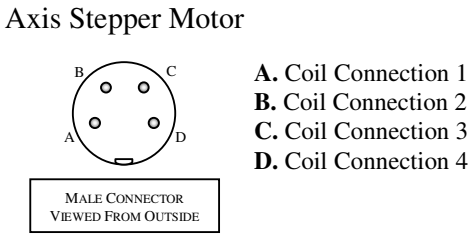

Figure 2.3.23: Pin-out for the Axis Stepper Motor Connectors.

Limit switches

The signals from the 6 end of travel sensors on the scanning platform are taken to the interface unit via an 8-core cable, the other two cores take the supply voltages to the micro-switches. Figure 2.3.24 shows the pin-out for the 8 pin DIN connector used in the connection.

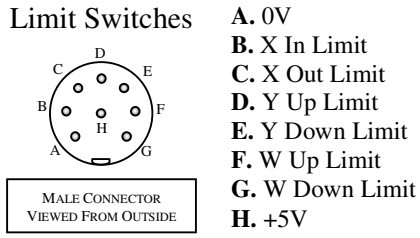

Figure 2.3.24: Pin-out for the Limit Switch Connector.

Parallel interface

A 37-pin parallel connector provides the primary link between the interface unit and the control hardware. This connector caries all the digital (0V or 5V) control information for the stepper motors, probe relays and limits switches. Figure 2.3.25 shows the pin-out for the 37-way D-connector mounted on the front of the unit.

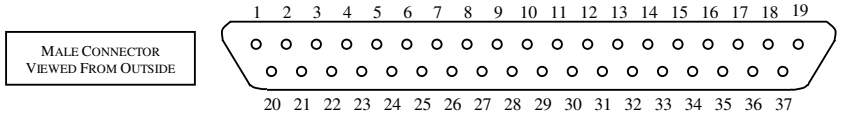

Pin	Description
1	Not used
2	Not used
3	Not used
4	X-axis Clock
5	X-axis Direction
6	X-axis Half/Full Stepping
7	Y-axis Clock
8	Y-axis Direction
9	Y-axis Half/Full Stepping
10	X and Y-axis Enable Motors
11	Ground Probe Relay
12	Z-axis Clock
13	Z-axis Direction
14	Z-axis Half/Full Stepping
15	W-axis Clock
16	W-axis Direction
17	W-axis Half/Full Stepping
18	Z and W-axis Enable Motors

19	Power Probe Relay
20	Y-axis Max Limit Switch
21	Y-axis Min Limit Switch
22	X-axis Min Limit Switch
23	X-axis Max Limit Switch
24	W-axis Min Limit Switch
25	W-axis Max Limit Switch
26	Spare Control Line
27	Spare Control Line
28	Not used
29	Not used
30	Not used
31	Not used
32	Not used
33	Not used
34	Not used
35	Not used
36	Not used
37	DIGITAL GROUND

Figure 2.3.25: Pin-out for the male 37-way D connector on the interface unit.

2.3.4 Scanning System Control Hardware

Overview

One of the main design ideologies for the surface charge distribution measurement system was ease of use; ideally the finished system should be able to obtain a distribution, display it, and save the data, at a press of a single button. The measurement system should be capable of doing this without any operator assistance. This will free the experimenter from the tedium of continuously monitoring the apparatus and make the measurement system a reliable laboratory instrument.

To make such a complicated system easy to use, some form of computer control is essential. Rather than designing a dedicated programmable system especially for the purpose, it was decided to base the control of the system around an existing computer using additional hardware. This allowed much greater flexibility during the development phase of the apparatus.

The measurement system is based around a Hewlett-Packard 386 computer with 8MB of RAM. The computer is equipped with two interface cards: a 24-line digital input/output card for platform control, and a 16-channel analogue to digital converter for voltage measurement.

Platform Control

Digital I/O card

To control the scanning platform a parallel interface is required. Unfortunately the parallel port provided as standard on the back of all PC's does not have enough data lines, so a digital I/O card is necessary.

The card used is the PC36AT, a 24-line digital I/O card from Amplicon Liveline Ltd. This card provides 24 lines of programmable digital I/O.

Mode of operation

As far as the computer is concerned, the I/O card is just another memory location it can read and write to. When the card was installed in the computer, it was assigned a base memory address location in hexadecimal. The 24 I/O lines are split into three 8-bit ports labelled A, B and C.

PORT REGISTER	I/O ADDRESS
Port A	BA + 0
Port B	BA + 1
Port C	BA + 2
Control Word	BA + 3

Base Memory Address =
310 Hex
784 Decimal

Table 2.3.5: Addresses for the digital I/O card.

The board features an uncommitted CMOS Programmable Peripheral Interface (PPI) which can be configured in a variety of operating modes. Each 8-bit port can be configured to operate in either input, output, bi-directional or mixed mode. For this application, ports A and B are configured as outputs and port C is configured as an input. The card operation mode is set by writing an 8-bit control word to the relevant memory address.

External Connections

The pin-out for the I/O card is shown in figure 2.3.26. The corresponding use for each bit of the three ports is also shown.

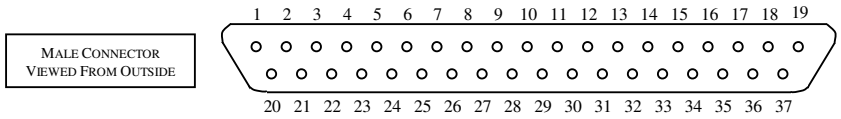

Pin	Description	Interface Unit Use
1	+12V out	Not used
2	+5V out	Not used
3	Not used	Not used
4	Port A - bit 0	X-axis Clock
5	Port A - bit 1	X-axis Direction
6	Port A - bit 2	X-axis Half/Full Stepping
7	Port A - bit 3	Y-axis Clock
8	Port A - bit 4	Y-axis Direction
9	Port A - bit 5	Y-axis Half/Full Stepping
10	Port A - bit 6	X and Y-axis Enable Motors
11	Port A - bit 7	Ground Probe Relay
12	Port B - bit 0	Z-axis Clock
13	Port B - bit 1	Z-axis Direction
14	Port B - bit 2	Z-axis Half/Full Stepping
15	Port B - bit 3	W-axis Clock
16	Port B - bit 4	W-axis Direction
17	Port B - bit 5	W-axis Half/Full Stepping
18	Port B - bit 6	Z and W-axis Enable Motors
19	Port B - bit 7	Power Probe Relay
20	Port C - bit 3	Y-axis Max Limit Switch
21	Port C - bit 2	Y-axis Min Limit Switch
22	Port C - bit 1	X-axis Min Limit Switch
23	Port C - bit 0	X-axis Max Limit Switch
24	Port C - bit 4	W-axis Min Limit Switch
25	Port C - bit 5	W-axis Max Limit Switch
26	Port C - bit 6	Spare Control Line
27	Port C - bit 7	Spare Control Line
28	Not used	Not used
29	Not used	Not used
30	-5V out	Not used
31	Not used	Not used
32	Not used	Not used
33	-12V out	Not used
34	Not used	Not used
35	Not used	Not used
36	Not used	Not used
37	GROUND	GROUND

Figure 2.3.26: Pin-out for the male 37-way D connector on the digital I/O card.

Voltage Measurement

Analogue to Digital Converter Card

Previous measurement systems implemented in the High Voltage Department at UMIST (Vasconcelos, 1994) have used a digital storage oscilloscope to store the probe signal, this trace then being downloaded to a computer via a standard interface (i.e. GPIB). This method of data acquisition is laborious, time consuming, and ties up another piece of apparatus.

The solution is to use an Analogue to Digital (A to D) converter card directly in the back of the PC. This way the same computer that is controlling the movement of the probe can also acquire the signal from the probe, thus allowing not only ease of synchronisation but simplification of the scanning system as a whole.

The A to D card used is the PC27E, a 12-Bit Card from Amplicon Liveline Ltd. This card provides a very good resolution at a reasonable price. It also allows up to 16 individual voltages to be measured.

Card Specifications

16 Input Channels

12-Bit Resolution (4096 quantisation levels = +/- 0.012%)

Input Ranges: Bipolar ±4.0 Volts

±2.0 Volts

Unipolar 0 to +4 Volts

Conversion time: 10μs

For this application the input range was set to ±2.0 Volts.

Additional Hardware

To allow connection to the scanning apparatus, a specially constructed screened breaker box with 16 individual BNC connectors is used to take the input signals to the 37-way D connector on the back of the A to D card.

A screened variable voltage divider is employed to allow a range of probe voltages to be measured. A multi-pole switch is used to switch in different resistors to change the divider ratio. Each range setting has a small internal pot used to fine-tune the divider ratio.

Mode of operation

Like the digital I/O card, the computer communicates with the card as if it were a memory location. When the card was installed in the computer, it was assigned a base memory location in hexadecimal.

PORT REGISTER	I/O ADDRESS
A/D Output word (lo byte)	BA + 0
A/D Output word (hi byte)	BA + 1
Start Conversion	BA + 2
Multiplexer Select	BA + 3
Timer/Counter 0	BA + 4
Timer/Counter 1	BA + 5
Timer/Counter 2	BA + 6
Timer/Counter Control Word	BA + 7

Base Memory Address =

300 Hexadecimal

768 Decimal

Table 2.3.6: Addresses for the A to D card.

When the computer reads or writes to, the Start Conversion address, the A to D card is triggered and samples the input voltage on the requested channel. Around 10μs later the conversion is complete and the 12-bit binary value appears split between two memory locations.

Screened enclosure

The computer used was found to have quite a poor immunity to electromagnetic interference. Very high levels of interference are common place in a high voltage laboratory, and previous experience has shown that problems often occur when using computers in such surroundings. The computer is most susceptible to interference when it is writing to its internal hard disc; errors occur on the disc, which then requires fixing. The computer was housed in a screened enclosure to provide extra protection from electromagnetic interference. The problem could never be completely solved, however the screened enclosure greatly reduced the computer's susceptibility to the interference. Whenever possible it is advisable to have the computer switched off when conducting the high voltage test.

2.3.5 System Commissioning

Calibration Test Piece

It is not possible to construct a calibration test piece that would allow a specific charge density to be applied to an insulating surface and the probe voltage recorded. However it is possible to use a conducting surface set at a specific voltage. This will not allow a direct calibration of charge density to probe voltage, but will allow the simple capacitive model of probe operation to be studied and the surface to probe capacitance to be evaluated. The test piece does allow an indirect calibration to be made because the test piece can be modelled using finite element techniques. This will allow the reliability of the modelling technique used to find the ϕ-Function (probe response function) to be assessed. Thus the accuracy of the Φ-Matrix technique can be proved. The modelling of the test piece is discussed in the chapter on field studies.

The test piece consisted of a cylindrical insulating former upon which a copper foil was glued, a strip about 10mm wide was isolated by removing two thin strips of foil about 2mm wide. The isolated copper strip could be set at a potential, as shown in figure 2.3.27. The charging voltage from a camera photo-flash was used as a simple compact DC voltage source for the copper strip.

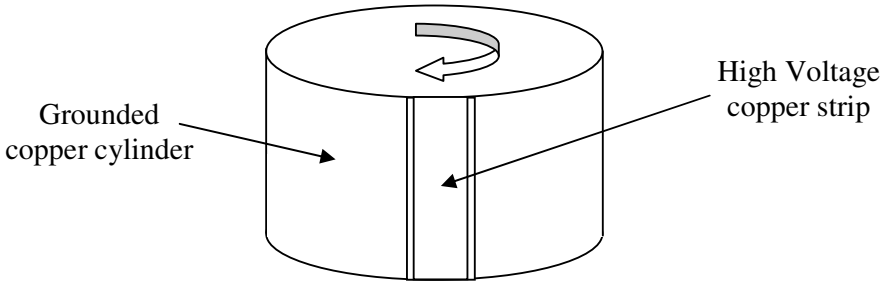

Figure 2.3.27: Calibration test piece.

Linearity of Response

Consider the simple capacitive model of probe operation detailed in figure 2.1.2. The probe sets up a capacitive voltage divider where V_s, the surface potential is divided down to the give the probe voltage, V_{out}. The relevant equation is:

$$V_{out} = V_s \frac{C_{sp}}{C_{pg} + C_{sp}}$$

where C_{sp} is the capacitance between the probe and the surface and C_{pg} is the capacitance between the probe and ground, which has been measured as 10.8pF.

This is a linear relationship and by altering the voltage on the test piece, the constant of proportionality $\frac{C_{sp}}{C_{pg} + C_{sp}}$ can be found.

Figure 2.3.28 shows the probe output voltage as it was scanned across the test piece with different voltages on the copper strip. The distance between the probe and the surface was set at 1mm. The edges of the copper strip were not perfectly smooth which caused the probe surface separation to vary slightly. This caused the probe output voltage to have small distortions at the edges of the strip.

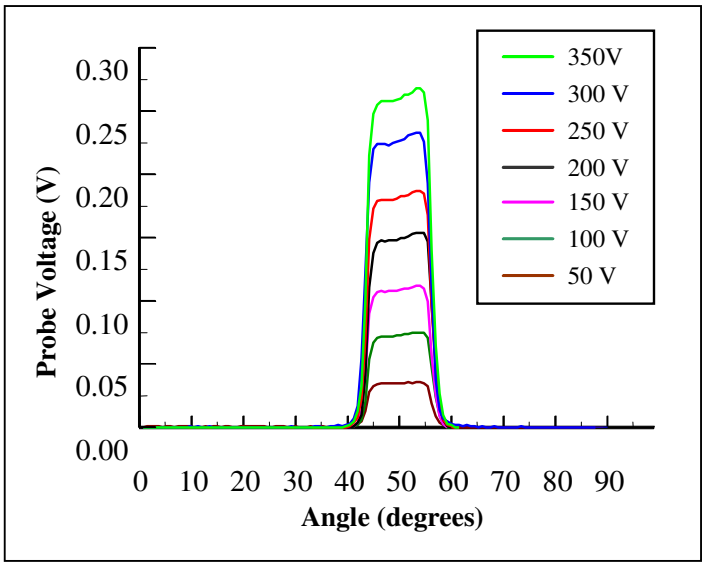

Figure 2.3.28: Probe output voltage as the voltage on the copper strip is varied.

Figure 2.3.29 shows the probes output voltage at 50° for each of the scans versus the voltage of the copper strip. A very strong linear relationship is apparent.

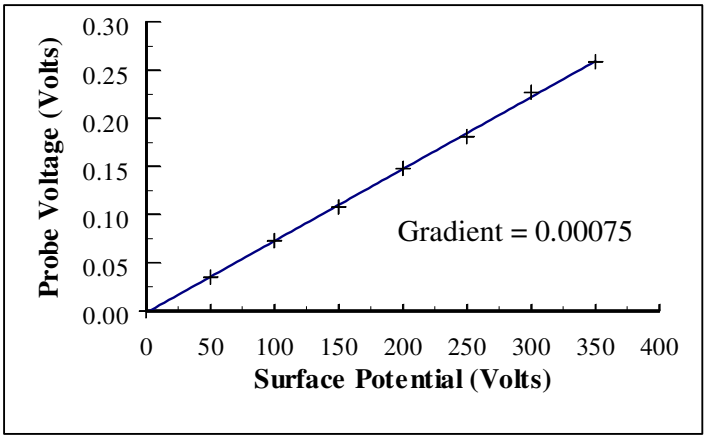

Figure 2.3.29: Relationship between probe output voltage and surface voltage.

If the equation for the probe voltage is rearranged the capacitance between the probe and surface can be calculated.

$$C_{sp} = C_{pg}\left[\frac{\left(\frac{V_{out}}{V_s}\right)}{1-\left(\frac{V_{out}}{V_s}\right)}\right]$$

For the probe 1mm away from the surface and taking C_{pg} as 10.8pF the probe-surface capacitance works out as 8.1fF.

Probe-Surface Separation

The effect of probe distance from the surface was also studied, figure 2.3.30 shows the probe output voltage as it is scanned across the test piece at different distances from the surface.

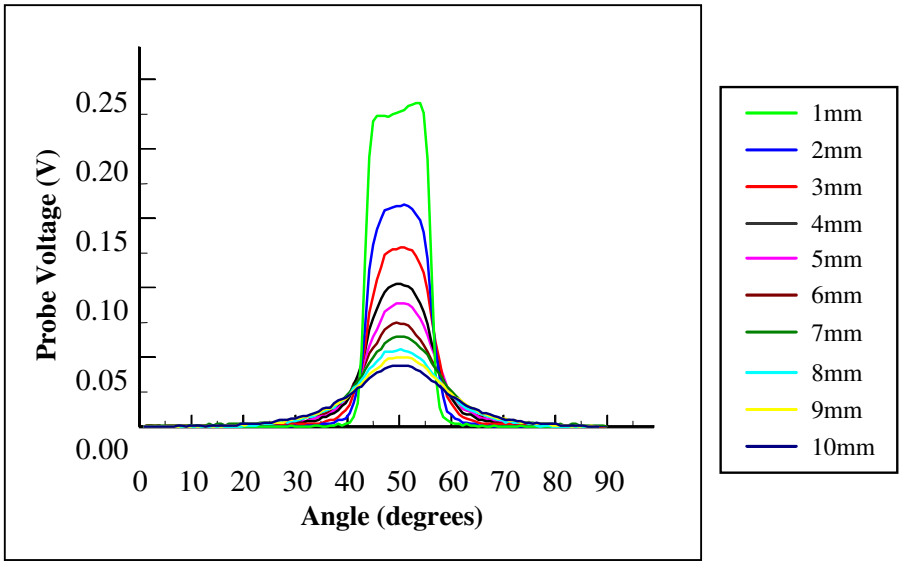

Figure 2.3.30: Probe output voltage as the surface is scanned at different distances.

As the probe scans further away from the surface the measured voltage distribution becomes more and more spread-out, effectively the probe resolution becomes poorer. The peak voltage also decreases as the probe-surface capacitance decreases. Figure 2.3.31 shows the probes output voltage at 50° for each of the scans.

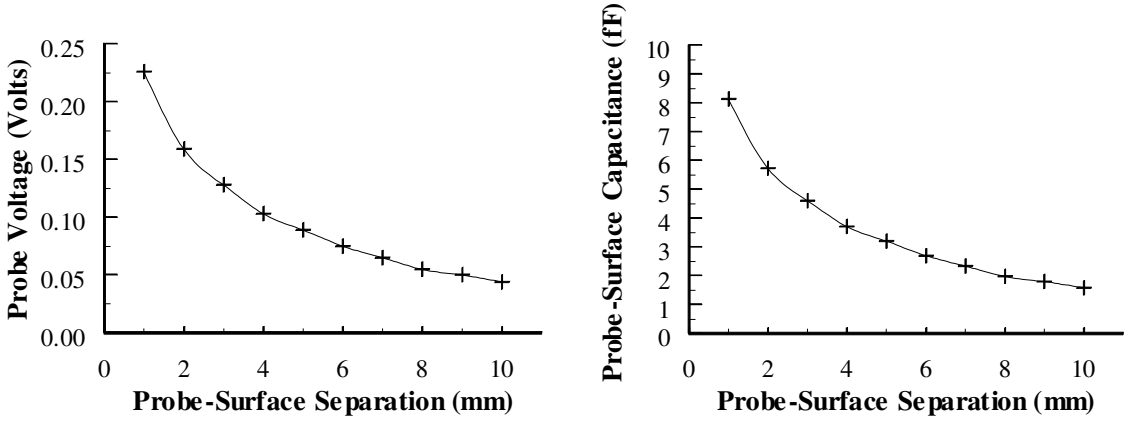

Figure 2.3.31: Relationship between probe voltage and probe-surface capacitance versus distance.

Using the formula stated previously the probe-surface capacitance can be calculated for each probe-surface separation.

Probe Frequency Response

To find the probe frequency response a 400Hz, ±4V Square-wave was applied directly to the probe sensor plate, figure 2.3.32 shows the probe output voltage.

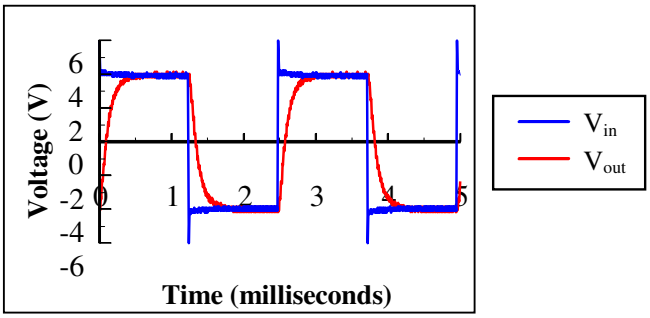

Figure 2.3.32: The response of the probe to a 400Hz square wave.

The probe has a rise time of about 0.5ms. This is twice as fast as the fastest rise time that could possibly be experienced by the scanning system. For the scanning system the absolute fastest scanning speed is 1 step per ms and the system can only take one measurement per step so the fastest rise time that is likely to be experienced is in the order of 1ms. In practice the probe rarely scans this fast so a probe rise time 0.5ms is adequate.

2.4 Scanning System Control Software

2.4.1 Introduction

The hardware is one aspect of the solution to the scanning problem, the software that will control the entire scanning operation is equally as important. The main point of the software is to remove the burden of complexity from the user, making the apparatus easy and intuitive to use.

When designing a piece of software the first question to ask is: what does it need to do?

2.4.2 Requirements

Probe Movement

The software must control the movement of the probe over the surface and avoid colliding with it. This is quite a substantial task, because there are four motors controlling the probe and hence four degrees of freedom.

Probe Control

The software should be capable of controlling and monitoring the operation of the electrostatic probe. This involves, recording the probe power supply voltage, grounding the probe, and measuring its drift characteristics.

Data Storage

The program must also control the acquisition of the signal from the probe. As was mentioned earlier a very large number of measurements are required to define a surface if a high-resolution charge density map is required. This means that it is essential at the design stage of the software that the substantial task of dealing with such large quantities of data be removed from the user, to whom each charge density measurement should appear as one object. To achieve this, the program must store all the data for the surface in one file. Details of all the scanning parameters (such as the distance of the probe from the surface) should also be stored in the same file.

A new surface data file is created for each surface charge distribution measured, this file contains all the probe voltage measurements and all the scanning parameters. The apparatus will be used to measure many surface charge distributions; it is therefore essential that the surface data files generated be organised in some manner so that they can easily be retrieved at a later date.

Displaying Data

Basic graph plotting facilities (3-dimensional surface plots, contour plots and two-dimensional slices through the surface) in the program itself will facilitate instant decisions to be made about the measured distribution without the user having to go away and analyse the data. Graphing each layer as it is scanned in will allow the scanning procedure to be monitored.

Compatibility

The program must also allow the surface data to be accessible to other applications, such as specialised 3-Dimensional graph plotting packages and Matlab for further analysis.

Data Processing

Basic data analysis and processing functions should be available, such as removing the probe drift and ground response.

Flexibility

Because this was still being developed and evaluated, the program must be flexible enough to allow almost all parameters involved in the scanning process to be varied. Parameters such as: the speed the probe moves over the surface, the direction the probe moves over the surface, the distance between the probe and the sample, the physical dimensions of the surface, the path the probe takes over the surface, the number of data points that make up the surface.

User Friendliness

Another important point that is often overlooked in software solutions to specialist problems is user friendliness; the finished program should be easy and straightforward to use. This can be achieved by having auto set-up facilities, and having the ability to save the scanning set-up.

Implementation

Development Language

Pascal was chosen as the programming language in which to develop the control software. The compiler used was Borland Turbo Pascal V7.0 for DOS. Pascal was selected because the source code was available for a program used in an undergraduate laboratory in the Electrical and Electronic Engineering Department at UMIST. The laboratory involved designing and writing a program to control an X-Y plotter driven by stepper motors. An interface program unit was used to reduce the task of stepper motor control to simple commands that can be called in the Pascal programming language. The source code for the X-Y plotter interface program unit formed the starting point for the development of the scanning system Interface Program Unit.

Program Files

The scanning system control software is called 'SCAN', the files required to run the software are as follows:

SCAN.EXE – The main scanning system control software.

PROCEDS.TPU – A program unit containing procedures used by the main program.

PROBEM.TPU - The scanning system interface program unit.

CONFIG.DAN - The SCAN configuration file; contains all the set-up information.

During the process of development a number of revisions were made to the software, the rest of this section describes the final version of the scanning software.

2.4.3 Interface program unit

Purpose

The purpose of the interface program unit is to provide a link between the main program and the 24 bit digital I/O card, its relative position in the scanning system is indicated in figure 2.4.1. This allows the main program to have full control over the stepper motors without having to be concerned with the timing problems involved in generating the square waves required for the stepper motor clock pulses, and checking to see if the motors have hit their limit switches.

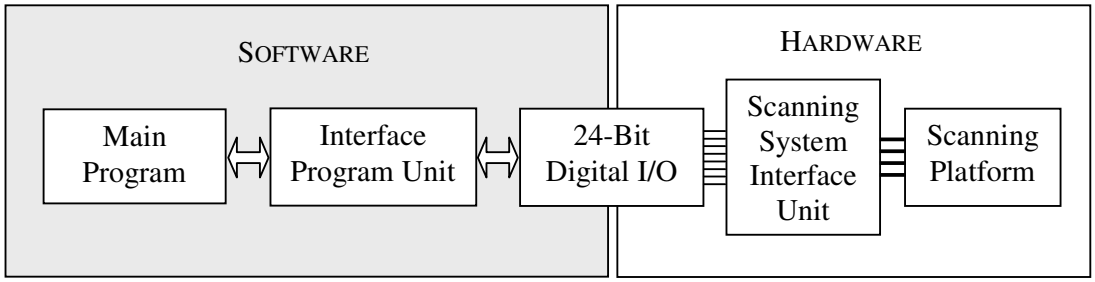

Figure 2.4.1: A schematic showing the functional position of the interface program unit.

Interface Unit Procedures

The end user need not have any knowledge of the program interface unit. It is there simply to allow the main program to control the stepper motors with simple commands. The main program can tell the interface unit which motors to move, for how many steps, how quickly, and in which direction. The main program can also ask about the status of the limit switches.

The interface unit has to be able to generate accurate clock pulses for the stepper motors to run smoothly, so timing is critical. To enable it to do this, the interface unit takes control of the computer's internal timer by disabling the interrupt lines. As a result of this the program can only operate in MS-DOS because Windows operating systems become very unstable when the interrupt lines are altered.

The procedures available to the main program are described and their syntax defined in Appendix B.

2.4.4 Probe Movement

Axis Definition

The scanning platform has four axes that allow the relative movement of the probe over the surface; X-Axis, Y-Axis, W-Axis and Z-Axis as shown in figure 2.4.2. The X-Axis and Y-Axis are both linear and scaled in mm, the W-Axis and Z-Axis are rotational and scaled in degrees.

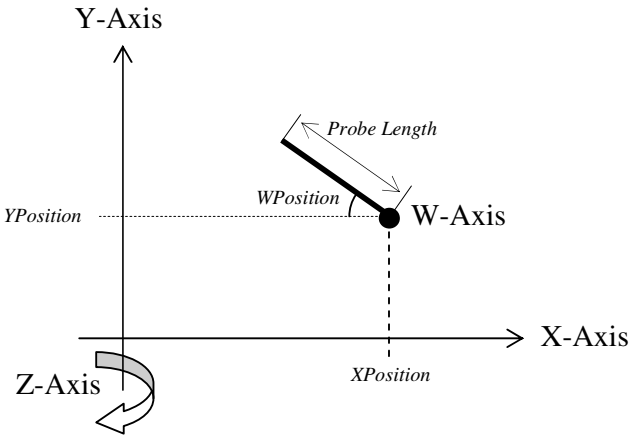

Figure 2.4.2: The scanning platform axis.

Axis positioning

The program must have control over the movement of the probe. To do this it keeps track of the position of the probe using 4 variables; *XPosition, YPosition, WPosition* and *ZPosition*.

XPosition and *YPosition* are the horizontal and vertical co-ordinates of the *W-Axis*. They are both measured in millimetres to a precision of a tenth of a millimetre. *XPosition* is measured relative to the position of the *Z-Axis,* and *YPosition* is measured relative to the lowest vertical position of the platform.

WPosition is the yaw angle of the probe, when the probe is horizontal *WPosition* is defined as zero, when the probe yaws up *WPosition* is positive, and when it yaws down *WPosition* is negative.

ZPosition is the angular position of the test object; it is measured in degrees relative to an arbitrary start position. The four positioning variables are stored in the configuration file. This allows the program to know where the probe is even if the computer has been turned off and the program restarted.

Probe Tip Position

The program must also keep track of the position of the probe tip. Its X and Y co-ordinates can be obtained using simple trigonometry:

$$X = XPosition - ProbeLength \times \cos(WPosition)$$

$$Y = YPosition + ProbeLength \times \sin(WPosition)$$

Kick-Back Compensation

The W and Z-Axis are not driven directly from the stepper motors like the threaded rod arrangement for the X and Y-axis; instead they are driven through a gear chain. The inherent problem with gearboxes is that there will be some slack in the gear chain; this is called backlash. This means that when the motor changes direction, before the probe (or the test object in the case of the Z-Axis) starts to move, the cogs must take up the slack. This has implications for the positional accuracy of the axes.

The amount of slack in the gear chain can be measured and compensated for in the software. Once the backlash setting is known the software applies the correction whenever the motor changes direction, the end-user need not have any knowledge of the compensation factors involved.

The kickback setting for the Z-Axis is mainly used to remove the over-rotate characteristics of large test objects. When heavy test objects are rotated their angular momentum tends to keep them rotating, the kick back setting for Z-Axis is used to give the test object a small nudge in the opposite direction to stop it rotating. This allows the Z-Axis to maintain angular precision.

2.4.5 Defining a Test Object

Shape of a Test Object

The shape of the test object must be known by the scanning system to allow it to move the probe over the surface. All test objects are axi-symmetric and the same axes as defined for the scanning platform are used to define the contour of the test object.

The contour of the test object is defined using an (x,y) list of co-ordinates, the shape of the entire test object is generated with a 360 degree rotation about the Z-Axis; this is shown in figure 2.4.3.

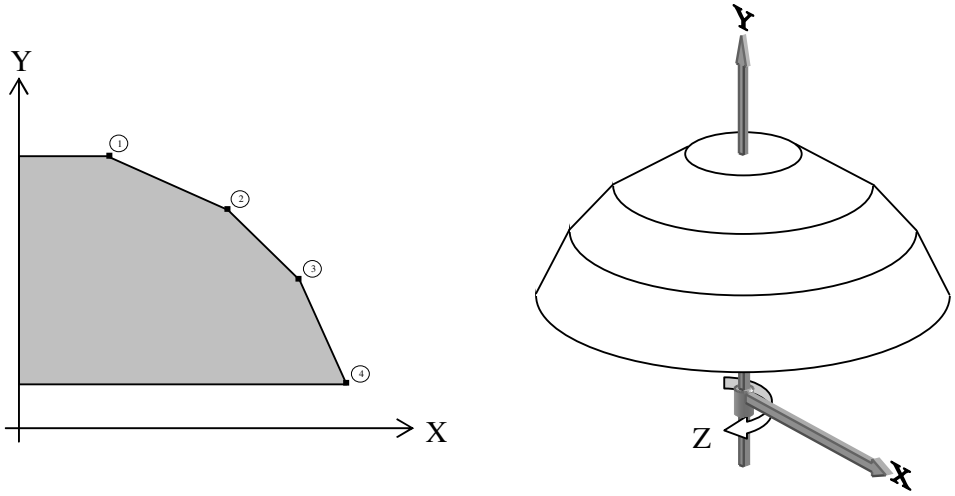

Figure 2.4.3: The definition of an example test object; the contour of the test object is defined with four Surface Points.

Each point that defines the surface contour is called a Surface Point. For more complicated test object geometries or test objects with smooth curves, more Surface Points are required; this is shown in figure 2.4.4.

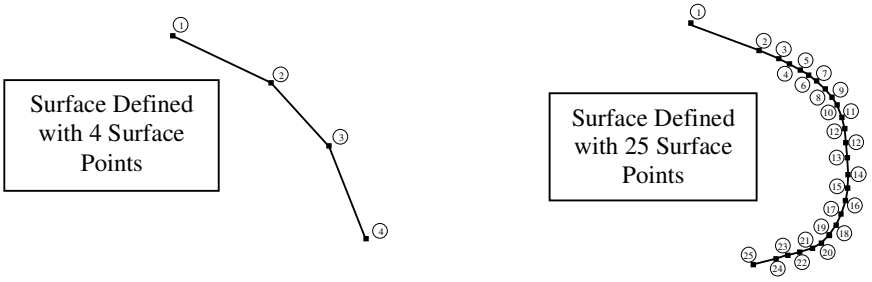

Figure 2.4.4: Examples of test object surface geometries. The more complex, the more Surface Points are needed to define the shape.

Test object geometry files

The co-ordinates of surface points that define the contour of test object are stored in text files with the extension: ***.OBJ**. These test object geometry files are stored on the hard-drive of the computer in a directory named **C:\OBJECTS\.** The x-y co-ordinates for each of the Surface Points are listed in two columns. All values are in mm. When the scanning software reads in the object text file it assumes that the test objects surface is defined from the top down, if the Surface Points are listed from the bottom up this will result in the scanning system scanning the layers from the bottom up.

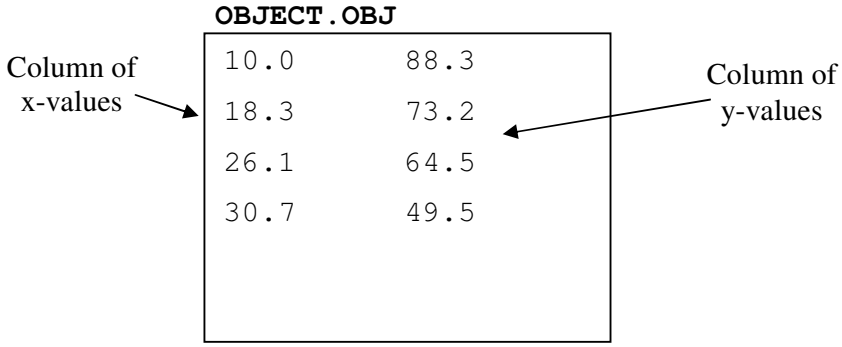

Figure 2.4.5: An example test object geometry file containing the co-ordinates for 4 surface points.

2.4.6 Scanning Parameters

Introduction

The scanning procedure itself has many parameters, all of which will affect the surface charge distribution generated. It is therefore essential that the user has full control over all these variables. The program has been written to allow the user to easily vary the scanning parameters, and the configuration file stores all the settings so that the apparatus remembers the previous set-up.

Mechanical Variables

Direction

The test object can be rotated in either direction; this sets whether the probe scans from left to right or from right to left. This can be used to test the probe's dynamic response.

Speed

Altering the step period of the Z-Axis stepper motor can alter the speed of rotation of the test object. This can also be used to test the probe dynamic response.

Probe Length

The length of the probe is measured from probe tip to the centre of W-axis rotation, the program needs to know how long the probe is in order to calculate the positions of the axes whilst carrying out a surface scan.

Probe-Surface Distance

The distance the probe scans above the test object's surface can easily be varied, the positions for the scanning axes are automatically re-calculated. The probe surface distance is important when determining the probe's response function.

Division of the Surface

Scan Angle

Any angular section of the test object can be scanned, but to scan the entire surface the scan angle should be set to 360 degrees. Smaller scan angles are used to study sections of the surface, this reduces the number of surface elements per layer, thus reducing the size of the matrix required to find the charge distribution.

The size of the scan angle and the radius of the test object set the length of each layer. For contoured test objects the circumference of each layer varies so for a constant scan angle the length of each layer will also vary.

Elements per Layer

Once the scan angle has set the portion of the test object surface to be scanned, that area must be divided into elements. When the probe scans through each layer, probe voltage measurements are recorded above the centre of each element. Either the number of elements per layer can be set, or the element width, dx. The two are obviously related and the program automatically changes one when the other is varied. For contoured surfaces the element width will vary between layers so the program allows the user to set an average element width and it will then display the resultant element widths for each layer.

It is important note that the maximum angular resolution of the Z-Axis is 0.75 degrees so the maximum number of elements in a full rotation is 480. This means the minimum element width is related to the radius of the test object. Because only certain element widths can be used there will sometimes be a small remainder (< 1 element width) left after the division of the layer, the program will indicate this amount. Figure 2.4.6 shows the division of a surface and the measurement points.

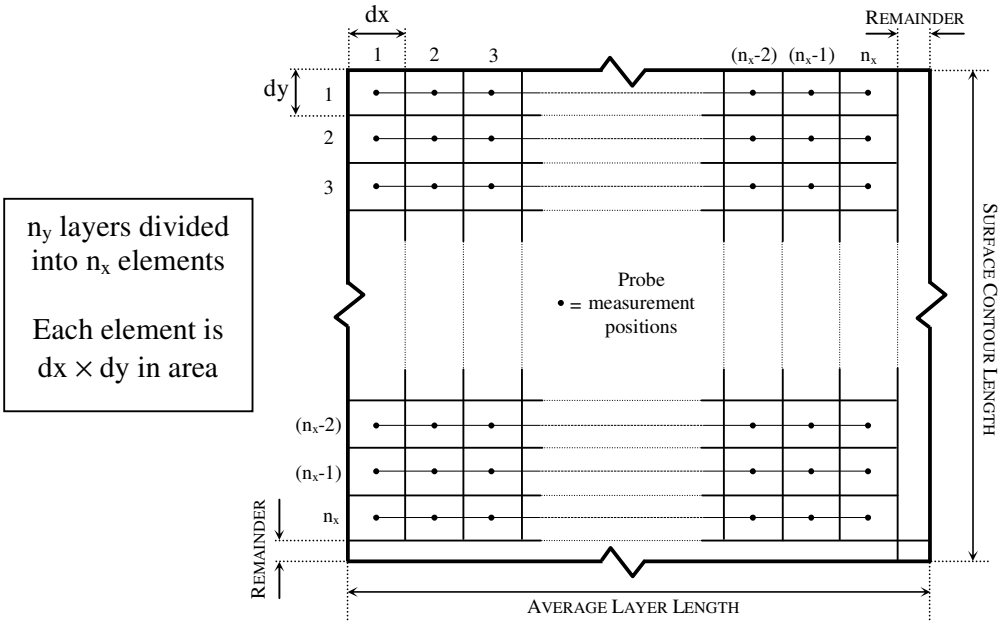

Figure 2.4.6: The division of the insulator surface area to be scanned.

Number of Layers

In the same way as for the number of points, either the total number of layers or the element height (dy) can be varied, and again the program will automatically re-calculate the other variable. The surface contour length is found from the sum of the distances between each of the surface contour points given in the test object definition file. Again because the positional resolution of the scanning system has a limit there will sometimes be a small remainder of the surface contour left.

The program can also be made to automatically set the element width (dy) to be the same as the element height (dx) thus creating square elements.

2.4.7 Generating Scan Points

Once the surface has been divided into elements, the program must work out the positions of the X, Y and W-axis to position the probe for each layer. The probe must be orthogonal to and at certain distance from each element. The X, Y and W positions for each layer are referred to as Scan Points.

The program generates the Scan Points by first finding on which section of the test object surface contour the measurement point lies. It then works out the yaw angle of the probe to make it at 90 degrees to the section of the surface. Figure 2.4.7 illustrates the calculation of 5 Scan Points for a surface with 4 Surface Points. The first Scan Point will always position the probe directly above the first Surface Point. The yaw angle of the probe for the first Scan point is given by:

$$\mathrm{WPosition}_1 = 90° - \mathrm{Tan}^{-1}\left(\frac{\mathrm{YSurfacePoint}_1 - \mathrm{YSurfacePoint}_2}{\mathrm{XSurfacePoint}_1 - \mathrm{XSurfacePoint}_2}\right)$$

Then using simple trigonometry the position of the X and Y-Axis positions can be found:

$\mathrm{XPosition}_1$ = $\mathrm{XSurfacePoint}_1$+ (ProbeLength+ProbeSurfDis)*Cos(Angle);

$\mathrm{YPosition}_1$= $\mathrm{YSurfacePoint}_1$ - (ProbeLength+ProbeSurfDis)*Sin(Angle);

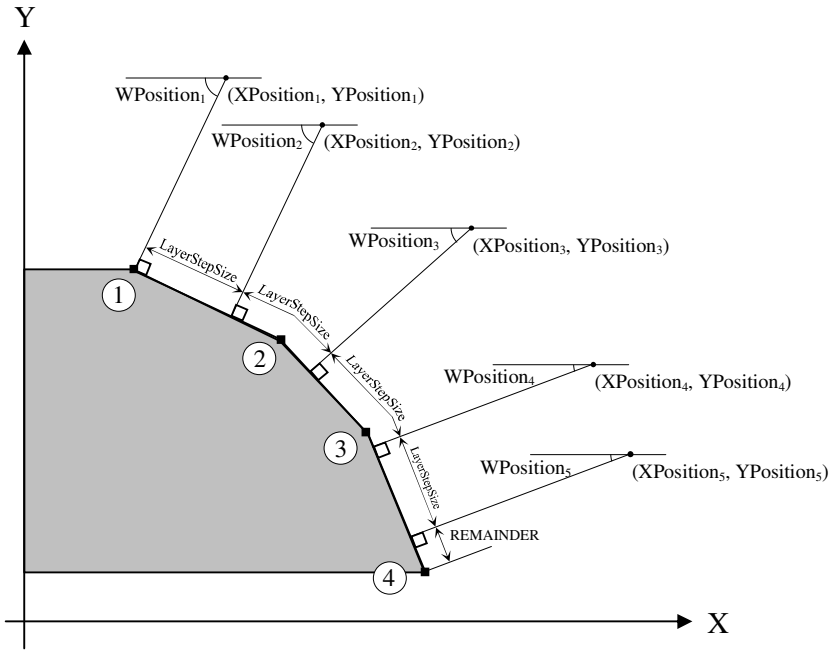

Figure 2.4.7: Calculating Scan Points from Surface Points.

The next measurement point is found by moving one element height (dy) down the surface contour, in the program code this distance is called LayerStepSize. The program will automatically step over a surface point to make sure all the elements are the same height. For each layer the Scan Points are calculated in the same manner as the first one. Whenever any of the scanning parameters change the program will automatically recalculate the Scan Points.

2.4.8 Collision Avoidance

Introduction

The Scan Points generated in the previous section give the three co-ordinates of the probe position for each layer. The Stepper motors that drive the axis are capable of moving at different speeds, and all moving at the same time. To scan in each layer the probe must move to the new co-ordinates without hitting the surface of the test object.

Of the three axes the X and Y-Axes are the slowest, the W-Axis is not only the fastest but also causes the greatest movement in the position of the probe tip. As a result of

this the axes cannot all just move at their top speeds when moving to the next layer. In certain circumstances this would result in the probe yawing too quickly before the X and Y-Axes have had a chance to move back far enough to prevent the probe tip from hitting the surface.

Technique

There are several different ways of approaching the problem, one could be to continuously monitor the position of the probe tip and compare it to the position of the test object surface. The problem with this is that it would tie up the main program because it would continuously have to ask the program interface unit for the positions of the motors. Instead a simpler twofold approach was used.

1. All axis finish at same time:

All the motors have a different top speed. The time for the slowest motor to move to its new position is calculated and the other motors slowed down so that if all three axes are started together they will all finish at the same time. The main effect of this procedure is that the W-Axis is slowed down, which greatly minimises the surface collision problem.

2. Move through transitional points:

The problem is greatest when the W-Axis has to move through large angles. The solution to this is to make the probe move through some transitional points when the W-axis has to move more than 5 degrees, this is illustrated in figure 2.4.8.

The transitional points are calculated by dividing the distance between the probe tip at each of the scanning points into equal measures, the W-Axis angle to move is also divided accordingly. In addition the probe tip position at each of the transitional points is stepped back from the surface by 1mm.

The combination of these two strategies ensures that the probe tip is kept clear of the surface when scanning contoured test objects.

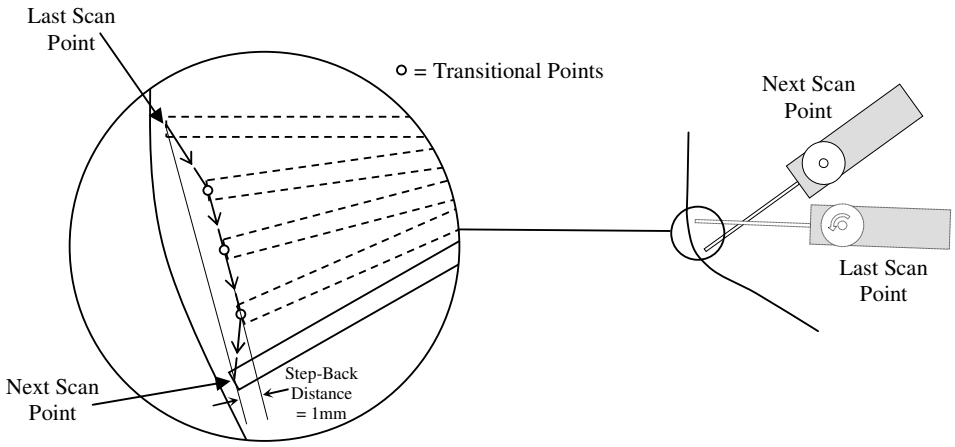

Figure 2.4.8: The probe moving to the next scan point via 3 transitional points.

2.4.9 Probe Control

Power Supply

The software can control and monitor the operation of the electrostatic probe. The probe power supplies are monitored using two channels of the A to D card. The probe power supply voltages can be set anywhere between about ±5 and ±15 V. The voltages are stepped down to a measurable range by the scanning system interface unit. To obtain the probe supply voltages the program multiplies the measured voltages by the relevant divider ratio. The probe supply voltages are then stored in each surface data file. In normal operation the probe supply voltage was set to ±10V.

Drift Rate

The average probe drift rate measured in mV per minute can be obtained by positioning the probe away from any surfaces and leaving it stationary. By monitoring the probe voltage over time the drift rate can be calculated. This drift rate value can then be used to remove the drift component from the surface voltage data. The software can automatically measure and correct for the drift rate. The drift rate is stored in each surface data file.

Probe Grounding

The software can ground the probe; this discharges the probe capacitance thus removing the offset voltage that has built up due to the probe voltage drift caused by the buffer circuit input bias current. The probe ground relay connects the probe to ground for a second, when the relay opens the probe voltage is not always exactly zero due to the characteristics of the buffer circuit. The probe voltage directly after grounding is referred to as the Probe Ground Offset. This value is stored in each surface data file and can easily be corrected for.

2.4.10 Data Storage

Surface Data Files

When a surface charge distribution is measured it is stored as a Surface Data File which provides a convenient and compact method of archiving surface data. The surface data files have a suffix ***.DAT**, and are composed of two main parts: the configuration header and the surface data. The configuration header contains all the information about the surface and how it was scanned in. It starts with a code number that the program looks for to check if the file is actually a surface data file.

The file is a file of bytes with most of the data values comprising of two-byte numbers. The structure of a surface data file is shown in figure 2.4.9. A two-byte number can range from 0 to 65535 and can have only integer values. So to allow negative and non-integer values to be stored some form of encoding is required. The type of encoding used sets the maximum range of permissible values for each data variable:

Variable	**Range**	**Increment**
Number of Layers	0 to 65535	1
Steps per Layer	0 to 65535	1
Steps per Measurement	0 to 65535	1
Display y-axis Zoom	0.000 to 65.535	0.001
Display y-axis Offset	–32.767 to 32.767	0.001
Layer Step Size	0.00 to 655.35 mm	0.01
Z-Axis Period	0 to 65535 ms	1
Probe Length	0.00 to 655.35 mm	0.01
Probe-Surface Separation	0.00 to 655.35 mm	0.01
Positive probe supply voltage	–3276.7 to 3276.7 V	0.1
Negative probe supply voltage	–3276.7 to 3276.7 V	0.1
Probe Drift Rate	–3276.7 to 3276.7 mVm^{-1}	0.1
Probe Ground Offset	-32.767 to 32.767 V	0.001
Data Value Multiplier	0.00 to 327.67	0.01
Test Object File Name	12 Characters Max	N/A

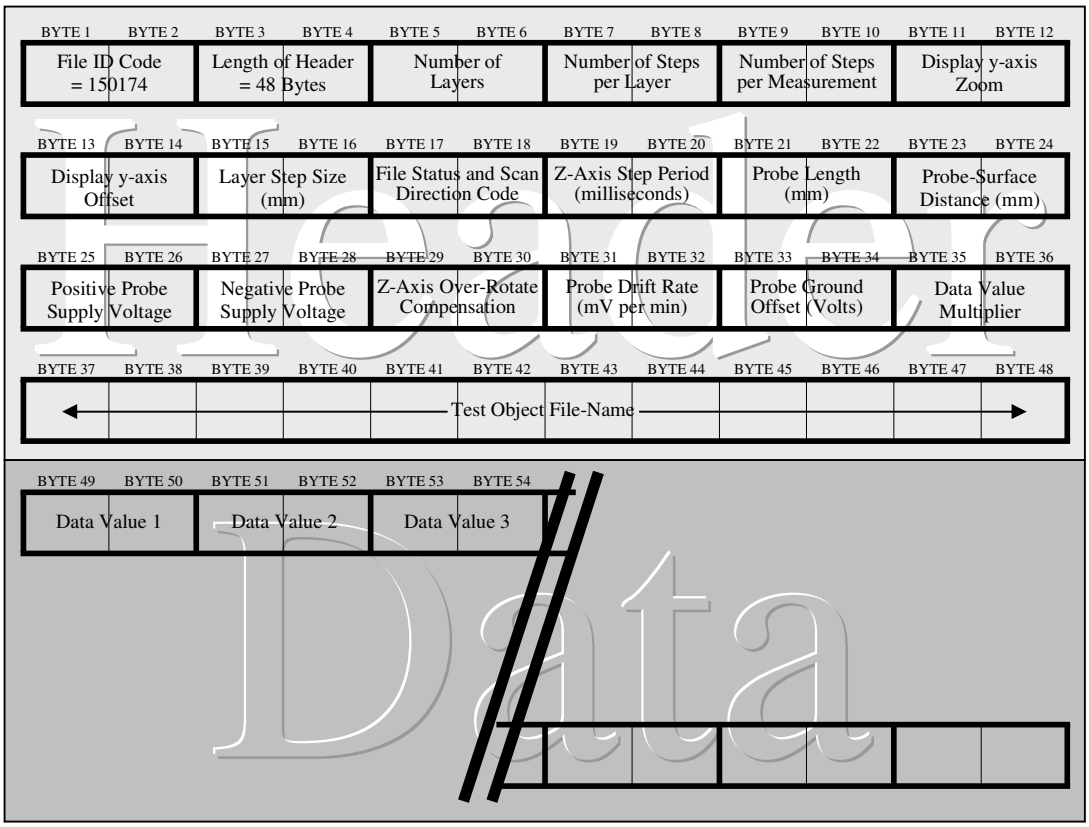

Figure 2.4.9: The structure of a Surface Data File

The ranges given are the maximum possible values that can be stored in the surface data file header, in practice the values for most of the variables are limited by other factors for example the probe is never going to be set to scan 655.35mm away from the surface.

The number of measurements per layer is not explicitly stored in the header. Instead it is calculated from the number of steps per layer divided by the number of steps per measurement.

Directly after the header information finishes the surface data starts, each data value is a two-byte value. The data is encoded so that each raw data value can range from –2 to +2 in 0.001 increments. The true data value is found by multiplying the raw value by the data value multiplier stored in the header.

The surface data is stored sequentially one layer after another with no breaks until all layers have been stored.

Surface Data Libraries

Each surface scan generates a surface data file; in practical use the scanning system will generate a large number of data files. It is therefore essential to have some technique to organise the surface data files. A simple automated system is used in which a new directory is created every day the scanning system is used, the directory name is automatically generated based on that day's date. All surfaces measured on that day are stored in the directory along with a copy of the relevant test object geometry files and any auto set-up information.

The base location of the Surface Data Library is **C:\SURFDATA** and all surface data directories are generated within it.

2.4.11 Program Operation

Configuration Information

The parameters that set how the program scans the surface are kept in a file called 'CONFIG.DAN'. Using a configuration file allows users to exit the program and return to it at a later date with all the settings unchanged from when they last used it.

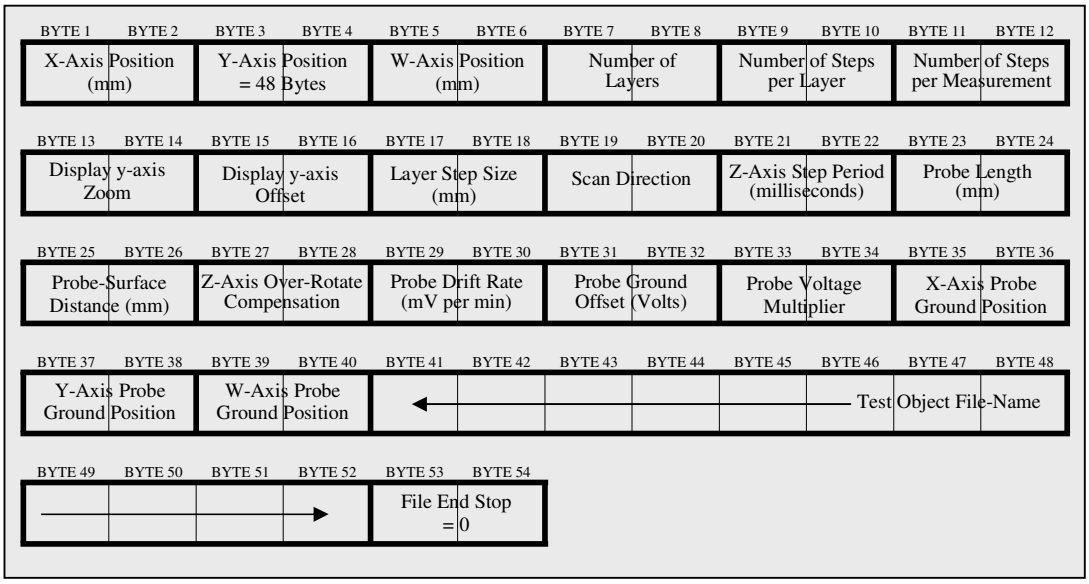

Figure 2.4.10: The structure of the configuration file.

The structure of the configuration information file is shown in figure 2.4.10. The variables are encoded in the same way as they are in the header of the surface data files. Most of the variables stored are the same as in the header file, except there is no need to record the probe power supplies; instead the current probe position is stored along with the probe ground position.

Flow Charts

The complicated task of scanning a surface can be reduced to several simple functions, which can then be combined. The simplest way to illustrate the scanning procedure is to use flow charts.

Figure 2.4.11 shows the process of scanning one layer. The Z-Axis motor is started then the program then takes probe voltage measurements every step and plots the voltage signal on the screen to allow the scanning procedure to be monitored. The probe voltages are recorded in a temporary layer data array.

Figure 2.4.12 illustrates the entire scanning procedure. Before the scanning starts the program checks the probe is switched on. It then asks the user what name to give the surface data file. After alignment and grounding the scanning procedure begins which involves moving to each layer in turn, scanning a layer, storing the layer data array in the surface data file and rotating back to the start position if necessary.

Throughout the scanning procedure the user has the opportunity to abort scanning by pressing the escape key.

When the scanning of the surface is complete a 3-D probe voltage distribution map is automatically generated. Once the scanning process has been set up, surfaces can be repeatedly scanned at the touch of a button.

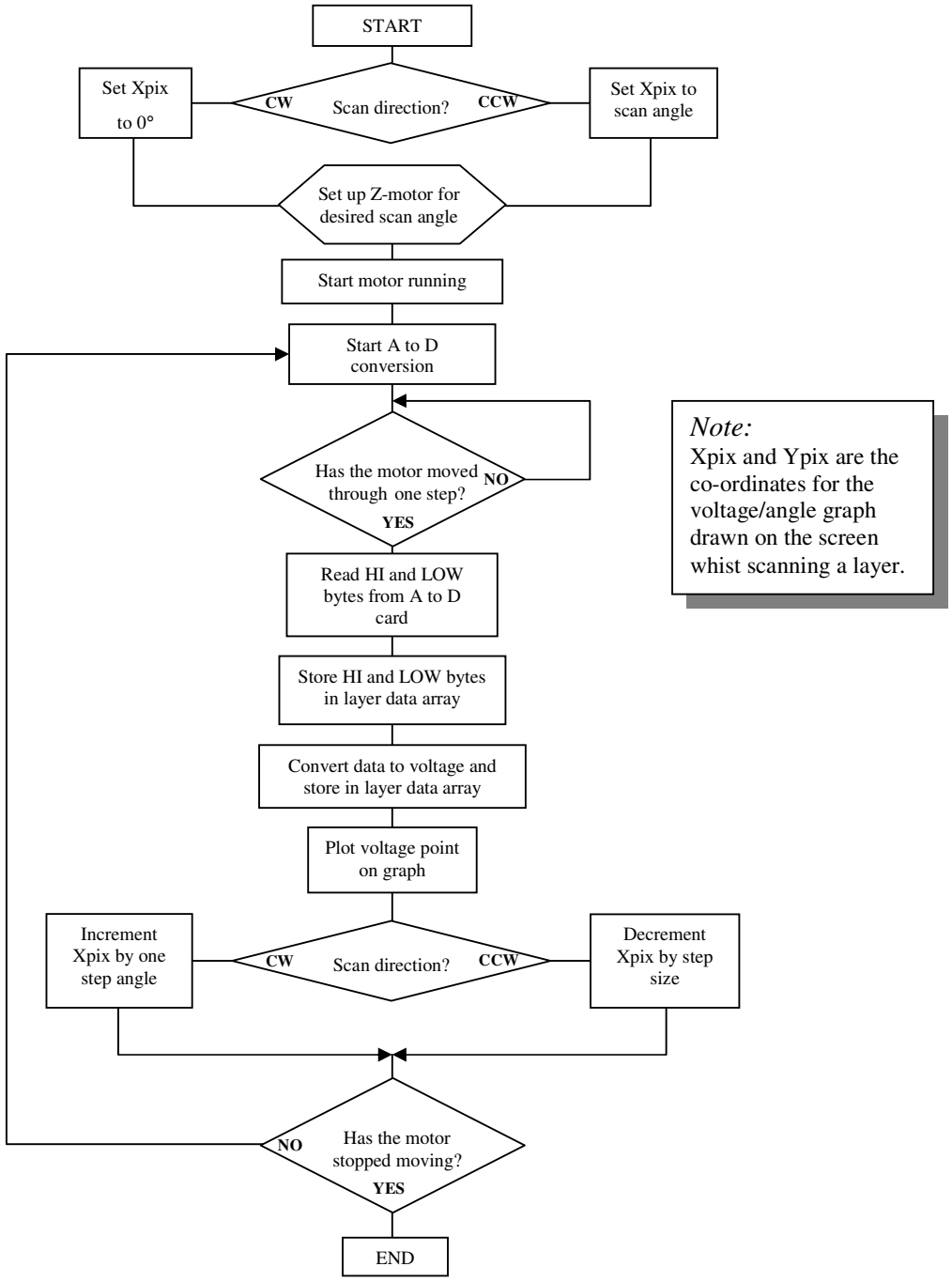

Figure 2.4.11: Flowchart showing the processes involved in scanning one layer.

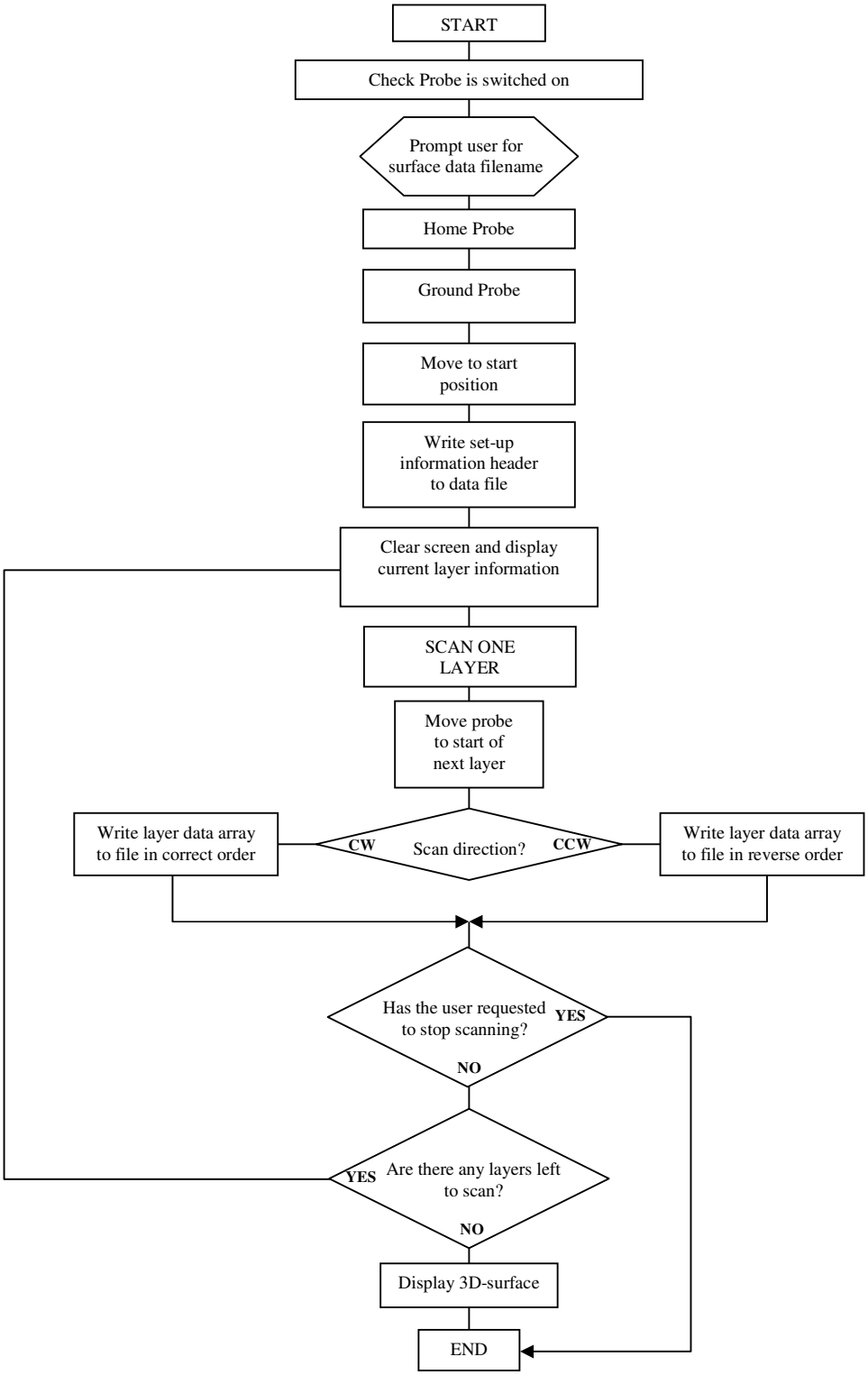

Figure 2.4.12: Flowchart showing the processes involved in scanning a complete surface.

2.4.12 Menus

Main Menu

The user interface for the scanning software is menu driven. When the program starts the user sees the intro screen. On pressing any key the screen clears and the user is given the option to run the Auto-SetUp utility by pressing the spacebar. The Auto-SetUp utility shown in figure 2.4.13, warms the probe up and measures the probe drift rate. After this the user is presented with the main menu shown in figure 2.4.14. The user can navigate around the menus using the cursor keys and the next level menu will pop up when selected. A single sentence at the bottom of the screen in yellow text offers help for each of the menu items.

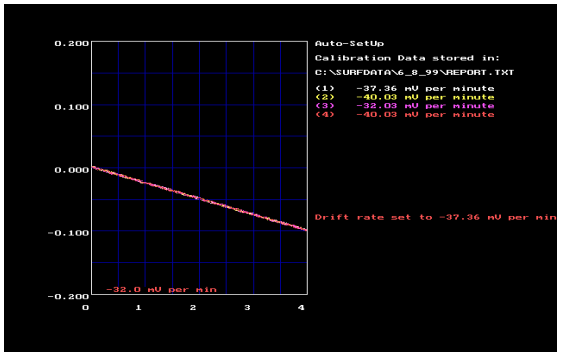

Figure 2.4.13: The Auto-SetUp utility.

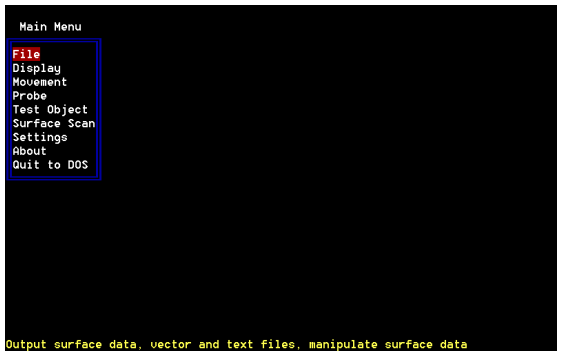

Figure 2.4.14: The Main Menu.

File Menu

Using the file menu shown in figure 2.4.15, files from the floppy drive can be copied to the surface data libraries and vice-versa. The surface data can also be converted to an ASCII text format to allow other software packages to import the surface data. Two text formats are available: text array or x-y-z column format.

The surface data files can be processed to remove probe drift and ground offset characteristics. The program always keeps track of the original measured probe voltage distribution to allow the data to be reverted to its original format.

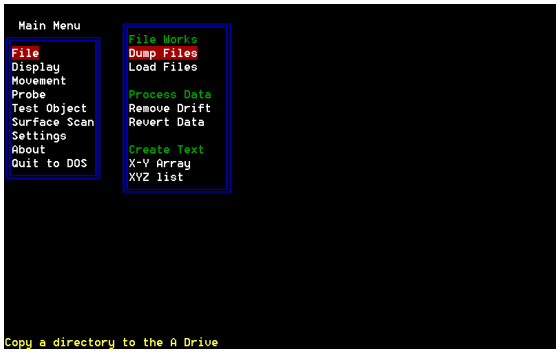

Figure 2.4.15: The file menu.

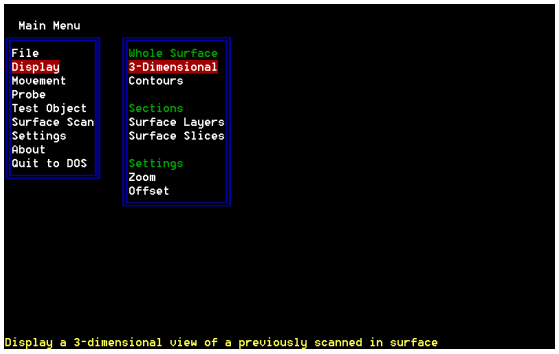

Figure 2.4.16: The display menu.

Display Menu

The display menu shown in figure 2.4.16 offers four basic graph plotting facilities to display previously scanned-in surface data files. The data can be displayed in full or as two-dimensional plots of slices through the surface. Figure 2.4.17 shows the surface displayed in layers as they were scanned in. The up and down cursor keys can be used to step through each layer. The position of the probe above the test object is also shown.

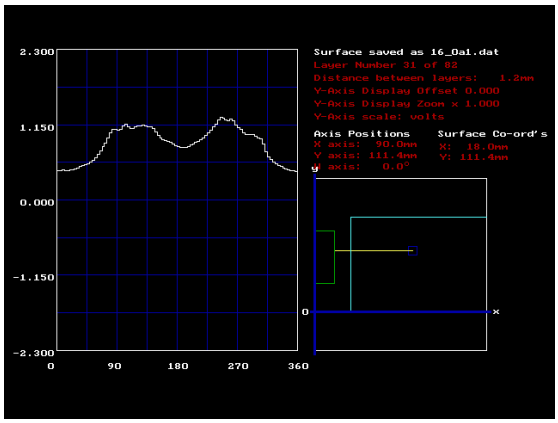

Figure 2.4.17: Displaying surface layers.

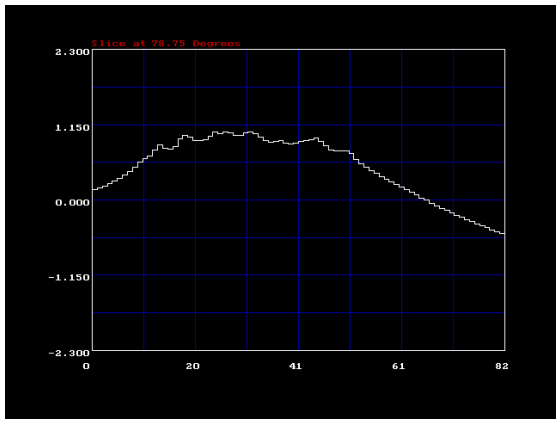

Figure 2.4.18: Displaying surface slices.

It is also possible to display slices through the distribution at different angles as shown in figure 2.4.18, again the cursor keys can be used to display slices at different angles.

To provide an overall view of the whole distribution either a 3D plot or a contour map can be used. Examples of these are shown in figures 2.4.19 and 2.4.20.

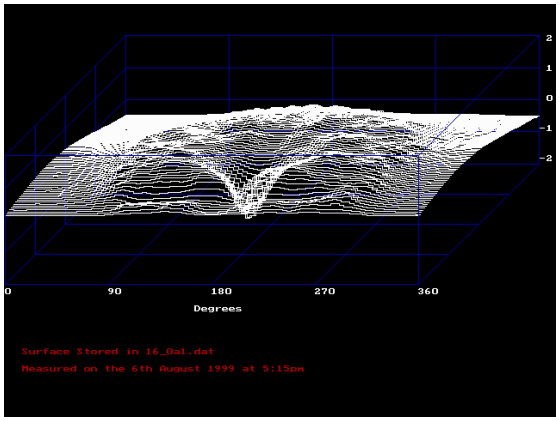

Figure 2.4.19: Displaying a 3D Surface.

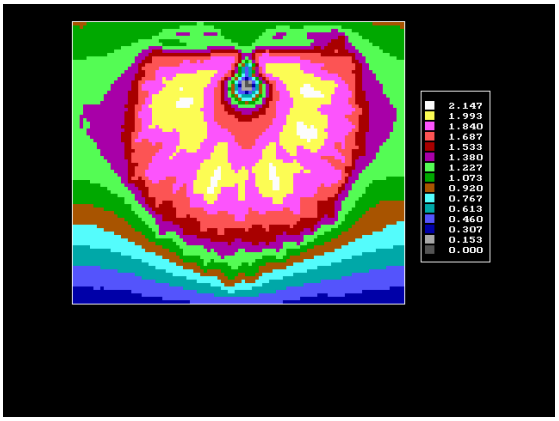

Figure 2.4.20: Displaying a Contour Map.

Varying the y-axis display and zoom and offset settings can change the appearance of all the plots. This can be useful when studying fine detail in the distribution.

Movement menu

The movement menu shown in figure 2.4.21 allows the user to control the position of the probe. The probe can manually be moved to any position, or it can be told to move to a specific location. There are facilities to move the probe directly to important positions, such as hiding it out of the way whilst the high voltage test is carried out and homing the probe for positional reference purposes. The position to which the probe moves when it grounds itself is also set in this menu.

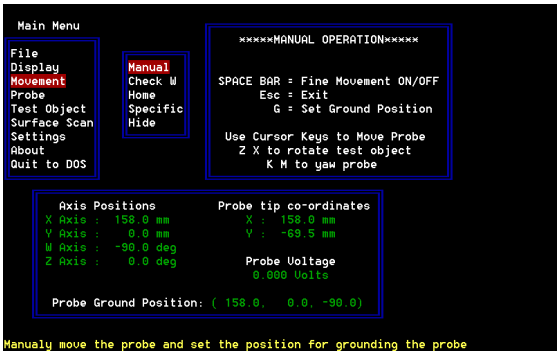

Figure 2.4.21: The manual movement menu.

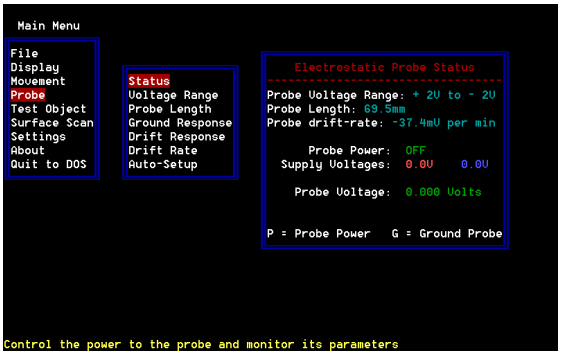

Figure 2.4.22: The probe status menu.

Probe menu

The probe menu shown in figure 2.4.22 allows the user to change probe settings, such as probe length and probe voltage divider ratio (i.e. the probe voltage range). The power supply to the probe can be turned on and off. There are also options for the probe characteristics: the probe ground response can be measured and set, and the probe drift rate can be measured and set.

Test object menu

The test object menu shown in figure 2.4.23 is used to define the shape of the test object to be scanned. Test objects can be measured using the sprung loaded position sensor. To do this the sensor is positioned manually at the top of the contour of the test object to be measured. The scanning platform will then track down the insulator surface recording the profile until any key is pressed. The user is then prompted to give a file name for the test object. It is not advisable to try to measure highly contoured test objects with the position sensor because sharp changes in geometry may cause the position sensor to get stuck and possibly cause damage to the platform.

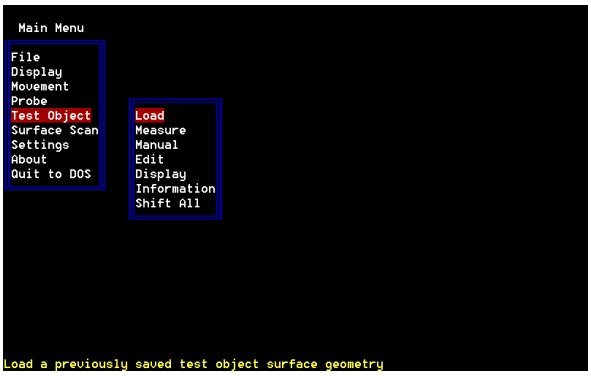

Figure 2.4.23: The test object menu.

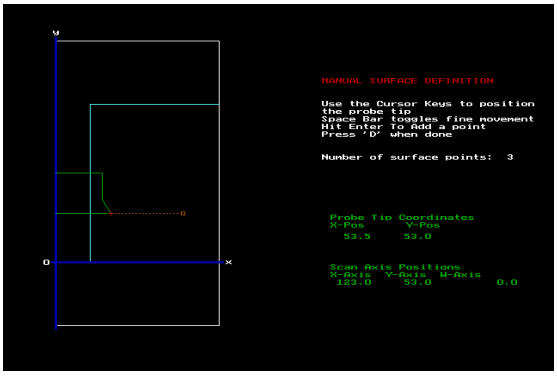

Figure 2.4.24: Manual test object definition.

Test objects can be generated manually using the manual definition utility shown in figure 2.4.24. The probe tip position is used to define surface contour points. A graphical display allows the user to see the position of the probe. When the return key is pressed the current probe tip position is used to define a surface contour point. The user continues to input surface contour points until the definition of the test object is complete at which point the user is prompted for a surface data file name.

Previously defined test objects can be loaded and edited using the test object editing utility shown in figure 2.4.25. The position of each surface point can be moved.

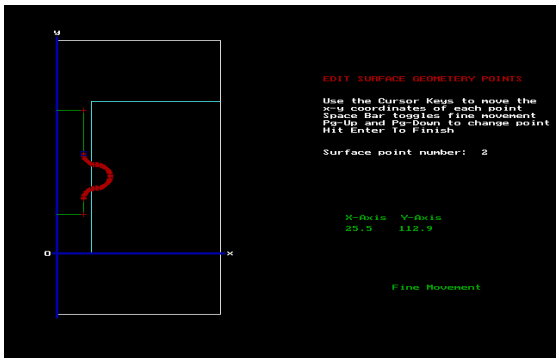

Figure 2.4.25: Test object edit utility.

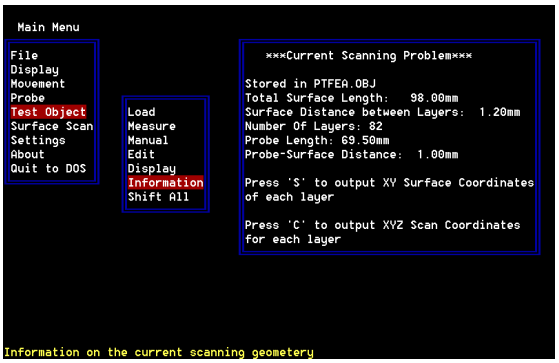

Figure 2.4.26: Scanning problem information.

Information about the current test object and scanning problem can be obtained as shown in figure 2.4.26. The co-ordinates on the surface contour above which each of the probe measurements is taken can be outputted as a list of x-y co-ordinates in a text file. The X-Y-Z co-ordinates for the position of the probe at each scan point can also be generated in a similar manner.

A simple utility is also available to translate the test object surface points up or down and left or right. This is used to fine-tune the alignment of the test object.

Surface Scan Menu

To perform a scan of the current test object the surface scan menu is used as shown in figure 2.4.27. Before scanning, the user is prompted to give a filename for the surface data file. To test the scanning system is working correctly the option is available to scan in a single layer on its own. It is also possible to scan one layer in both directions using the double back command. Both scans are displayed on the same axis so the dynamic response of the probe can be observed.

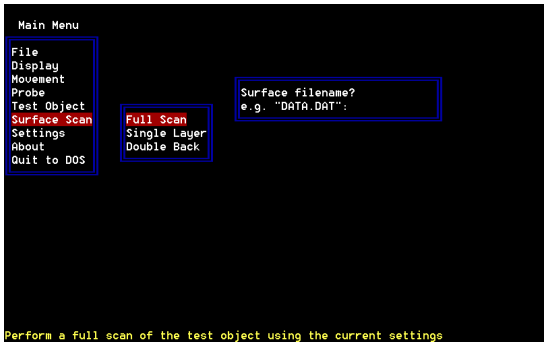

Figure 2.4.27: Surface scan menu.

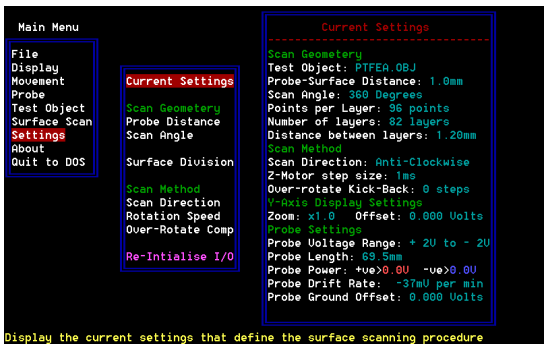

Figure 2.4.28: Scan settings menu.

Settings Menu

Before any measurements are made on the surface the scanning settings should be checked. This is done using the settings menu shown in figure 2.4.28. Using this menu all the scanning parameters can be varied. The program will automatically recalculate the scanning points when any changes are made.

Figure 2.4.29 shows how to set the division of the surface. Either the number of elements or the size of the elements can be varied and the program will alter each accordingly. By pressing the 's' key the program will make the elements square. For contoured test objects the width of elements on different layers will vary, the program can display the element width on each layer by pressing the 'w' key this is shown in figure 2.4.30.

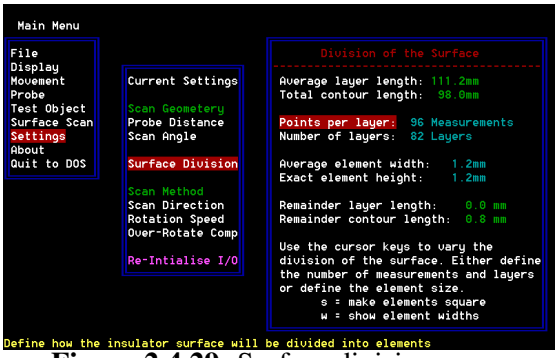

Figure 2.4.29: Surface division menu.

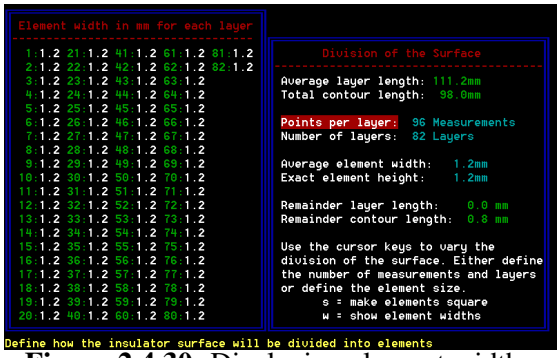

Figure 2.4.30: Displaying element widths.

The rotation speed can be set by giving the Z-Axis motor step period as shown in figure 2.4.31. After the step period has been set the program rotates the test object to allow the user to see if it rotates properly. For large heavy test objects the Z-Axis tends to over-rotate, carried forward by its own angular momentum. To prevent this the program can add a few steps in the opposite direction after each layer rotation to bring the test object to a halt. A utility to help the user apply the correct kick-back setting to maintain angular alignment is shown in figure 2.4.32.

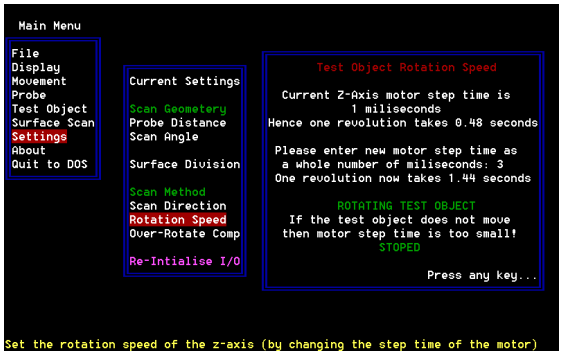

Figure 2.4.31: Setting rotation speed.

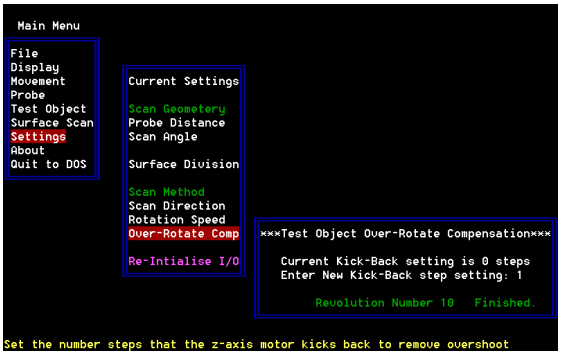

Figure 2.4.32: Setting kick-back.

2.5 Solver Software

2.5.1 Introduction

The aim of the solver software is to reduce the extremely complex task of calculating surface charge distributions to a few simple steps. The solver software is the practical implementation of the Φ-Matrix Calibration technique described at the start of this chapter. The solver software is fully compatible with the scanning software.

2.5.2 Memory Implications

The solution process involves huge amounts of data. An n×n distribution contains n^2 numbers and requires an $n^2 \times n^2$ Φ-Matrix to solve. The matrix thus contains n^4 values; each a 64-bit (8-byte) floating-point number. This means that the computer used to invert the matrix must be able to store $8n^4$ bytes to solve an n×n distribution. This relationship is shown in figure 2.5.1. The inversion time of the matrix will depend on the speed at which the computer can access the matrix data. With the access times for hard disks measured in milliseconds, and for memory in nanoseconds, it is obvious that the computer must store the whole matrix in its memory. Figure shows how quickly the amount of memory required increases with matrix resolution. To solve a 100×100 distribution 800MB of RAM is required; the Φ-Matrix contains 100,000,000 values.

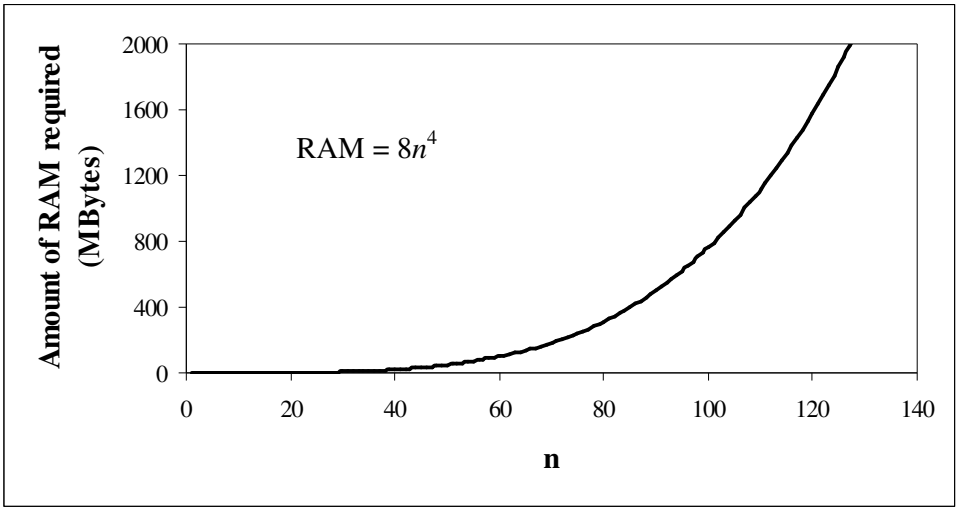

Figure 2.5.1: How the amount of RAM required varies with the surface division, n.

2.5.3 The Galaxy

The memory requirement of the solution process is one of the factors that limit the maximum resolution achievable. This has led to the use of the largest available computer. UMIST has recently acquired a high power computer: The Galaxy, which is a Fujitsu AP3000 series distributed-memory parallel compute server, employing UltraSPARC workstations as node host processors. Each node has either 256 or 512MB of RAM and runs the SUNSolaris operating system. A job can be executed on single node and use the distributed memory from the other nodes, this allows up to 5GB of RAM to be available for use. Telnet and ftp are used to communicate with each of the nodes in Galaxy. The Φ-Matrix is generated using compiled Pascal source code and inverted using Matlab. The whole solution process is controlled by batch files: simple text files that contain UNIX command line instructions.

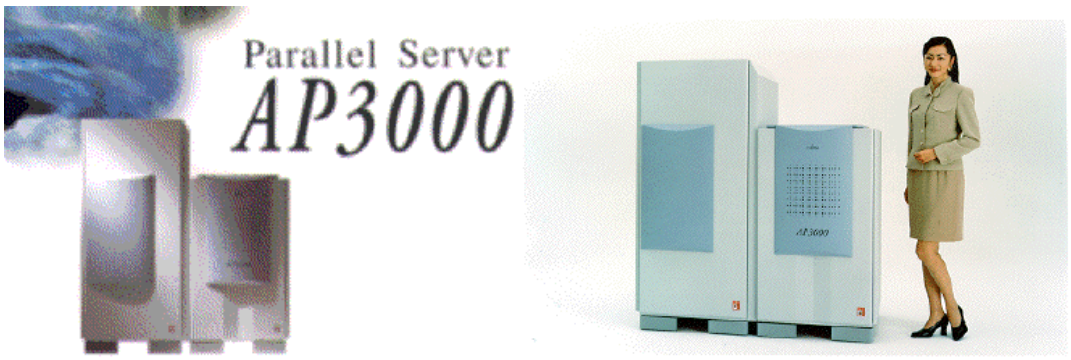

Figure 2.5.2: The Galaxy - a Fujitsu AP3000.

2.5.4 Solver Requirements

- The huge size of the Φ-Matrix means that it cannot possibly be stored whilst the solver is not being used, thus the solver must be capable of automatically generating the matrix from the file containing the key values defining the ϕ-functions.
- There are several parameters that define the scanned surface geometry and the Solver must be capable of automatically adjusting the size and scaling of the Φ-Matrix accordingly.
- The Solver must be able to read the surface data files generated by the Scanning Software and convert them into voltage vectors.

- The Φ-Matrix must be inverted and multiplied by the voltage vectors to produce the charge density vectors.
- The solved charge density distributions must be stored in a format that can be read by the Scanning Software and other applications.
- Sets of surface data files with the same scanning parameters and thus the same Φ-Matrix must be solved together, not one at a time. This will obviously reduce the number of matrix inversions required and thus minimise the solution time.
- The whole process must be automated.

2.5.5 Solution Procedure

Overview

The solution procedure is quite complicated, figure 2.5.3 shows a schematic representing the overall operation of the solver. However all the user has to do is copy the surface data files they wish to solve and the relevant test object geometry file into the users home directory and type 'solve'. The rest of the solution technique is fully automated.

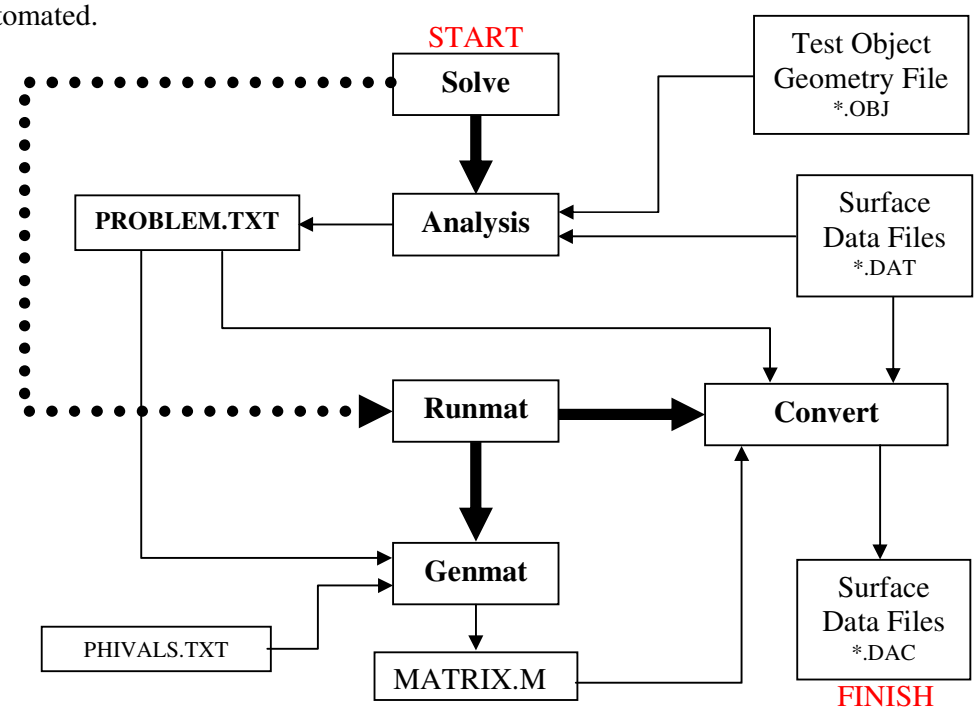

Figure 2.5.3: An overview of the Solver software operation.

Solve

The Solve batch file first runs the Analysis program that looks for surface data files in the directory, reads their header information and using the relevant test object geometry file calculates surface division and element sizes. The Analysis program then prompts the user for two correction factors that in normal operation should be set to 1. These two correction factors were used in the development process and allow scaling of the Φ-Matrix in the x and y directions. This allowed the effect of the Φ-Matrix to be studied. Finally the Analysis file generates a text file called PROBLEM.TXT which contains a summary of the problem to be solved. This file is used by the rest of the programs in the solution process.

The Solve batch file then submits the Runmat batch file (which controls the rest of the solution process) to LSF, the Galaxy's Unix Batch System.

Batch Job Processing

Batch Processing provides more efficient execution of resource intensive jobs. Rather than running immediately a command is entered, batch jobs are kept on a list of jobs called a queue.

The LSF Batch system runs jobs from the queue when the appropriate resources are available. By making sure that every job has the resources it needs, resource intensive jobs can be processed more efficiently. In LSF, batch queues can have access to all the hosts in Galaxy. The job can be run as soon as any suitable host becomes available. The user does not need to hunt round Galaxy to find an idle host. The jobs output is stored in a text file so that it can be examined when the job has finished.

There are four queues to which jobs can be submitted: the short queue for jobs that last up to one hour; the medium queue, 3 hours; the long queue, 25 hours, and the CIF queue. If the job is still running after its allocated CPU time it is shut down. The CIF (Compute Intensive Facility) has no time limit.

The Galaxy is used by a large number of people and only one job can run at a time in the CIF queue, so the waiting time is often very long. Most jobs are therefore submitted to the long queue, which runs at night and is suspended during the day and allows a total of 25 hours CPU running time for each job.

Solution Time

The inversion time of the Φ-Matrix is the dominant factor in the total solution time. The inversion time increases rapidly with the size of the Φ-Matrix. For the algorithm used by Matlab the inversion time increases as the square of the number of elements in the matrix. It has already been shown that the number of elements in the Φ-Matrix varies as the fourth power of the surface division. Hence the solution time will increase as the sixth power of the surface division. This means that the solution time will increase very rapidly for higher resolution surfaces.

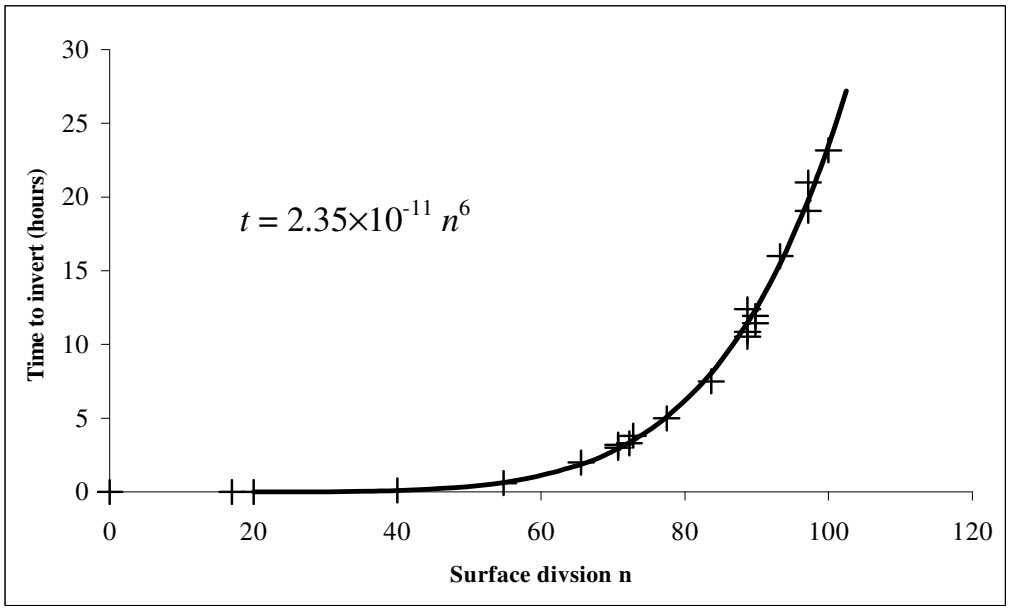

Figure 2.5.4: The increase in solution time with surface division, n.

The points in figure 2.5.4 show the time it took to solve several charge distributions with different numbers of surface elements. Surface division, n is the square root of the total number of elements in each distribution. It is the mean one-dimensional division of the surface. The curve shown is the best-fit sixth power.

The approximate solution time for a charge distribution can be found from:

$$t = 2.35\times10^{-11}\ n^6$$

So the maximum division of the surface that can be solved in the long queue is:

$$n = \sqrt[6]{t / 2.35\times10^{-11}} = \sqrt[6]{25 / 2.35\times10^{-11}} = 101.036$$

Hence, the maximum number of surface division that can be solved in the 25 hour, long queue is: 101×101 elements.

Runmat

The Runmat batch file orchestrates the rest of the solution process. When it is run by the Batch File Processing System it first generates a temporary directory in the system workspace and copies all the files required for the rest of the solution process into it. It then runs Genmat, which generates the Φ-Matrix using the text file, PHIVALS.TXT containing key values that define the ϕ-functions. Matlab is started and the program Convert is evoked which applies the Φ-Matrix Calibration technique to the surface data files. Finally Runmat copies the solved data files back to the users home directory and tidies up after itself by deleting the generated files and removing the temporary directory.

Genmat

Genmat is a compiled program that generates the matrix used in the Φ-Matrix Calibration technique. The structure of the Φ-Matrix is shown in figure 2.2.7. To generate the Φ-Matrix the ϕ-functions for each layer must be calculated. This is done by quadraticaly and radially interpolating key values contained in the text file PHIVALS.TXT.

Key Values are points, that when a smooth curve is drawn through them, define the one-dimensional ϕ-functions along the x and y-axis for each scanned layer. The process of generating the ϕ-functions by quadratic interpolation is detailed in figure 2.5.5.

The two single dimension ϕ-functions are then combined by radial interpolation to give the full two-dimensional ϕ-function for each layer as shown in figure 2.5.6.

Every layer has its own ϕ-function, each slightly different from the next; as the probe approaches any grounded surfaces the ϕ-function is distorted slightly. Key values are not required for every layer, only a few sets of key values for important layers (where the ϕ-function changes shape significantly) are necessary. The program calculates the key values for the missing layers by quadratic interpolation of the key values on the layers it does have. These interpolated key-values are then interpolated as normal into full ϕ-functions for every layer.

Key Values

x	ϕ_x	y	ϕ_y
x_1	ϕ_{x1}	y_1	ϕ_{y1}
x_2	ϕ_{x2}	y_2	ϕ_{y2}
x_3	ϕ_{x3}	y_3	ϕ_{y3}
x_4	ϕ_{x4}	y_4	ϕ_{y4}
x_5	ϕ_{x5}	y_5	ϕ_{y5}
x_6	ϕ_{x6}	y_6	ϕ_{y6}
x_7	ϕ_{x7}	y_7	ϕ_{y7}
x_8	ϕ_{x8}	y_8	ϕ_{y8}
:	:	:	:
:	:	:	:

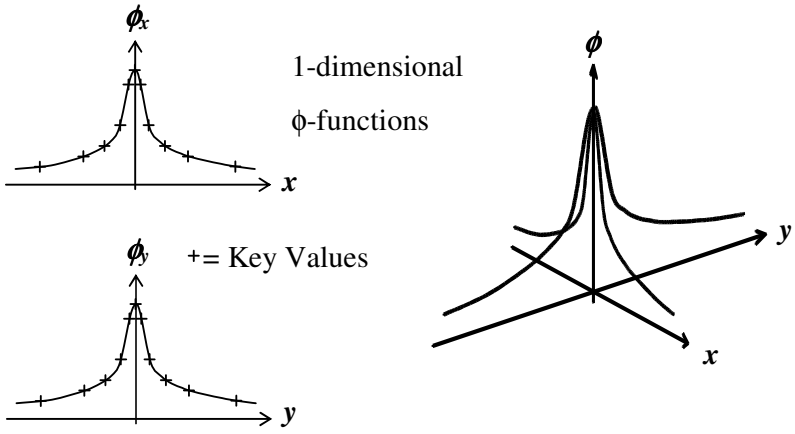

By quadratic interpolation:

$$\phi_x(x) = \phi_{x(m-1)} + (x - x_{m-1})\left(\frac{\phi_{xm} - \phi_{x(m-1)}}{x_m - x_{m-1}}\right) + (x - x_{m-1})(x - x_m)\left[\frac{\left(\frac{\phi_{x(m+1)} - \phi_{xm}}{x_{m+1} - x_m}\right) - \left(\frac{\phi_{xm} - \phi_{x(m-1)}}{x_m - x_{m-1}}\right)}{(x_{m+1} - x_{m-1})}\right]$$

Where m is set so: $x_{m-1} < x < x_{m+1}$

Similarly:

$$\phi_y(y) = \phi_{y(m-1)} + (y - y_{m-1})\left(\frac{\phi_{ym} - \phi_{y(m-1)}}{y_m - y_{m-1}}\right) + (y - y_{m-1})(y - y_m)\left[\frac{\left(\frac{\phi_{y(m+1)} - \phi_{ym}}{y_{m+1} - y_m}\right) - \left(\frac{\phi_{ym} - \phi_{y(m-1)}}{y_m - y_{m-1}}\right)}{(y_{m+1} - y_{m-1})}\right]$$

Where m is set so: $y_{m-1} < y < y_{m+1}$

Figure 2.5.5: Generating one dimensional ϕ-functions from key values by quadratic interpolation.

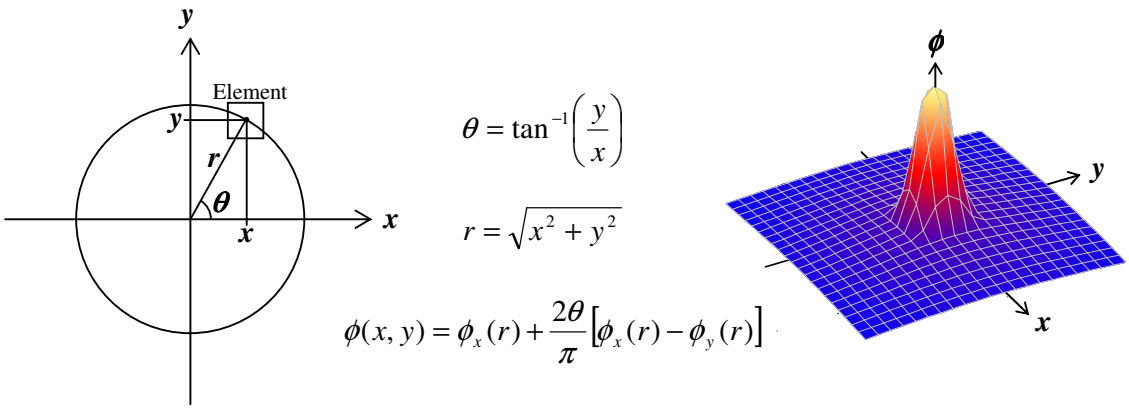

Figure 2.5.6: The full 2-dimensional ϕ-function is generated by radial interpolation of the two 1-dimensional ϕ-functions.

When the ϕ-function for each layer has been found they must be converted into a Φ-Matrix. The number of elements per layer, the number of layers and the element width on each layer is given by the text file PROBLEM.TXT that was generated by the Analysis program. Using this information Genmat constructs a Φ-Matrix of the correct proportions. The ϕ-functions are scaled accordingly for each layer depending on the element width. This allows contoured surfaces to be accurately solved.

The Φ-Matrix is stored as 32-bit floating point numbers column by column in a file called MATRIX.MAT for use by the Convert program.

Convert

The final stage of the solution procedure is the implementation of the Φ-Matrix Calibration Technique. The Convert program that runs under Matlab first gets the list of surface data filenames to be solved from PROBLEM.TXT; up to 50 files can be solved at one time. It then loads in the Φ-Matrix and inverts it. The surface data files are then converted into probe voltage vectors and multiplied by the inverted matrix. The resulting charge density vectors are converted back into surface data file format and saved with the same filename but the extension is changed from *.DAT to *.DAC. The file status flags in the headers of the solved surface data files are also changed to allow the viewer software to know that the files have been solved.

2.6 Viewer Software

2.6.1 Introduction

The scanning software is capable of displaying the surface charge distributions and doing basic total charge calculations. To enable a detailed analysis of the solved charge distributions a software viewer was specially written. Matlab was used as the development language because of its excellent in-built data handling facilities and graphical utilities. It also has the advantage of running under the Windows operating system.

2.6.2 Implementation

In order to run the viewer Matlab is required. The program is stored as a text file and is called VIEWER.M, it is evoked from the Matlab Command Window by typing viewer. The user is then prompted for the filename of the Surface Data File they wish to view. The program then loads the desired file as shown in figure 2.6.7. The viewer can read surface data files containing probe voltages or surface charge density measurements, the viewer can tell which is which automatically because of the file status flag in the header.

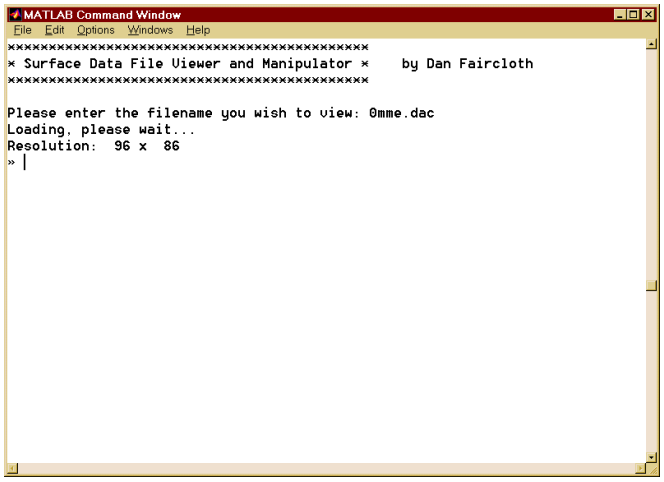

Figure 2.6.7: The Matlab Command Window.

The main data file viewer then opens in a new window, this is shown in figure 2.6.8. The name of the file being viewed is shown in the name bar at the top of the window. The top graph displays layers through the distribution and the bottom shows slices though the distribution. Different layers and slices can be viewed by simply moving the slider bars beneath the plots. The displayed layer or slice number is shown in the slider bar.

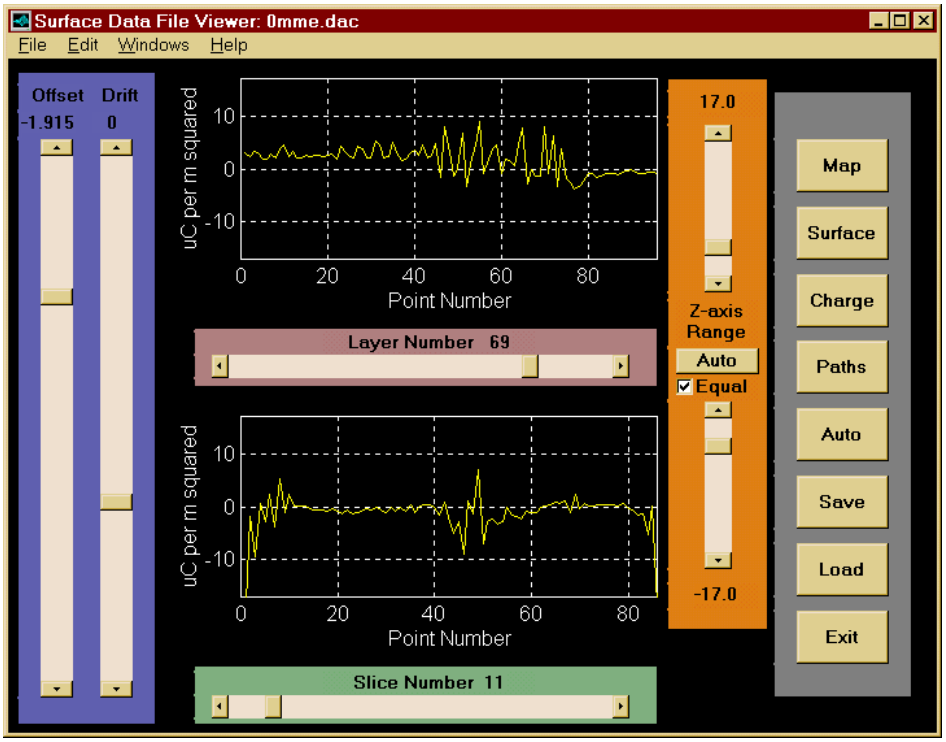

Figure 2.6.8: The Surface Data File Viewer main window.

The charge density (or probe voltage) axis range can be varied using the two sliders on the right of the plots. The upper and lower limits of the range can be varied independently or they are kept equal if the 'Equal' box is checked. Pressing the 'Auto' button will set the range to the maximum and minimum values in the distribution.

On the left of the plots are two sliders; one for the offset, the other for the drift rate. By varying these sliders the user can remove probe drift and offset from measured probe voltage distributions. The drift and offset are removed as the slider is moved, this allows the effect of probe drift removal to be visualised as it happens. The effect of distribution offset is discussed fully in appendix A.

Rather than using the sliders the user can type the required settings directly into the editable text above each of the sliders.

The large buttons on the right of the main window allow a more detailed analysis of the distribution. The map button opens a new window and plots a contour map of the distribution. Contour maps offer the best overall view of a charge or voltage distribution, key features can easily be observed Two examples of contour maps are shown below. Figure 2.6.9 is a probe voltage distribution and figure 2.6.10 is the resultant charge density distribution. The overall effect of the Φ-Matrix calibration technique is evident.

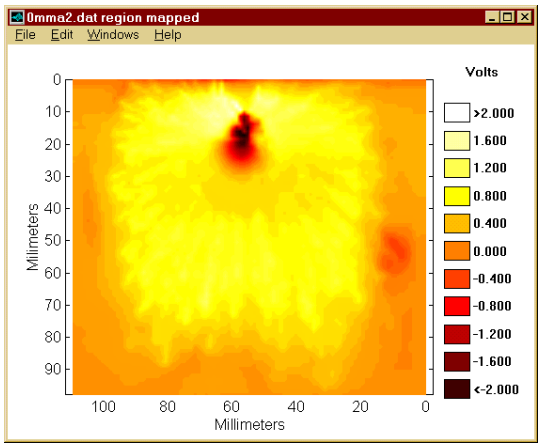

Figure 2.6.9: A contour map of a probe voltage distribution.

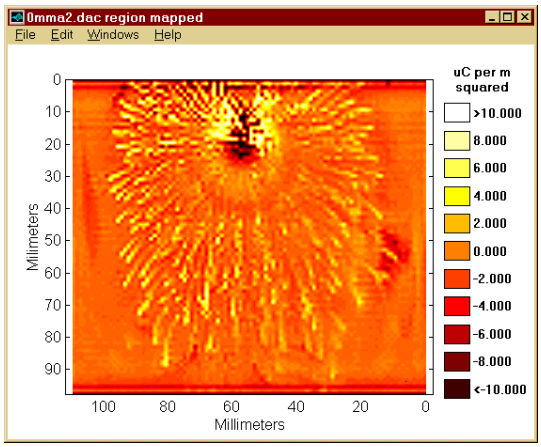

Figure 2.6.10: A contour map of a surface charge distribution.

The axes are automatically scaled in millimetres and a legend is generated showing the colour contour values. The z-axis range in the main window sets the contour range.

By using the mouse the user can select a region of interest on the contour map. Pressing the right mouse button completes the region selection, and the program calculates the net positive and negative charge in the selected region as shown in figure 2.6.11.

A new window as shown in figure 2.6.12 then opens, containing a light source shaded 3D surface plot of the selected region. The user can study the selected region using the four buttons in the top-right corner of the window that allow the surface plot to be rotated.

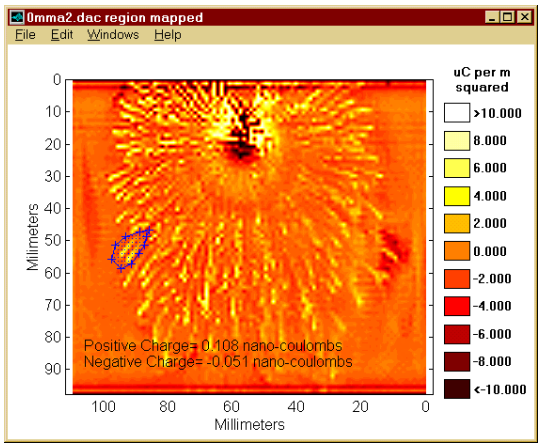

Figure 2.6.11: A region selected on the contour map.

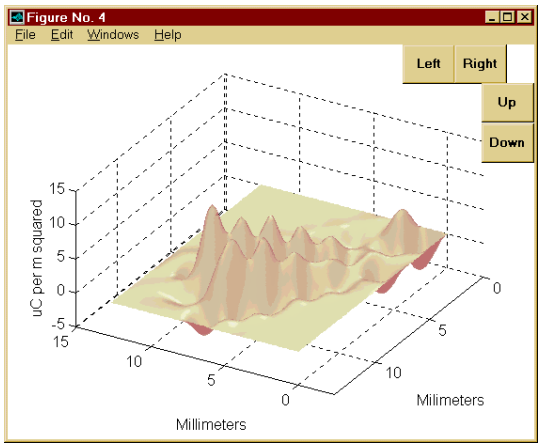

Figure 2.6.12: A 3-D surface plot of the selected region.

It is also possible to plot the entire distribution as a 3D surface using the 'Surface' button on the main viewer window. An example of an entire surface 3D plot is shown in figure 2.6.13. Probe voltage distributions can be displayed with good results, however surface charge density distributions do not look very good when plotted as 3D surfaces because of the fine detail in the distributions. It is advisable to view charge density distributions as contour maps.

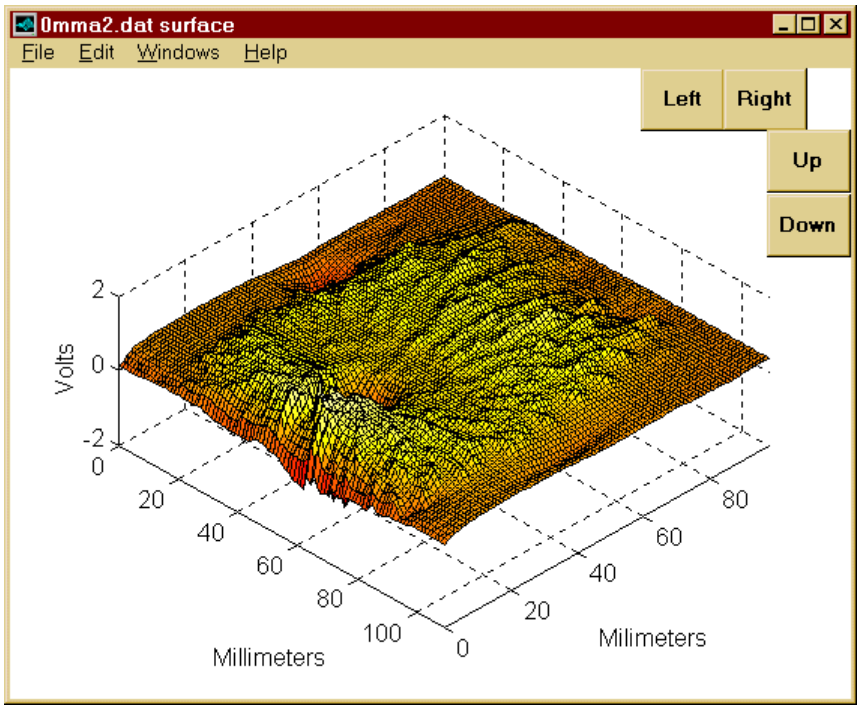

Figure 2.6.13: A 3-D surface plot of a probe voltage distribution.

A button labelled 'Charge' on the main window operates in a similar manner to the 'Map' button, however it allows a number of regions to be selected on the same contour map and does not plot the selected region in a separate window. This button is useful when finding the total charge contained in various parts of the distribution.

The charge density along paths through a distribution is obviously of importance when studying a surface. The 'Paths' button on the main window plots a contour map of the loaded distribution and using the mouse the user can select straight-line paths. The paths are defined by two mouse points and as many paths as the user wants can be plotted on the same map as shown in figure 2.6.14. The charge densities along each path are cubicly interpolated from the surrounding values in the charge distribution and plotted in separate windows, an example of which is shown in figure 2.6.15.

When the user has finished plotting paths the right mouse button is pressed and the program generates a text file containing the charge density along each of the path

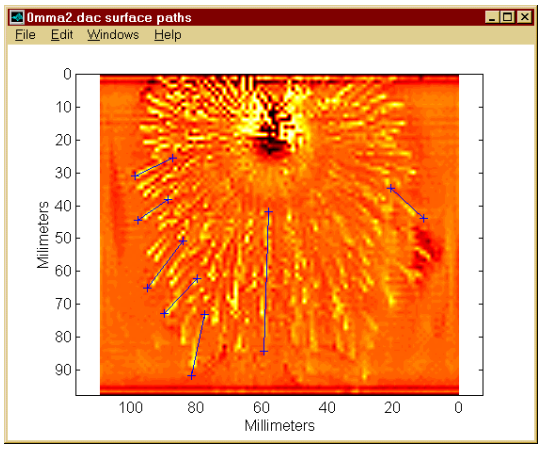

Figure 2.6.14: Paths selected on a contour map.

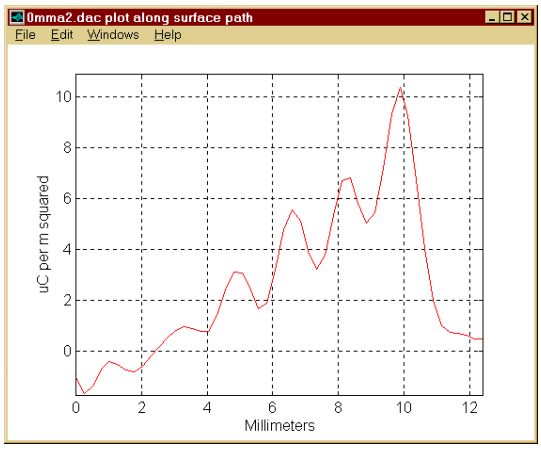

Figure 2.6.15: A plot of the surface charge density along a path.

Chapter 3: EXPERIMENTS

3.1 Introduction

Very few detailed studies have been undertaken on the surface charging of insulators and none to the resolution obtainable by the scanning system described in this thesis. It was therefore essential to start with simple insulator geometries.

The experiments conducted had a dual purpose; to evaluate the effectiveness of the scanning system and then to further our knowledge of the role surface charge plays in the surface flashover of insulators. The main aim of the experimental work was to obtain as much information as possible about individual discharge events. The next section describes the apparatus required to generate the discharge events and monitor them.

3.2 Apparatus

3.2.1 Electrodes

The high voltage electrodes between which the discharges were produced had to be chosen to generate a reliable and controllable discharge event that could be readily observed.

The main electrode configuration studied was the rod-plane gap. This geometry represents a practical arrangement; in HV plant, flashover is always initiated in regions of enhanced field caused by conducting protrusions.

The rod-plane gap also offers a number of advantages for the study of discharges:

1. It only has one region of enhanced non-uniform field.
2. It is often used as a reference gap.
3. There is a large body of literature available on the gap for comparison.
4. It produces a simple streamer discharge.

Rods of three different radii shown in figure 3.2.1 were used to allow a range of fields to be studied. Each rod was made from copper and the electrode surface was smoothly finished. The rods were all over 150mm long. The blunt rod had a small hole directly up the central axis.

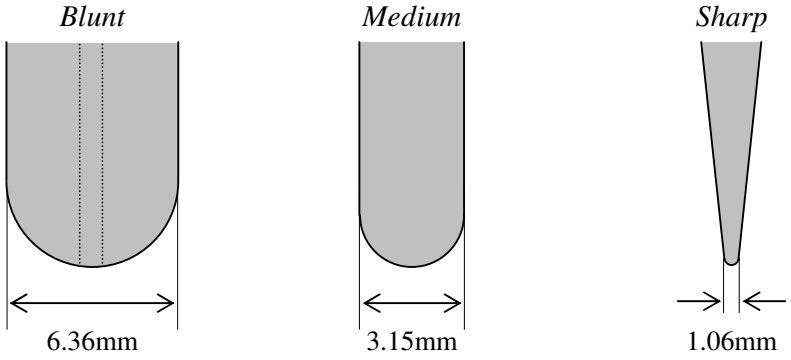

Figure 3.2.1: The three different rod electrodes used in the experiments.

The plane electrode comprised of a flat disc electrode shown in figure 3.2.2. The disk was made of polished stainless steel with a diameter 300mm and a thickness of 25mm. The edge of the electrode was rounded.

A small register was machined into the centre of the electrode to allow exactly repeatable alignment of the insulator test objects. A matching register was machined in the bottom of each test object. The register was only 1mm deep with a diameter of 20mm. The smallest diameter test object used was 40mm so the register was always far enough away from the triple junction to prevent additional field enhancement.

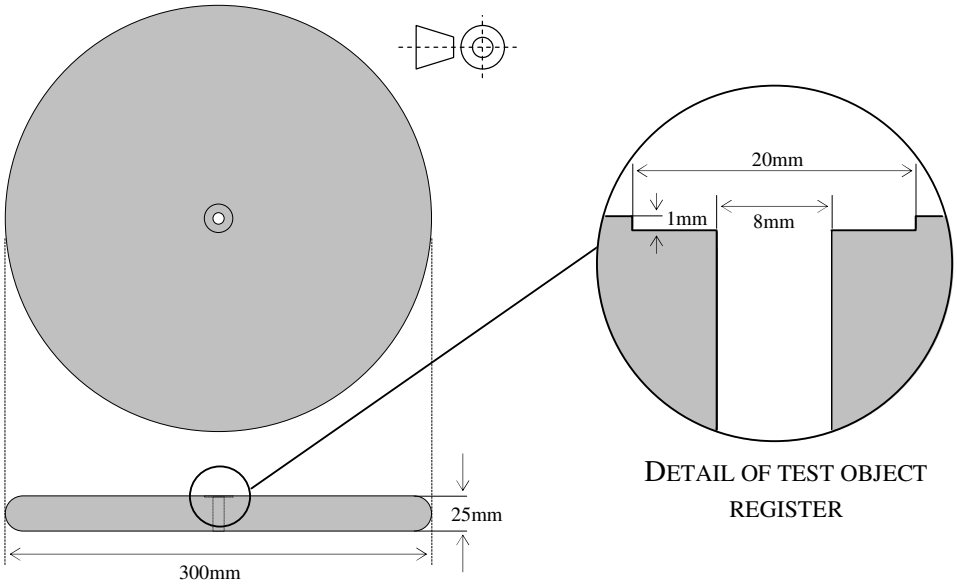

Figure 3.2.2: The plane electrode used in the experiments.

An 8mm diameter hole was drilled through the centre of the electrode to allow, if required, the insulator specimen to be bonded tightly to the electrode using a PTFE screw. The screw passed through the electrode and into a threaded hole in the insulator specimen.

Figure 3.2.3 shows the rod-plane gap used in the experiments, with a 100mm tall cylindrical insulator specimen positioned in the gap. Several gap lengths were employed depending on the size of the insulator and the desired rod position on the insulator. The photo-multipliers used to observe the streamers traverse the gap can just be seen on the right of Figure 3.2.3.

A second plane electrode identical to the first was also used to make a plane-plane gap for a few experiments requiring a uniform field.

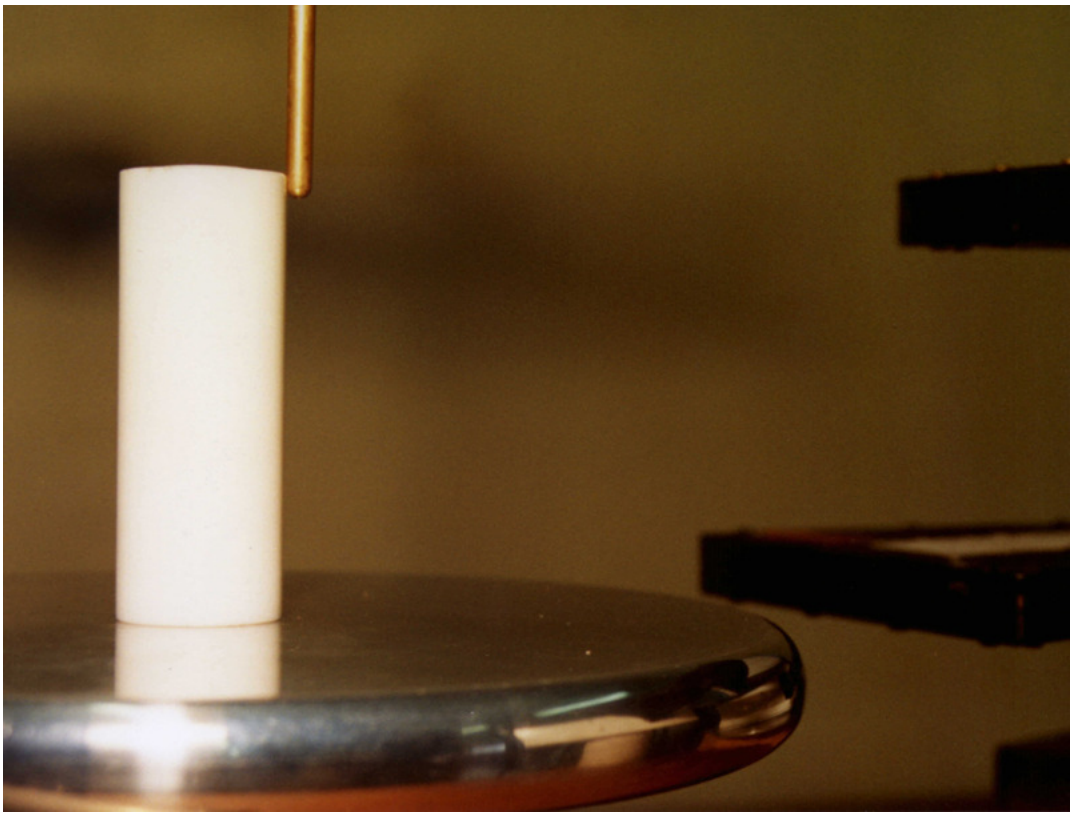

Figure 3.2.3: The electrode arrangement and a cylindrical insulator specimen.

3.2.2 HV Generation

Impulse Generators

Introduction

In order to study the surface charging of insulators, a technique was required to produce controllable discharge activity. When a test voltage was applied to the rod it was essential to record all discharge activity to allow a correlation with measured surface charge on the test insulator. Discharge activity in air occurs on the sub-microsecond time scale, so to reduce the complexity of analysis the test voltage could only be applied for a short time. An impulse generator provided a convenient method of applying a transient voltage to the rod.

An impulse wave can be considered to be a double exponential, i.e. a curve that is made up of two exponential curves (V_1 and V_2 in figure 3.2.4) subtracted from each other.

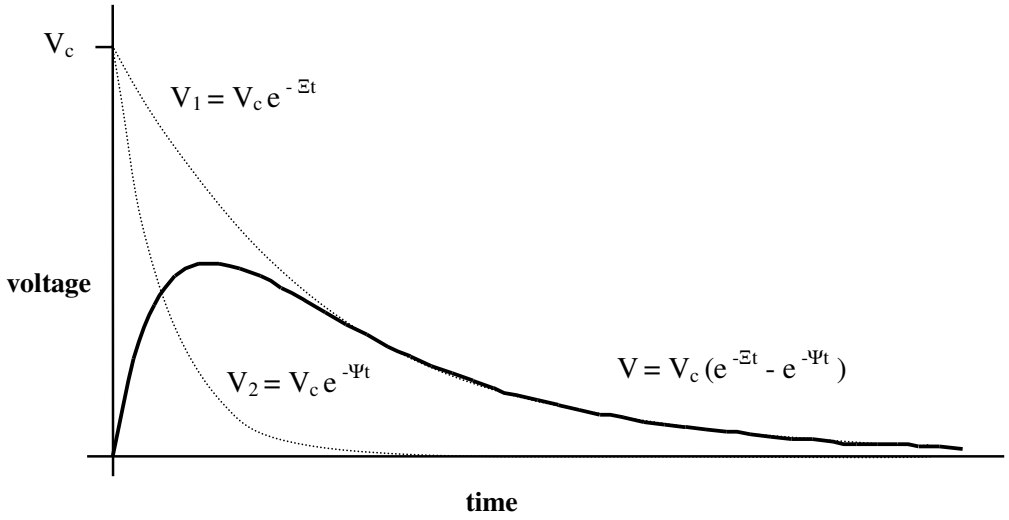

Figure 3.2.4: The impulse wave represented as a double exponential

The three points that can be used to specify an impulse wave are; peak impulse voltage, front time and tail time, they are shown in figure 3.2.5. The peak impulse voltage is the maximum voltage in the wave shape. The front time is specified in IEC standards as follows: draw a straight line through the points where the voltage is 30% and 90% of its peak value, the front time is then the time for the line to go from zero to the peak voltage. It is often, however simply measured as the time to peak. The tail time is the time for the voltage to drop to half its peak value.

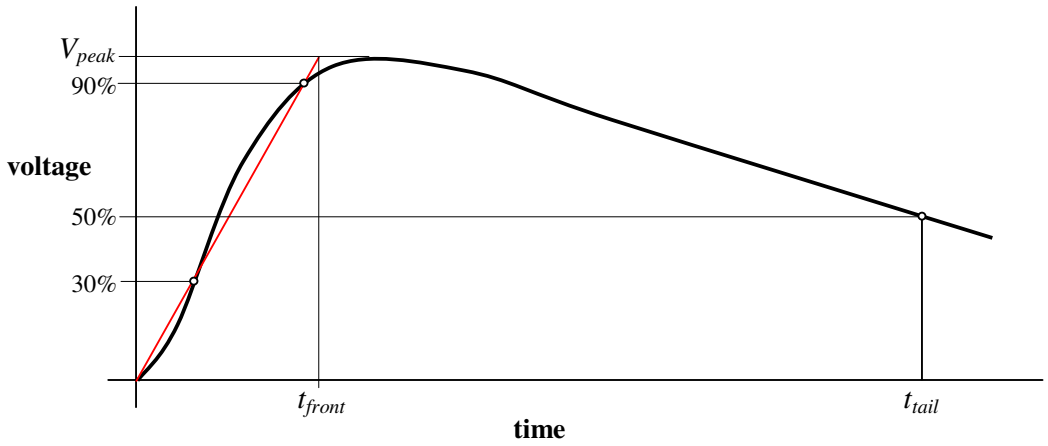

Figure 3.2.5: The points used to define the shape of an impulse voltage wave shape.

The shape of the impulse voltage wave was required to be short enough to produce a single discharge event. Another practical factor influenced the impulse wave shape: when the impulse generator fired the very fast rise of current in the spark gaps produced a large electromagnetic pulse. A combination of this pulse and high frequency current and voltage oscillations in the high voltage circuit was visible as noise in the measuring equipment. The noise decayed to a negligible value by about 1μs after the generator fired. It was therefore essential to delay the onset of corona activity beyond this time. The standard IEC 1.2/50μs lighting impulse wave had too fast a front time, so a non-standard wave shape had to be employed. A wave with a front time between 3 and 5μs and with a tail time of about 50μs proved satisfactory in producing a single discharge event delayed enough to be clear of the noise, and therefore readily observable.

Mode of operation

The basic method of operation of an impulse generator is as follows:

n stage capacitors are charged in *parallel* to a voltage, V_{stage}. Using spark gaps the capacitors are discharged in *series* to produce an impulse voltage of magnitude approximately equal to $n \times V_{stage}$. The wave shape of the impulse voltage is governed by an RC network.

The approximate wave shape can be calculated by using the simplified generator circuit shown in Figure 3.2.6. The capacitance C_T represents the stage capacitors of the generator in series, this equivalent capacitance is charged to a voltage $V_c = nV_{stage}$. The other components R_T, R_F and C_F can be varied to change the shape of the voltage wave, labelled V in figures 3.2.4 and 3.2.6.

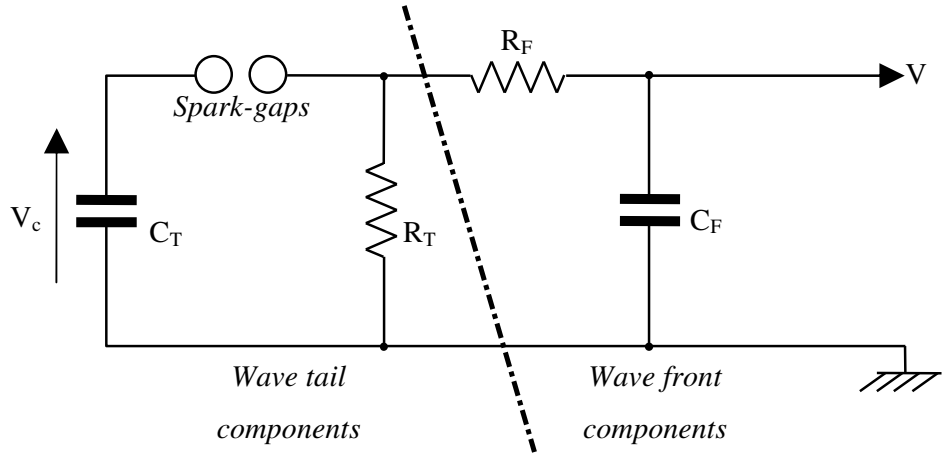

Figure 3.2.6: A simplified impulse generator circuit diagram

The peak value of the impulse wave, V_{peak} will be less than V_c. The ratio of V_{peak} over V_c is referred to as the generator efficiency, *Eff*. The front time is approximately defined by the values of R_F and C_F, and the tail time is defined by the values of R_T and C_T.

From figure 3.2.4 it can be seen that after the peak impulse voltage the wave shape is mainly defined by V_1, V_2 having decayed to a negligible value. Thus to find the tail time only V_1 needs to be calculated. This is done by neglecting the front components and reducing the generator circuit diagram to that shown in Figure 3.2.7.

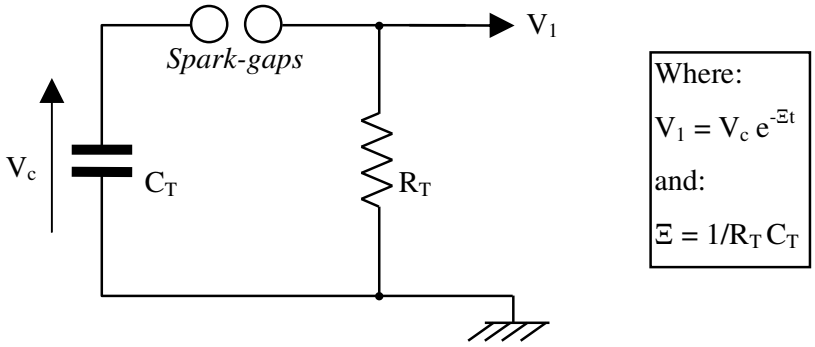

Figure 3.2.7: Simplified generator circuit diagram for tail time calculation.

The tail time of the wave is defined as the time for the voltage to decay to 50% of the peak voltage: $V_{50\%} = \frac{V_{peak}}{2} = \frac{Eff \cdot V_c}{2}$

To find the tail time this voltage must be equated with the equation for V_1 and rearranged thus:

$$\frac{Eff \cdot V_c}{2} = V_c e^{-\Xi t_{tail}}$$

$$\ln\left(\frac{Eff}{2}\right) = -\Xi t_{tail}$$

$$t_{tail} = -C_T R_T \ln\left(\frac{Eff}{2}\right)$$

neglecting any loss of charge: $V_c C_T = V_{peak}(C_T + C_F)$

hence: $$Eff = \frac{V_{peak}}{V_c} = \frac{C_T}{C_T + C_F}$$

In practice *Eff* will be less than this value when determined experimentally.

The wave front time can be found by assuming the wave tail resistor R_T can be neglected during the fast initial period. The equivalent circuit then becomes:

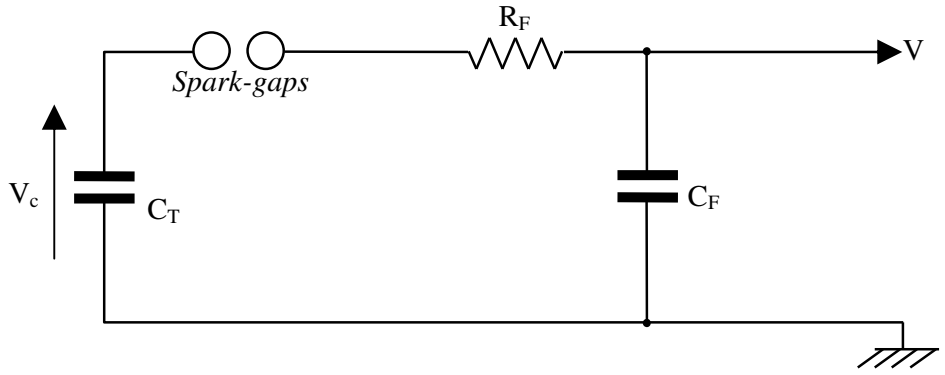

Figure 3.2.8: Simplified generator circuit diagram for front time calculation.

If the capacitor C_F is initially uncharged, then the voltage V can be shown to be:

$$V = V_c \frac{C_T}{C_T + C_F}\left(1 - e^{-\left(\frac{C_T + C_F}{C_T C_F R_F}\right)}\right)$$

Hence V rises to its asymptotic value of $V_c \frac{C_T}{C_T + C_F}$ with a time constant $\frac{C_T C_F R_F}{C_F + C_T}$.

After 3 time constants the voltage will have risen to within 5% of its final value, which approximates to the front time: $t_{front} = \frac{3C_T C_F R_F}{C_F + C_T}$

Calibration Technique

A method is required to conveniently calibrate the peak impulse voltage generated. This is achieved by calibrating an easily measurable generator circuit parameter against peak impulse voltage.

The usual measurand is the generator stage charging voltage. All impulse generators offer a signal derived from the charging voltage of the stage capacitors to allow the user to monitor generator operation. This is usually obtained from the small current flowing through a high resistance connected to the stage charging voltage.

Peak impulse voltages are measured using standard sphere gaps. Tables of breakdown voltages for spheres of certain sizes and separations are well established. The tables give the peak impulse voltage that results in a 50% probability of breakdown. For a certain sphere gap setting, the stage voltage reading that causes the spheres to spark over is found using the "up down method".

In the "up down method" the impulse voltage is set to a value just below the expected breakdown voltage of the sphere gap. The applied impulse voltage is then increased in small steps, until the sphere gap breaks down. The impulse voltage is then decreased by one step. The step size should be chosen to be about 1% of the gap breakdown voltage. The following process is then repeated; if the gap does not breakdown then the voltage is *increased* by one step, if the gap does breakdown then the voltage is *decreased* by one step. This process of increasing and decreasing the voltage is continued until at least 20 impulses have been applied after the first breakdown. The average of the meter readings is the stage voltage reading at which the gap breaks down.

The table gives the breakdown voltage for standard atmospheric conditions, so a correction factor is calculated to find the gap breakdown voltage for the temperature and pressure in the laboratory.

Spark Gaps

When the generator fires the stage capacitors have to be discharged in series, this is achieved using small sphere gaps mounted horizontally one above each other on the generator chassis. The sphere size is chosen so that the spacing to withstand the maximum charging voltage does not exceed its diameter.

The spheres are mounted so that their spacings can be adjusted to allow different impulse voltages to be generated.

As well as all the gaps having to open and close for different test voltages the gaps have to be precisely set to fire accurately and in the correct order. Figure 3.2.9 shows the impulse generator circuit diagram. When the impulse generator is fired the first (lowest) gap is triggered to break down first, that causes the voltage to double at the second gap thus causing that gap to break down. The voltage at the third gap is then tripled, which breaks down and so on. To make sure the gaps break down in the correct order the gap

setting should get slightly larger further up the generator. In other words the gap settings should be graduated in a tapered manner. Poorly graduated sphere gaps either produce a stepped front wave due to gaps firing in the wrong order, or a smaller overall wave because not all of the stages fire. The graduation involved is quite fine and requires some patience to achieve.

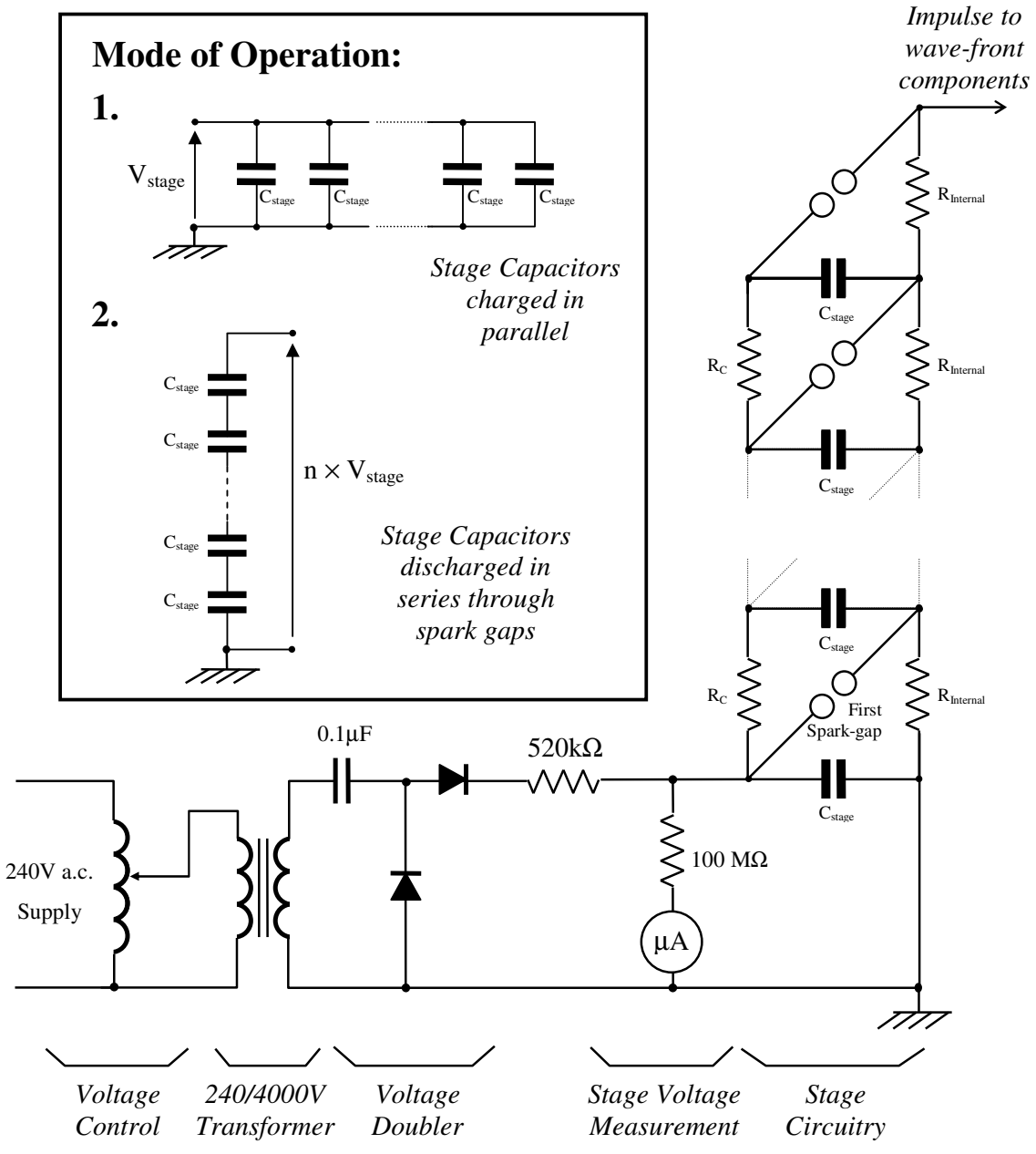

Figure 3.2.9: Impulse Generator circuit diagram and mode of operation.

There are a number of ways to trigger an impulse generator. In the simplest method, known as self-triggering, the bottom spark gap is set to flashover at a specific voltage. The stage capacitors charge up until they reach the flashover voltage of the first gap, which breaks down and trips the generator.

The first gap can also be fired manually using a number of techniques, the most common being the trigatron gap in which a small spark is generated across an annular gap on the surface of the grounded sphere that initiates breakdown of the main gap.

Impulse Generator No1

Two different impulse generators were used in the experiments because the stage charging circuitry in the first generator became damaged during the course of the experimental work. A second generator was available as a quick replacement. Both generators were based on the Marx principle.

The first generator was a five-stage generator, with motorised sphere gap control and an external wave tail resistor.

The generator had the following nominal values for its wave shape components:

$C_{stage} = 0.05\mu F$ $C_{front} = 2160pF$

$R_{tail} = 6k\Omega$ $R_{front} = 800\Omega$

Each 0.05μF stage capacitance was constructed from four 0.05μF capacitors connected in series and parallel to provide the necessary voltage and current ratings.

The nominal generator capacitance is the capacitance per stage, C_{stage} divided by the number of stages. For five stages the nominal capacitance (C_T) was 10nF.

The nominal energy of an impulse generator is denoted by its maximum stored energy, which can be calculated from $\frac{1}{2}n\, C_{stage}V^2$. For this generator using the maximum stage charging voltage of 30kV the maximum stored energy was 112.5J.

The wave front capacitance was made up of a 2000pF capacitor in parallel with a potential divider (160pF nominal capacitance) for measuring the impulse wave shape.

When calculated using the equations derived earlier the generator wave shape was very close to the required voltage impulse required.

The actual front and tail times of the generator were measured using the oscilloscope traces shown in figure 3.2.10 and figure 3.2.11.

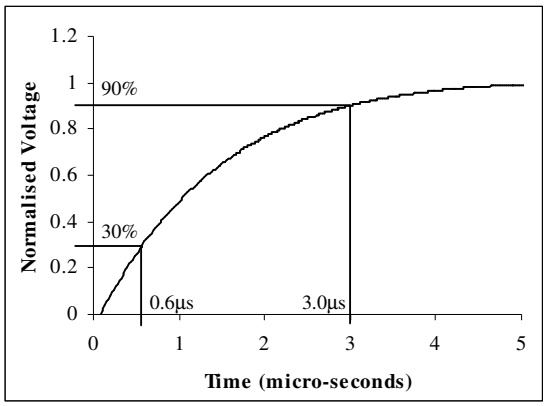

Figure 3.2.10: IG No.1 front-time

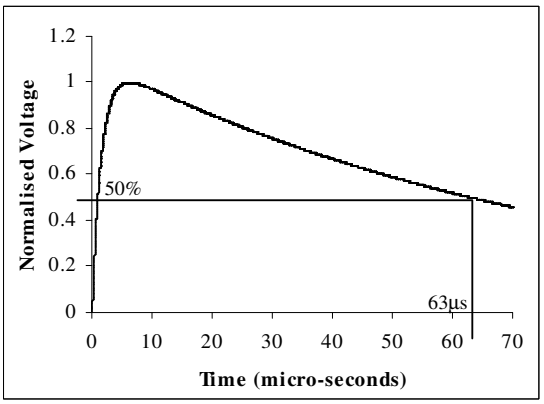

Figure 3.2.11: IG No.1 tail-time

From figure 3.2.10 the front time of the impulse wave was found to be: 2.4µs / 0.6 = **4µs**. From figure 3.2.11 the impulse tail time was found to be **63µs**.

The generator stage charging voltage could be measured from a meter in place on the generator control panel. This stage voltage reading was calibrated against peak impulse voltage using the up-down method described earlier. A summary of the calibration is shown below.

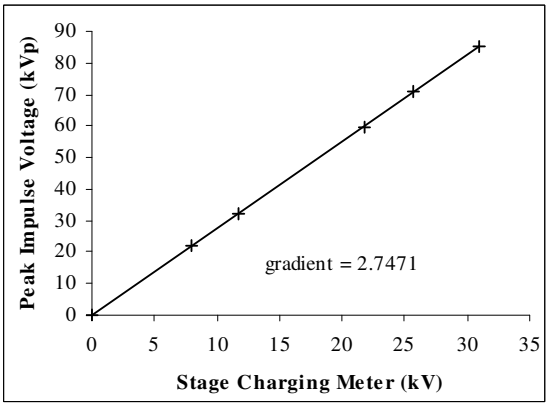

Figure 3.2.12: IG No.1 positive calibration

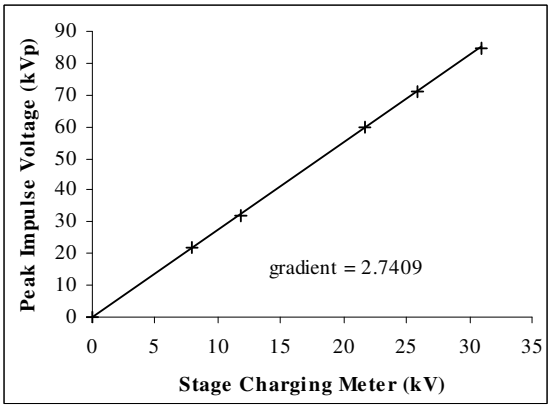

Figure 3.2.13: IG No.1 negative calibration.

Impulse Generator No2

The second generator was an 8-stage generator with internal tail resistors and manual sphere gap control.

The generator was set up with following nominal values for its wave shape components:

C_{stage} = 0.05μF C_{front} = 160pF

R_{tail} = 12kΩ R_{front} = 7.72kΩ

Using the maximum stage charging voltage of 11kV the maximum stored energy was 24.2J. The nominal generator capacitance was 6.25nF.

From figure 3.2.14 the front time of the impulse wave was found to be: 1.9μs / 0.6 = **3.2μs**. From figure 3.2.15 the impulse tail time was found to be **41μs**.

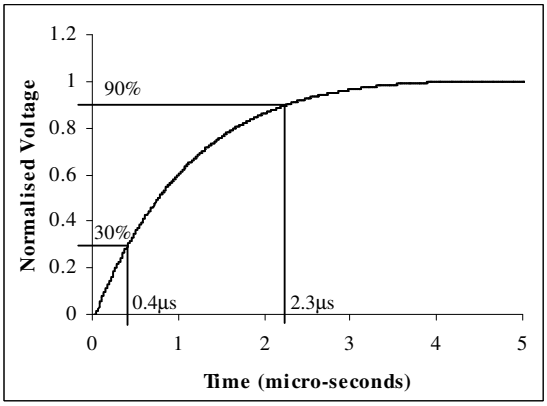

Figure 3.2.14: IG No.2 front-time

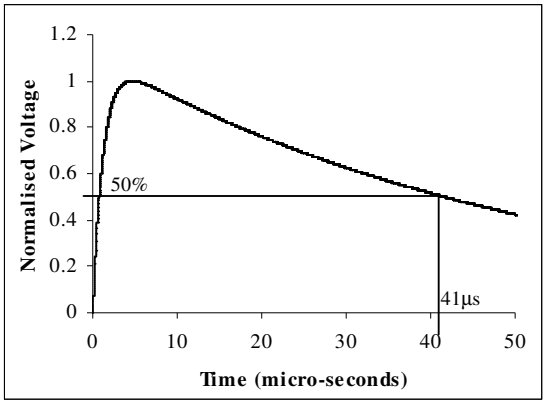

Figure 3.2.15: IG No.2 tail-time

The small current flowing through a 100MΩ resistor connected to the stage charging voltage was calibrated against peak impulse voltage.

A summary of the calibration is shown below.

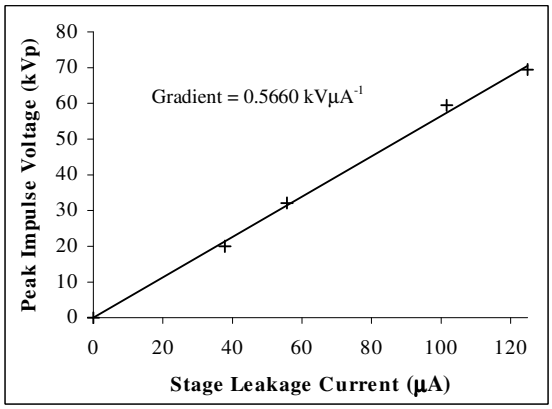

Figure 3.2.16: IG No.2 positive calibration

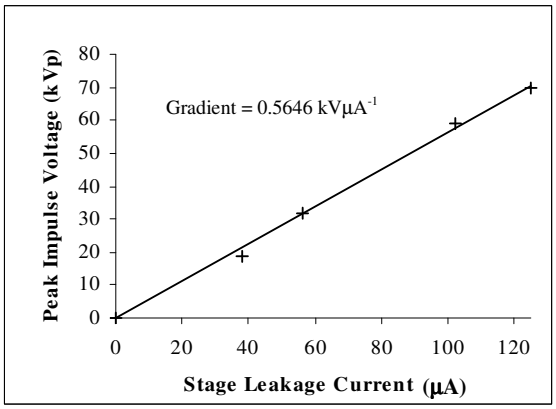

Figure 3.2.17: IG No.2 negative calibration.

DC Generation

A 50kV Brandenburg DC set was used whenever a constant voltage was required. The set was capable of generating DC of both polarities.

AC Generation

A 20kVA 100kV single phase transformer was used to generate an alternating voltage.

3.2.3 Earthing and Safety

All points of the high voltage circuit that required earthing were connected to one point on the impulse generator chassis; that point was then solidly bonded to the laboratory high voltage earth.

Extra care and attention to safety was required when operating the impulse generators because it was not possible to arrange an automatic earthing system to short out the stage capacitors when the charging voltage was removed. An earthing stick was used to earth down the capacitors. It was essential to remember to attach the earthing stick before approaching the generators.

3.2.4 Measurement Equipment

Photo-Multipliers

A photo-multiplier is a sensitive device that can measure low levels of light and give an analogue output voltage that is related to the intensity of the light. Three identical photo-multipliers (EMI Type 9781 B) were used to observe the discharge traverse the gap. The devices used were particularly sensitive to light in the UV part of the spectrum. They work on the principle of photo-emission of primary electrons. These primary electrons are accelerated and multiplied using a strong electric field generated by a series of electrodes. They are thus amplified by a factor of about 10^9.

Each photo-multiplier was mounted in a light-tight housing with an aperture so its vertical field of view was very narrow. Figure 3.2.18 shows the photo-multiplier housing and the aperture made up of two slits through which the light entered. The slit aperture was 1.8mm and the two slits were 160mm apart.

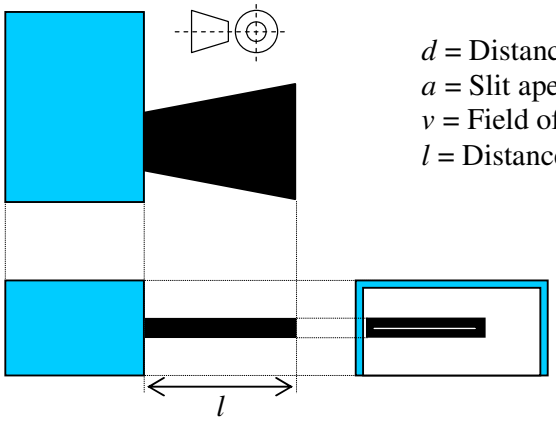

Photo-multiplier Housing

d = Distance between photo-multiplier and test object
a = Slit aperture
v = Field of view
l = Distance between slits

By similar triangles and rearranging:

$$\frac{a}{\left(l/2\right)} = \frac{v}{\left(d + l/2\right)}$$

$$v = a\left(1 + \frac{2d}{l}\right)$$

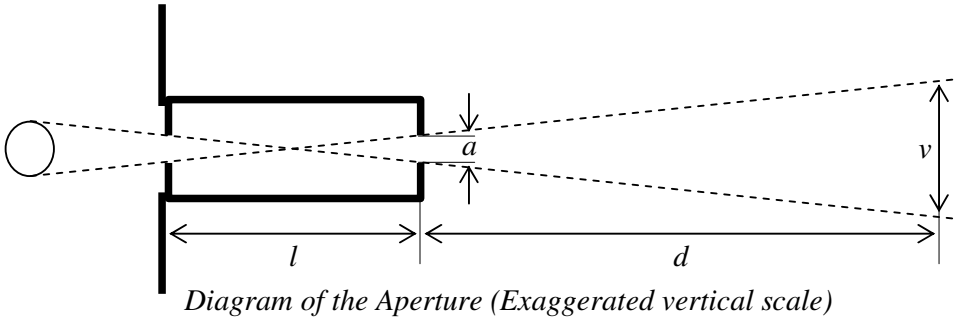

Diagram of the Aperture (Exaggerated vertical scale)

Figure 3.2.18: A photo-multiplier housing and calculation of vertical field of view.

The photo-multipliers were positioned 300mm away from the central axis of the rod as shown in figure 3.2.19. The physical size of the photo-multipliers required them to be offset slightly to allow them to be stacked closely. The horizontal field of view was wide enough to look at a horizontal slice through the entire discharge. Putting values into the equation shown in figure 3.2.18 gives the vertical field of view as 8.5mm for each photo-multiplier

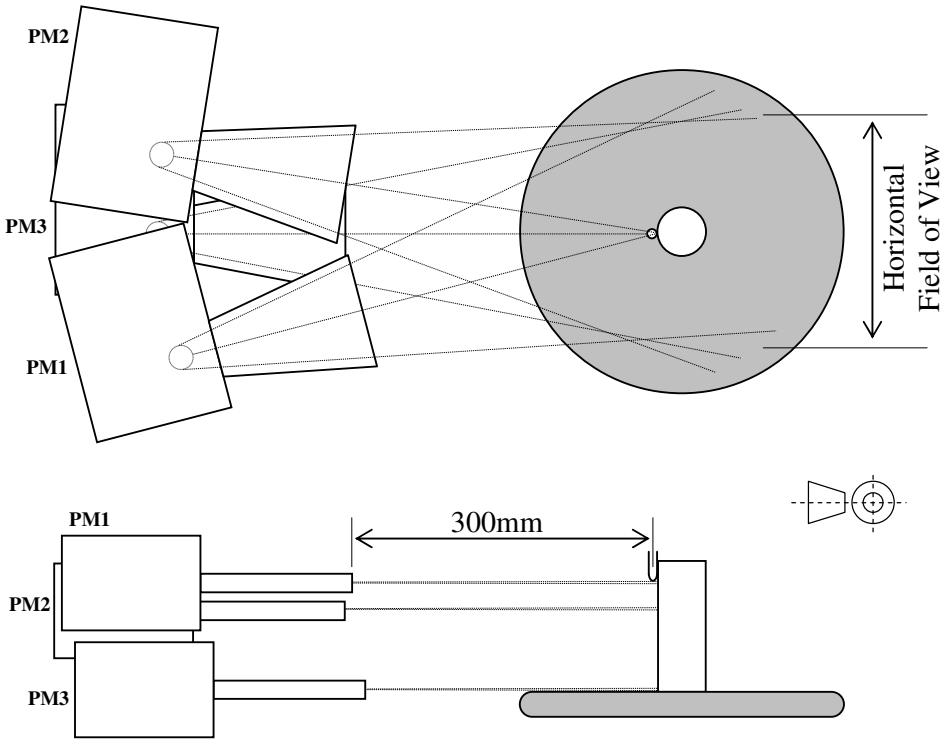

Figure 3.2.19: The positioning of the photo-multipliers.

The photo-multipliers were aligned using a laser pointer. The first photo-multiplier was positioned to look directly at the tip of the rod, the second a short distance beneath the tip and the third just above the level of the ground plane. The three photo-multiplier signals allowed the propagation of the streamers to be time resolved.

Power supply for the multiplier was from a 12V battery with a DC-DC converter to increase the voltage to 200V DC. Using the photo-multipliers discharges could be measured indirectly, thus achieving electrical isolation from the test circuit and minimising interference pickup.

The electron transit time from the cathode to the collecting anode of the photo-multiplier tube is approximately 20 nanoseconds, added to this is the transit time of the connecting cables between the photo-multipliers and the oscilloscope. By using identical photo-multipliers connected to the oscilloscope with identical lengths of cable any relative timing error was minimised.

Current Measurement

Measuring the current flowing in the rod-plane gap allowed the discharge characteristics to be studied, the total charge injected into the gap to be evaluated, and comparisons to be made with the photo-multiplier signals. The current could either be measured in the high voltage or the earthed side of the circuit.

Current measurement in the high voltage side would require optical isolation in the form of a fibre-optic link to allow connection to the storage oscilloscope. Streamer current pulses have a rise-time in the order of 10ns; the fibre-optic link would therefore require a bandwidth of at least 100MHz, more if greater resolution was required. During the course of the research work a fibre-optic link was considered on several occasions. Commercially available links did not have large enough bandwidths or were overly expensive. The problem of specially designing a link is compounded by the difficulty of analogue circuit design when dealing with frequencies around and above 100MHz.

The main advantage of a fibre-optic link is that it would provide optical isolation between the high voltage and measurement circuit, but the added complexities led to the use of low voltage current measurement by means of a resistive current shunt. The obvious advantage of low voltage current measurement was that no complicated electronic circuitry was required, however care was necessary because of the direct connection between the high voltage and measurement circuit.

A fully screened high voltage co-axial shunt was used. Peak streamer currents were in the order of 1A so to produce a good voltage signal the largest value shunt available was used. The 70Ω (±0.5%) shunt was solidly bonded to the plane via a very short length of thick copper braid and the shunt case then connected to the impulse generator earth via a short copper earthing strip to complete the high voltage circuit. The generated voltage signal was taken from the shunt by a length of 75Ω cable as shown in figure 3.2.20.

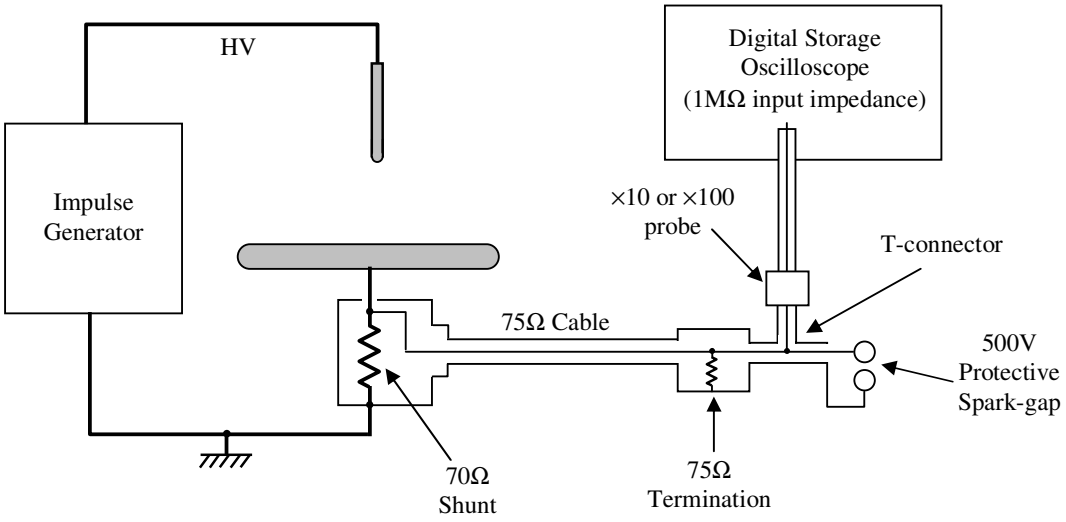

Figure 3.2.20: Current measurement technique.

The 75Ω cable was then terminated in an attempt to reduce reflections and a T-piece connector fitted. One arm of the T-connector went to a ×10 or ×100 probe to step the voltage down to a value measurable by a digital storage oscilloscope. The other arm went to a 500V protective spark gap so that in the event of an over-voltage caused by breakdown of the main rod-plane gap the oscilloscope would not be damaged.

The response of the current measurement apparatus was found by injecting a 1V 60ns duration voltage pulse into the shunt using a signal generator and recording the output voltage. The injected pulse and the resultant output voltage for different measurement configurations is shown in figure 3.2.21. The need for the 75Ω termination was evident; without it reflections of the original pulse were observed on the input and output voltage. The input impedance of the oscilloscope could be set to either 50Ω or 1MΩ. The 50Ω setting reduced the severity of the reflections however it attenuated the magnitude of the voltage pulse.

The best arrangement was found to be with the 75Ω termination and an oscilloscope input impedance of 1MΩ. The current measurement apparatus had a transit time of 40ns.

There was no measurable difference in the traces whether the oscilloscope was grounded directly or through the current measurement cable.

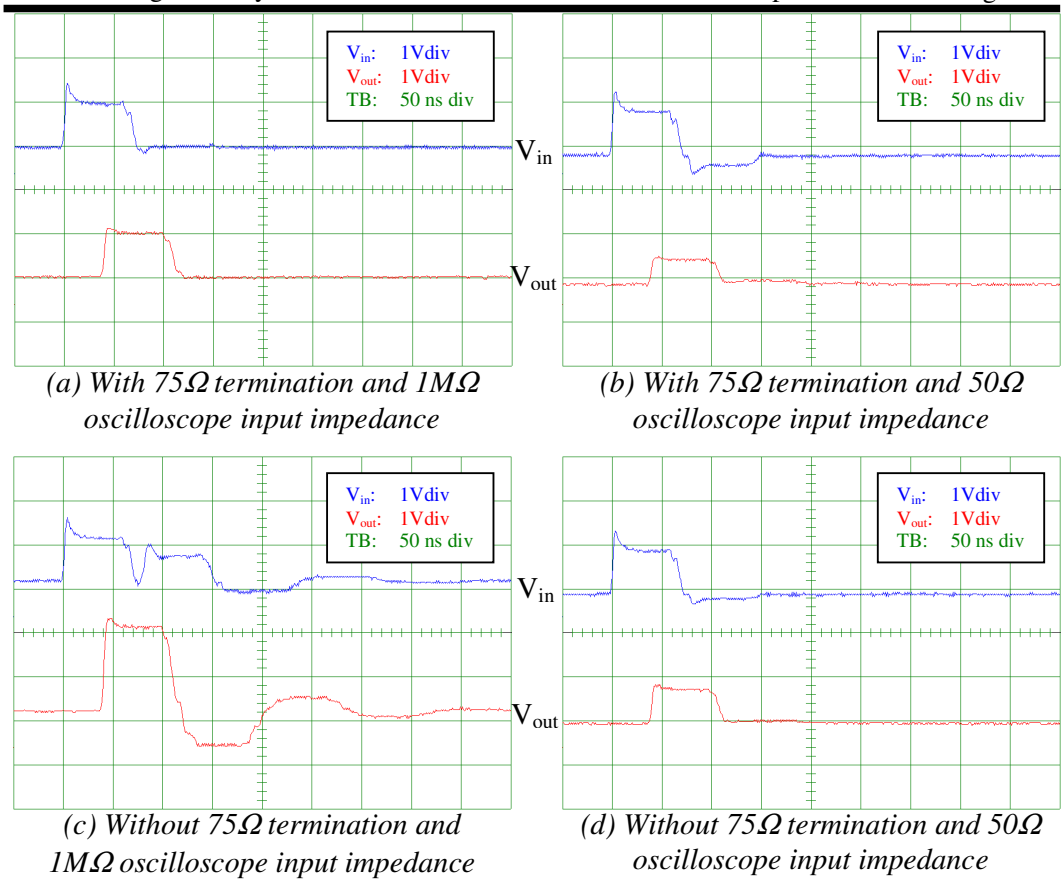

(a) With 75Ω termination and 1MΩ oscilloscope input impedance

(b) With 75Ω termination and 50Ω oscilloscope input impedance

(c) Without 75Ω termination and 1MΩ oscilloscope input impedance

(d) Without 75Ω termination and 50Ω oscilloscope input impedance

Figure 3.2.21: Current measurement equipment response to a 1V 60ns duration pulse.

To check that the measurement system was not picking up unwanted signals the 70Ω current shunt was grounded and the photomultipliers were masked out. The impulse generator was then used to produce discharges in the gap. The resulting traces are shown in figure 3.2.22. Only the interference pickup from the generator firing, which is over in 1μs, is visible on all the traces.

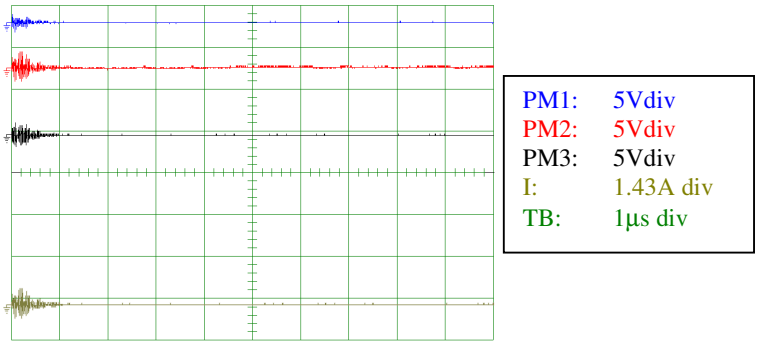

Figure 3.2.22: The level of interference in the measurement system.

Oscilloscope

A 400MHz 2GSs^{-1} Gould Classic 9500 Digital Storage Oscilloscope was used to record the three photo-multiplier and current signals. It was capable of sampling 4 inputs every 2ns or 1 input every 0.5ns. Disk drive storage of the traces was available for archiving data.

Figure 3.2.23: The Gould Classic 9500 Digital Storage Oscilloscope used in the experiments.

Dust Figures

To provide a pictorial representation of the charge deposited on the insulator surface black photocopier toner was used to generate dust figures. The background to dust or Lichtenburg figures was given in the Introduction. The extremely fine toner particles adhered to regions of charge to produce a pattern of the charge distribution with a very good spatial resolution but no real indication of magnitude. The manufacturers of the toner stated that it adhered to positively charged regions. This was confirmed by experiment.

The toner was loaded into a large syringe that was used to generate a fine cloud of toner powder to which the charged insulator surface was exposed. This operation was undertaken in a fume cupboard to avoid human exposure to the toner and to keep the very messy procedure in one place.

The toner particles obtain a negative charge by frictional or triboelectric charging as they are ejected from the syringe, they then drift in a cloud and adhere to regions of positive charge on the insulator surface.

Using a retort stand the generated dust figure was held just above a flatbed computer scanner and scanned in a section of the circumference at a time. The scanned sections were then reconstructed to provide a permanent record of the dust figure.

Pressure, Temperature and Humidity

For each set of measurements the atmospheric conditions in the laboratory were recorded. The atmospheric air pressure was measured in mm-Hg by means of a Barometer. Humidity was measured using a Hygrometer consisting of two ventilated thermometers; one dry and the other wetted. The absolute humidity was determined using IEC 60-1 (1973) tables, where the absolute humidity was a function of the two thermometer readings. The dry thermometer reading gave the room temperature.

3.2.5 Insulator Test Objects

Materials

A number of materials were investigated during the course of the experimental work. Study focused on materials that could store enough charge for long enough to be detectable by the scanning system. The large proportion of the work was conducted using PTFE as the insulator material because of its common usage in high voltage puffer-breaker nozzles and its high susceptibility to surface charging.

Material	Relative Permitivity	Dielectric Strength Vmm^{-1}	Volume Resistivity Ωcm	Detectable Surface Charging
Pure PTFE	2.2	480	$>10^{15}$	yes
Carbon Filled	2.05	480	$10^{17.4}$	yes
Epoxy Resin	3.62	400	10^{16}-10^{17}	yes
Glass	5	170	10^{12}-10^{14}	some
Nylon	3.5	470	4×10^{14}	yes
Polyethylene	2.3	460	1.6×10^{13}	yes
Un-Glazed Porcelain	6-8	50-400	10^{12}-10^{14}	some
Glazed Porcelain	6-8	50-400	10^{12}-10^{14}	no

Table 3.2.1: Material properties.

.

Geometries

The three different insulator geometries studied are shown in figure 3.2.24. Each of the insulator materials was manufactured into type A or B geometries. Only carbonised PTFE, glazed porcelain and unglazed porcelain were made in type C geometries. The simple cylindrical insulator specimens were used in most of the experiments. The type C geometry was used to test the operation of the scanning system on contoured insulator specimens.

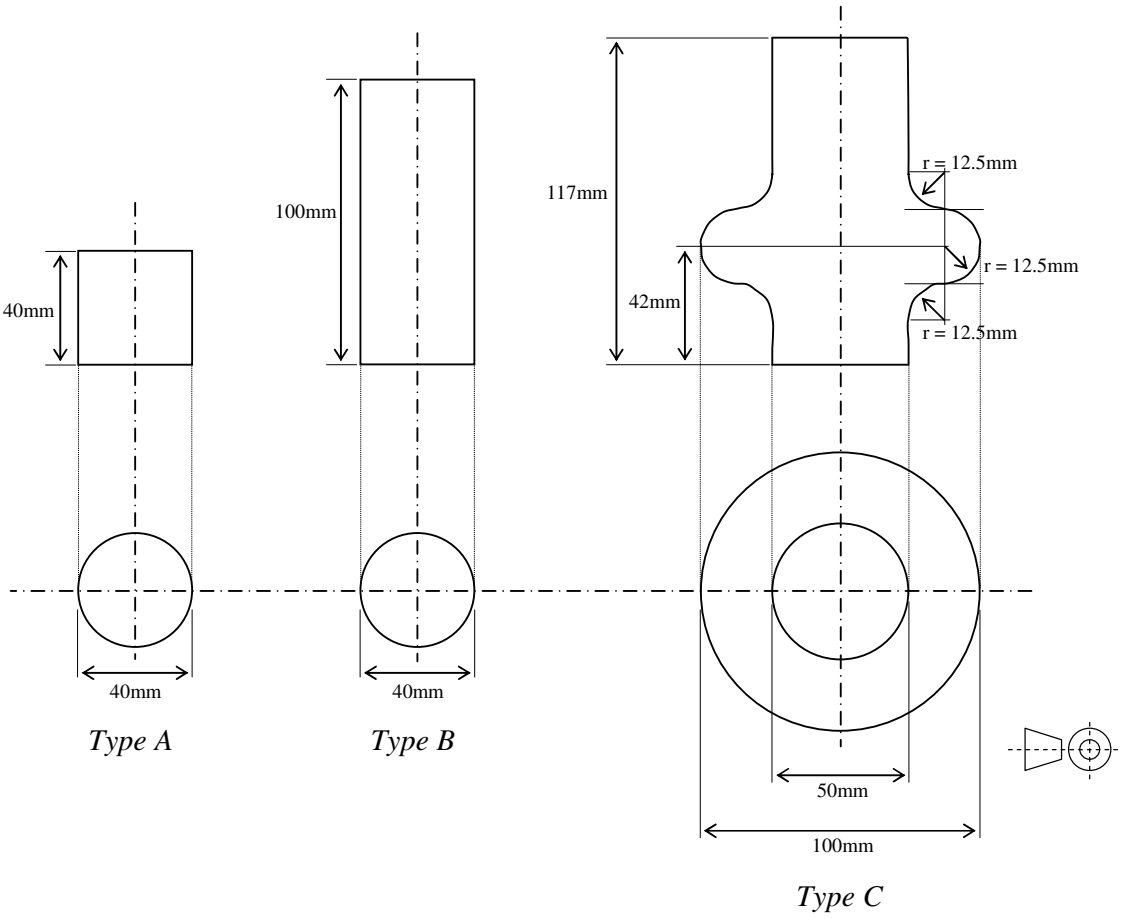

Figure 3.2.24: Insulator test object geometries used in the experiments.

All the insulators had a register matching that in the ground plane electrode to allow repeatable alignment of the test objects on the electrode assembly (figure 3.2.2). A threaded hole in the rotational axis of the insulator specimens allowed them to be mounted securely on the scanning platform, or to be tightly bonded to the plane electrode using a PTFE screw.

Insulator Handling

It had been hoped to be able to scan the insulator *in situ* by having the electrode arrangement built into the scanning platform. Difficulties in achieving isolation between the high voltage circuit and the scanning system led to the damage of several interface cards in the computer. So an insulator handling procedure was developed to transfer test objects from the electrode arrangement to the scanning rig.

A PTFE screw was put into the register machined into the top and bottom of each test object. The insulator could then be carried to, and loaded into the scanning rig without disturbing the surface charge as shown in figure 3.2.25.

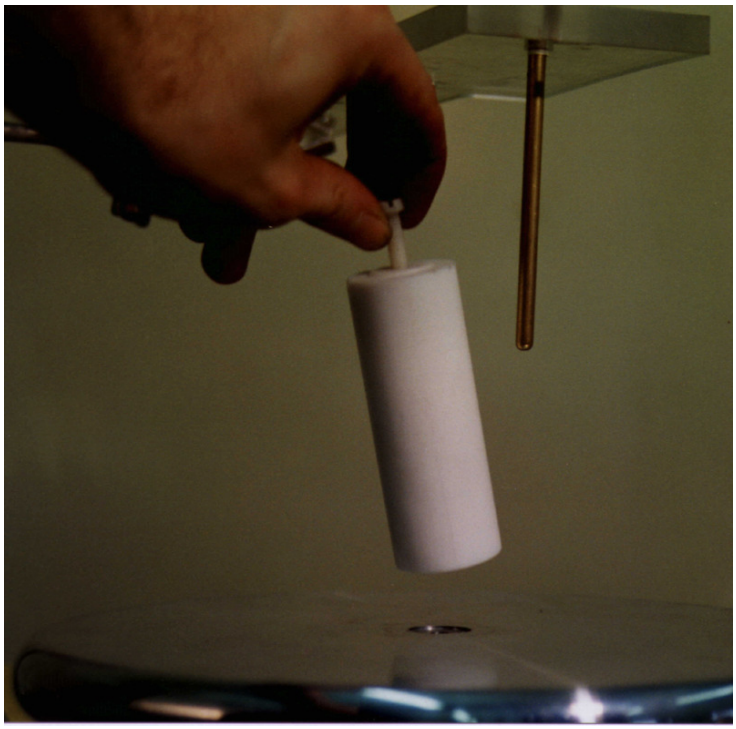

Figure 3.2.25: Transporting the insulator specimens.

The repeated angular alignment of the test object was achieved using very small marks made with a permanent pen on the bottom of the insulator and the plane electrode.

Cleaning

To allow the study of charge deposited by individual discharges it was necessary to develop a strategy for neutralising the test object surface charge before the application of any test voltages. Over the years researchers have employed a number of techniques to 'clean' the insulator of surface charge. The scanning system allowed an evaluation of the efficacy of each method.

The worst previously reported method (Gallimberti, 1991) of insulator cleaning was found to be rubbing with an earthed copper braid. This actually had the reverse effect and produced a significant charge distribution (also noted by Ghaffar, 1994). Figure 3.2.26 shows a surface charge density map obtained using the scanning system of a PTFE insulator after ten up and down strokes on one side of the insulator.

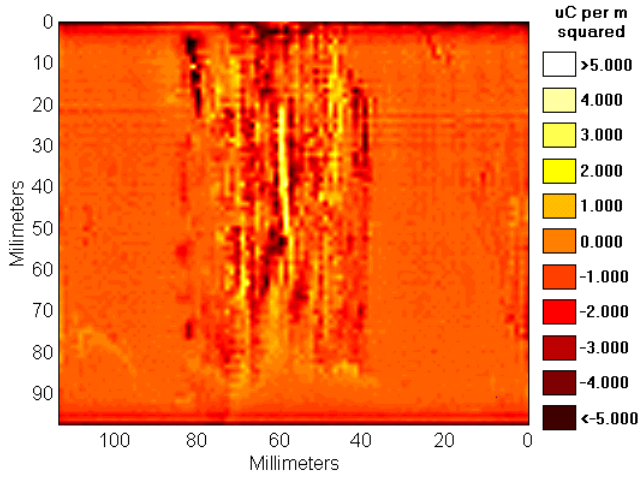

Figure 3.2.26: The surface charge deposited by rubbing an earthed braid up and down an initially neutralised PTFE insulator specimen.

Rubbing the insulator caused triboelectric charging of the surface. The earthed braid provided multiple contact points and a low impedance path for electrons to flow to and from the surface. Significant surface charge densities of up to $\pm 5 \mu C m^{-2}$ were measured. However the overall net surface charge deposited was almost zero, comprising of just under 2nC of positive charge and just over 2nC of negative charge. This explains why previous investigators using very poor resolution surface charge measurement techniques considered the surface to be neutralised. It is important to remember that all charge detection techniques give a measurement of the net charge over their region of minimum resolution.

Other techniques have included exposing the insulator surface to an AC corona from a fine wire loop. This was slightly more effective but could also lead to a residual charge distribution.

The effective techniques of surface charge neutralisation involve washing the insulators in water then washing in solvents then drying them in an oven, however this was a very time consuming process. A quick and effective method was developed that, to the resolution of the scanning system, was as good as washing and drying.

A clean disposable lint free paper towel was soaked in pure ethanol and wrapped smoothly once around the insulator surface. The towel was held and tightly and motionless for about 20 seconds, then very carefully the towel was removed from the surface ensuring that the towel came cleanly away from the surface with no surface rubbing.

Limit of Charge Measurement Resolution

Figure 3.2.27 shows the charge distribution calculated after the surface had been neutralised. This distribution was more a measure of noise in the measuring system than surface charge because an identical distribution was obtained when no insulator was present. The distribution was random with peak values of about $\pm 0.05 \mu Cm^{-2}$. The calculated net charge was zero comprising of positive +0.1nC and negative –0.1nC.

Hence it can be said that $\pm 0.05 \mu Cm^{-2}$ is effectively the limiting accuracy of the scanning system.

The cleaning technique is therefore the same as or better at neutralising the surface than this limiting accuracy.

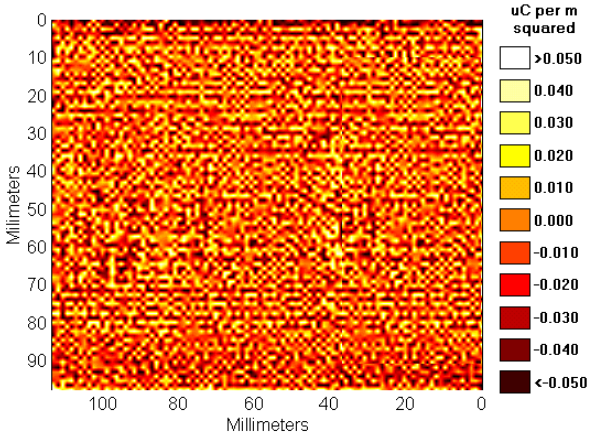

Figure 3.2.27: A neutralised surface.

3.3 Initial Experiments

3.3.1 Introduction

The first set of experiments was designed to evaluate the effectiveness of the scanning system and calibration technique. Preliminary experiments had indicated that PTFE was the best material to study initially because of its ease of surface charging helped by its very high surface resistivity.

3.3.2 Set-up

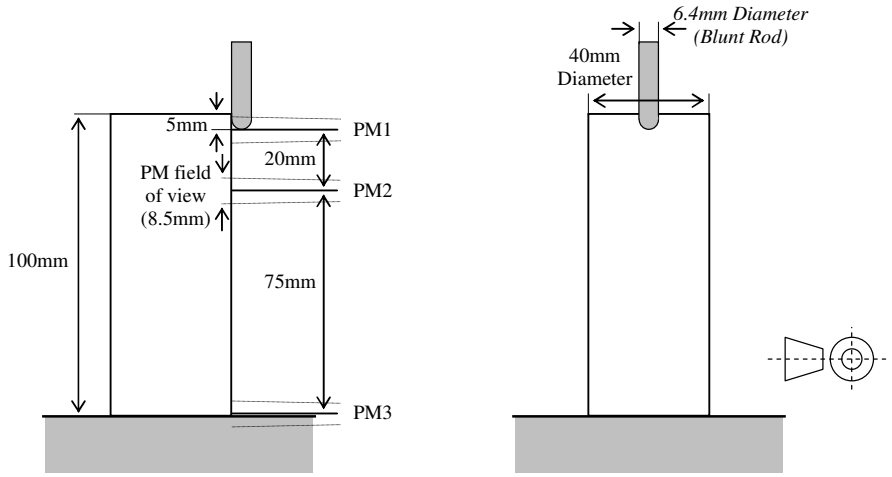

Figure 3.3.1: The apparatus set-up for the initial experiments.

The electrodes and photo-multipliers were set up as shown in Figure 3.3.1. The current was measured at the ground plane using the 70Ω shunt described in the Section 3.2.4. Positive impulses of various voltages were applied to the rod using impulse generator No.1.

3.3.3 Air

Prior to investigating the effect of the insulator the characteristics of the gap on its own were studied. Ten different peak impulse voltages were used as shown in the table below. At each voltage, impulses were applied until 20 discharges were observed or until 80 shots had been applied, (which ever came first).

Voltage	No. Discharges	No. Gap flashovers	No. Shots	Minimum Peak Current	Maximum Peak Current
29.9 kVp	13	0	80	0.137 A	0.68 A
34.3 kVp	7	0	80	0.47 A	0.92 A
39.3 kVp	6	0	80	0.848 A	1.09 A
43.9 kVp	5	0	80	0.955 A	2.179 A
49.4 kVp	1	0	80	2.97 A	2.97 A
55.7 kVp	20	0	32	1.67 A	3.28 A
52.2 kVp	6	0	80	2.36 A	4.81 A
59.9 kVp	20	1	33	2.98 A	5.6 A
63.1 kVp	20	3	21	1.87 A	6.6 A
67.3 kVp	20	5	20	1.533 A	7.68 A

Table 3.3.1: Summary of results from impulse voltages applied to the rod.

The 118 discharges that occurred were processed to obtain peak current, injected charge, velocity and instantaneous voltage. Figure 3.3.2 shows the current waveform for a typical discharge obtained in the rod plane gap, the start of the discharge has been moved to t = 0. The current signal was approximately double exponential in shape with a rise time of approximately 6ns and a tail time to 50% of around 100ns.

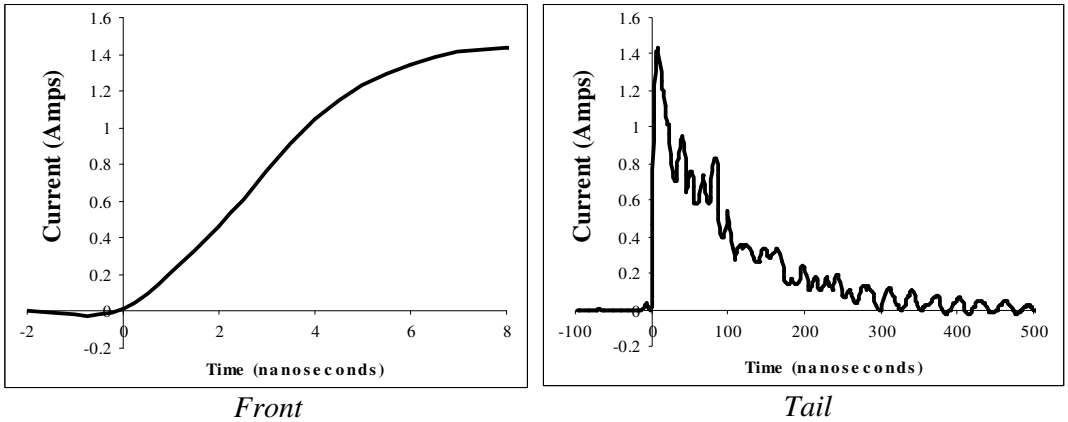

Front *Tail*

Figure 3.3.2: A typical current signal for a discharge event in air.

The current signals contained a small oscillatory component introduced by unavoidable reflections in the current measurement system. When analysing the current signals these osscillations should be disregarded. To obtain the total charge injected into the gap the current signal is intergrated. The integrated current for the example discharge shown in figure 3.3.3.

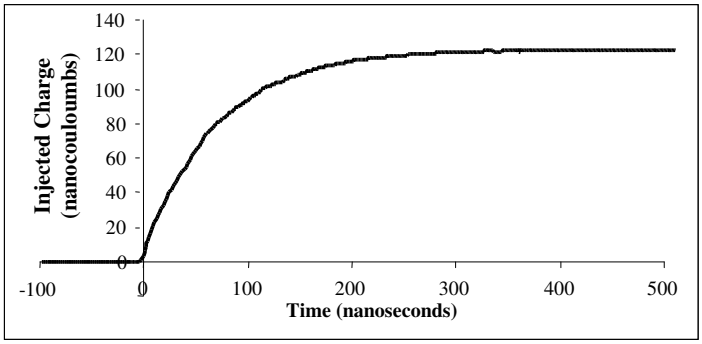

Figure 3.3.3: Integrating the current pulse provides the injected charge.

The integration procedure removes the high frequency oscillatory components and provides an accurate representation of total injected charge.

The initial velocities of the discharges were found using the signals from photo-multipliers No.1 and 2. The exact time of arrival into the photo-multipliers field of view was defined as the instant at which the photo-multiplier output voltage began to rise. The overall gap velocity was found from photo-multipliers No.1 and 3. It is the average velocity for the discharge crossing the complete gap. No overall velocities could be calculated for streamers that did not cross the gap.

The instantaneous voltage at which the discharge occurred was obtained using the impulse generator voltage wave shapes. The exact time the discharge occurred after the generator fired was converted into an instantaneous voltage.

The graphs on the following pages show the data from all the 118 discharges measured. Each point represents a single discharge event. The discharges were all measured on the same day. The temperature and pressure on that day were 17°C and 750mmHg. The specific humidity was found to be 6.8gm-3.

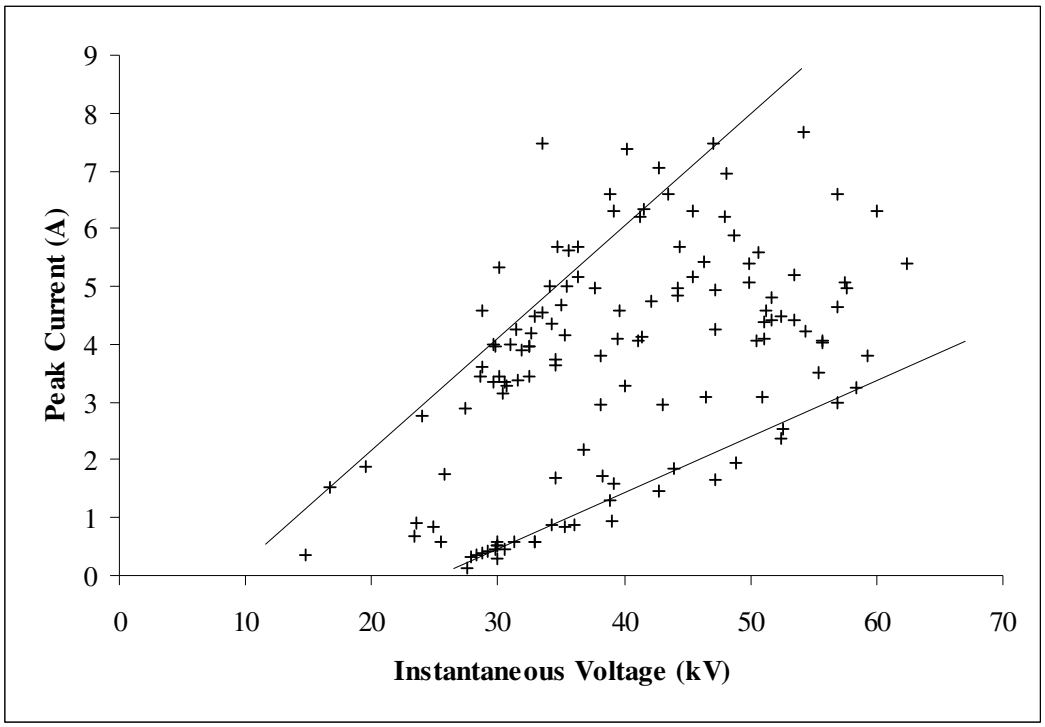

Figure 3.3.4: Peak discharge current versus instantaneous voltage.

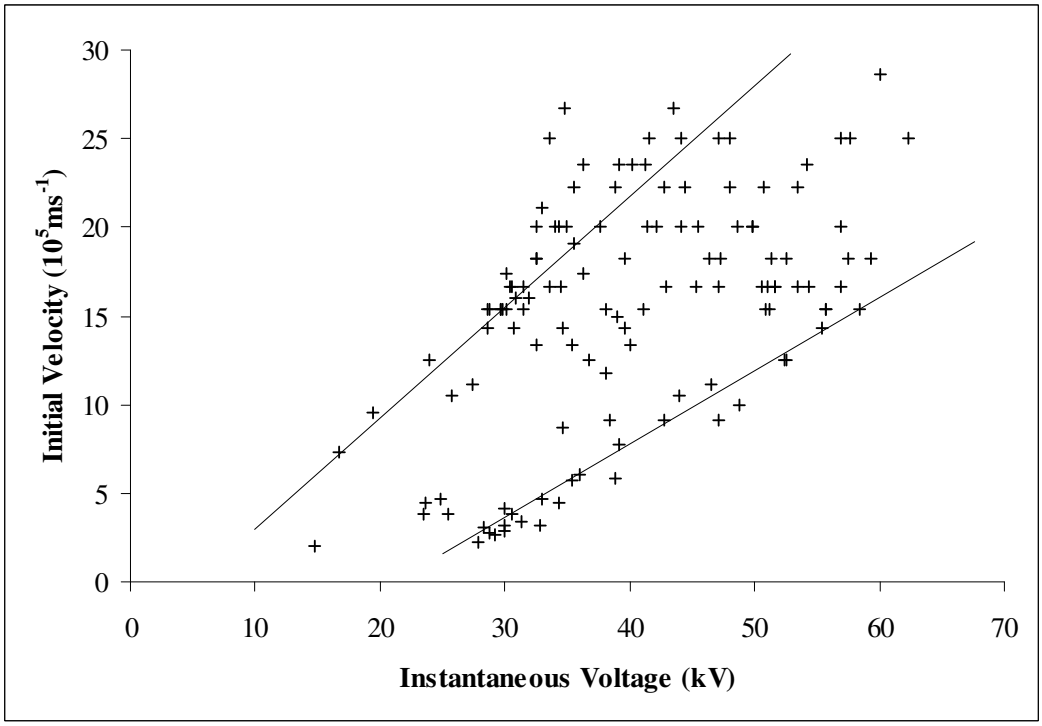

Figure 3.3.5: Initial discharge velocity versus instantaneous voltage.

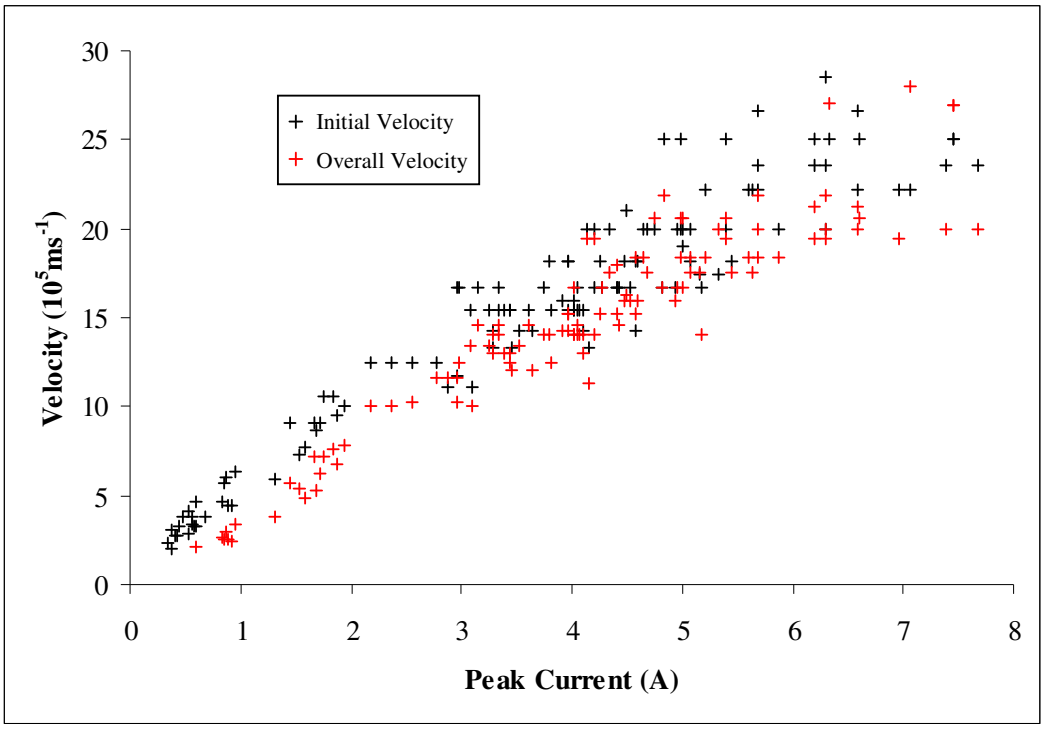

Figure 3.3.6: Discharge velocity versus peak current.

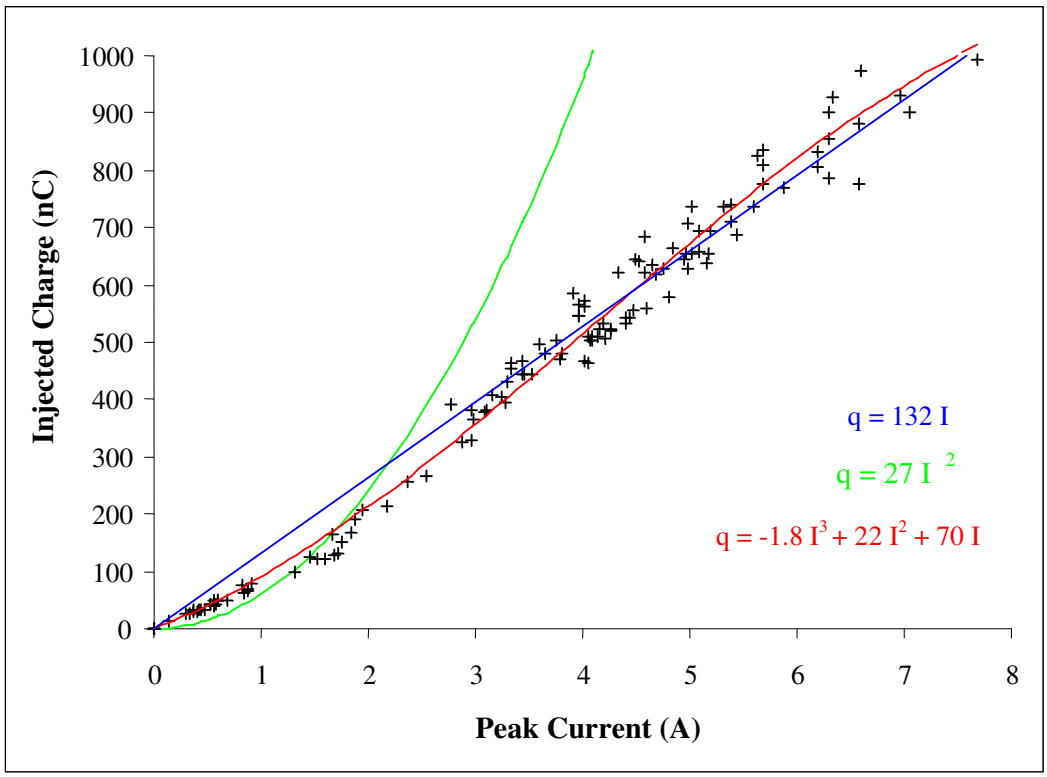

Figure 3.3.7: Injected charge versus peak discharge current.

Figures 3.3.4 and 3.3.5 show the variation of peak discharge current and initial velocity with instantaneous voltage. The general trend is that greater instantaneous voltages produced faster discharges with higher peak currents. There is a lot of scatter in both graphs; this could be because the variables were weakly dependent, or the accuracy of the calculated the instantaneous voltage was poor. However on closer inspection the data appears scattered at the edges of the distribution, as indicated by the two thin black lines in each graph. This suggests that two separate discharge initiation sites with different characteristics may be present on the rod.

Figure 3.3.6 shows the initial and overall discharge velocity plotted against peak discharge current. The scatter in both these graphs is much smaller than when plotted against instantaneous voltage. Higher peak currents produced faster discharges. The initial velocity of the discharge is greater than the overall velocity. This was to be expected because of the greater electric field in the vicinity of the rod.

Figure 3.3.7 shows the relationship between injected charge and peak discharge current. The scatter of the data points is small; this allows an attempt to fit curves to the distribution. The injected charge is the area under the current waveform. If the shape of the current waveform does not change for different peak currents then by the laws of geometric scaling; the injected charge should be related to the square of the peak current. A squared relationship cannot be found between the two variables as is shown by the green line in figure 3.3.7. The relationship is closer to linear than square, which indicates that the discharge current changes shape as the peak current increases. The straight line does not fit the data accurately and the red curve shows the cubic line of best fit.

A measure of the shape of the discharge current waveform can be obtained from the ratio of injected charge to peak current. This simple value is referred to as the shape factor of the discharge current waveform and it provides a simple indication of the waveform shape. Figure 3.3.8 shows this shape factor plotted against peak impulse voltage.

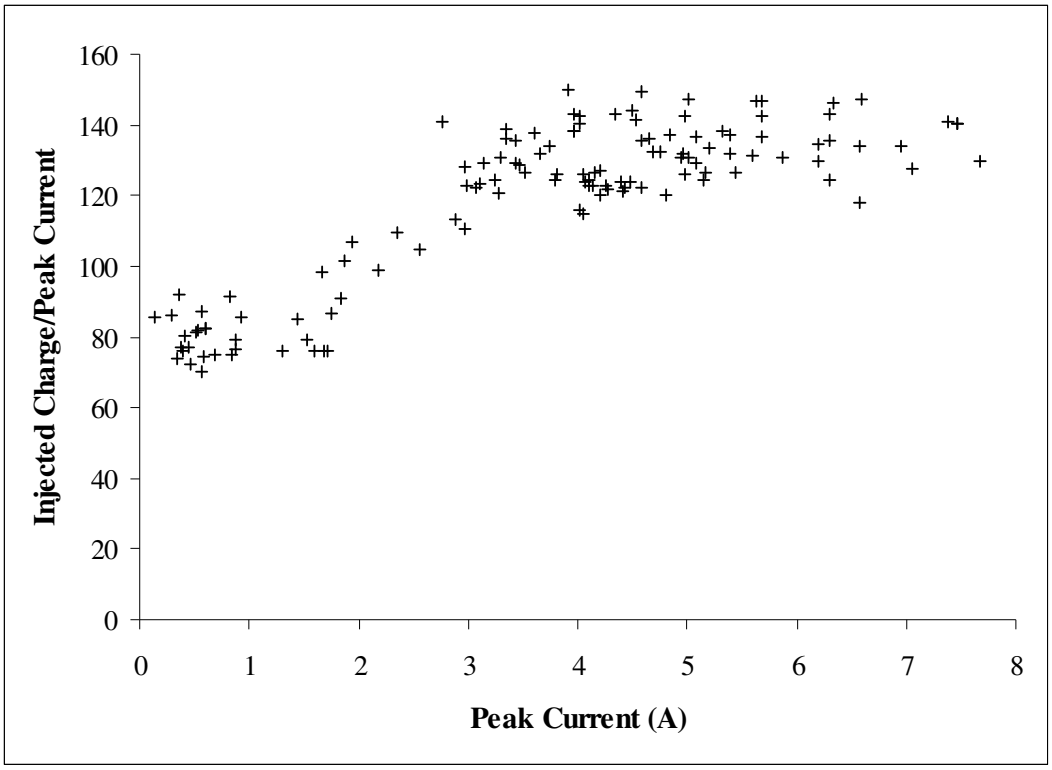

Figure 3.3.8: Variation of waveform shape factor with peak discharge current.

The non-linear relationship between discharge current shape factor and peak current indicates that the shape of the discharge current waveform must change for higher peak currents.

Figure 3.3.9 shows some example discharge current wave shapes for different peak discharge currents. For peak currents above about 2A a second peak begins to occur. By about 4A peak current the second peak is about the same size as the first. Above 4A the second peak dominates.

Figure 3.3.10 shows the oscilloscope traces obtained for a high current discharge. The double peak is clearly visible in the current waveform and a matching double peak is also observable in the first photo-multiplier signal. This indicates that the current double peak is not a measurement error.

The small hole drilled in the end of the blunt rod, directly up its central axis may cause this behaviour, resulting in two separate discharge sites with different inception voltages.

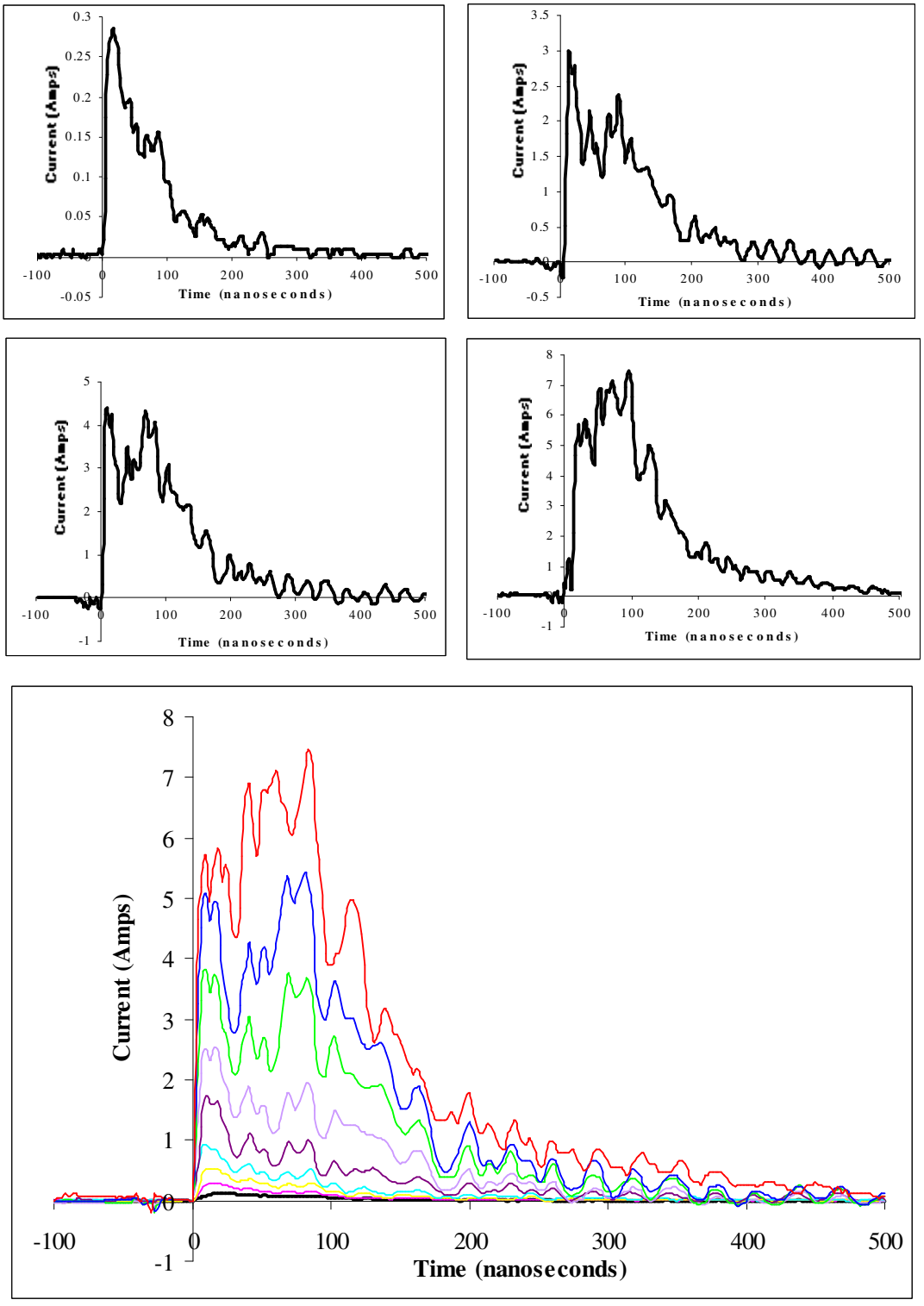

Figure 3.3.9: Examples of discharge current waveforms in air.

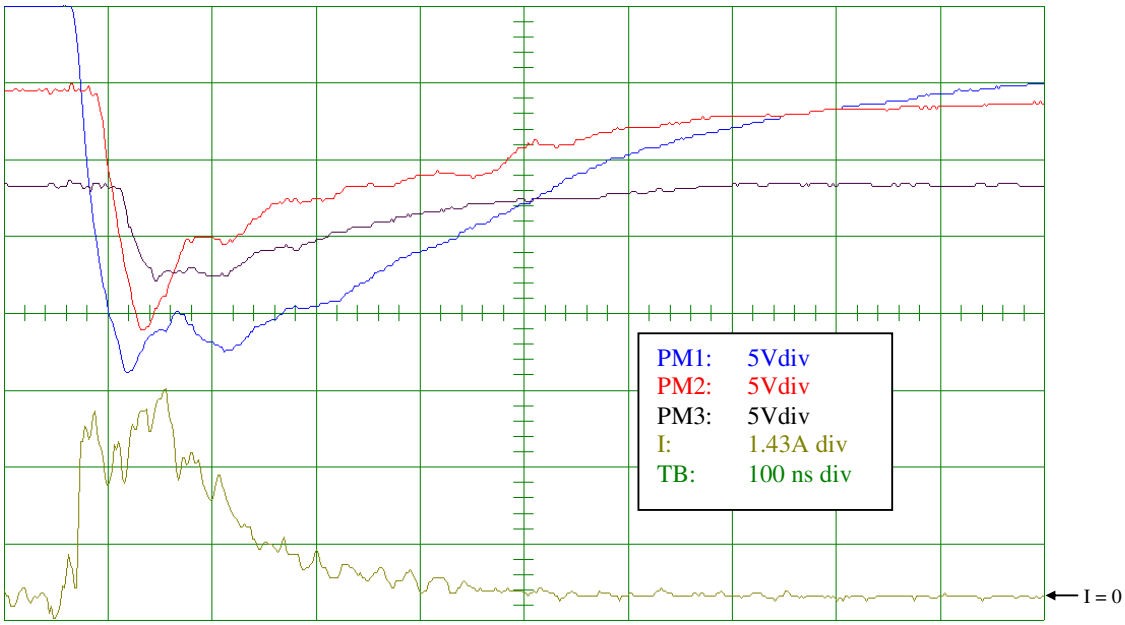

Figure 3.3.10: Oscilloscope trace showing the current and photo-multipliers signals for a high current discharge pulse in air.

3.3.4 Insulator

The insulator was then placed into the gap and positive impulses were applied to the rod. Before each impulse the insulator specimen was cleaned to neutralise any surface charge. After each applied impulse the insulator was scanned and a dust figure taken of the deposited charge. The length of time required to create and record the dust figures limited the number of impulses that could be applied.

The following pages show the detailed results obtained for each discharge.

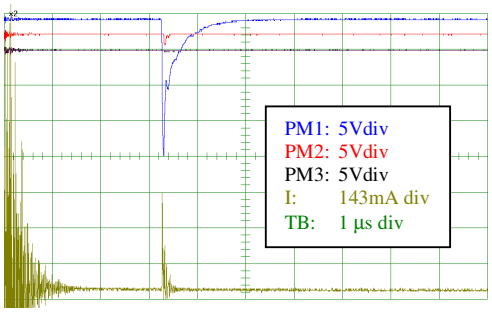

Oscilloscope Traces

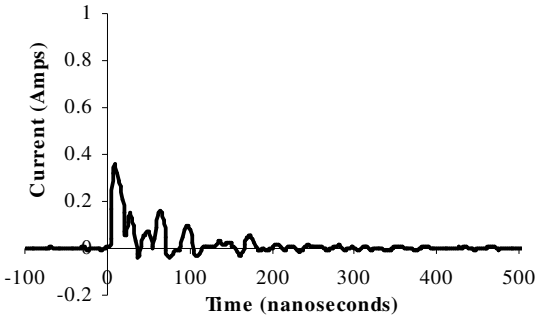

Current Signal

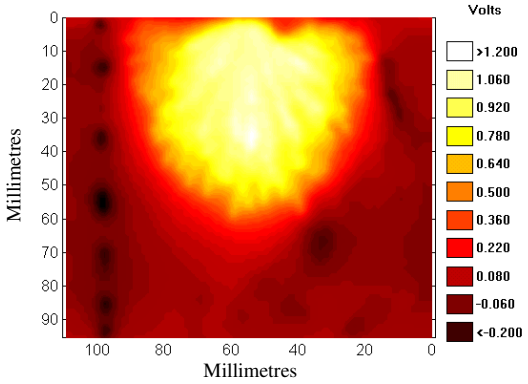

Probe Voltage Distribution

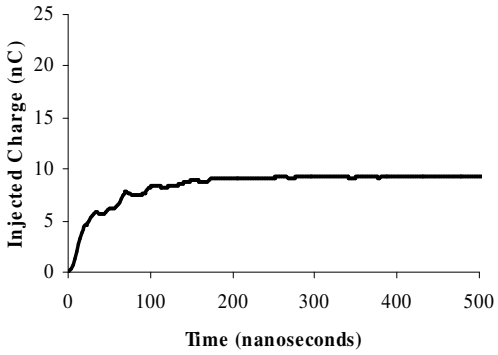

Injected Charge

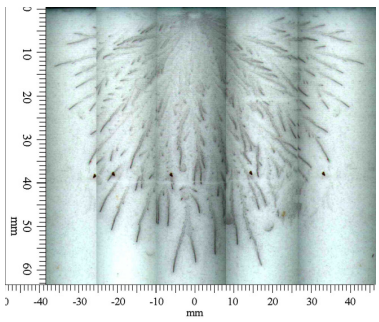

Dust Figure

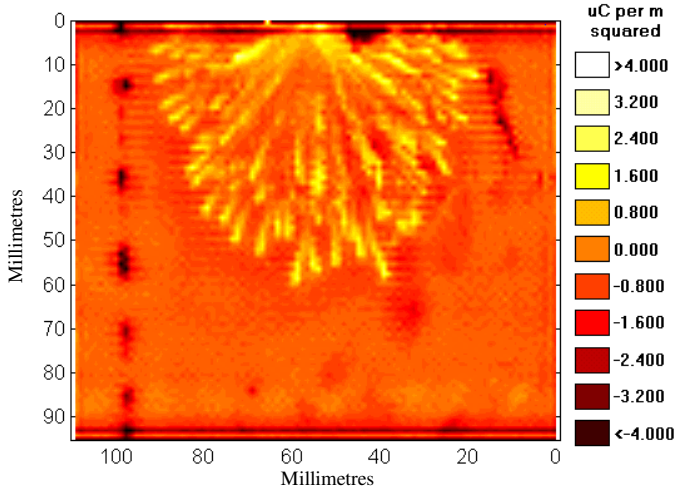

Charge Distribution

Applied Impulse:	**+29.5kVp**	Ipeak:	**+0.36A**
Time of corona:	**3.272µs**	Injected Q:	**+9.3nC**
Instantaneous Voltage:	**+27.3kV**	Net Surface Charge:	**+1.23nC**
Initial Velocity:	**$4.4\times10^{5}ms^{-1}$**	Total Positive:	**+ 1.70nC**
Distance Travelled:	**61mm**	Total Negative:	**-0.47nC**

Figure 3.3.11: +29.5kVp applied impulse.

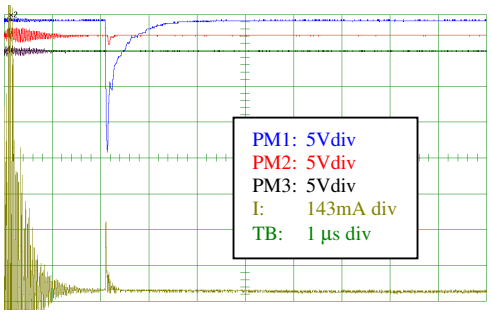

Oscilloscope Traces

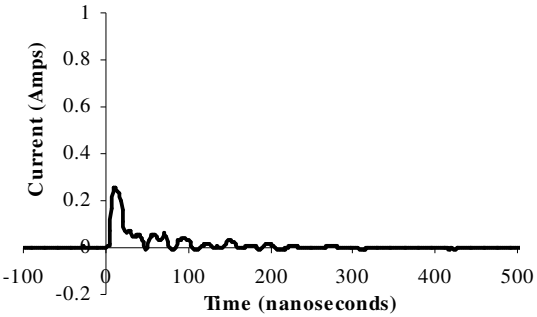

Current Signal

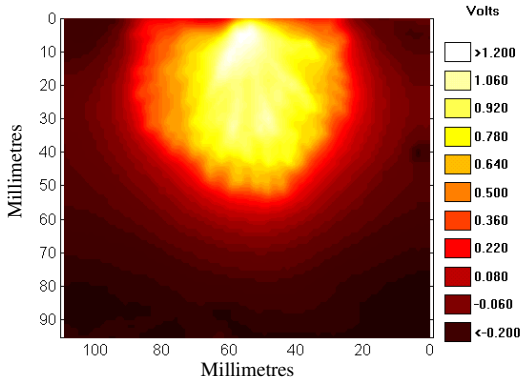

Probe Voltage Distribution

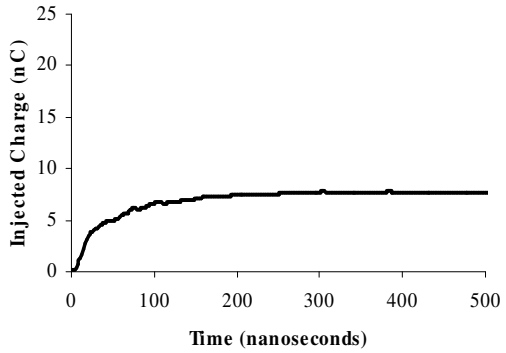

Injected Charge

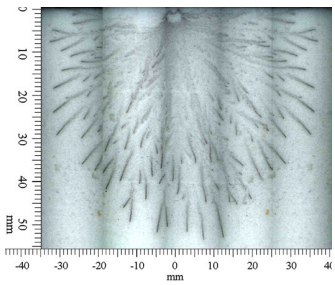

Dust Figure

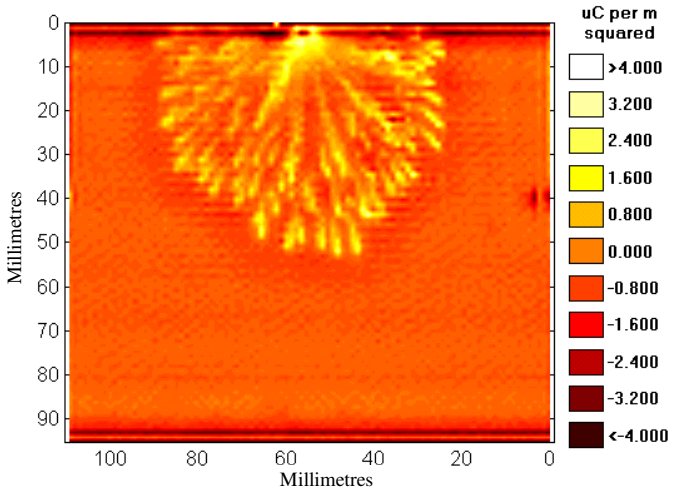

Charge Distribution

Applied Impulse:	**+32.3kVp**	Ipeak:	**+0.25A**
Time of corona:	**2.112µs**	Injected Q:	**+8.7nC**
Instantaneous Voltage:	**+25.4kV**	Net Surface Charge:	**+1.12nC**
Initial Velocity:	**$3.9\times10^{5}ms^{-1}$**	Total Positive:	**+ 1.54nC**
Distance Travelled:	**53mm**	Total Negative:	**-0.42nC**

Figure 3.3.12: +32.2kVp applied impulse.

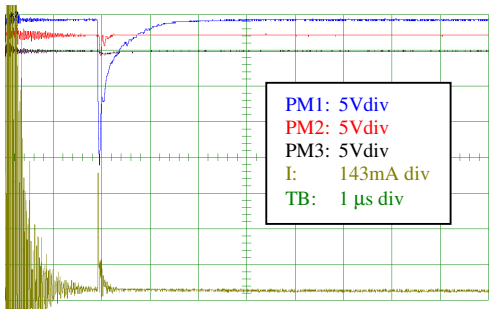

Oscilloscope Traces

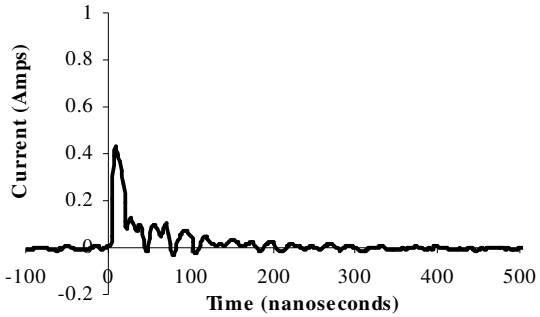

Current Signal

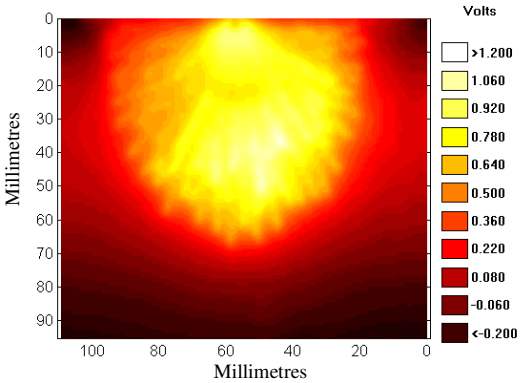

Probe Voltage Distribution

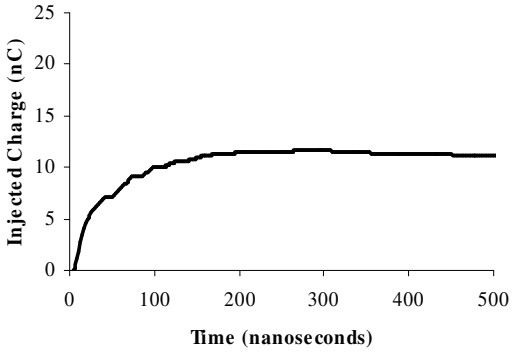

Injected Charge

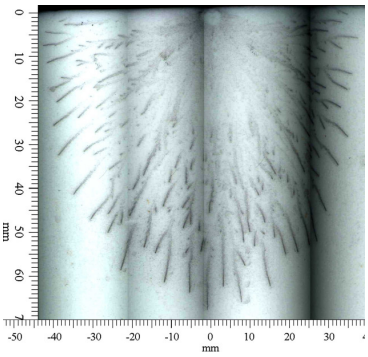

Dust Figure

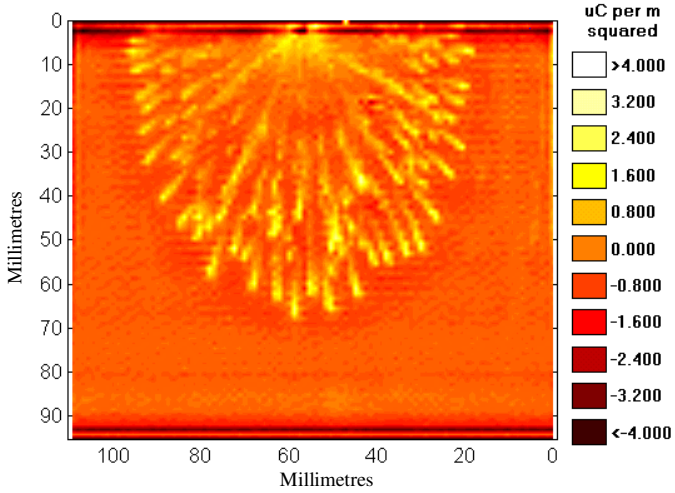

Charge Distribution

Applied Impulse:	**+36.0kVp**	Ipeak:	**+0.43A**
Time of corona:	**1.920µs**	Injected Q:	**+11.7nC**
Instantaneous Voltage:	**+27.0kV**	Net Surface Charge:	**+1.25nC**
Initial Velocity:	**$4.8\times10^{5}ms^{-1}$**	Total Positive:	**+ 1.80nC**
Distance Travelled:	**68mm**	Total Negative:	**-0.55nC**

Figure 3.3.13: +36.0kVp impulse applied

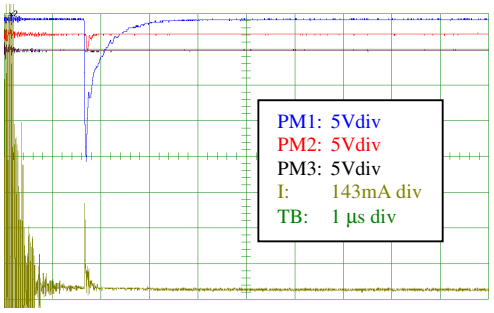

Oscilloscope Traces

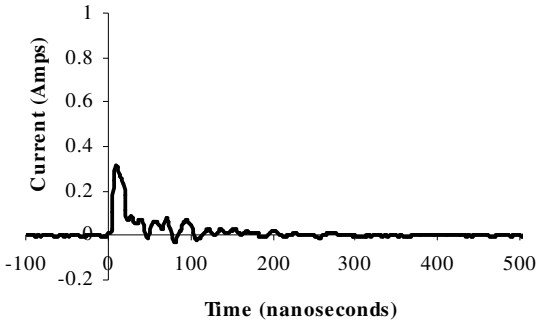

Current Signal

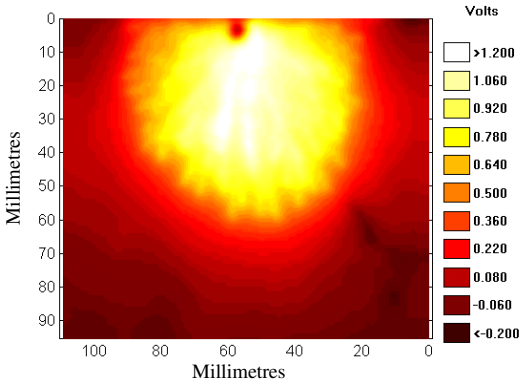

Probe Voltage Distribution

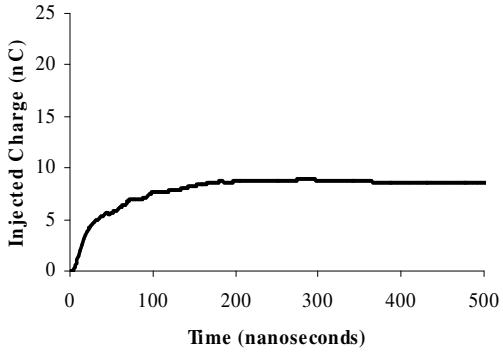

Injected Charge

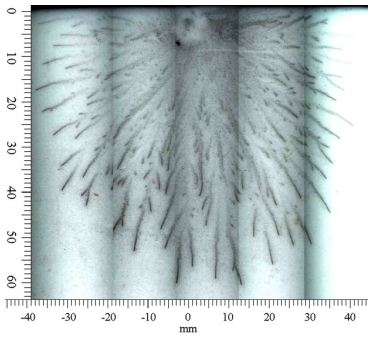

Dust Figure

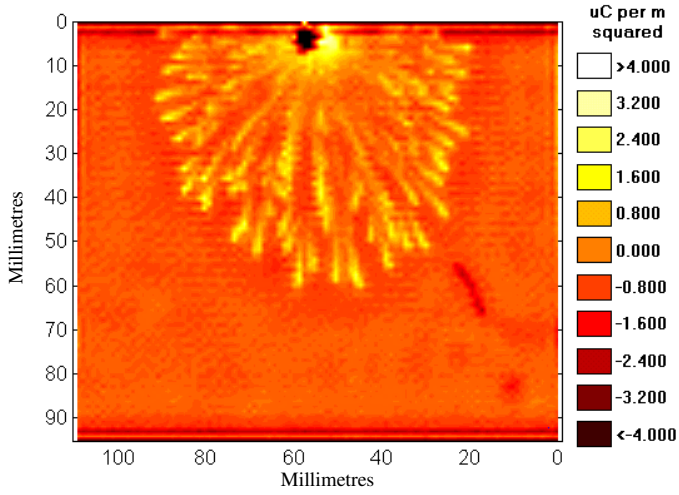

Charge Distribution

Applied Impulse:	**+36.0kVp**	Ipeak:	**+0.31A**
Time of corona:	**1.660µs**	Injected Q:	**+8.8nC**
Instantaneous Voltage:	**+24.9kV**	Net Surface Charge:	**+0.83nC**
Initial Velocity:	**$4.6\times10^{5}ms^{-1}$**	Total Positive:	**+1.46nC**
Distance Travelled:	**61mm**	Total Negative:	**-0.63nC**

Figure 3.3.14: +36.0kVp impulse applied (repeat).

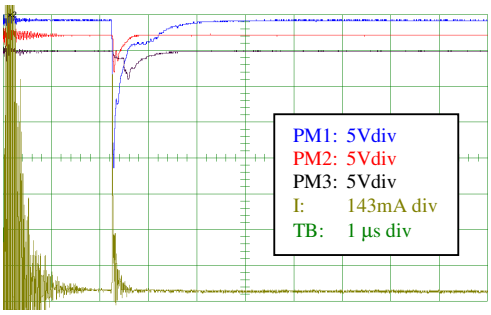

Oscilloscope Traces

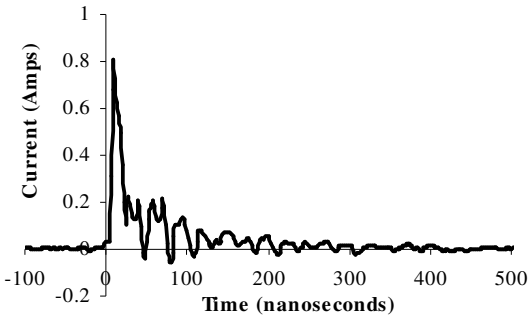

Current Signal

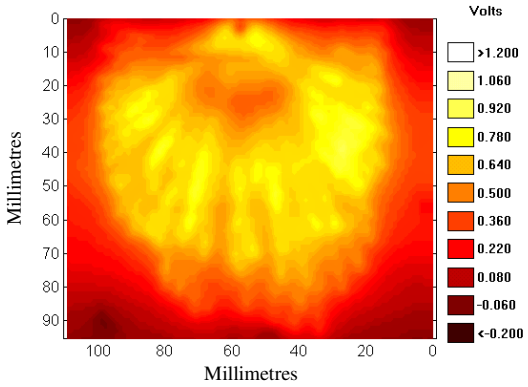

Probe Voltage Distribution

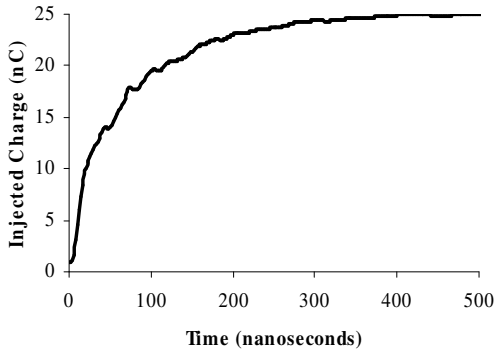

Injected Charge

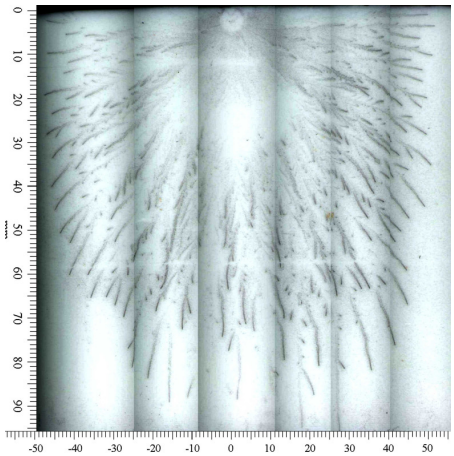

Dust Figure

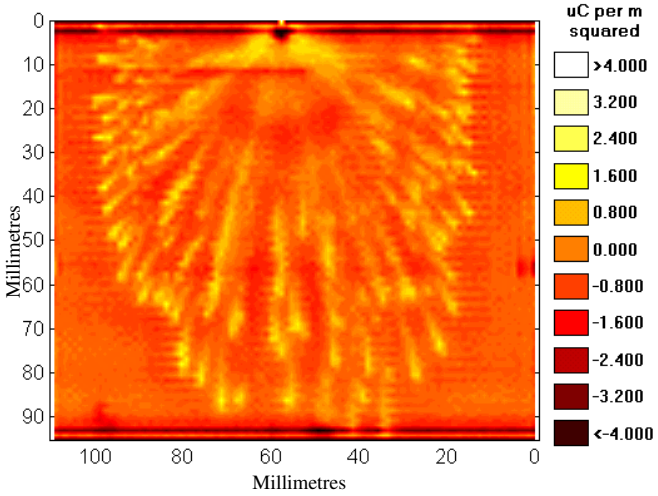

Charge Distribution

Applied Impulse:	**+41.9kVp**	Ipeak:	**+0.81A**
Time of corona:	**2.254µs**	Injected Q:	**+25nC**
Instantaneous Voltage:	**+34.0kV**	Net Surface Charge:	**+1.20nC**
Initial Velocity:	**$7.7\times10^{5}ms^{-1}$**	Total Positive:	**+ 2.07nC**
Distance Travelled:	**96mm**	Total Negative:	**-0.87nC**

Figure 3.3.15: +41.9kVp impulse applied.

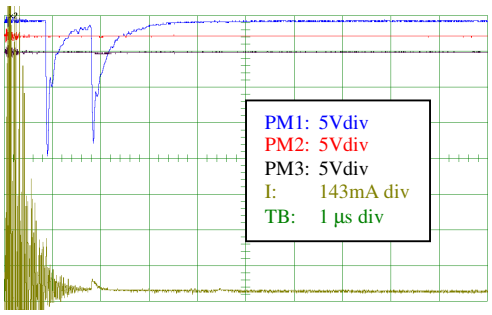

Oscilloscope Traces

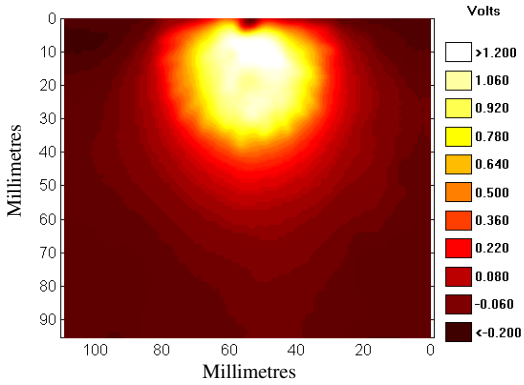

Probe Voltage Distribution

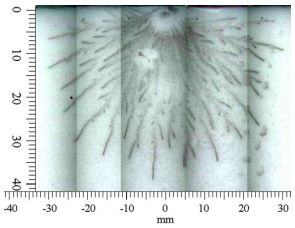

Dust Figure

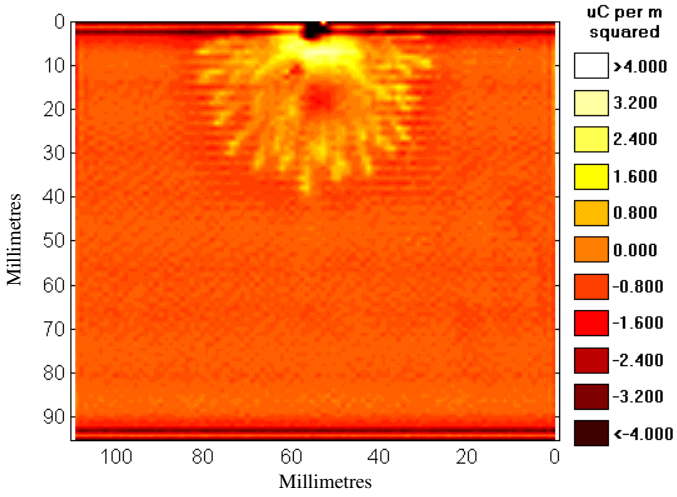

Charge Distribution

This is an example of an 'unusual' discharge event. The photo-multipliers signals indicate that two small discharges occurred. The first discharge appeared too early for the current signal to be free of noise.

Figure 3.3.16: +30.5kVp impulse applied.

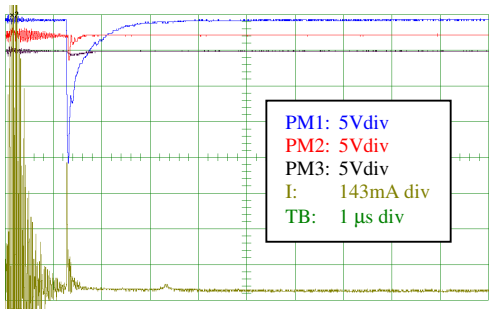

Oscilloscope Traces

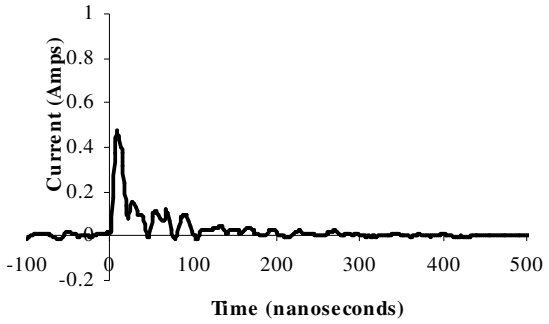

Current Signal

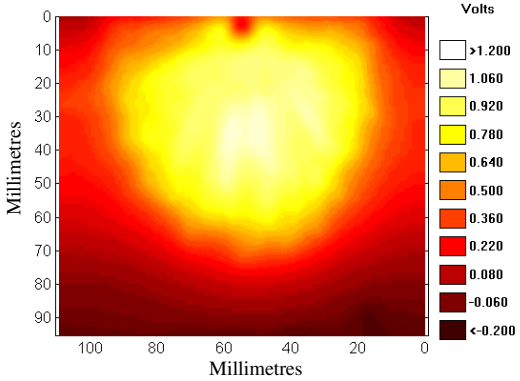

Probe Voltage Distribution

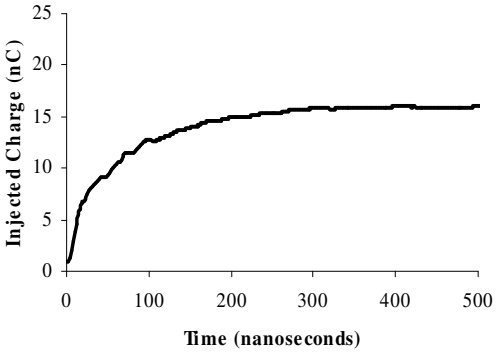

Injected Charge

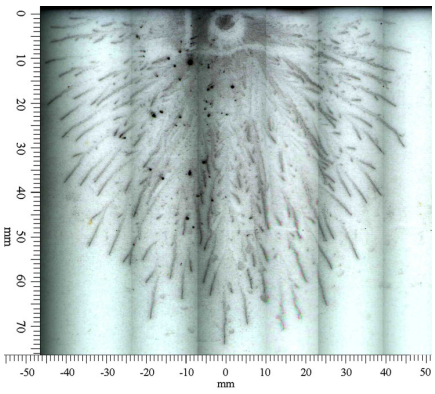

Dust Figure

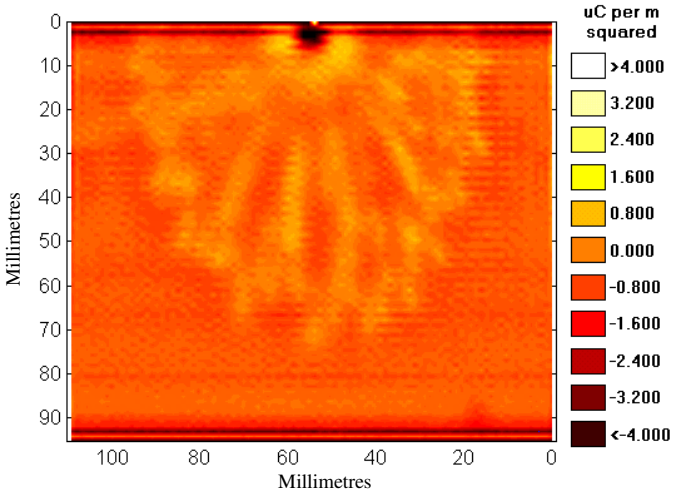

Charge Distribution

Applied Impulse:	**+48.0kVp**	Ipeak:	**+0.47A**
Time of corona:	**1.274µs**	Injected Q:	**+16nC**
Instantaneous Voltage:	**+28.1kV**	Net Surface Charge:	**+1.37nC**
Initial Velocity:	**$5.9\times10^{5}ms^{-1}$**	Total Positive:	**+1.64nC**
Distance Travelled:	**74mm**	Total Negative:	**-0.27nC**

Figure 3.3.17: +48.0kVp impulse applied.

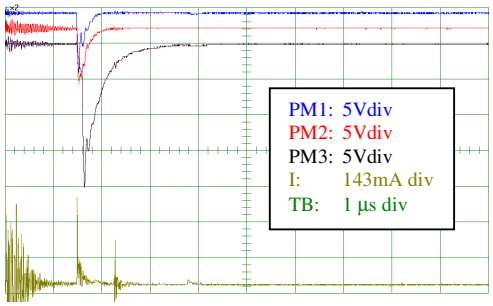

Oscilloscope Traces

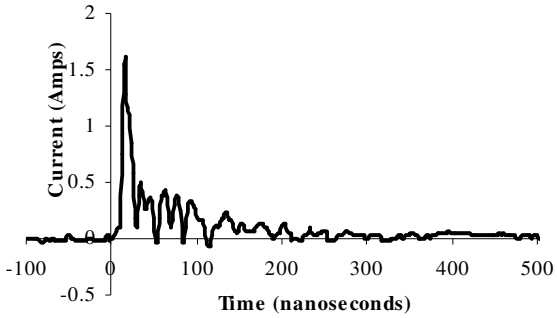

Current Signal

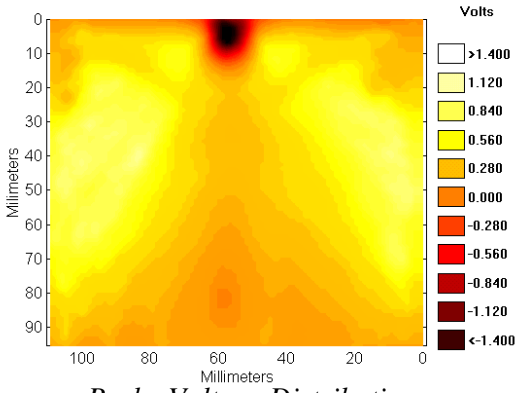

Probe Voltage Distribution

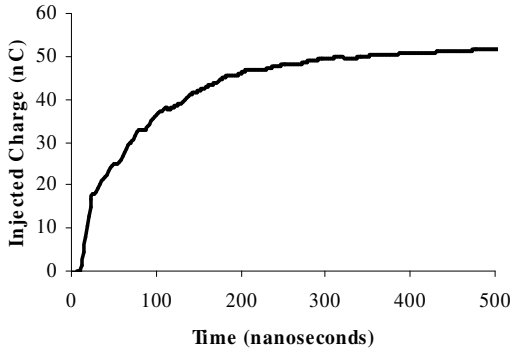

Injected Charge

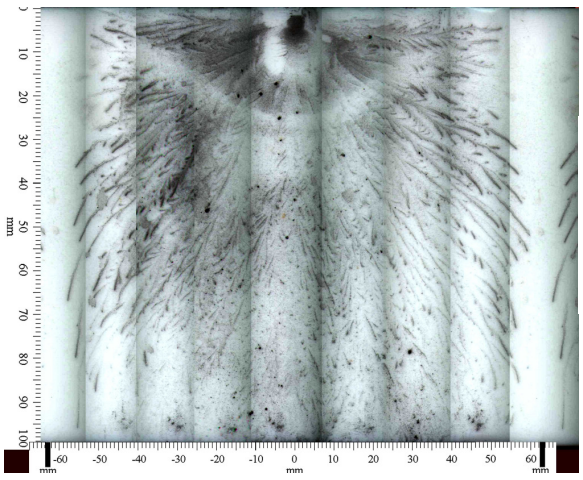

Dust Figure

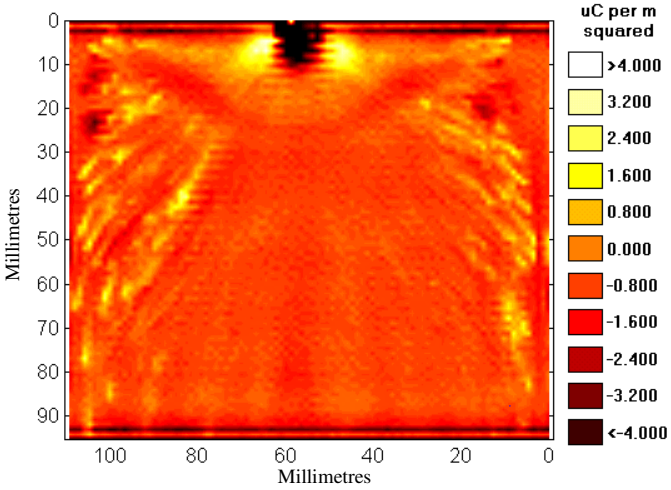

Charge Distribution

Applied Impulse:	**+63.1kVp**	Ipeak:	**+1.63A**
Time of corona:	**1.488µs**	Injected Q:	**+66nC**
Instantaneous Voltage:	**+41.0kV**	Net Surface Charge:	**-0.93nC**
Initial Velocity:	**$16.7\times10^{5}ms^{-1}$**	Total Positive:	**+1.46nC**
Distance Travelled:	**100mm**	Total Negative:	**-2.33nC**

Figure 3.3.18: +63.1kVp impulse applied.

The current wave shapes obtained in the presence of the insulator were much shorter in duration than those in air alone.

The charge distributions measured using the scanning system showed great similarities with the obtained dust figures. Each discharge was made up of a complex interaction of streamers propagating outwards from the rod. For higher applied voltages the streamers propagated almost all the way around the circumference of the insulator. The charged paths left on the surface by individual streamers could be resolved by the scanning system. This allowed a study of the charge distributions left by single streamers.

The overall measured surface charge distribution in each case could be divided into two regions: directly under the rod and the rest of the insulator surface. The small region directly under the rod was negatively charged with a density between –5 μCm^{-2} and –10μCm^{-2}. The rest of the insulator surface exhibited localised positive surface charging from the streamer channel distribution.

The rod was positioned very close to the top of the insulator; as such the region of surface directly under the rod could not be completely scanned in all cases. When the total surface charge deposited was calculated the region directly under the rod was neglected to allow a valid comparison to be made between the discharges. Experiments from this point on have the rod positioned further down the insulator surface to allow surface scans to measure fully the region directly under the rod.

The data from the results shown on the previous pages are summarised in the following graphs. The air data is shown as grey points for comparison.

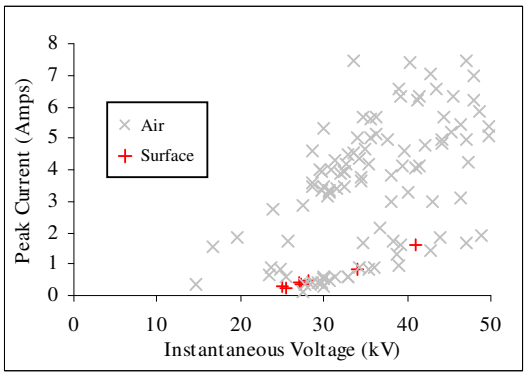

Figure 3.3.19: Peak current versus instantaneous voltage.

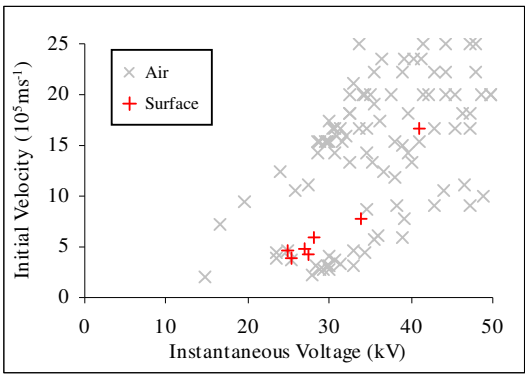

Figure 3.3.20: Initial velocity versus instantaneous voltage.

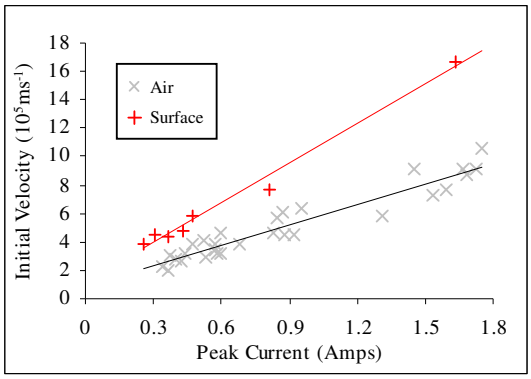

Figure 3.3.21: Initial velocity versus peak current.

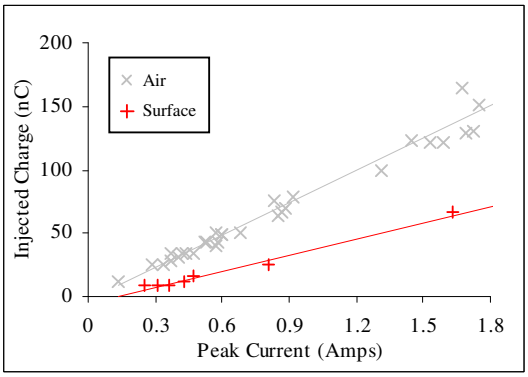

Figure 3.3.22: Injected charge versus peak current.

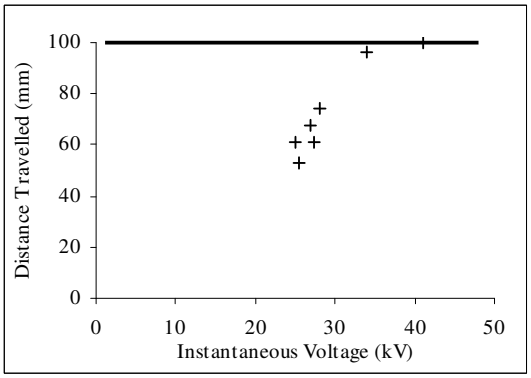

Figure 3.3.23: Distance travelled versus instantaneous voltage.

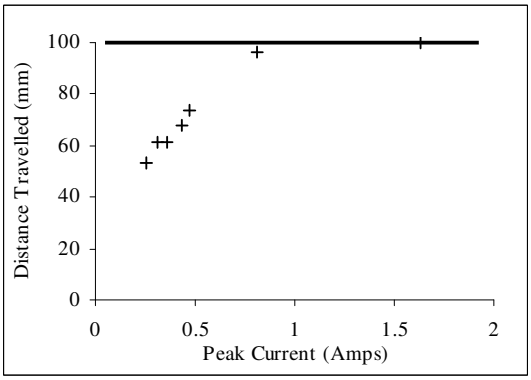

Figure 3.3.24: Distance travelled versus peak current.

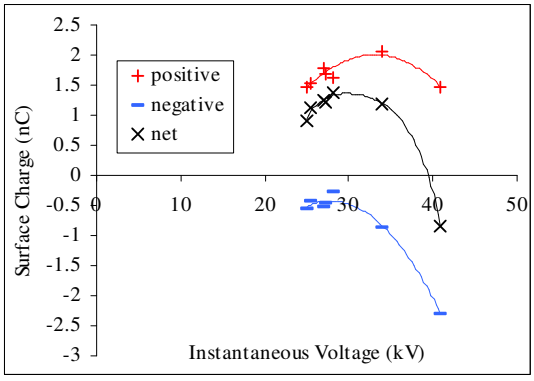

Figure 3.3.25: Surface charge versus instantaneous voltage.

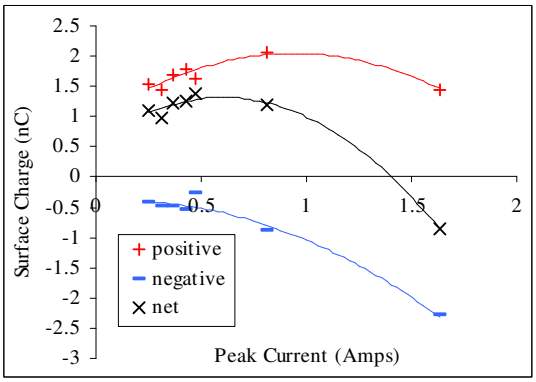

Figure 3.3.26: Surface charge versus peak current.

Only initial velocity measurements are shown because the discharge only crossed the complete gap on a couple of occasions. When peak current and initial velocity are plotted against instantaneous voltage, as shown in figures 3.3.19 and 3.3.20, there is much less scatter in the insulator data than the air. Peak currents in the presence of the insulator are in the lower range of air peak currents. Initial velocities are in the centre of the range for air.

When initial velocity is plotted against peak current, as shown in figure 3.3.21 there is a clear difference; discharges of the same peak current travel faster across the insulator.

Figure 3.3.22 shows the relationship between injected charge and peak current. In the presence of the insulator less charge is injected for the same peak current.

Figures 3.3.23 and 3.3.24 show the distance the discharge travelled across the insulator surface plotted against instantaneous voltage and peak current. Discharges that occurred at an instantaneous voltage greater than about 35kV or those with a peak current of more than 0.8A crossed the gap.

It was not possible to obtain distance travelled data for the air gap but by using the photo-multiplier No.3 signals it could be determined whether or not the discharge reached the plane. In air discharges could be detected by photo-multiplier No.3 at instantaneous voltages as low as 20kV and peak currents of 0.6A. When considering this information it should be remembered that the air data comprised of results from over 100 discharges, which means that a larger range of values is expected. It should also be noted that photo-multiplier No.3's field of view is almost a centimetre at the bottom of the gap, whereas using the dust figures and surface scans the distance travelled is measured as the furthest streamer charge channel on the surface.

Figures 3.3.25 and 3.3.26 show the variation of deposited charge with instantaneous voltage and peak current. It should be remembered that in this case the surface charge is calculated neglecting the region directly under the rod. Interestingly the amount of negative charge deposited increases as the streamer propagates further across the insulator. This may be to do with the high electronegativity of PTFE.

3.3.5 Scanning System's Affect Upon Surface Charge

One of the basic tenets of measurement is that it is not possible to measure a quantity without affecting its value slightly. A good measurement system has a minimal or undetectable affect on the measureand. The electrostatic probe has been designed to minimise the current drawn from the insulator surface charge distribution.

To see if the act of scanning disturbs the surface charge distribution, an insulator was repeatedly scanned. A charge distribution was generated on the insulator surface by applying a suitable impulse. The insulator was then scanned five times; each scan took approximately 3 minutes to complete. The measured charge distributions were analysed; no significant differences could be found between them. Only small variations of the order of the system accuracy could be detected.

It can therefore be concluded that the scanning system has an undetectable affect on the measured surface charge distribution.

3.4 Sharp Rod

3.4.1 Introduction

The blunt rod used in the initial experiments was considered to be too large for the gap length used. One indication of this was the poor correlation observed between discharge characteristics and instantaneous applied voltage. The rod diameter was large enough to support more than one discharge initiation site. The evidence for this is that although there is a scatter in the current values they appear grouped around two regions with the remaining values in-between. This indicates that at least two discharge initiation sites were operational on the rod. The changing shape of the current waveforms themselves also indicated that at higher currents multiple discharge initiation sites were present. These were presumably created by the hole drilled in the end of the rod.
To ensure a single discharge was initiated from one point a much sharper rod was utilised for the next series of experiments.

The initial experiments indicated that a highly charged region of insulator surface occurred directly under the rod tip. This region was suspected to be important so to allow its further study the main gap separation was decreased to 80mm; thus moving the rod tip to a point 20mm below the top of the insulator. The full region of surface directly beneath the rod tip could then be scanned using scanning system.
The rod was mounted at a slight angle to the vertical. This ensured that only the tip of the rod was closest to the surface and provided a single point of contact, thus reducing the likelihood of multiple discharge sites.
Another feature that was suspected to be important was the distance of the rod tip from the insulator surface. The rod could either be in contact with the surface or a distance away from it. The characteristics of the gap should tend to the air gap case as the rod-surface separation is increased to infinity. In this series of experiments a few trial rod-surface separations were employed.

The effect of repeated impulses was also studied by scanning the insulator after each shot. This provided a unique study because charge density distributions to the resolution

obtainable using the scanning system could only be obtained in the past using dust figures. Obviously after a dust figure has been taken the insulator is then contaminated and hence there is no opportunity to apply further shots, whereas the scanning system does not affect the charge distribution.

3.4.2 Set-up

Using the apparatus set-up as shown in figure 3.4.1, the rod axis was positioned at aproximatly 10° to the vertical. Impulse generator No.1 was used to apply voltages to the rod. Impulses of maginitude +28kVp and +44kVp were applied. Again PTFE was used as the insulator material.

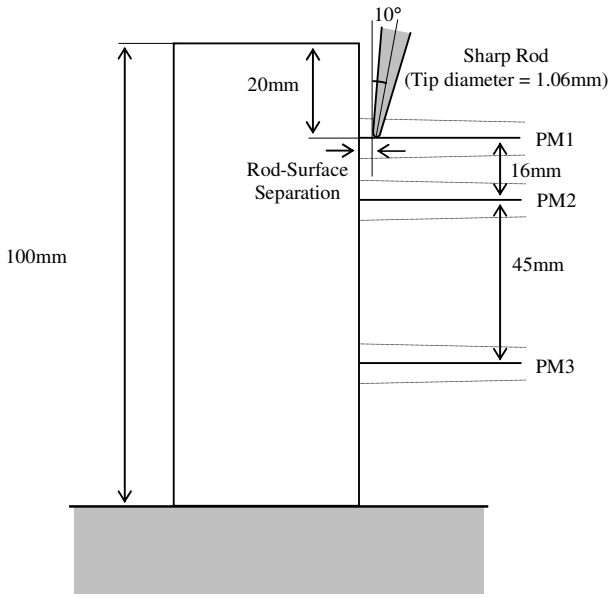

Figure 3.4.1: The apparatus set-up for the sharp rod experiments.

The temperature in the laboratory was 18°C. The atmospheric pressure was 753mmHg. The specific humidity was found to be 9.38gm^{-3}.

3.4.3 Air

+28kVp impulses were initially applied without the insulator to establish the gap characteristics. The results from 25 discharges are shown in the graphs below, the blunt rod air gap results are also shown for comparison.

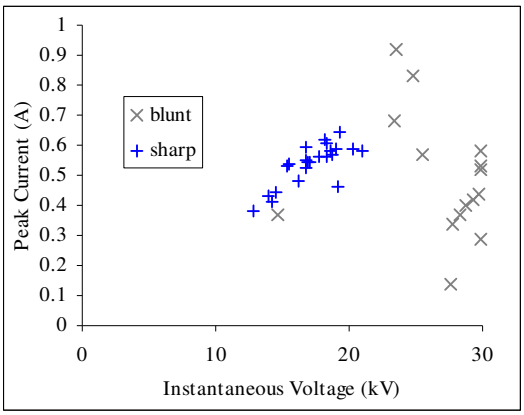

Figure 3.4.2: Peak current versus instantaneous voltage in air.

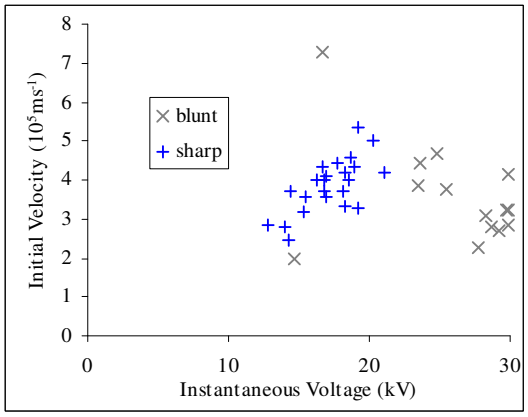

Figure 3.4.3: Initial velocity versus instantaneous voltage in air.

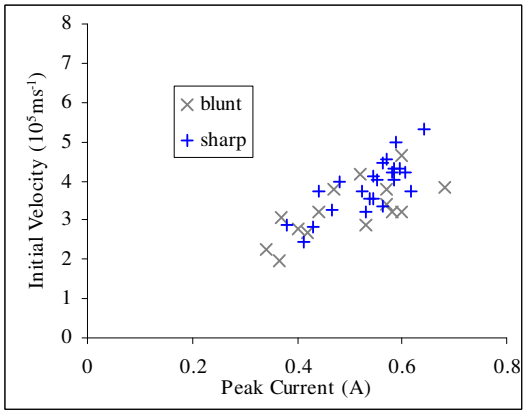

Figure 3.4.4: Initial velocity versus peak current in air.

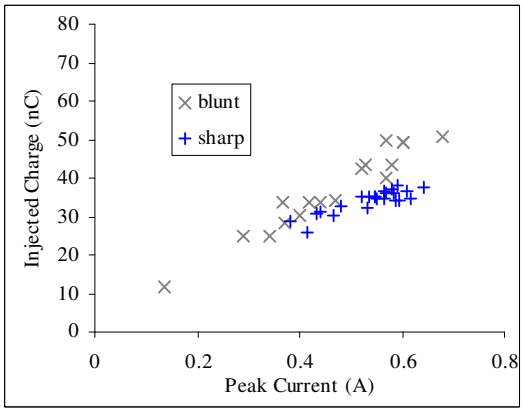

Figure 3.4.5: Injected charge versus peak current in air.

When plotted against instantaneous applied voltage the points are much less scattered than for the blunt rod case. This indicates that the sharper rod produces a more repeatable discharge. A similar variation of initial velocity and injected charge with peak discharge current exists for both the sharp and blunt rod.

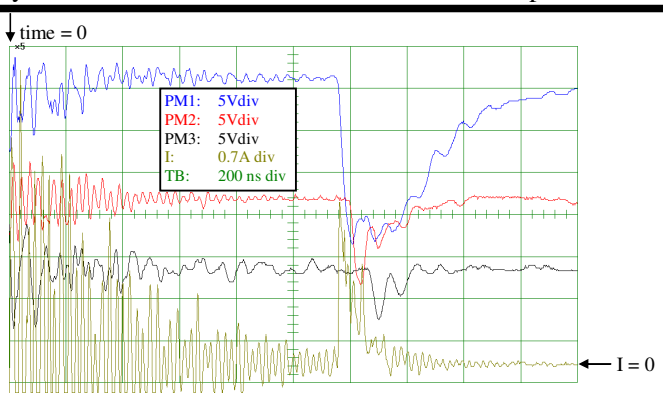

Figure 3.4.6: Typical oscilloscope traces obtained for +28kVp impulses applied to the sharp rod in air.

Figure 3.4.6 shows a typical oscilloscope trace obtained for an impulse applied to the sharp rod without the insulator present.

3.4.4 Insulator

The previously neutralised insulator was placed in the gap with the rod 0.5mm away from the surface and ten +44kVp impulses were applied to the rod. The surface was scanned after the 1st, 2nd, 3rd, 4th, 5th and 10th impulse. The calculated charge distributions are shown below. After the 10th impulse another impulse was applied with the insulator rotated through 90°. This was to see what would happen when there was a prior charge distribution.

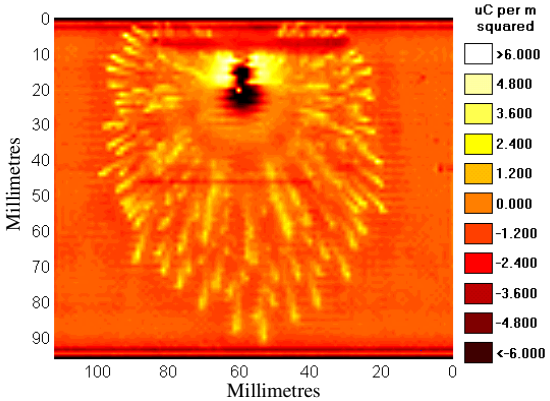

Figure 3.4.7: Surface charge deposited after a 44kVp impulse, sharp rod 0.5mm away from insulator.

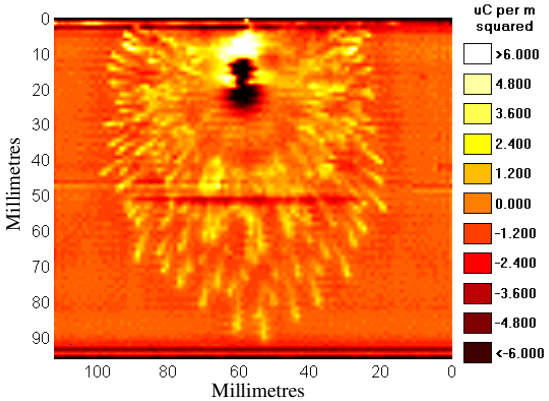

Figure 3.4.8: Surface charge deposited after two 44kVp impulses, sharp rod 0.5mm away from insulator.

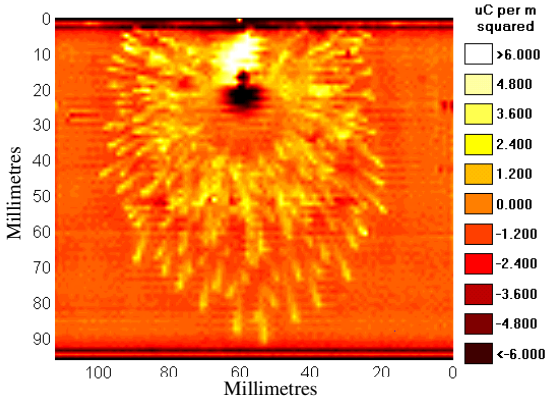

Figure 3.4.9: Surface charge deposited after three 44kVp impulses, sharp rod 0.5mm away from insulator.

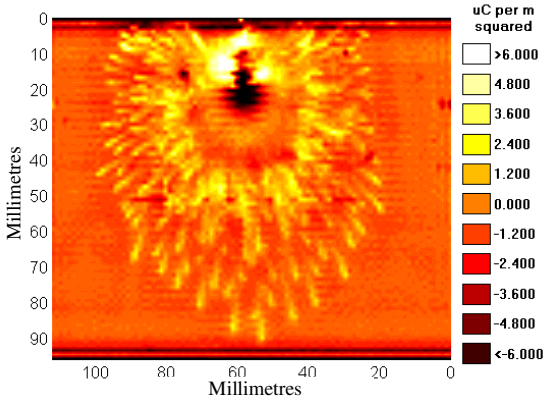

Figure 3.4.10: Surface charge deposited after four 44kVp impulses, sharp rod 0.5mm away from insulator.

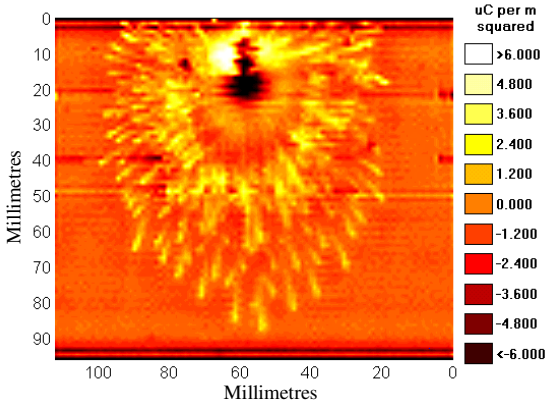

Figure 3.4.11: Surface charge deposited after ten 44kVp impulses, sharp rod 0.5mm away from insulator.

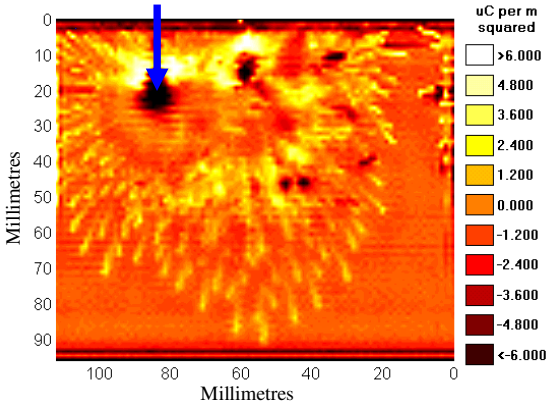

Figure 3.4.12: Surface charge deposited after a 44kVp impulse applied to the rod at the blue arrow 0.5mm away from insulator.

The charged channels deposited indicate that the streamers that form the discharge propagate a long way around the circumference of the insulator. The charge distributions show the effect of repeated impulses; each discharge adds to the distribution of surface charge. Figure 3.4.13 shows the calculated charge deposited after each impulse.

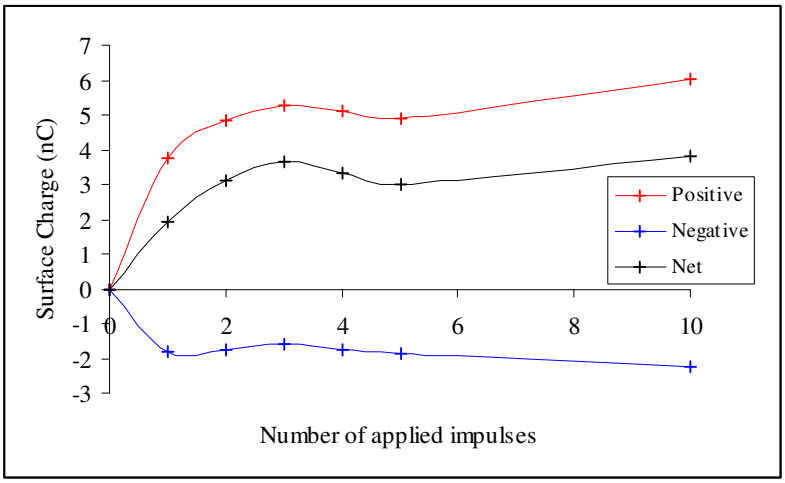

Figure 3.4.13: Calculated surface charge deposited after each +44kVp impulse

After about 3 impulses the net amount of surface charge reaches a limit and further discharges serve only to redistribute the surface charge. It is interesting to note that even after ten impulses had been applied the original streamer channel tips left by the first discharge remained untouched. This implies that none of the other discharges propagated further than the first on the initially neutralised surface.

Figure 3.4.12 shows the charge deposited after another +44kVp impulse was applied in the position of the blue arrow. The surface previously had the charge distribution shown in figure 3.4.11 with calculated charges of positive +6.03nC negative -2.23nC and net +3.80nC. The discharge produced another charge distribution on top of the previous one with calculated charges of positive +6.419nC negative -3.556nC and net +2.863nC. The main contribution to the change in total charge was from the addition of another highly negatively charged region directly under the rod. This region contained a net charge of about -1nC.

The major disadvantage of the sharp rod is that it has a much lower corona inception voltage because of the field enhancement around the sharp tip. The result of this is that the discharge is initiated much earlier in the impulse voltage wave. This meant that the current signal was lost in the noise of the impulse generator firing. This is not desirable if a detailed study is to be undertaken.

A lower impulse voltage of +28kVp was used in an attempt to delay the discharge just long enough to be free from noise. The rod was positioned in contact with the insulator surface and 4 impulses were applied. The insulator was neutralised prior to the application of impulses and scanned after each impulse. The four calculated surface charge distributions are shown in the following figures.

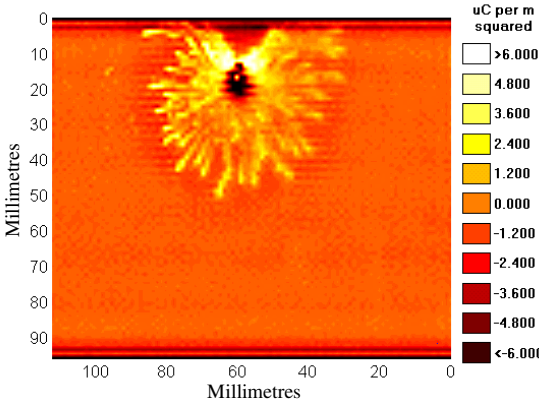

Figure 3.4.14: Surface charge deposited after a single +28kVp impulse, sharp rod in contact with insulator.

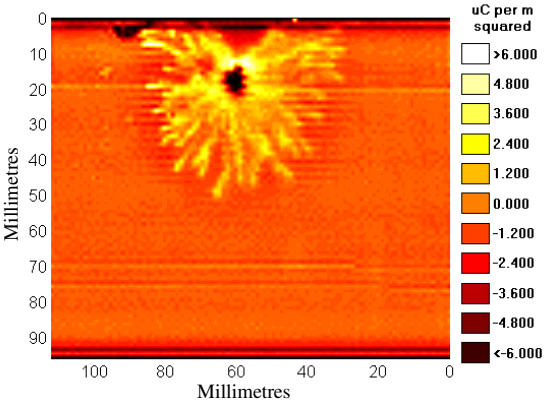

Figure 3.4.15: Surface charge deposited after a second +28kVp impulse, sharp rod in contact with insulator.

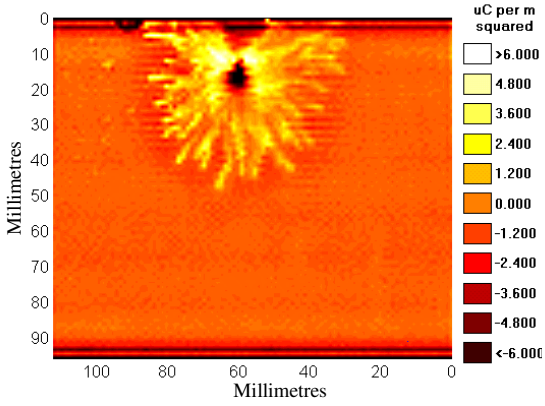

Figure 3.4.16: Surface charge deposited after a third +28kVp impulse, sharp rod in contact with insulator.

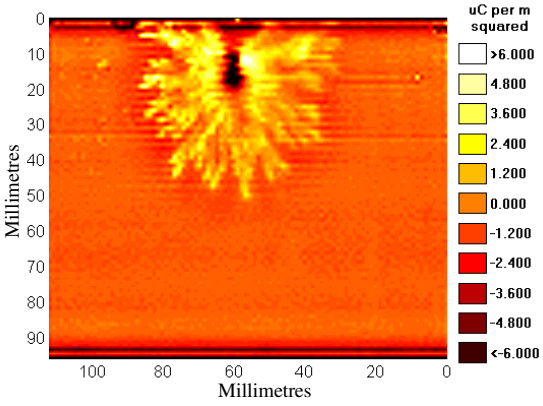

Figure 3.4.17: Surface charge deposited after a fourth +28kVp impulse, sharp rod in contact with insulator.

Each impulse changes the surface charge distribution slightly, the fourth impulse shown in figure 3.4.17 has added a few extra streamer tips to the distribution. The charge deposited is shown in figure 3.4.18. Less charge is deposited than for the previous +44kVp impulses, though this is to be expected because the streamers have not propagated as far.

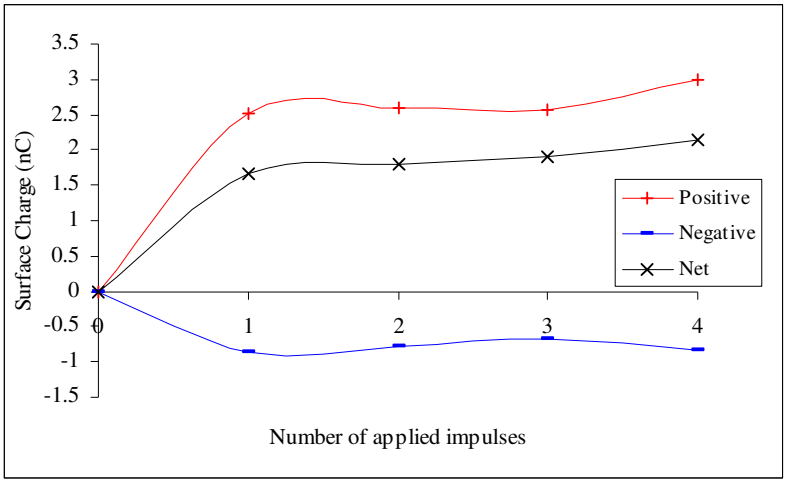

Figure 3.4.18: Calculated surface charge deposited after each +28kVp impulse

Unfortunately even at this lower voltage the presence of the insulator led to low a corona inception voltage and hence the discharge still occurred too early to be visible clearly above the generator firing noise.

In a last attempt to get a clean current signal from the sharp rod, the rod-surface distance was increased because current signals were observable without the insulator. With all parameters kept exactly the same, the rod-surface separation was increased to 1mm and the insulator surface neutralised. Two +28kVp impulses were applied to the rod with surface scans taken after each impulse. The calculated charge distributions are shown below.

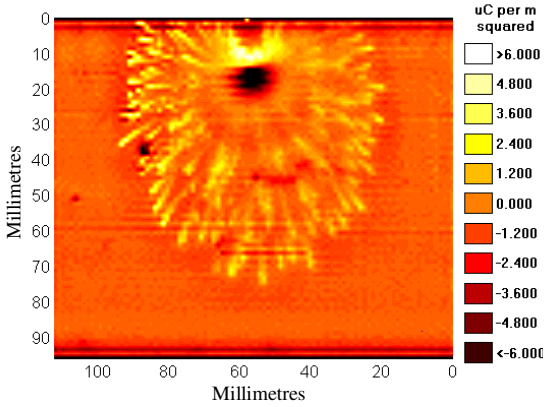

Figure 3.4.19: Surface charge deposited after a single +28kVp impulse, sharp rod 1mm away from insulator.

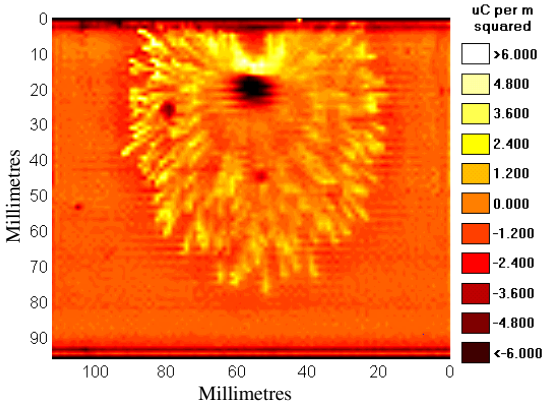

Figure 3.4.20: Surface charge deposited after a second 28kVp impulse, sharp rod 1mm away from insulator.

The most striking difference between the charge distributions generated with the rod in contact with the surface and the two shown in the figures above is the distance travelled. When the rod was in contact with the surface the streamers only travelled 30mm from the tip. Whereas with identical conditions apart from the rod being 1 mm away from the surface the streamer propagated 55mm; almost twice as far. The main reason for this was the discharge occurred later in the applied impulse voltage wave shape and hence had a higher instantaneous voltage. By separating the rod from the surface by a small amount the field enhancement effect, caused by the triple junction, is reduced. More charge was deposited on the surface than when the rod was in contact. It is important however to remember that the discharges occurred at higher voltages and hence propagated further when the rod was not in contact with the surface. The two discharges occurred at a late enough time in the impulse wave to be free of noise and to have a clean current wave shape.

The insulator surface was then neutralised again and two more +28kVp impulses were applied with the rod-surface distance increased to 2mm. The surface charge density distributions after each impulse are shown in figures 3.4.21 and 3.4.22.

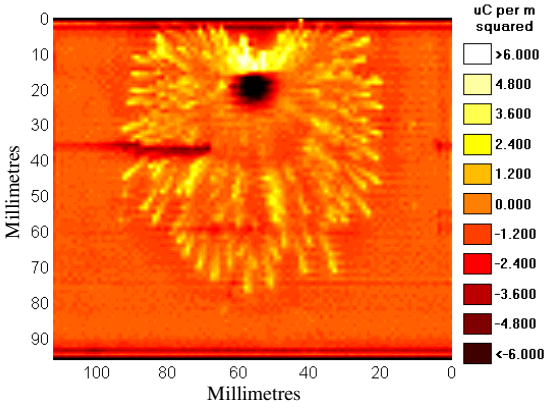

Figure 3.4.21: Surface charge deposited after a single +28kVp impulse, sharp rod 2mm away from insulator.

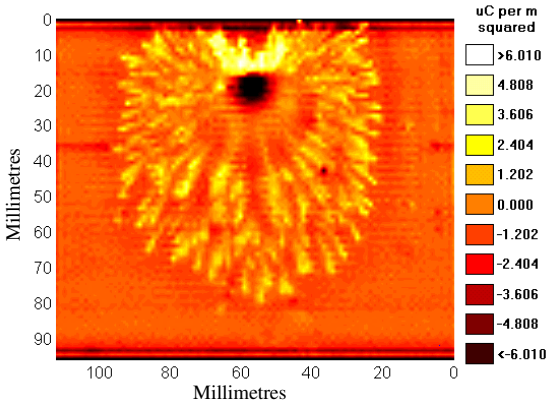

Figure 3.4.22: Surface charge deposited after a second +28kVp impulses, sharp rod 2mm away from insulator.

The charge distributions obtained are very similar those with a 1mm rod-surface separation. The current signals obtained were processed the results obtained are shown below. The data with no insulator present (air) is also shown.

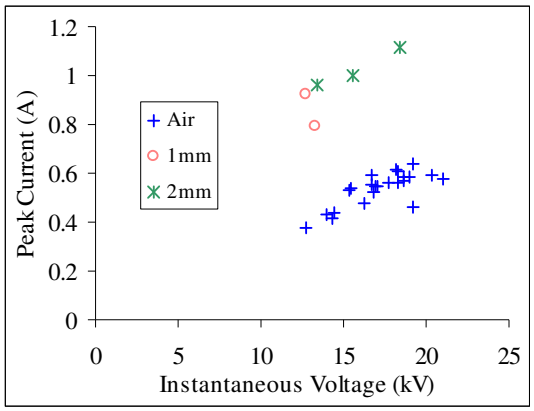

Figure 3.4.23: Peak current versus instantaneous voltage for the sharp rod.

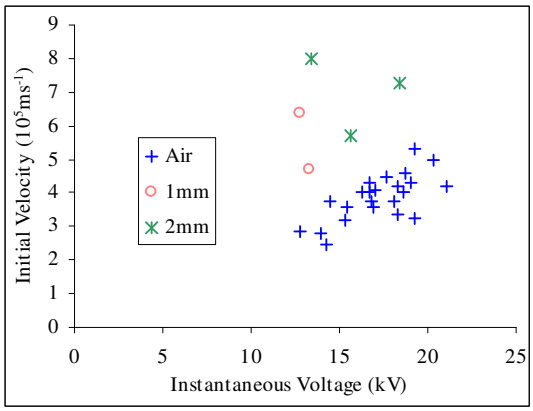

Figure 3.4.24: Initial velocity versus instantaneous voltage for the sharp rod.

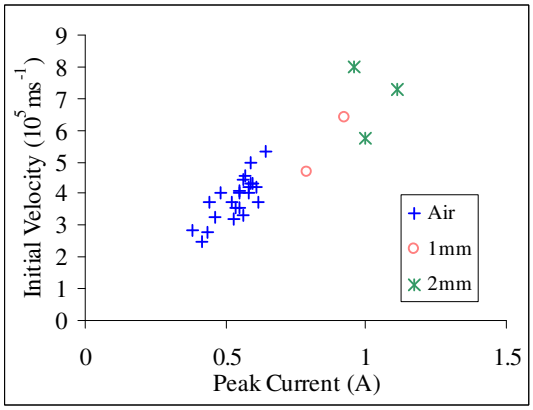

Figure 3.4.25: Initial velocity versus peak current for the sharp rod.

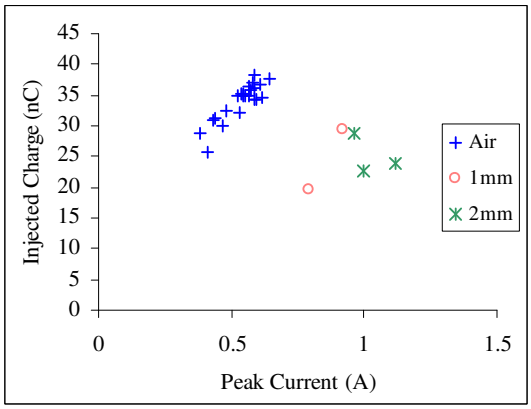

Figure 3.4.26: Injected charge versus peak current for the sharp rod.

Figure 3.4.23 shows that discharges propagating in the vicinity of insulator surfaces had a higher peak current and are faster for the same instantaneous voltage than those in air. They also inject less charge for a particular peak current.

3.5 Medium Rod

3.5.1 Introduction

The sharp rod produced a reliable discharge initiation site at the cost of a very low corona inception voltage. For the 80mm gap length under study the sharp rod's low inception voltage caused the discharge to occur too early in the impulse to permit oscilloscope measurements free of noise.

The solution was to use a medium rod with a diameter of 3.15mm which offered the best of both worlds; a single reliable discharge site with a corona inception voltage suitable for the gap length.

3.5.2 Set-up

The apparatus was set up as shown in figure 3.5.1, the rod axis was positioned at approximately 10° to the vertical. PTFE was used as the insulator material. Impulse generator No.1 was used to apply voltages to the rod. The atmospheric conditions in the laboratory were 19.5°C and 752mmHg. The specific humidity was 10.3gm^{-3}.

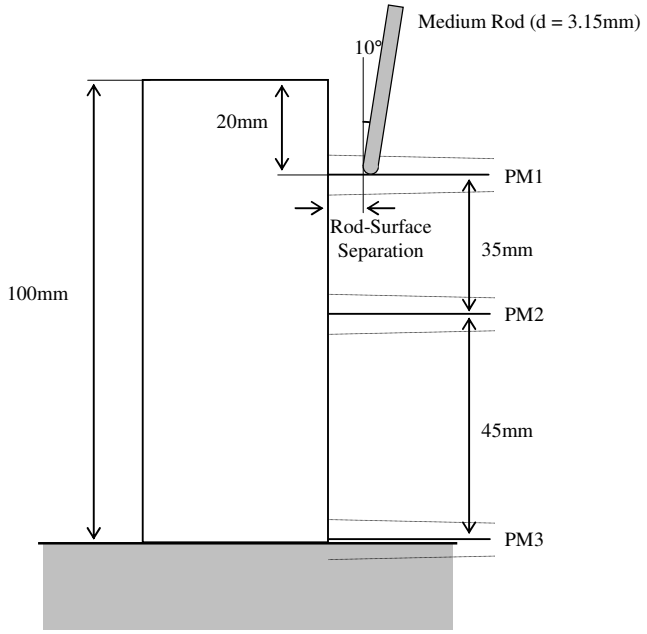

Figure 3.5.1: The apparatus set-up for the medium rod experiments.

3.5.3 Method

As before the gap characteristics without the insulator in place were obtained by applying twenty +45kVp impulses to the rod. Current and photo-multiplier signals were recorded for every shot. The neutralised insulator was then placed in the gap and twenty +45kVp impulses were applied. The insulator surface was scanned for surface charge after the 1st, 2nd, 3rd, 4th, 5th, 10th and 20th shot.

This process was repeated for rod-surface separations of 0mm, 5mm and 10mm. The insulator was neutralised for each new rod-surface separation

3.5.4 Results

Air

The results obtained for the medium rod air gap are summarised below. The previous results for different rod diameters are also given for comparison.

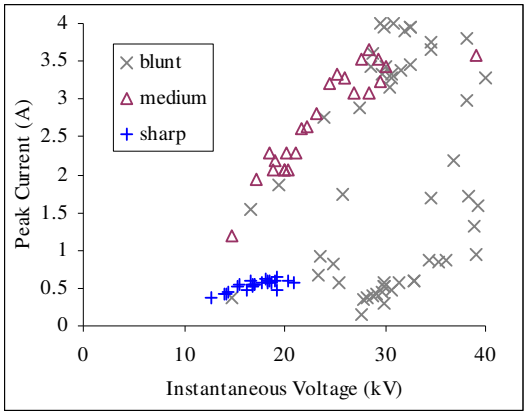

Figure 3.5.2: Peak current versus instantaneous voltage.

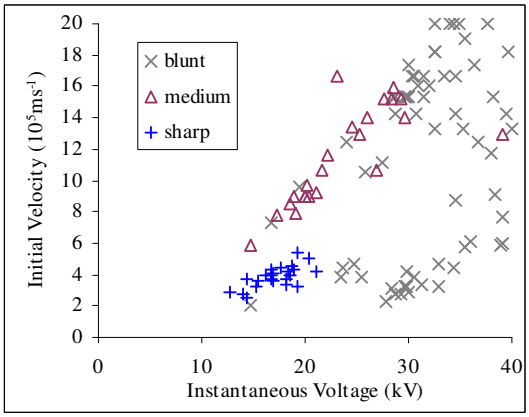

Figure 3.5.3: Peak current versus instantaneous voltage.

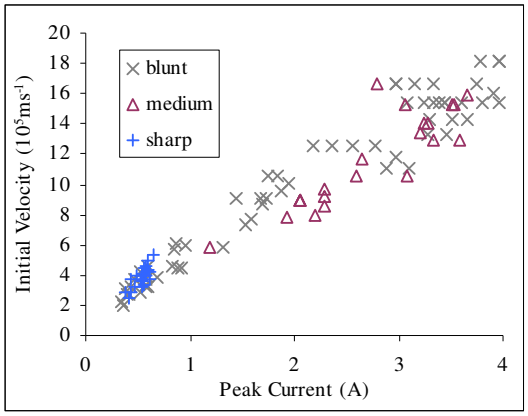

Figure 3.5.4: Initial velocity versus peak current.

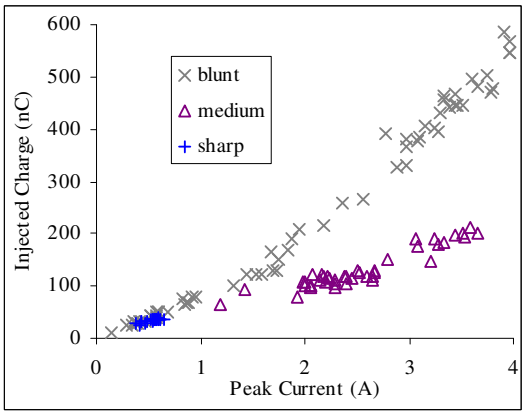

Figure 3.5.5: Injected charge versus peak current.

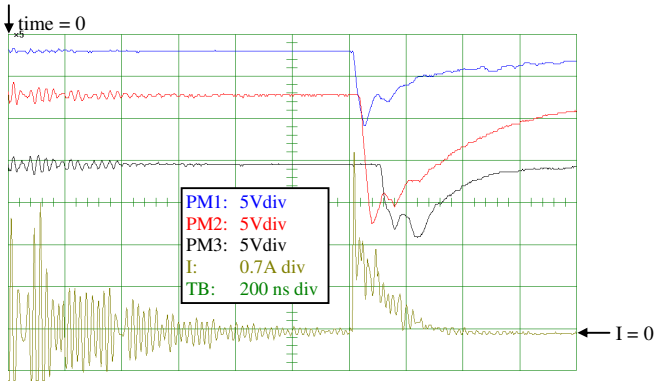

Figure 3.5.6: Typical oscilloscope traces for +45kVp applied to the medium rod in air.

Figure 3.5.6 shows a typical oscilloscope trace obtained for +45kVp impulses applied to the rod without the insulator present.

Insulator

The scans obtained of the surface charge density distributions produced for impulses applied with the insulator present are shown in the following figures. The distributions indicate that the streamers crossed the gap for all rod-surface separations. However for the case with the rod in contact with the insulator no signal could be detected from the photo-multiplier looking at the ground plane for all twenty impulses applied. This is an important point; the light emitted from some streamers may be too weak to be detected by the photo-multipliers. Absence of a photo-multiplier signal does not necessarily indicate that a streamer did not reach the region observed by the photo-multiplier.

Rod-Surface Separation = 0mm

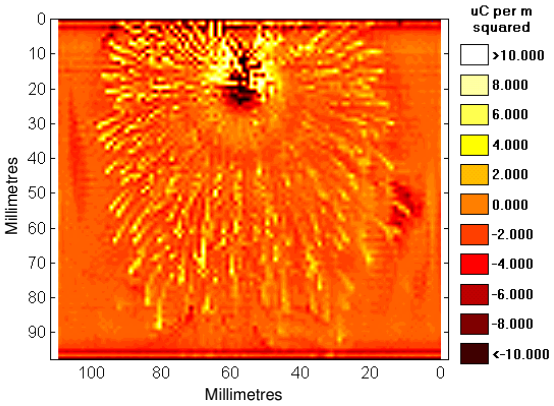

Figure 3.5.7: Surface charge distribution obtained after a single +45kVp impulse applied to rod in contact with insulator.

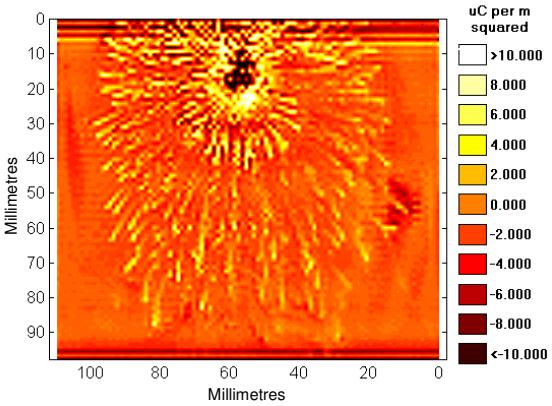

Figure 3.5.8: Surface charge distribution obtained after two +45kVp impulses applied to rod in contact with insulator.

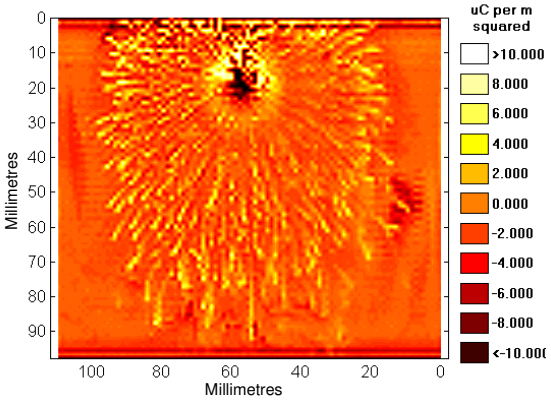

Figure 3.5.9: Surface charge distribution obtained after three +45kVp impulses applied to rod in contact with insulator.

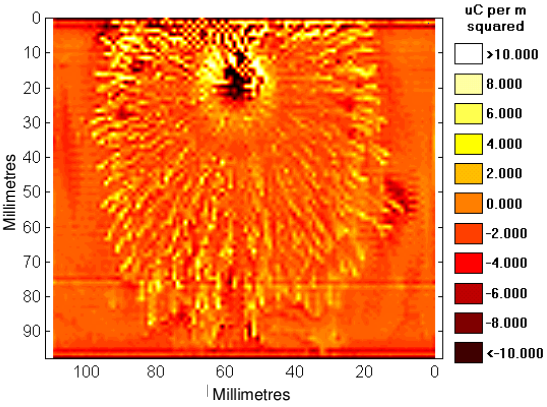

Figure 3.5.10: Surface charge distribution obtained after four +45kVp impulses applied to rod in contact with insulator.

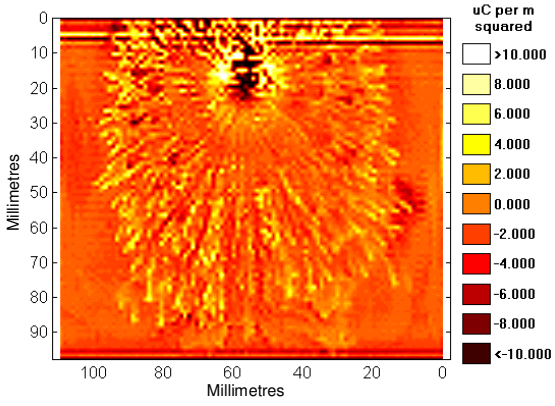

Figure 3.5.11: Surface charge distribution obtained after ten +45kVp impulses applied to rod in contact with insulator.

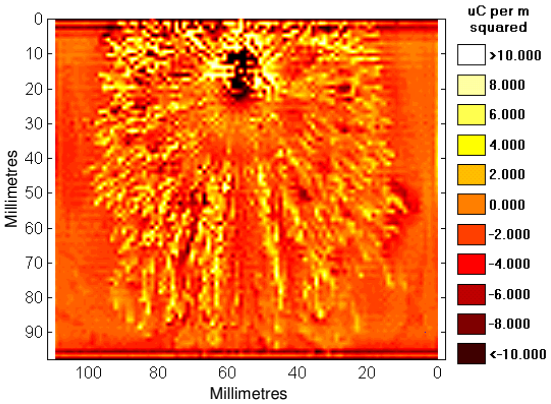

Figure 3.5.12: Surface charge distribution obtained after twenty +45kVp impulses applied to rod in contact with insulator.

Rod-Surface Separation = 5mm

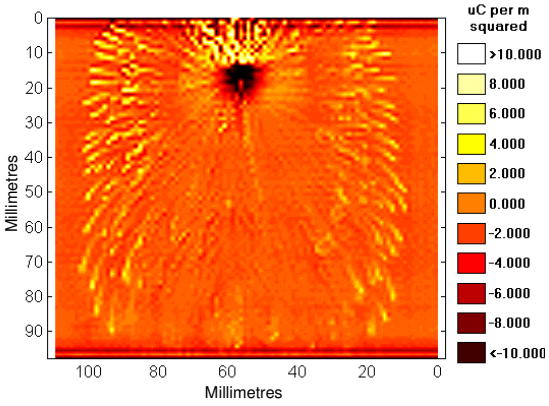

Figure 3.5.13: Surface charge distribution obtained after a single +45kVp impulse applied to rod 5mm from insulator.

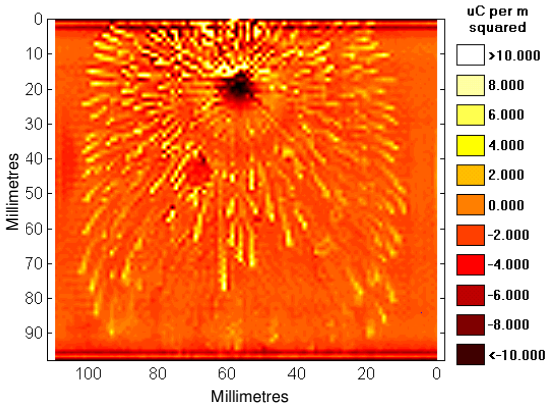

Figure 3.5.14: Surface charge distribution obtained after two +45kVp impulses applied to rod 5mm from insulator.

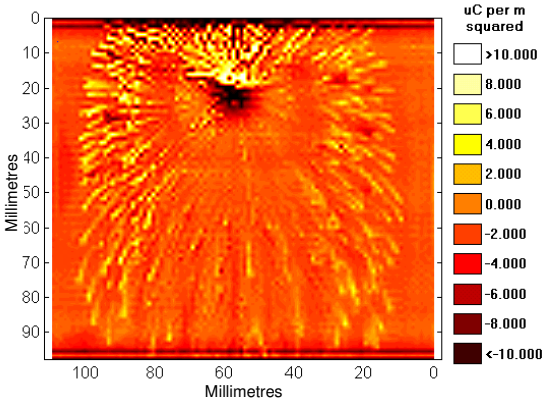

Figure 3.5.15: Surface charge distribution obtained after three +45kVp impulses applied to rod 5mm from insulator.

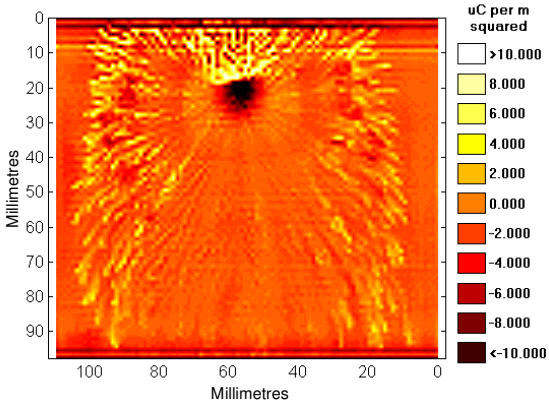

Figure 3.5.16: Surface charge distribution obtained after four +45kVp impulses applied to rod 5mm from insulator.

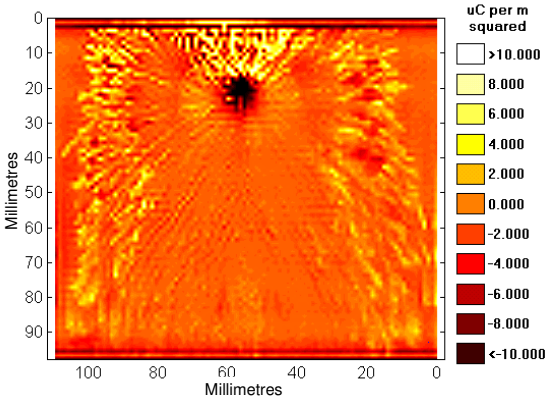

Figure 3.5.17: Surface charge distribution obtained after ten +45kVp impulses applied to rod 5mm from insulator.

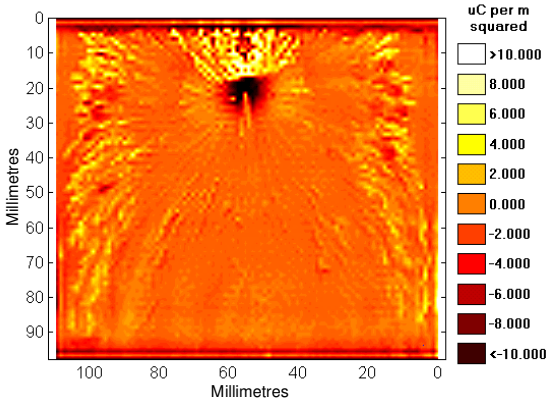

Figure 3.5.18: Surface charge distribution obtained after twenty +45kVp impulses applied to rod 5mm from insulator.

Rod-Surface Separation = 10mm

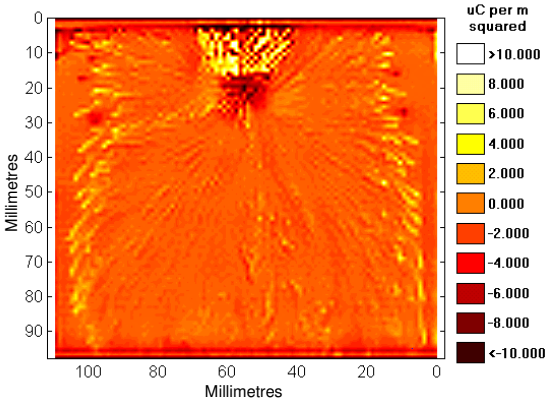

Figure 3.5.19: Surface charge distribution obtained after a single +45kVp impulse applied to rod 10mm from insulator.

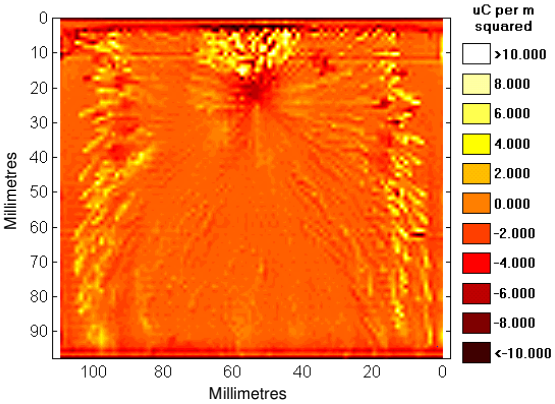

Figure 3.5.20: Surface charge distribution obtained after two +45kVp impulses applied to rod 10mm from insulator.

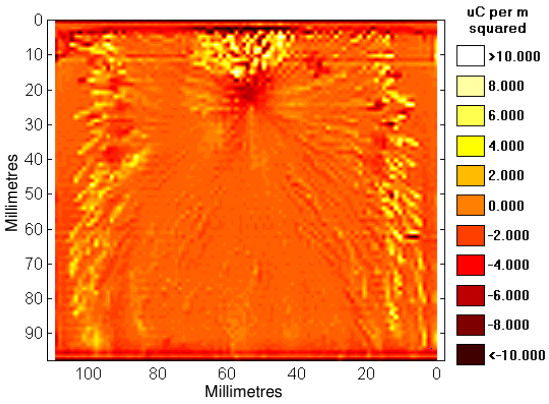

Figure 3.5.21: Surface charge distribution obtained after three +45kVp impulses applied to rod 10mm from insulator.

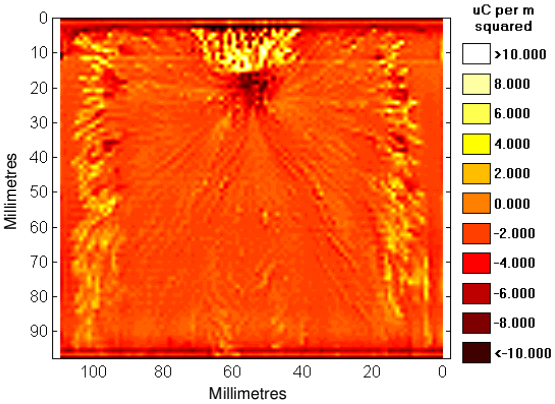

Figure 3.5.22: Surface charge distribution obtained after four +45kVp impulses applied to rod 10mm from insulator.

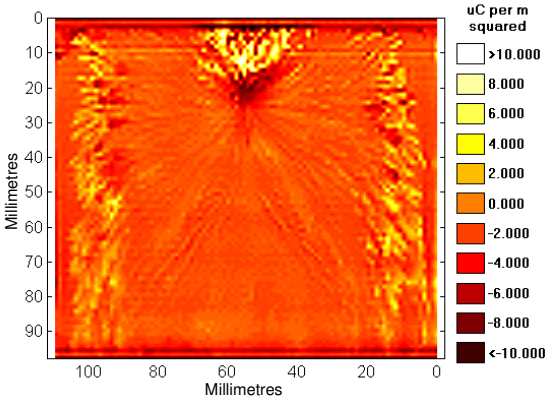

Figure 3.5.23: Surface charge distribution obtained after ten +45kVp impulses applied to rod 10mm from insulator.

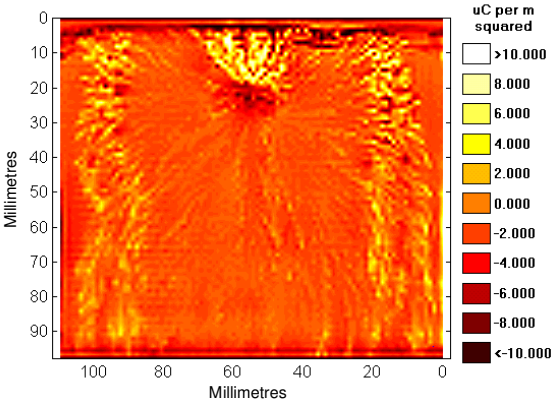

Figure 3.5.24: Surface charge distribution obtained after twenty +45kVp impulses applied to rod 10mm from insulator.

The effect of multiple impulses with the rod in contact with the insulator can be seen in figures 3.5.7, 3.5.8 and 3.5.9. The first discharge sets up the initial distribution on the neutralised insulator, a second very small discharge can be seen to fill the region around the rod left from the first discharge. This second small discharge, with a lower current occurred very early in the applied impulse voltage wave and was partially obscured by noise. The third applied impulse generated a larger discharge that covered the distribution caused by the second. The corresponding three oscilloscope traces are shown in figure 3.5.25. The charge distribution set up by the first discharge distorts the electric field around the rod and affects the next discharge.

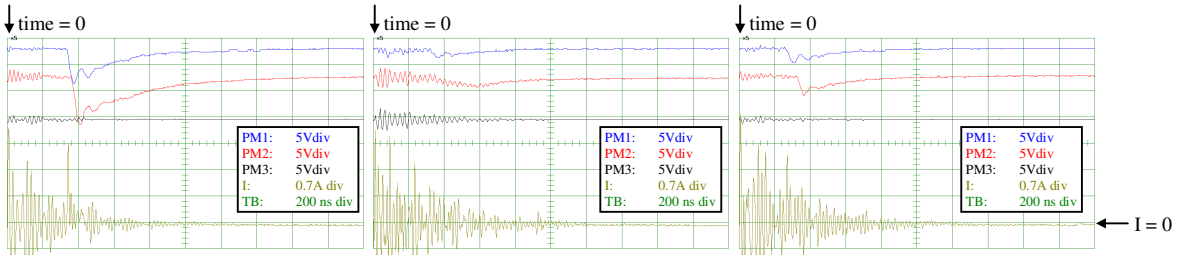

Figure 3.5.25: The first three oscilloscope traces for a rod-surface separation of 0mm.

A similar effect can be seen for the rod 5mm away from the surface in figures 3.5.13, 3.5.14 and 3.5.15. The corresponding three oscilloscope traces are shown in Figure 3.5.26.

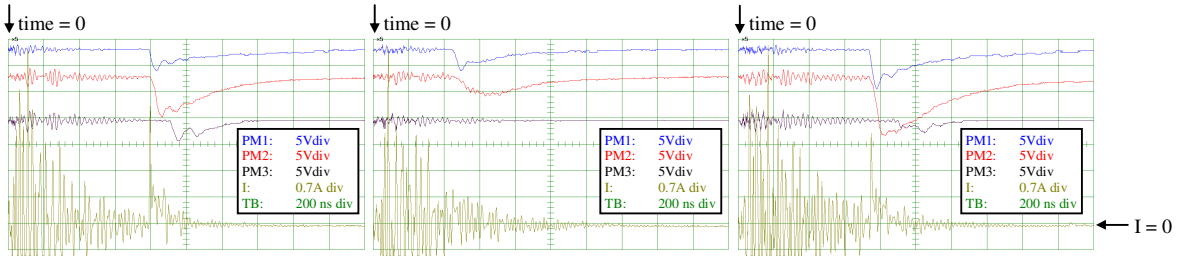

Figure 3.5.26: The first three oscilloscope traces for a rod-surface separation of 5mm.

For the 10mm rod-surface separation this effect was not visible, the first three discharges are of similar magnitude.

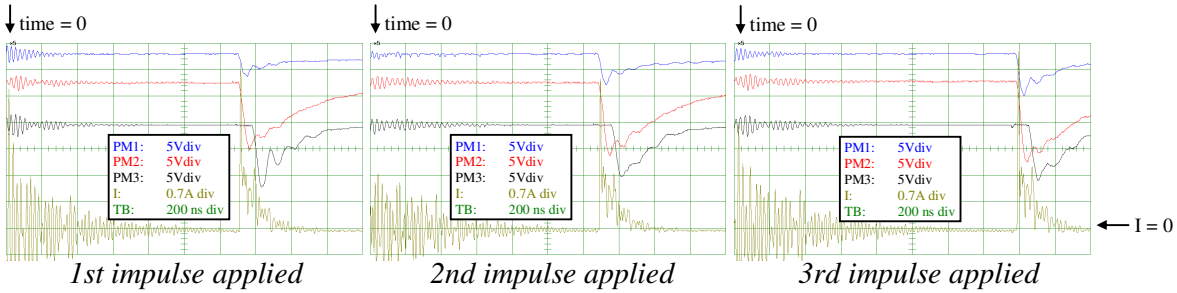

Figure 3.5.27: The first three oscilloscope traces for a rod-surface separation of 10mm.

The effect of moving the rod away from the surface is clearly visible in the surface charge distributions; the streamers propagate further down and around the insulator. It should be remembered that the left and right-hand side of the charge distributions shown is the same point on the insulator surface. The cylindrical insulator surface is effectively unrolled onto the page. When the rod was moved away from the surface the streamers propagated so far around the insulator they almost met on the other side of the insulator. Moving the rod away from the surface resulted in only the streamer tips depositing a significant charge; a region of lower net charge was visible in the middle of the distributions.

The highly charged region directly under the rod became less charged as the rod was moved away from the surface. In all cases a lot of positive charge was deposited in the region of the surface directly above the rod tip. There appear to be positive streamer channels propagating up the insulator surface in the high field between the rod and the surface.

Figures 3.5.28, 3.5.29 and 3.5.30 show the total charge on the insulator surface after each impulse. As the rod was moved further away from the insulator the amount of surface charge deposited decreased.

The graphs on the following pages show the data from each of the 20 discharges measured at each rod-surface separation. The air gap data obtained without the insulator is also shown for comparison. The main gap velocity was not available for the rod in contact with the insulator surface because no streamers could be detected at the ground plane photo-multiplier.

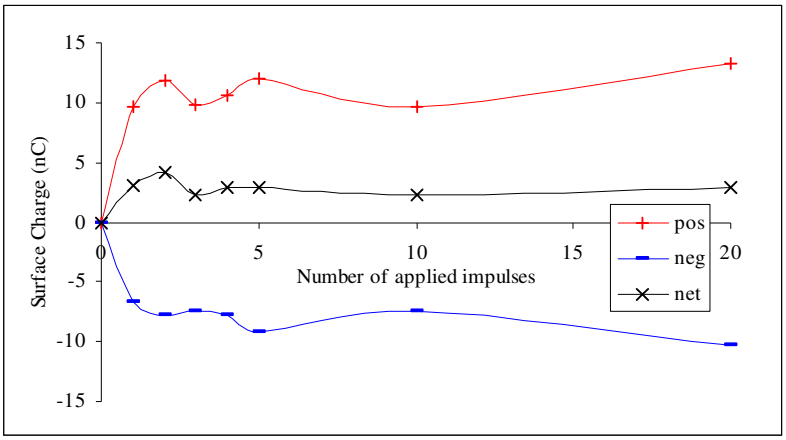

Figure 3.5.28: Surface charge after each shot for the rod in contact with the insulator surface.

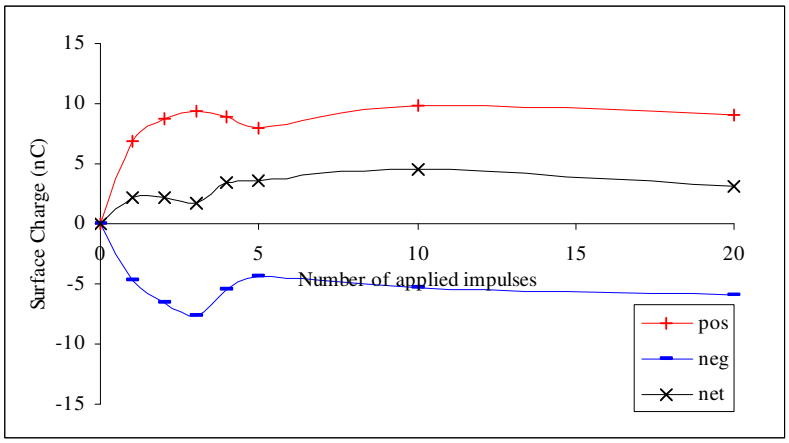

Figure 3.5.29: Surface charge after each shot for the rod 5mm from the insulator surface.

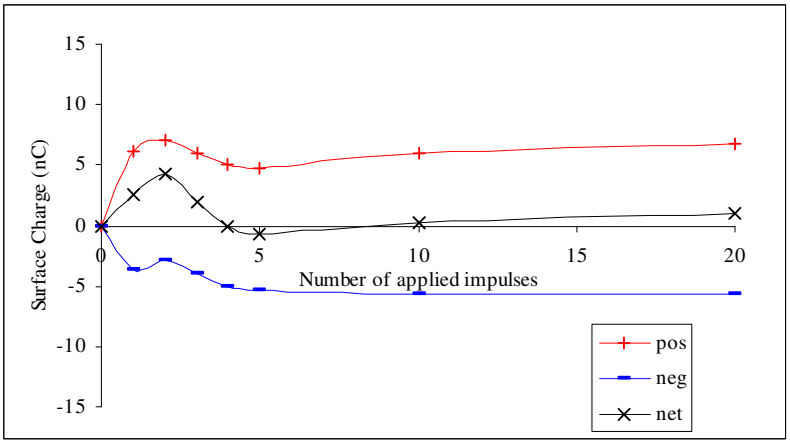

Figure 3.5.30: Surface charge after each shot for the rod 10mm from the insulator surface.

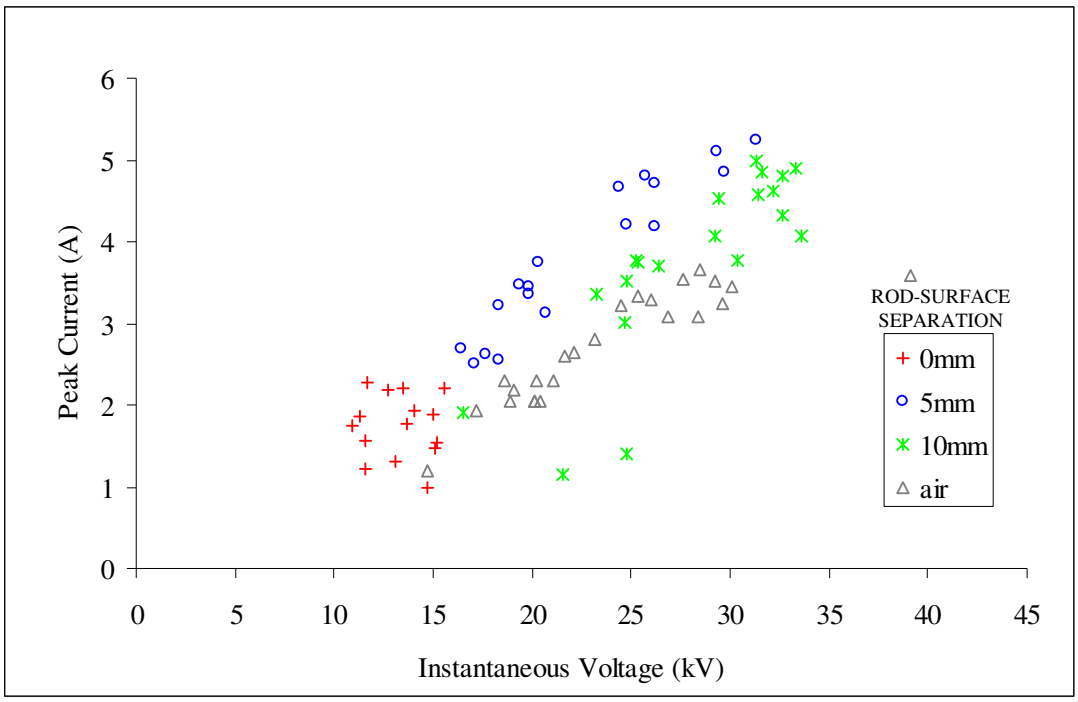

Figure 3.5.31: Variation of peak discharge current with instantaneous voltage.

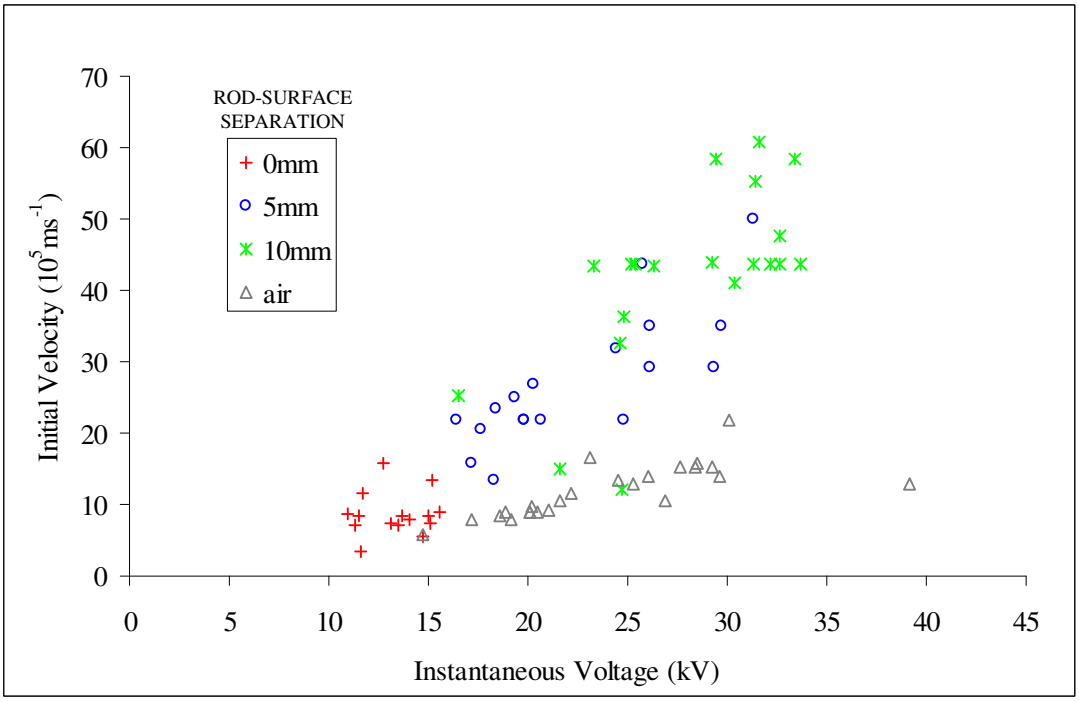

Figure 3.5.32: Variation of initial discharge velocity with instantaneous voltage.

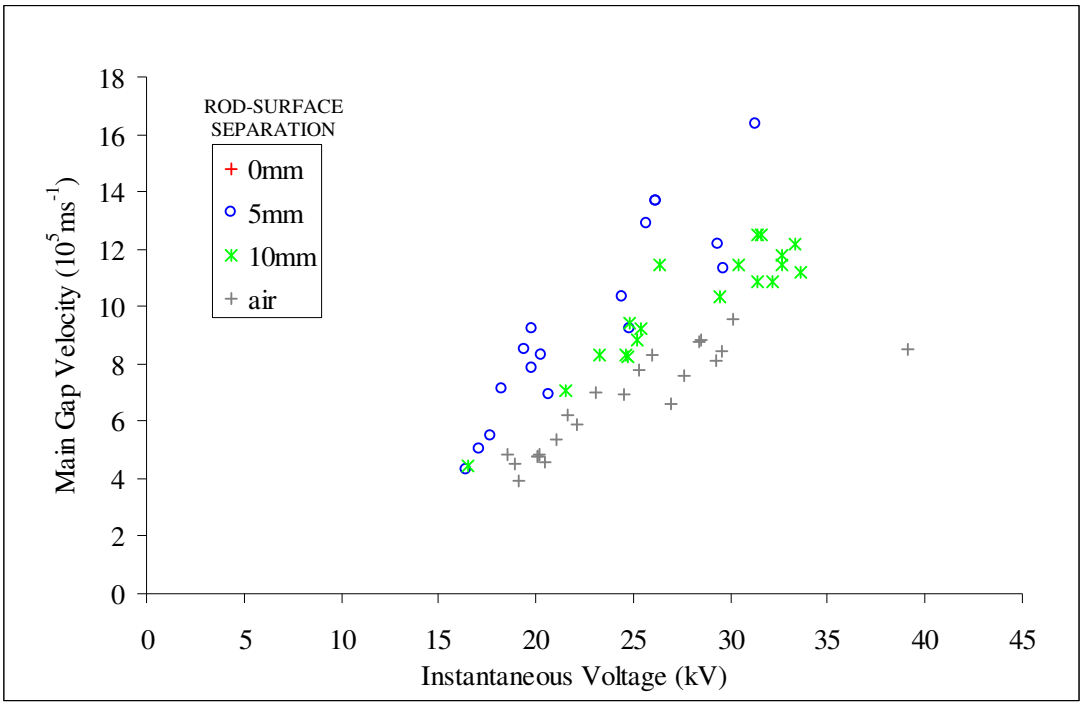

Figure 3.5.33: Variation of main gap velocity with instantaneous voltage.

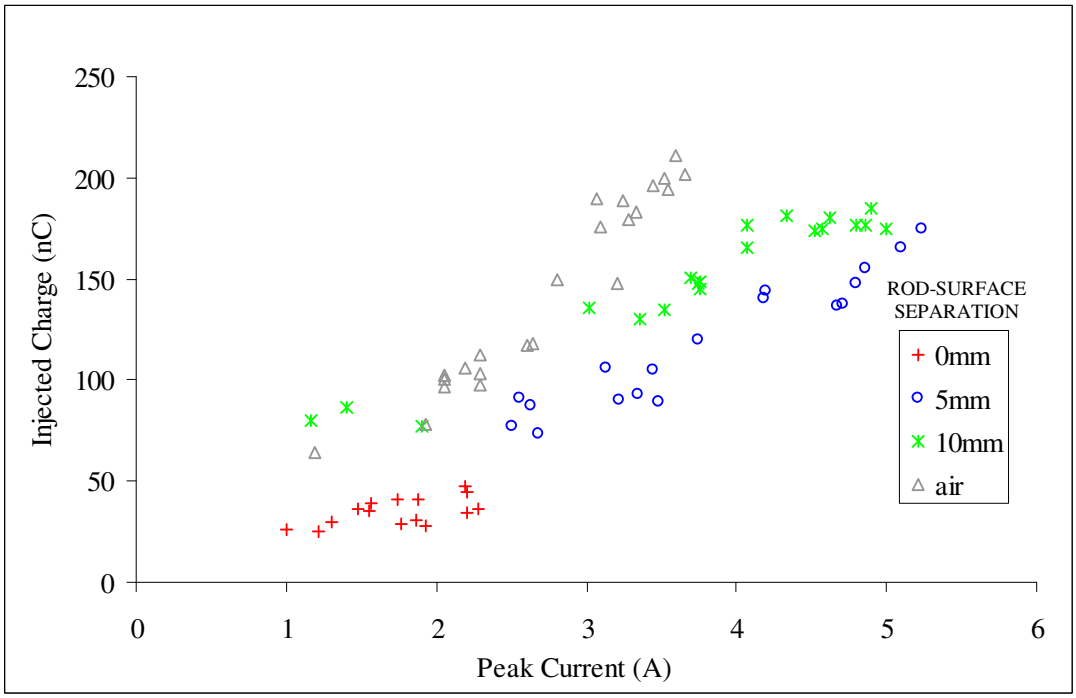

Figure 3.5.34: Variation of injected charge with peak discharge current.

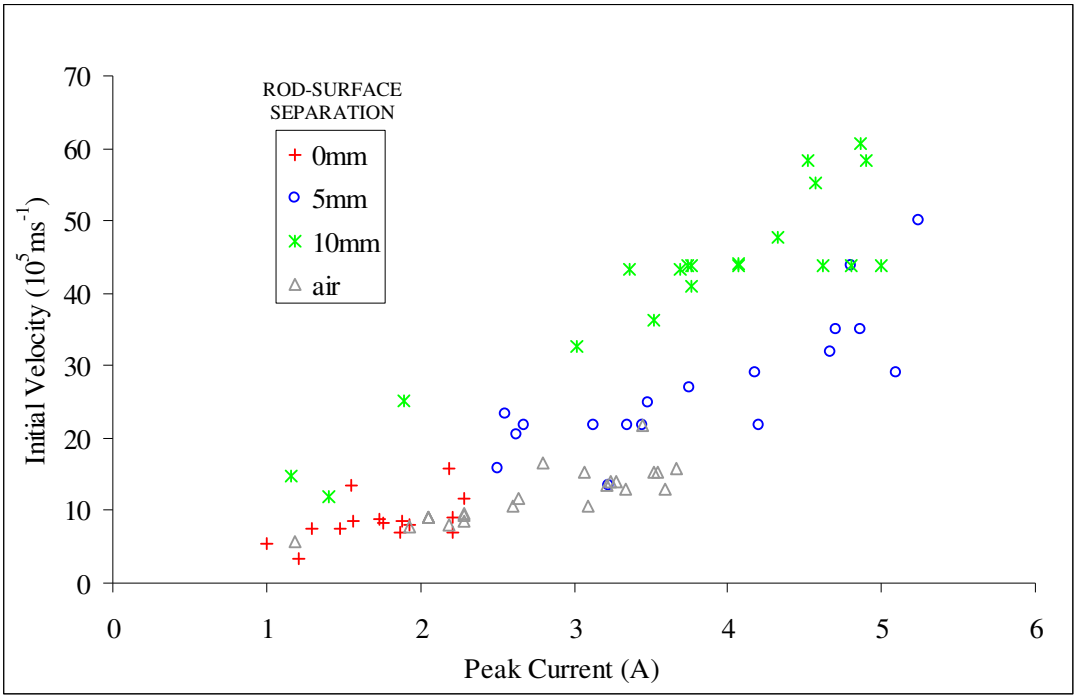

Figure 3.5.35: Variation of initial discharge velocity with peak discharge current.

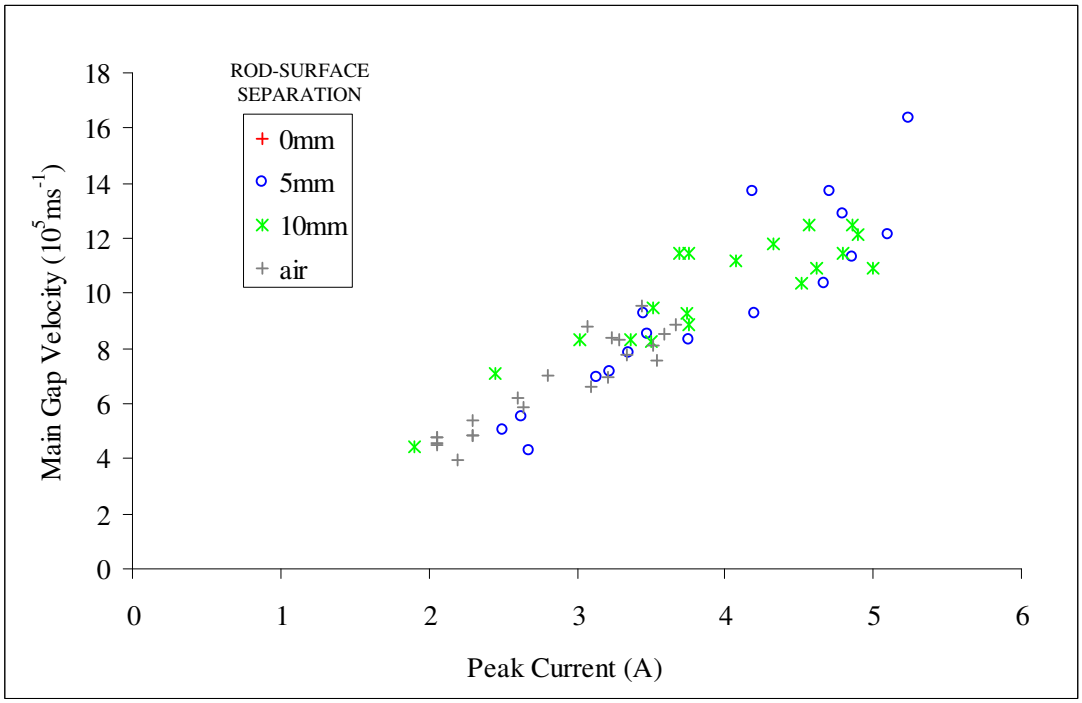

Figure 3.5.36: Variation of main gap velocity with peak discharge current.

The scatter of the data in the graphs on the previous pages is small which indicates that the rod is of a suitable diameter for the gap length.

In general the graphs show that discharges in the presence of the insulator have higher peak currents, inject less charge and travel faster initially than those in air.

It is also important to note that the discharges where the rod was in direct contact with the surface actually had lower peak currents than those in air. Figure 3.5.37 shows the average peak current of the 20 discharges observed at each rod-surface separation plotted against rod-surface separation. The air gap current data is plotted as a rod-surface separation of 100mm, although the distance at which the insulator no longer affects the discharge may be less than this.

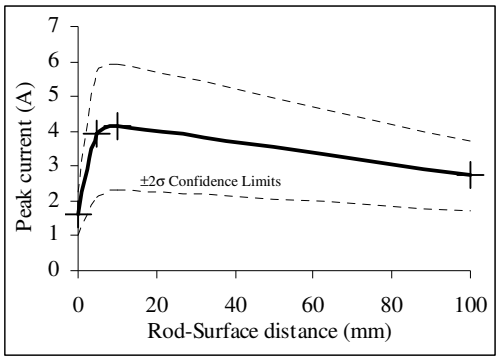

Figure 3.5.37: Average peak discharge current versus rod-surface separation.

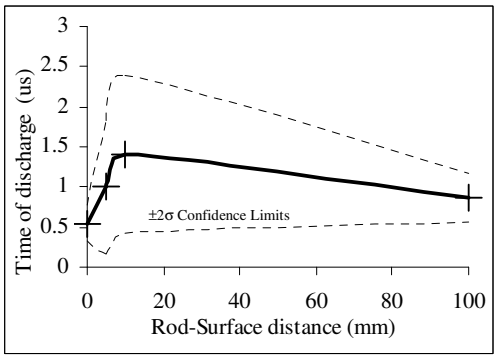

Figure 3.5.38: Average time of discharge versus rod-surface separation.

Figure 3.5.38 shows the time to discharge, as measured from the start of the impulse wave, plotted against rod-surface distance. When the rod is in direct contact with the insulator the very high fields in the triple junction cause the discharge to be initiated at a lower voltage and hence have a lower peak current.

The discharges with the greatest peak current and highest initial velocity actually occurred when the rod was 10mm away from the surface but there was a greater scatter in the values. At this distance the dielectric presence of the insulator only had a small effect on the electric field at the tip of the rod.

The fastest main gap velocities were observed for the 5mm rod-surface separation case, though this difference was only really visible when plotted against instantaneous voltage.

The injected charge versus peak current characteristics shown in figure 3.5.34 indicated that the current waveform changed shape as the rod-surface separation increased.

Figure 3.5.39 shows example current waveforms that had an average peak current for each particular rod-surface separation.

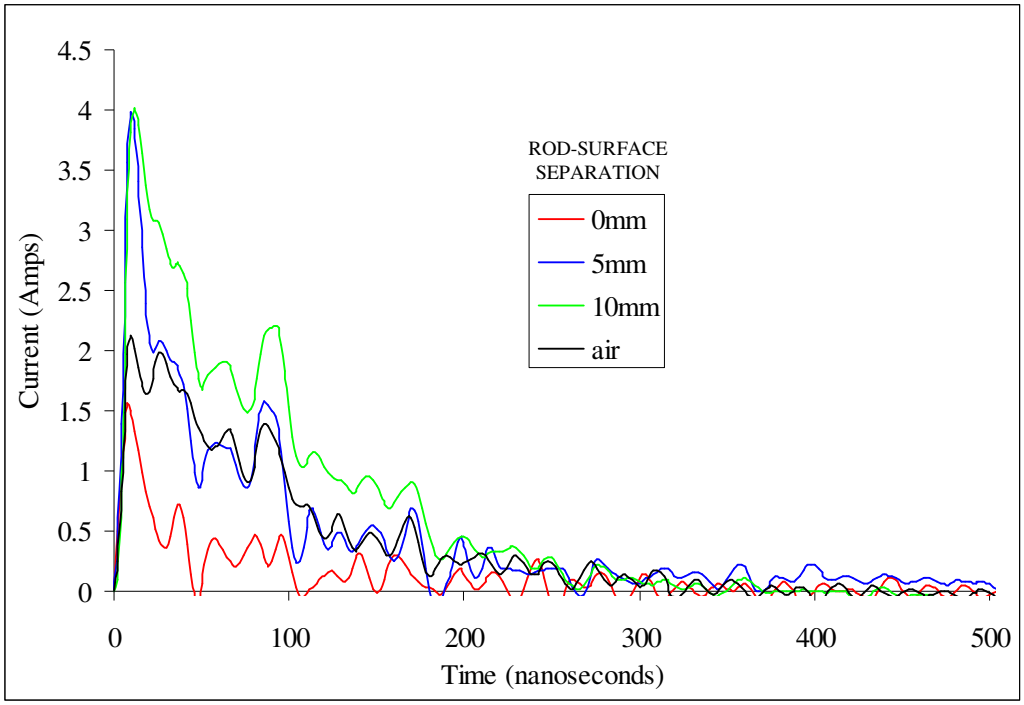

Figure 3.5.39: Typical current waveforms observed for different rod-surface separations.

The presence of the insulator causes the current waveforms to have much faster decay times. Within the time resolution obtainable there was no great difference in the rise time of the discharges.

3.6 Flashover

3.6.1 Introduction

The medium rod has been shown to be of a suitable diameter for the gap length. So far only pre-breakdown discharges have been described. This section studies the flashover of the gap and its effect on the deposited charge distribution.

3.6.2 Set-up

Using the apparatus set-up as shown in figure 3.6.1, the rod axis was positioned at approximately 10° to the vertical in contact with the insulator. Impulses of magnitude +85kVp were applied to the rod using impulse generator No.1. Again PTFE was used as the insulator material.

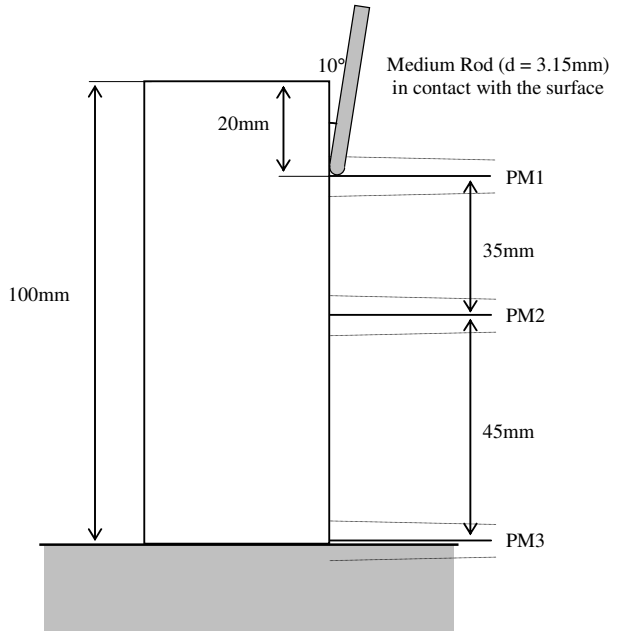

Figure 3.6.1: The apparatus set-up for the medium rod experiments.

The temperature in the laboratory was 19°C. The atmospheric pressure was 760mmHg. The specific humidity was found to be 8.97gm^{-3}.

3.6.3 Results

Rod in contact with surface

Twenty +85kVp impulses were applied to the gap without the insulator present. The gap did not flashover once in the twenty shots. The data obtained followed the trends for the medium rod air gap shown in the previous section.

The neutralised insulator was then put into the gap and nine +85kVp impulses were applied to the rod. The surface was scanned after each impulse. The first applied impulse did not cause the gap to flashover, however all the subsequent shots resulted in flashover. Two different types of flashover were observed as shown in figure 3.6.2.

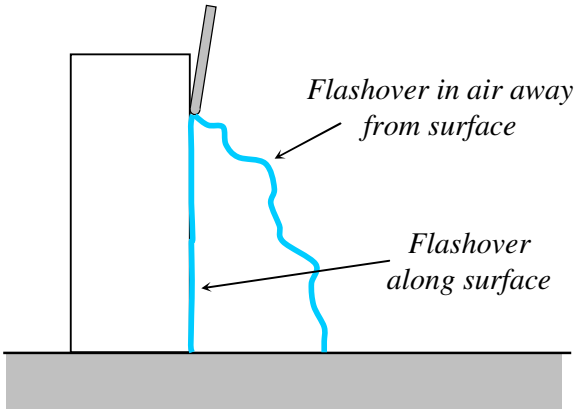

Figure 3.6.2: The two types flashover paths observed.

The two different types of flashover path were clearly detectable with the naked eye. Flashovers away from the surface appeared to propagate out some distance from the surface. Surface flashovers left carbonised track marks on the insulator surface.

The figures on the following pages show the oscilloscope traces for each applied impulse and the resultant surface charge distribution. The type of flashover path observed is also indicated.

Unfortunately the quality of the current signal was quite poor and contained a lot of oscillatory noise. However the isolated photo-multiplier signals provided useful information.

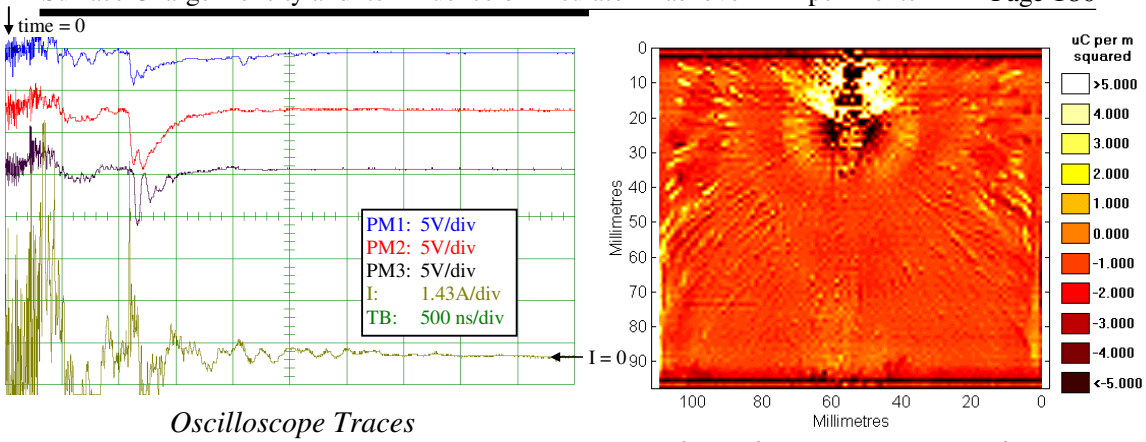

Oscilloscope Traces
No Flashover

Surface Charge Density Distribution

Figure 3.6.3: The oscilloscope traces and deposited surface charge for the first +85kVp impulse.

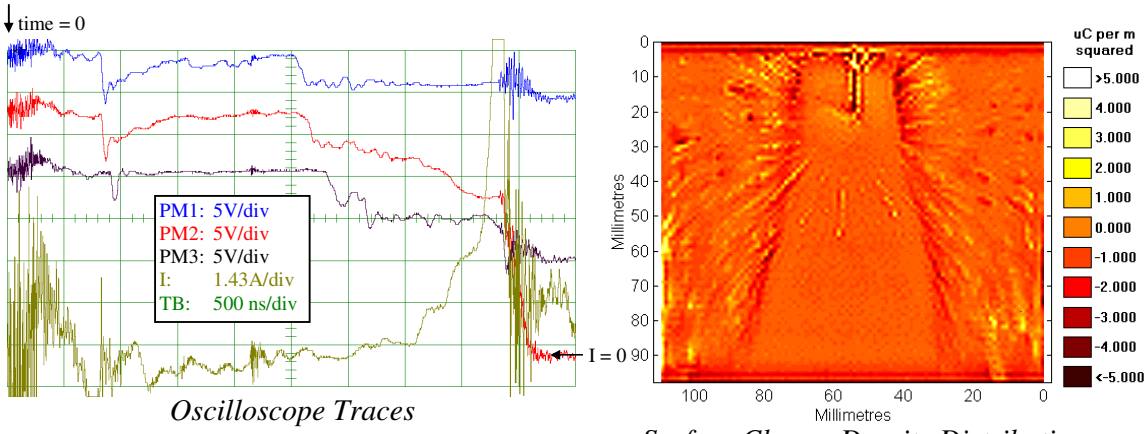

Oscilloscope Traces
Flashover away from surface

Surface Charge Density Distribution

Figure 3.6.4: The oscilloscope traces and deposited surface charge for the second +85kVp impulse.

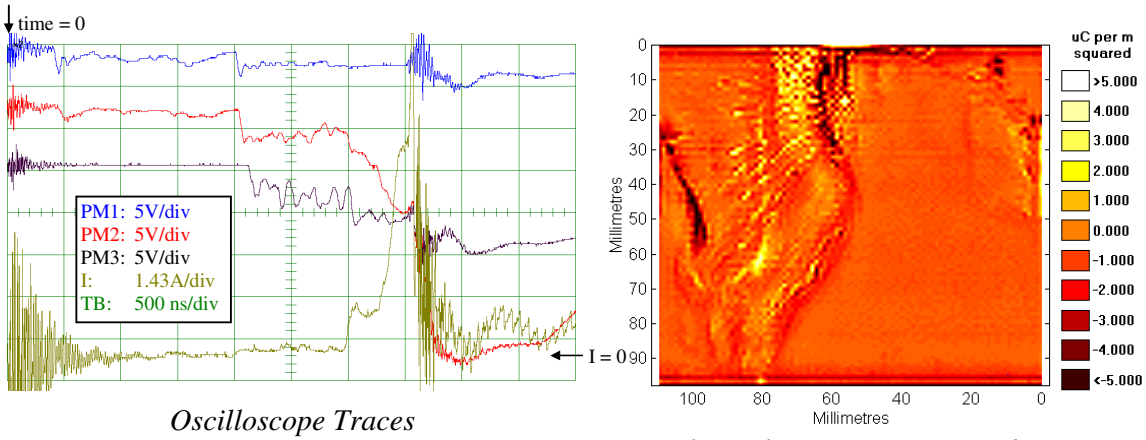

Oscilloscope Traces
Flashover along surface

Surface Charge Density Distribution

Figure 3.6.5: The oscilloscope traces and deposited surface charge for the third +85kVp impulse.

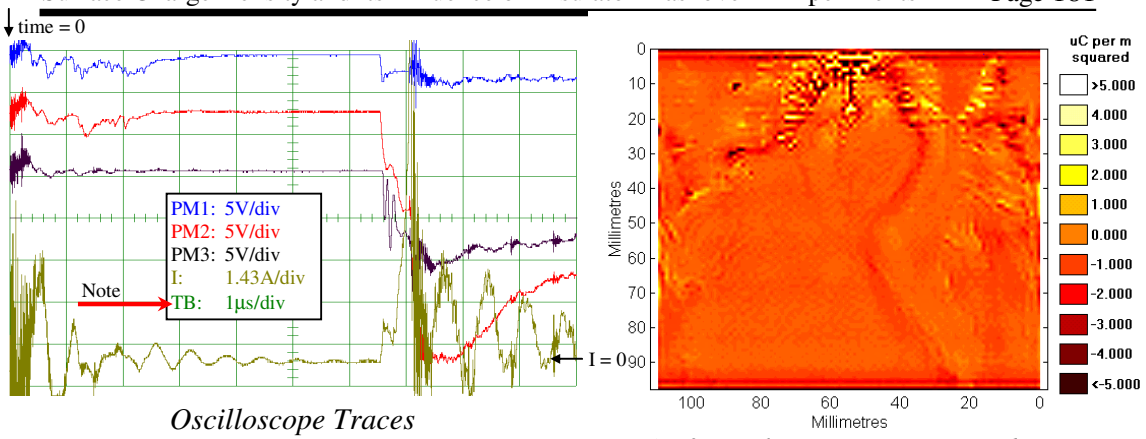

Oscilloscope Traces
Flashover along surface

Surface Charge Density Distribution

Figure 3.6.6: The oscilloscope traces and deposited surface charge for the fourth +85kVp impulse.

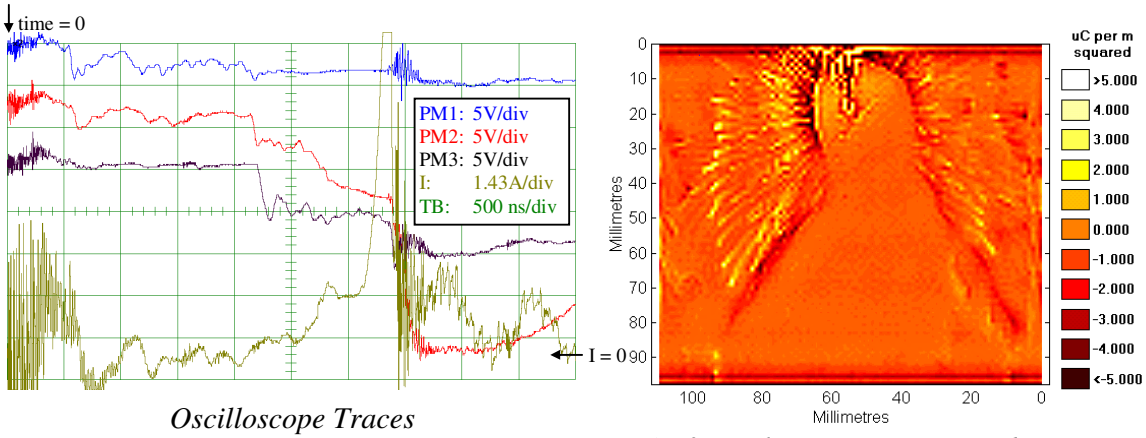

Oscilloscope Traces
Flashover away from surface

Surface Charge Density Distribution

Figure 3.6.7: The oscilloscope traces and deposited surface charge for the fifth +85kVp impulse.

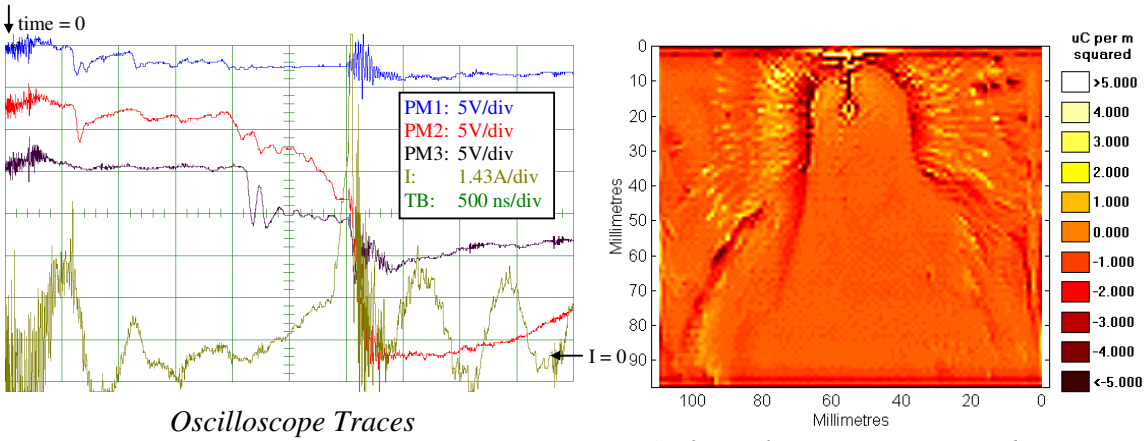

Oscilloscope Traces
Flashover along surface

Surface Charge Density Distribution

Figure 3.6.8: The oscilloscope traces and deposited surface charge for the sixth +85kVp impulse.

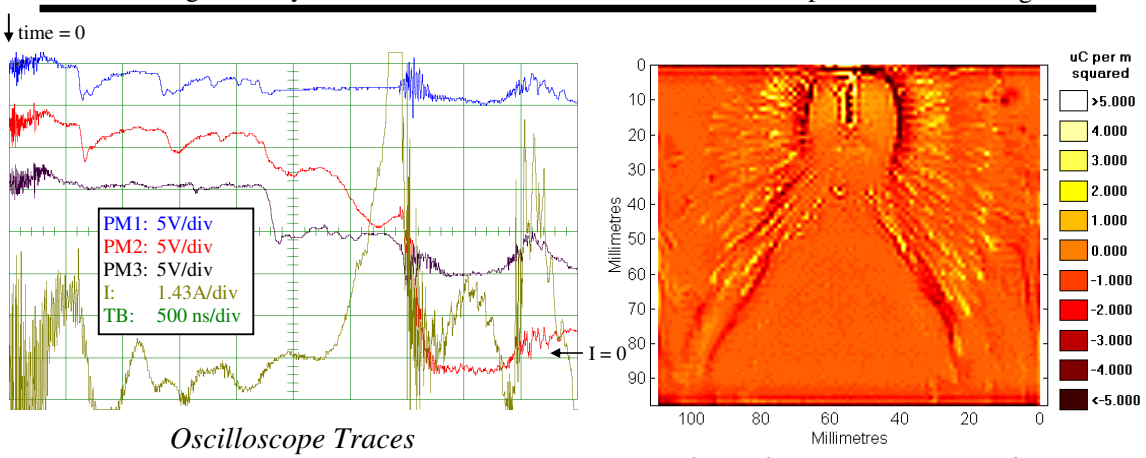

Oscilloscope Traces
Flashover away from surface

Surface Charge Density Distribution

Figure 3.6.9: The oscilloscope traces and deposited surface charge for the seventh +85kVp impulse.

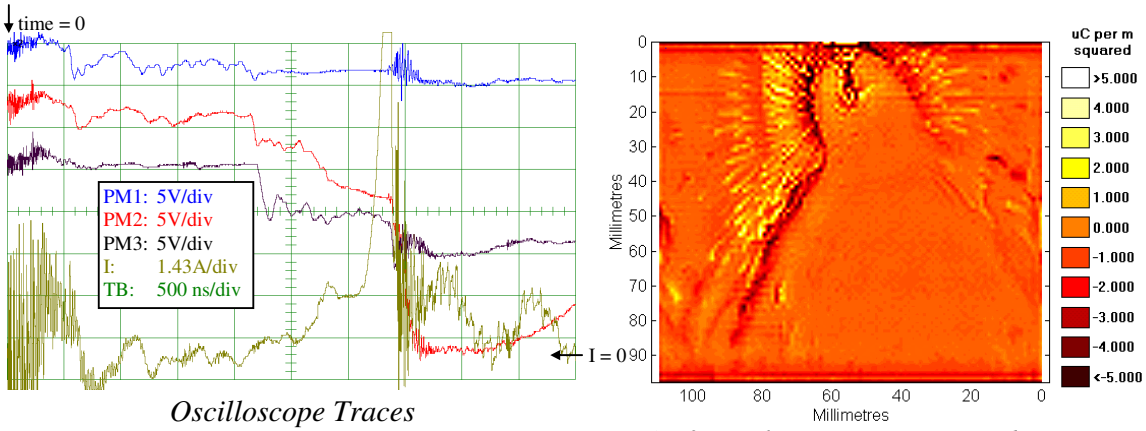

Oscilloscope Traces
Flashover away from surface

Surface Charge Density Distribution

Figure 3.6.10: The oscilloscope traces and deposited surface charge for the eighth +85kVp impulse.

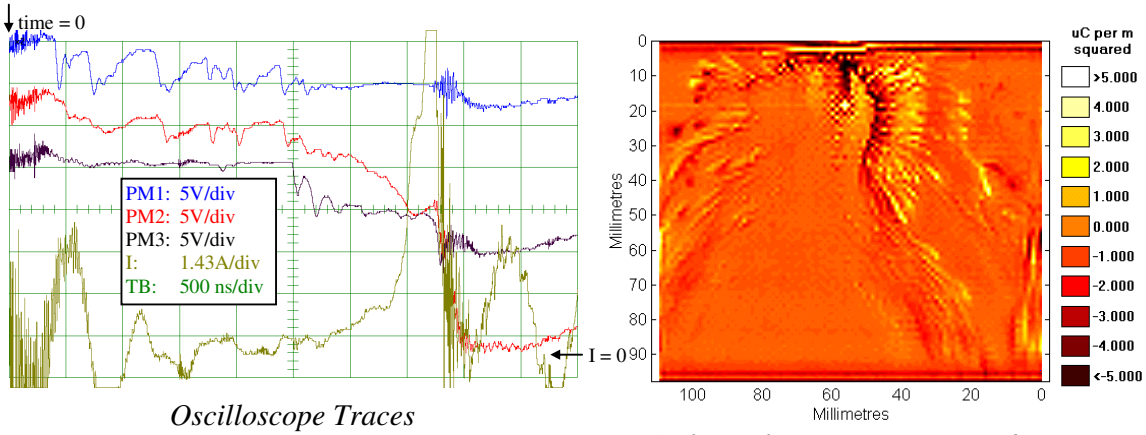

Oscilloscope Traces
Flashover along surface

Surface Charge Density Distribution

Figure 3.6.11: The oscilloscope traces and deposited surface charge for the ninth +85kVp impulse.

The presence of the insulator in the gap obviously lowered the flashover voltage because no flashovers were observed for the same impulse voltage without it.

The effect of flashover on a surface charge distribution was to cut a neutralised swathe through the distribution. The scanning system could not detect any charge in the region left by the flashover. Figure 3.6.12 shows a horizontal slice through a distribution after breakdown. The neutralised region can be seen between 38mm and 78 mm, regions of negative charge border it.

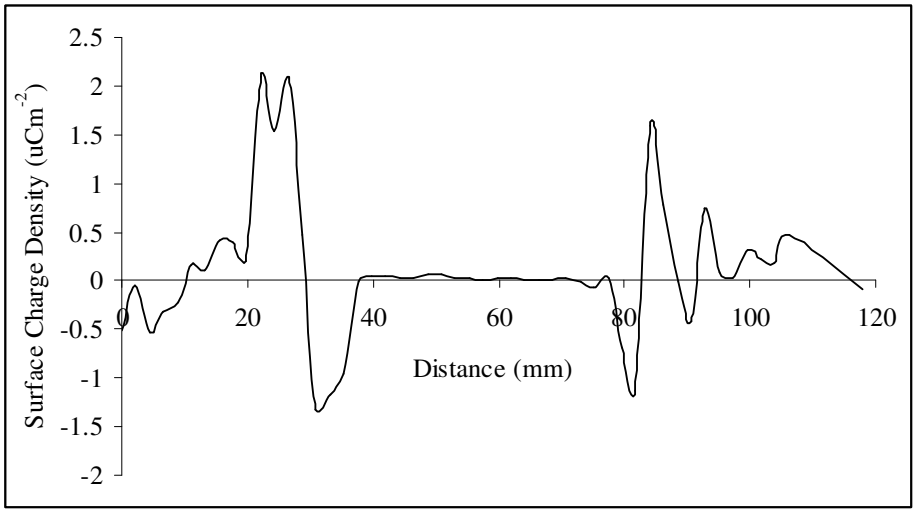

Figure 3.6.12: A horizontal slice at 60mm through the charge distribution for the seventh shot (as shown in figure 3.6.9).

The most interesting point was that the neutralised regions had distinct boundaries. This was surprising because of the widths of the neutralised regions involved; over half of the circumference of the insulator. The arc channel itself was very much thinner than this. The neutralised region became wider near the ground plane and often meandered down the insulator with slowly curving boundaries.

Figure 3.6.13 shows the charge distribution generated by the first impulse (shown in figure 3.6.3) applied to the rod, the charge density scale has been increased to $\pm 20 \mu Cm^{-2}$ to illustrate the charge distribution around the rod clearly. The total charge deposited on the whole surface comprised of +5.3nC and –9.7nC of charge resulting in a net overall negative charging of the surface of –4.4nC. The highly charged region around the rod comprised of +3.5nC and –3.5nC, a significant proportion of the total surface charge. Charge densities of up to $\pm 50 \mu Cm^{-2}$ were observed in the region around the rod.

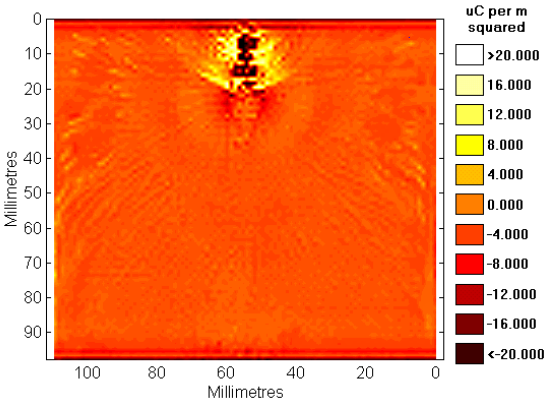

Figure 3.6.13: Charge distribution left after impulse applied without flashover (NOTE: charge density scale increased to illustrate region around rod).

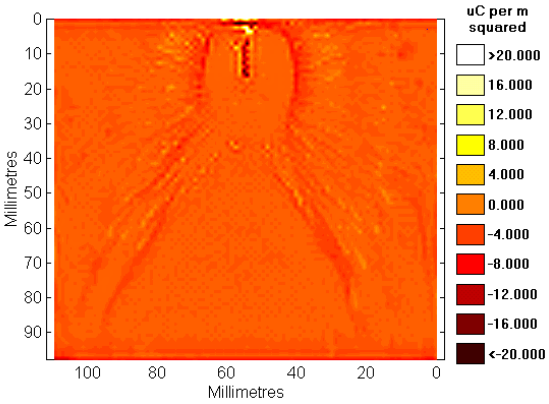

Figure 3.6.14: Charge distribution left after impulse applied with flashover (NOTE: charge density scale increased to illustrate region around rod).

The small region directly under the rod was highly negatively charged, a region of positive charge then surrounded this. This pattern of surface charging directly under and around the rod was also observed in all the previous experimental sections.

Figure 3.6.14 shows the charge distribution after a flashover on the same charge density scale, the region around the rod was still the most charged part on the surface. The charge is confined to a region directly under the rod with peak densities of ±20μCm-2. The total charge in this region comprised of only +0.15nC and –0.20nC which gave a small net negative charge. The charge distribution left under the rod was very similar for all the gap flashover cases. Flashover appears to remove most of the positively charged region around the rod. The negatively charged region directly under the rod remains but is reduced in magnitude.

Rod 5mm away from the surface

For comparison the rod surface distance was increased to 5mm and two +85kVp impulses were applied to a neutralised insulator. The first impulse did not cause the gap to flashover. The oscilloscope traces and resulting charge distribution are shown in figure 3.6.15.

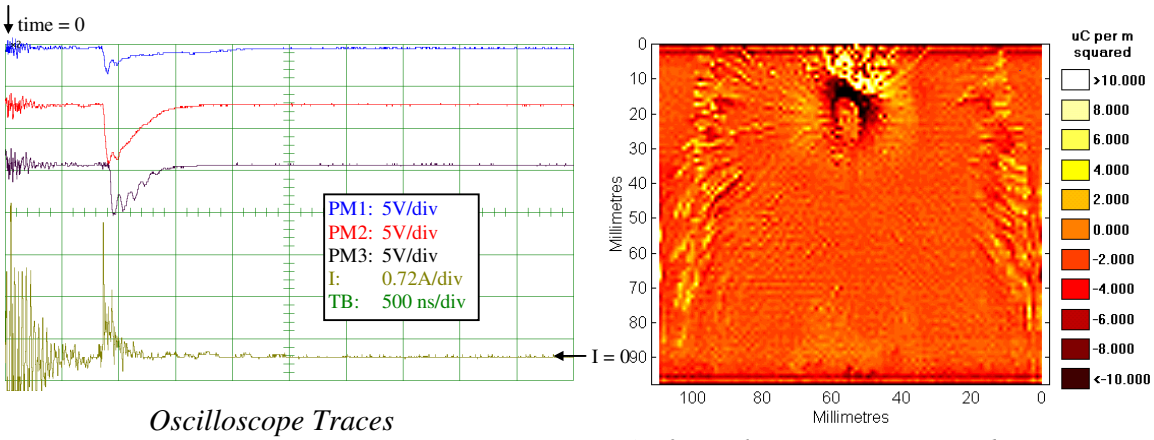

Oscilloscope Traces
No Flashover

Surface Charge Density Distribution

Figure 3.6.15: Oscilloscope traces and deposited surface charge after a single +85kVp impulse applied to the rod 5mm away from the surface.

The second applied impulse caused the gap to flashover away from the surface. The oscilloscope traces and surface charge distribution are shown in figure 3.6.16. The neutralised region extended to the area under the rod.

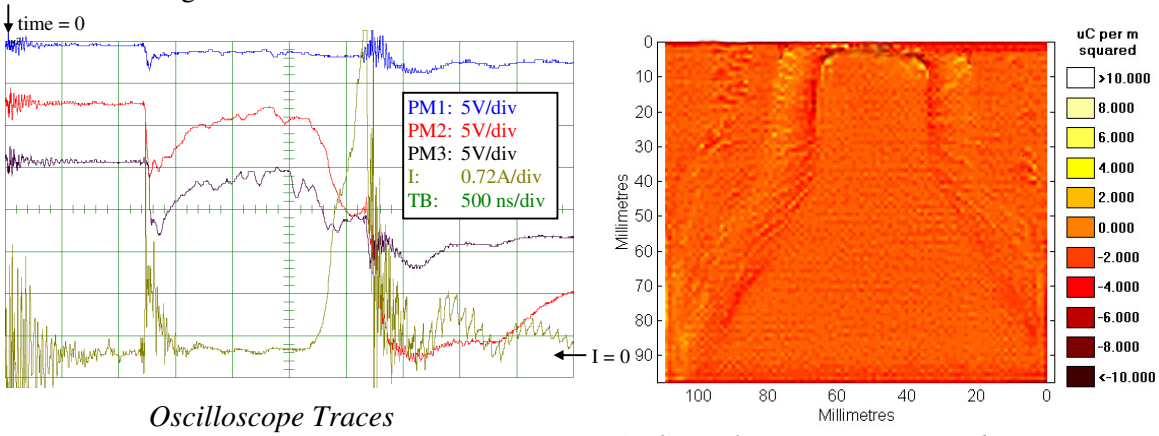

Oscilloscope Traces
Flashover away from surface

Surface Charge Density Distribution

Figure 3.6.16: Oscilloscope traces and deposited surface charge after a second +85kVp impulse applied to the rod 5mm away from the surface.

Rod 10mm away from the surface

The insulator was again neutralised and the rod-surface separation was increased to 10mm. This time ten +85kVp impulses were applied to the rod, none of which caused the gap to flashover. Typical oscilloscope traces are shown in figure 3.6.17. The surface charge density distribution obtained after the ten impulses had been applied is shown in figure 3.6.18.

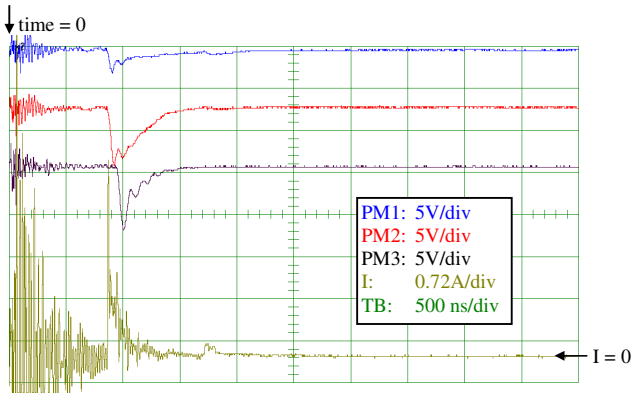

Figure 3.6.17: Example oscilloscope traces for a +85kVp impulse applied to the rod 10mm away from the surface.

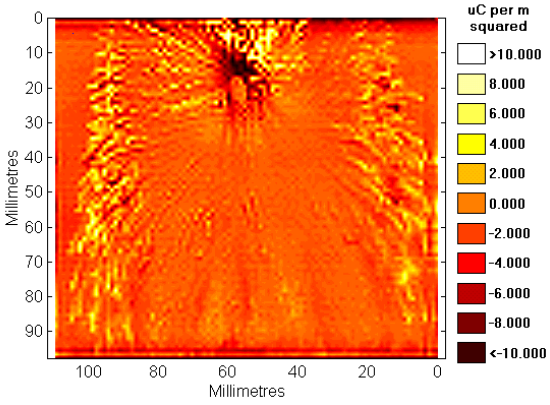

Figure 3.6.18: Surface charge density distribution obtained after ten +85kVp impulses applied to the rod 10 mm away from the surface.

3.7 Other Test Voltages

3.7.1 Introduction

This section contains example charge distributions caused by different types of test voltage. This section is in no way comprehensive; it merely offers an overview of the type of charge distributions generated.

3.7.2 Negative Impulses

Negative impulse voltages were applied using impulse generator No.2, to the rod to generate negative streamers. The electrodes were set up as shown in figure 3.7.1. PTFE was used as the insulator material. No current or photo-multiplier measurements were taken. Four –70.6kVp impulses were applied to the rod; the surface was neutralised before each impulse. After each impulse the surface was scanned, the resulting surface charge distributions and calculated total charge are shown in figures 3.7.2 to 3.7.5.

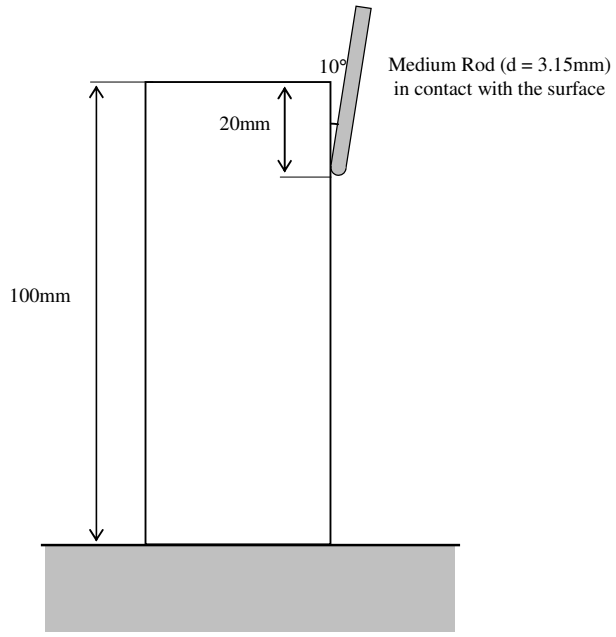

Figure 3.7.1: The apparatus set-up for the miscellaneous test voltage experiments.

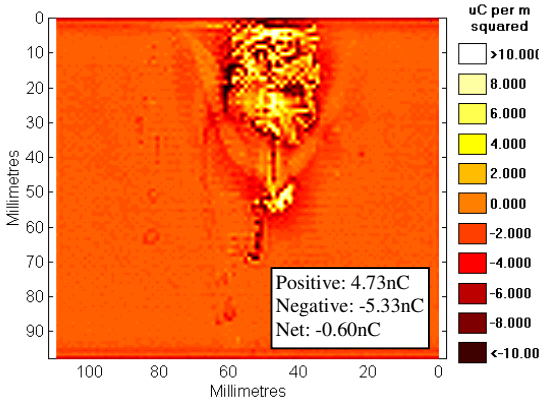

Figure 3.7.2: Surface Charge Deposited after a single –70.6kVp impulse applied to the rod (Surface Initially Neutralised)

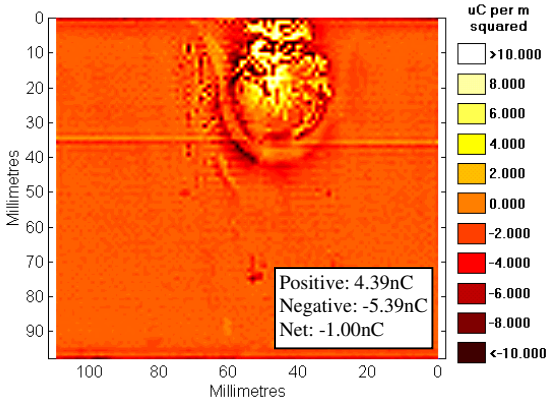

Figure 3.7.3: Surface Charge Deposited after a single –70.6kVp impulse applied to the rod (Surface Initially Neutralised)

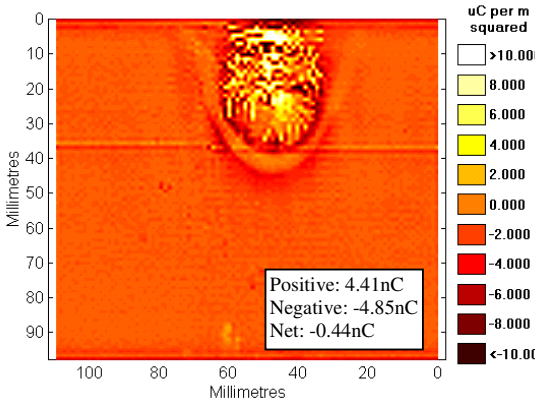

Figure 3.7.4: Surface Charge Deposited after a single –70.6kVp impulse applied to the rod (Surface Initially Neutralised)

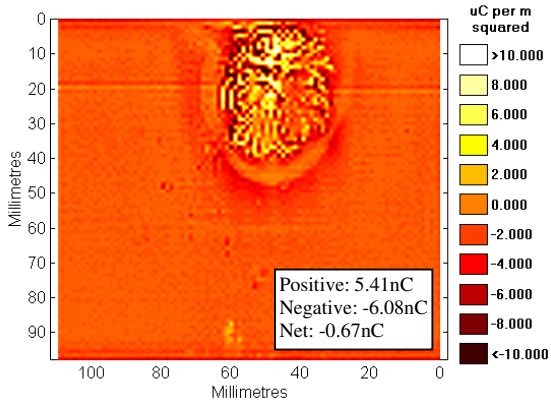

Figure 3.7.5: Surface Charge Deposited after a single –70.6kVp impulse applied to the rod (Surface Initially Neutralised)

The surface charge density distributions obtained were obviously very different from the positive corona cases studied in the previous sections. The region in which most of the charge was deposited was very clearly defined. Within that region very high surface charge densities of up to $20\mu Cm^{-2}$ were observed. A slice through one of the distributions is shown in figure 3.7.6. The amount of charge deposited for each shot was very similar with an overall net negative surface charge.

The general shape of each negative corona charge distribution was very similar, except in figure 3.7.2 where a charged channel has been created beyond the localised region of charge. This could be evidence of a breakdown channel beginning to form.

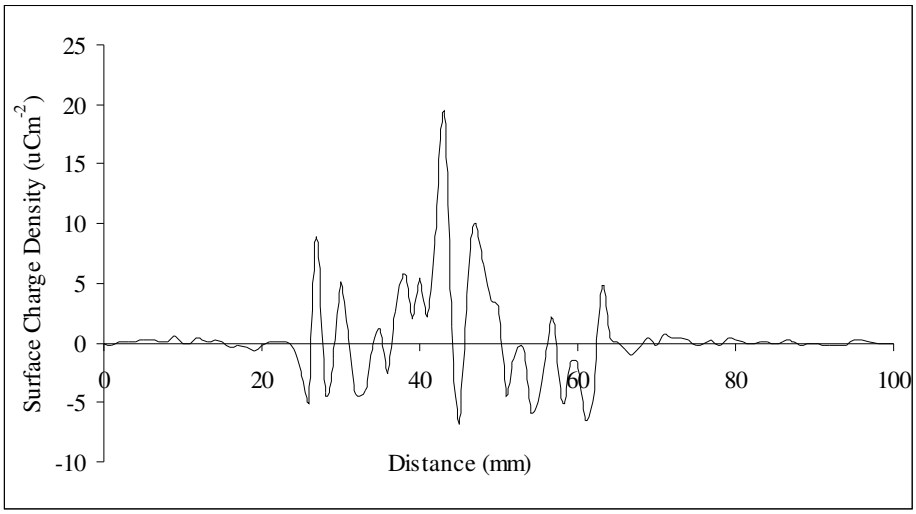

Figure 3.7.6: A horizontal slice at 20mm through the charge distribution shown in figure 3.6.3.

3.7.3 Direct Voltages

Using the same electrode set-up as for the negative impulses, positive and negative DC voltages were applied to the rod using a Brandenburg Generator. The voltages used were ±15kV and ±30kV DC, each of the four different voltages were applied for 1 minute to an initially neutralised insulator. After each application of the test voltage the surface was scanned. The obtained surface charge distributions are shown in figures 3.7.7 to 3.7.10.

At +15kV DC only a small region of positive surface charge was generated. At –15kV DC no significant surface charging occurred.

At +30kV DC corona discharge from the rod was audible. Figure 3.7.8 shows the obtained charge distribution, the surface exhibited charging in several regions. Positive streamer channels can be seen emanating from the tip of the rod.

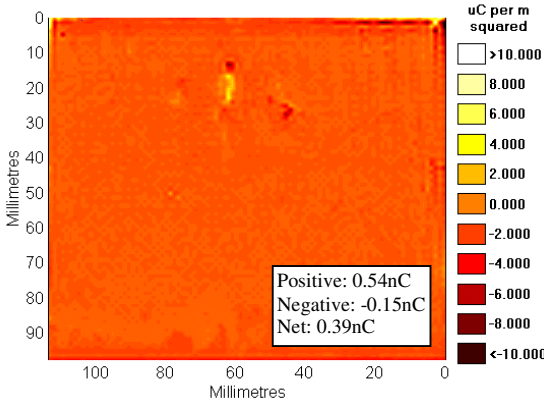

Figure 3.7.7: Surface charge deposited after +15kV DC applied to the rod for 1minute.

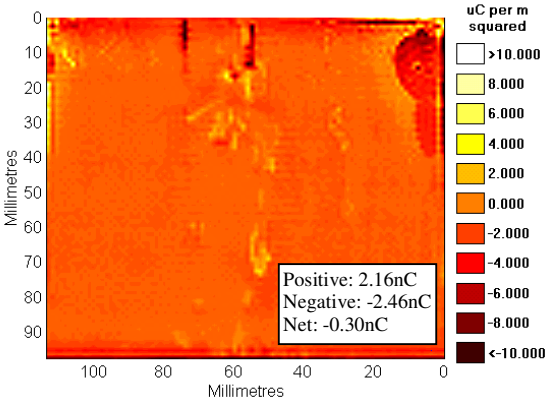

Figure 3.7.8: Surface charge deposited after +30kV DC applied to the rod for 1minute.

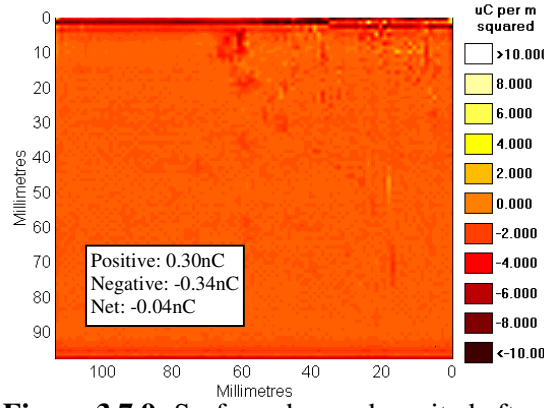

Figure 3.7.9: Surface charge deposited after -15kV DC applied to the rod for 1minute.

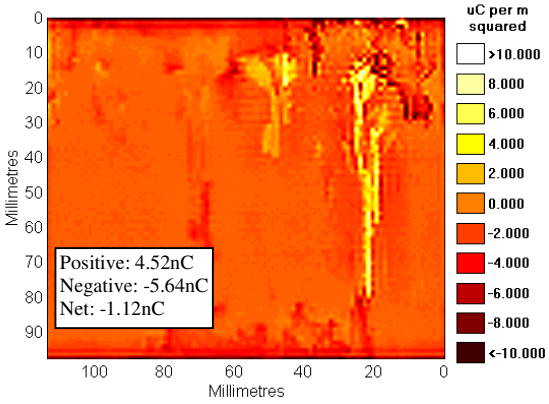

Figure 3.7.10: Surface charge deposited after -30kV DC applied to the rod for 1minute.

The corona activity was also audible at –30kV DC, the resulting charge distribution is shown in figure 3.7.10. Positive channels of charge were observed some distance away from the rod. The charged regions were centred around very small irregularities and manufacturing defects on the surface of the insulator. This effect is also observed in a later section on stressed charge decay, where a surface charge distribution is subjected to a DC field for a length of time.

3.7.4 Alternating Voltages

Using the same electrode set-up as before a transformer was used to supply 50Hz alternating voltages to the rod for 1 minute, at the end of that minute the voltage was switched off abruptly without first lowering the voltage. Two test voltages of 15kVrms and 30kVrms were used. Prior to application of each test voltage the insulator surface was neutralised.

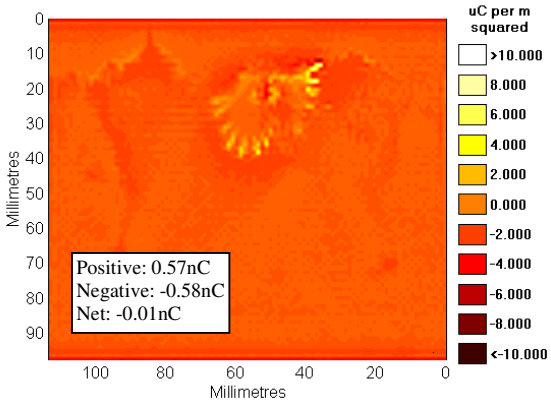

Figure 3.7.11: 15kVrms ac applied for 1 minute then abruptly switched off.

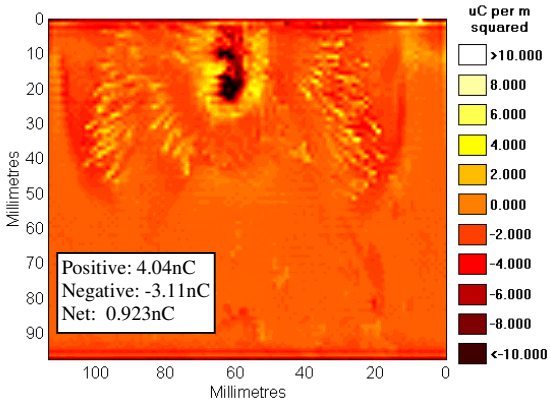

Figure 3.7.12: 30kVrms ac applied for 1 minute then abruptly switched off.

Figures 3.7.11 and 3.7.12 show the charge deposited after 15kVrms and 30kVrms respectively were applied to the rod. Significantly more charge was deposited at the higher voltage. Individual streamer channels are clearly visible.

The alternating voltage caused discharges of opposite polarities on each half cycle of the ac waveform. The voltage was abruptly switched off so the resultant surface charge distribution will be mainly comprised of the last discharge to occur.

For comparison the experiment was repeated at 30kVrms but this time the voltage was slowly reduced to zero over about 10 seconds. The resulting surface charge distribution is shown in figure 3.7.13. The charge deposited was much smaller than when the test voltage was abruptly removed. The distribution obtained appeared to be created by a small positive discharge. This can be explained as follows; as the voltage is slowly lowered the rod continues to produce smaller and smaller discharges, until the corona extinction voltage is reached at which point no further corona activity occurs and the surface is left with the charge distribution generated by the last discharge. In the rod-plane electrode configuration, negative corona inception and extinction voltages are

greater than positive ones when the voltage is applied to the rod. Thus as the voltage is lowered the rod will stop producing discharges on the negative half cycle before the positive half cycle as shown in figure 3.7.14.

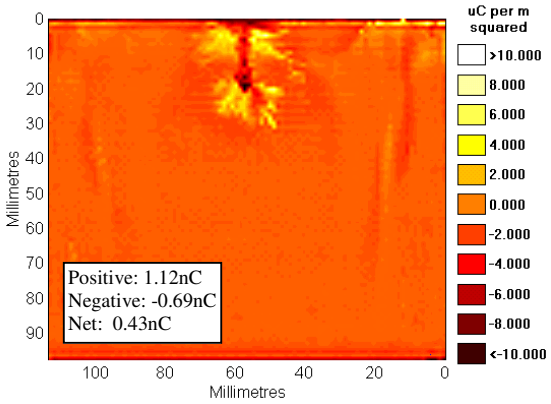

Figure 3.7.13: 30kVrms ac applied for 1 minute then slowly lowered.

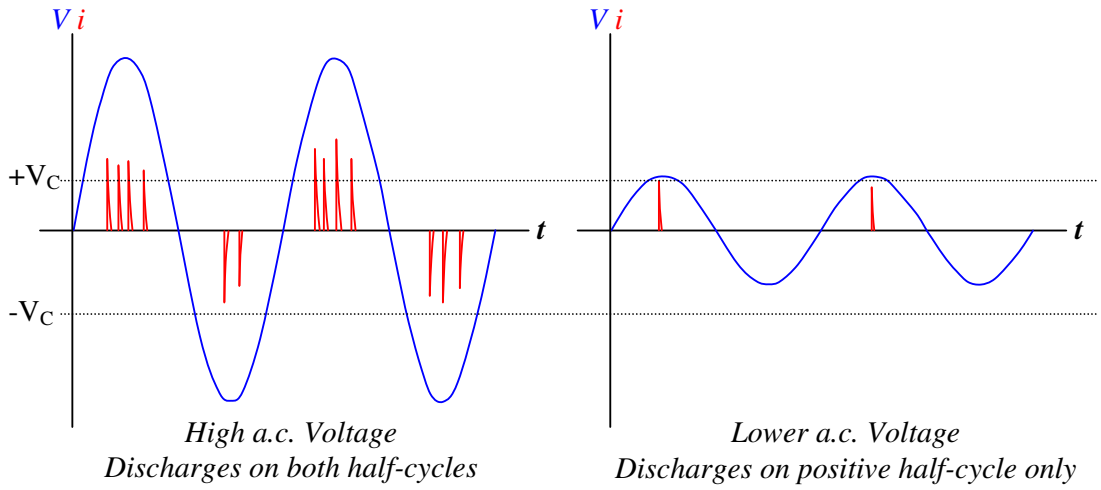

Figure 3.7.14: Voltage and current waveforms for an alternating voltage applied to the rod

3.8 Other Materials

3.8.1 Introduction

All the work so far has studied surface charge on pure white PTFE. It's excellent ability to hold surface charge made it the ideal test object for the development of the scanning system. PTFE is also commonly used in many high voltage applications including circuit breaker nozzles.

Various other materials were investigated to a limited extent. This section shows some of the measurements taken on different materials. Study focused on materials upon which the scanning system could detect charge.

3.8.2 Set-up

Identical sized insulator specimens were available as 40mm high, 40mm diameter cylinders. The electrodes were set up as shown in figure 3.8.1. The rod-plane gap was reduced to 38mm so that the tip of the rod just touched the top of the insulator. Positive 26.6kVp impulses were applied to the rod using impulse generator No.2.

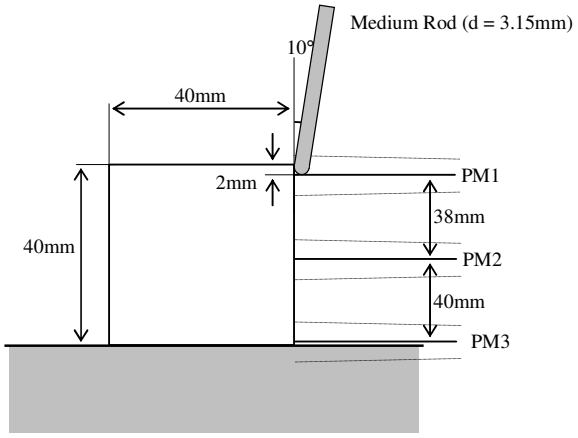

Figure 3.8.1: The apparatus set-up for the different material experiments.

The atmospheric conditions in the laboratory were 19.0°C and 767mmHg. The specific humidity was $10.3gm^{-3}$.

3.8.3 Air

Prior to putting an insulator in the gap ten +26.6kV impulses were applied to the gap. On each impulse only one discharge was observed, each discharge occurred near the peak of the impulse wave shape. Figure 3.8.2 shows a typical oscilloscope trace, the discharge just crossed the gap. The other oscilloscope traces were very similar.

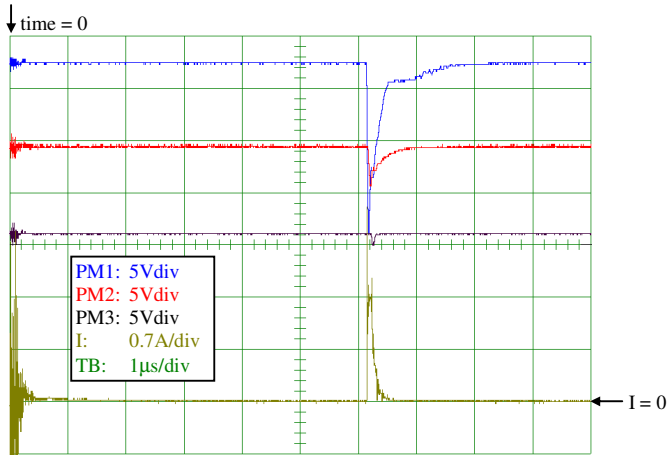

Figure 3.8.2: Typical oscilloscope traces for +26.6kVp impulses applied to the gap with no insulator present.

The current wave shapes were analysed, the relationship between injected charge and peak current is shown in figure 3.8.3 the air gap data from the larger gap is shown for comparison.

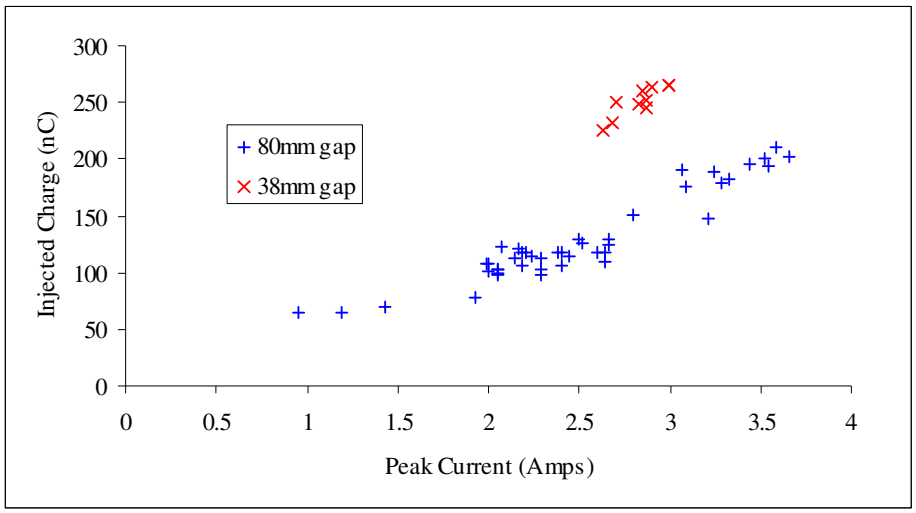

Figure 3.8.3: Graph showing the relationship between injected charge and peak current for the medium rod in air.

3.8.4 PTFE and its variants

A 40mm high specimen of PTFE was put in the gap. Several +26.6kV impulses were applied to the rod. Figure 3.8.4 shows some typical oscilloscope traces obtained. Multiple discharges were observed. The triple junction introduced by having the insulator in contact with the rod lowered the corona inception voltage and caused discharges to occur much earlier in the impulse voltage wave. The photo-multipliers indicated that the discharge did not even make it half way across the gap.

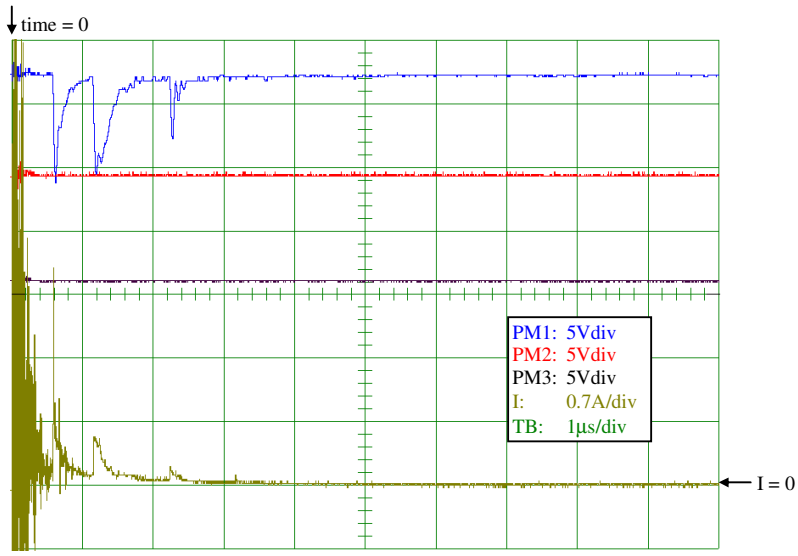

Figure 3.8.4: Typical oscilloscope traces for +26.6kVp impulses applied to PTFE in the gap.

Two other types of PTFE were tested; Molybdenum disulphide doped and carbon filled. They exhibited very similar charging patterns and discharge characteristics to pure white PTFE.

3.8.5 Polyethylene

An initially neutralised polyethylene test object was positioned in the gap and ten +26.6kVp impulses were applied to the rod. Figure 3.8.5 shows typical oscilloscope traces obtained. Again multiple discharges were observed for all ten of the applied impulses.

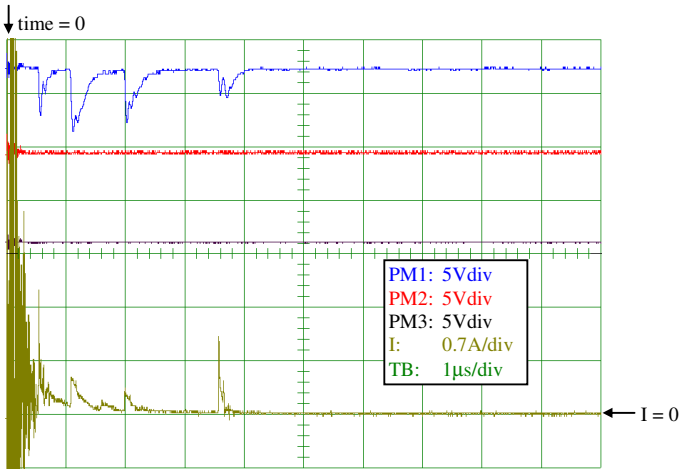

Figure 3.8.5: Typical oscilloscope traces for +26kVp impulses applied to polyethylene in the gap.

The surface was scanned after each the 1st, 2nd, 3rd, 4th, 5th and 10th impulse. Figure 3.8.6 shows the surface charge density distributions obtained.

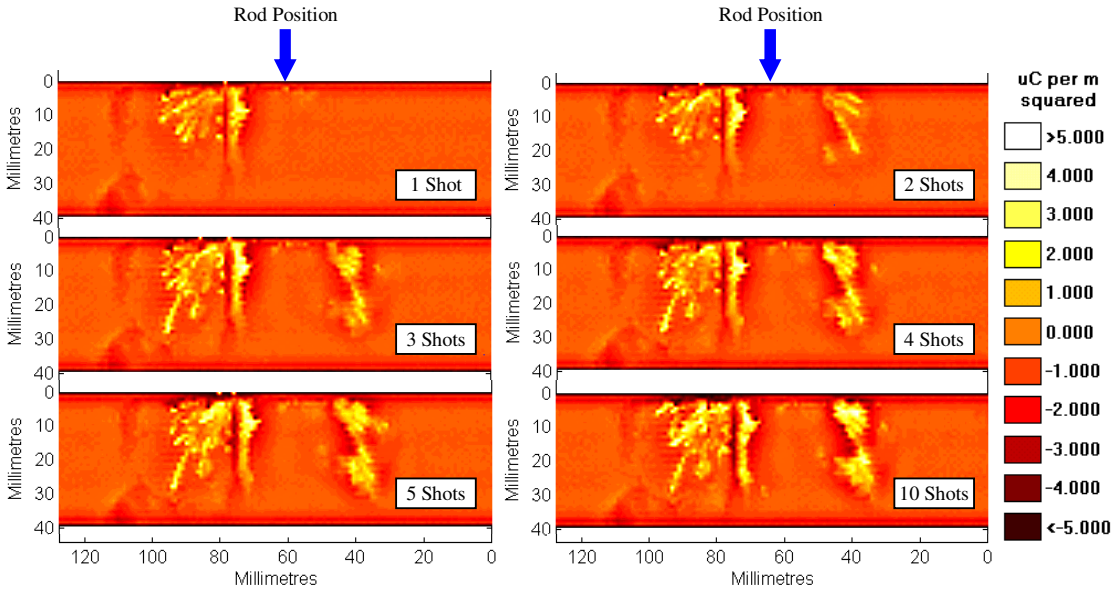

Figure 3.8.6: Surface charge density maps showing the charge deposited after a number of +26.6kVp impulses applied

Streamer channels are clearly visible in the charge density distributions. It is interesting to note that although the streamer channels appear to have crossed the halfway point in the gap no signal was detected from the middle photo-multiplier.

Figure 3.8.7 shows the total surface charge on the insulator after each shot. The net charge on the insulator remains close to zero.

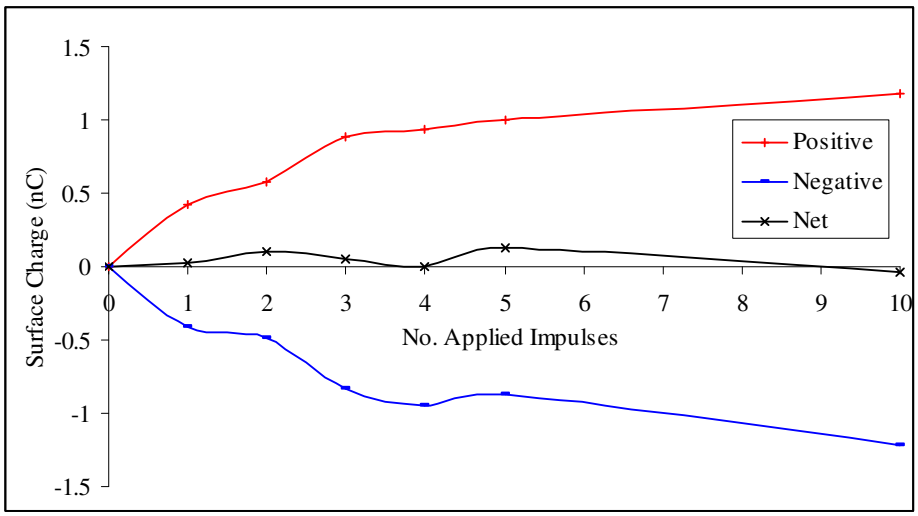

Figure 3.8.7: Graph showing total surface charge deposited on the surface of the polyethylene insulator after each +26.6kVp impulse.

After about three shots had been applied, the total surface charges on the polyethylene insulator began to level out and further impulses added little to the total surface charge.

3.8.6 Nylon

A nylon insulator specimen was placed in the gap and ten +26.6kVp impulses were applied to the rod. Figure 3.8.8 shows a typical oscilloscope trace obtained, multiple discharges were observed for each impulse.

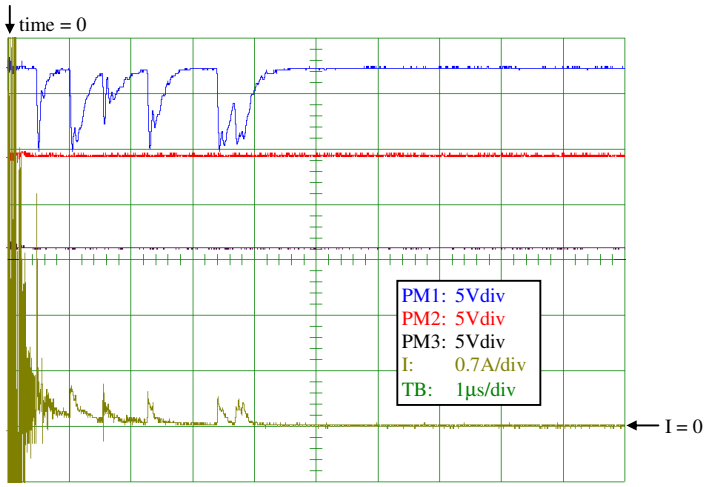

Figure 3.8.8: Typical oscilloscope traces for +26kVp impulses applied to nylon in the gap.

After each shot the surface was scanned but no surface charge could be detected. This means one of three things: either nylon does not attach surface charge; or it does but only very slightly and the scanning system cannot detect it; or it does but the surface charge decays away before the scanning system can measure it.

3.8.7 Porcelain

The only porcelain test objects available were manufactured into the shed type geometry. Glazed and un-glazed specimens were available. The glazed porcelain did not exhibit surface charging whereas the un-glazed specimen exhibited some surface charging.

3.8.8 Epoxy Resin

Small samples of epoxy resin were available and initial tests showed that they exhibited a high susceptibility to surface charging.

3.8.9 Glass and Fibreglass

It was found that both glass and fibreglass could be charged to some degree.

3.9 Charge Decay and Surface Condition

3.9.1 Introduction

In the cases where charge was detected it was found to stay on the surfaces for a substantial length of time. This section describes the experiments made on the subject of charge decay and surface mobility. It also details observations made on the condition of the insulator surface.

3.9.2 Initial Observations

The condition of the surface played an important part in the decay of charge from the insulator's surface. A dirty, greasy or track-marked surface would lose charge quicker than a clean one. To allow repeatable experiments to be made, all the insulator specimens used were thoroughly cleaned using ethanol to remove any greasy surface residue.

It had been observed that manufacturing marks on the surface of the insulator caused charged regions to appear when the surface was subjected to high fields or corona discharge activity. These manufacturing marks were barely visible to the naked eye but because they were effectively small distortions in the surface they could cause localised enhancements in the applied electric field. This effect was observed in all insulating materials on which surface charge could be detected.

3.9.3 Set-up

Figure 3.9.1 shows the electrode arrangement used to study charge decay from the surface. A high voltage applied to the sharp rod 1mm away from the insulating surface was used to generate charge distributions on the 40mm tall, 40mm diameter PTFE insulator specimen. The insulator was kept between two identical plane electrodes during and after the time for which the voltage was applied to the rod. Both planes could be grounded; this ensured that the insulator sat in a zero ambient field. The top plane could also be set at a DC potential when a uniform field was required. An identical, but longer in length, electrostatic probe was employed so that the insulator could be scanned without removing it from between the electrodes.

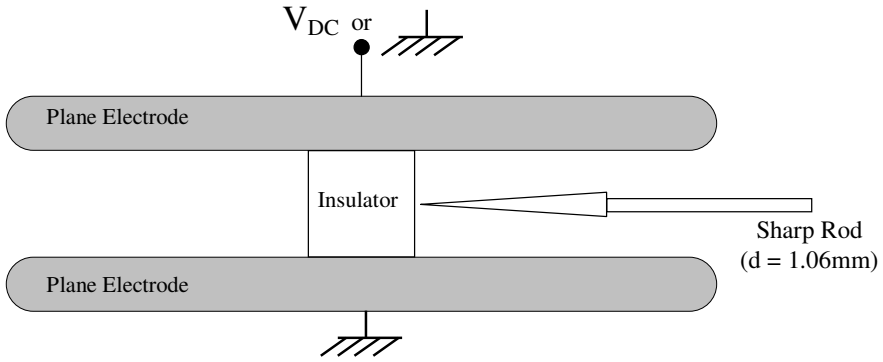

Figure 3.9.1: The experimental set-up used to study charge decay from the surface.

3.9.4 Natural PTFE Decay

To study charge decay from a surface a method was required to generate a charge distribution on the surface. Positive test voltages had been shown in a previous section to produce widely spreading streamers on the surface. Negative discharges from the rod had been shown to deposit a very well defined region of charge on the insulator surface, and were chosen for this experiment. Both the plane electrodes were earthed and negative 10kV DC was applied to the rod for approximately 1minute. The surface was then scanned. The insulator was kept in situ between the earthed electrodes and scanned for surface charge every few hours initially. The insulator was then left for 8 days and scanned occasionally. Some of the surface charge density maps obtained are shown in figure 3.9.2.

The DC corona caused a manufacturing defect in the material to acquire a positive charge. It is interesting to note that some of the charge appeared to redistribute itself along the manufacturing defect in the first couple of hours after the discharge had been applied to the surface.

Figure 3.9.3 shows horizontal slices at 20mm through the charge distributions shown.

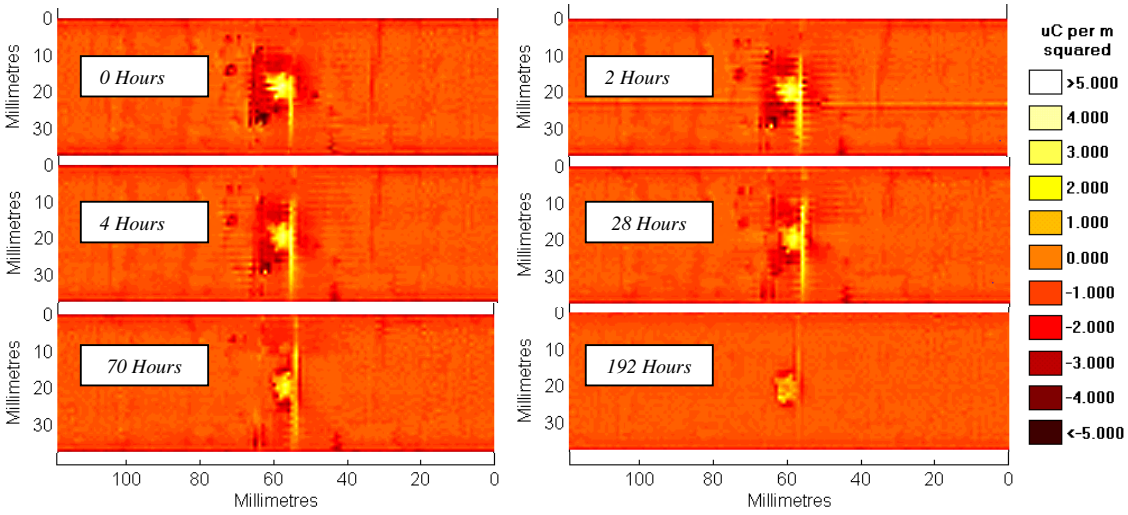

Figure 3.9.2: Surface charge density distributions showing charge decay from the PTFE surface after charging with a -10kV DC corona at the rod.

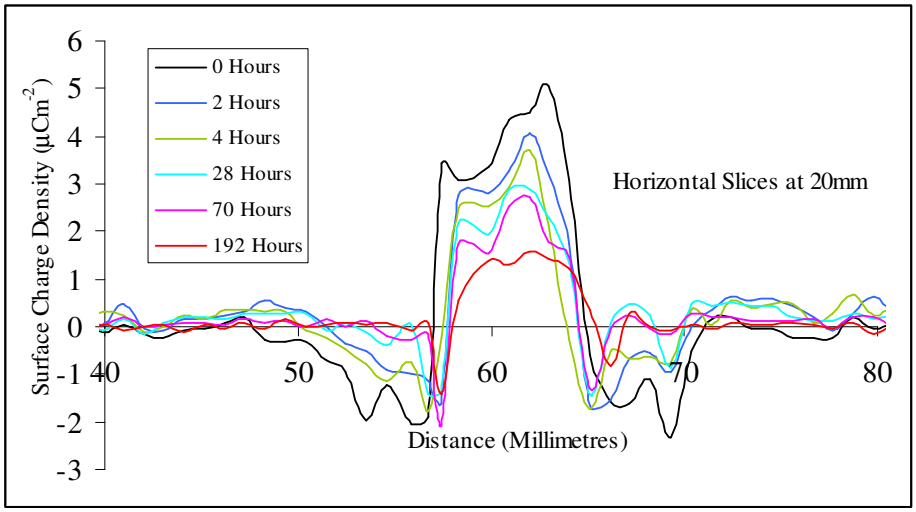

Figure 3.9.3: Horizontal slices at 20mm through the surface charge density distributions shown in figure 3.9.2.

The surface charge distribution does not spread out over time; it just slowly fades away as is shown by the horizontal slices through the distribution shown in figure 3.9.3. On this resolution nothing can really be said about charge movement within the distribution. Figure 3.9.4 shows how the total charge deposited varies with time, the surface stays negatively net charged. The decay rates for the positive and negative charges appear very similar with a half-life of approximately 120 hours or 5 days.

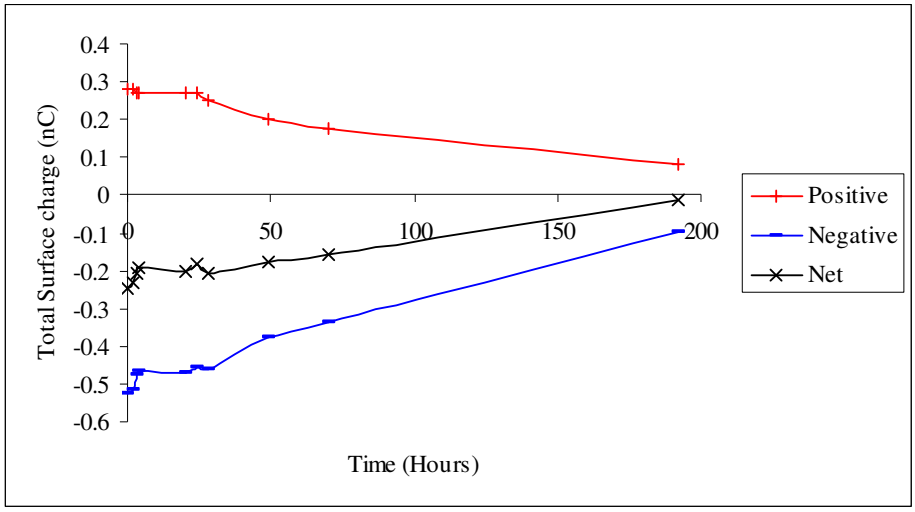

Figure 3.9.4: Total surface charge deposited versus time from applied discharge on PTFE.

3.9.5 Stressed PTFE Charge Decay

Introduction

It was important to discover what effect a strong electric field had on the deposited surface charge. This was for three reasons:

1. To give an indication of how tenaciously the charge clung to the surface.
2. In the experiments with an impulse voltage applied to the rod the gap remained stressed for a short time after the discharge had occurred. It was important in this case that this field did not affect the charge distribution deposited by the discharge.
3. Important implications where insulation is used in D.C. applications

Neutralised Insulator

A neutralised 40mm high PTFE insulator was placed between the plane electrodes as shown in figure 3.9.1 (but without the sharp rod electrode) and negative 30kV DC applied to the top electrode for 1 hour. This applied voltage and electrode spacing gave a uniform field of 750kVm^{-1} between the electrodes. The surface was then scanned to see what effect the DC stress had on a neutralised insulator.

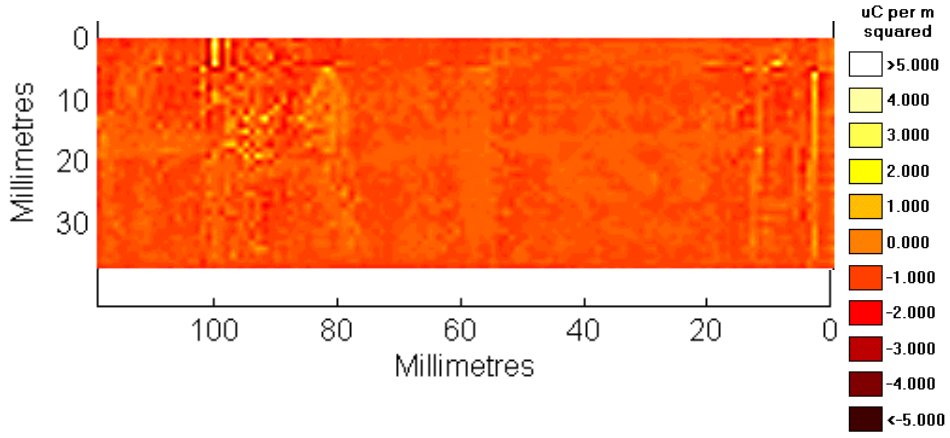

Figure 3.9.5: The surface charge deposited after a 750kVm^{-1} field was applied to an initially neutralised PTFE insulator for 1 hour.

Figure 3.9.5 shows the surface charge distribution obtained from the scan of the stressed insulator. Significant charge densities of around ±5μCm^{-2} were observed in the distribution. The total charge found on the surface comprised of +0.56nC -0.66nC giving a net negative charge of -0.1nC.

The triple junctions exacerbated by manufacturing defects near the electrodes were presumably the source of the discharge activity that produced the surface charge. The charge was mainly concentrated around small manufacturing defects on the surface.

Charged Insulator

The surface was then neutralised and the sharp rod electrode positioned in the gap. A single -28kVp impulse was then applied to the rod to generate a small charged region on the surface. The sharp rod was then removed and the insulator scanned to ascertain the initial surface charge distribution. Negative 30kV DC was then applied to the top electrode for 3 hours and the surface scanned every hour. The charge density distributions obtained are shown in figure 3.9.6.

The surface was then neutralised and the above repeated but with a +28kV impulse applied to the sharp rod to generate a more dispersed initial surface charge distribution. The surface charge distributions obtained are shown in figure 3.9.7.

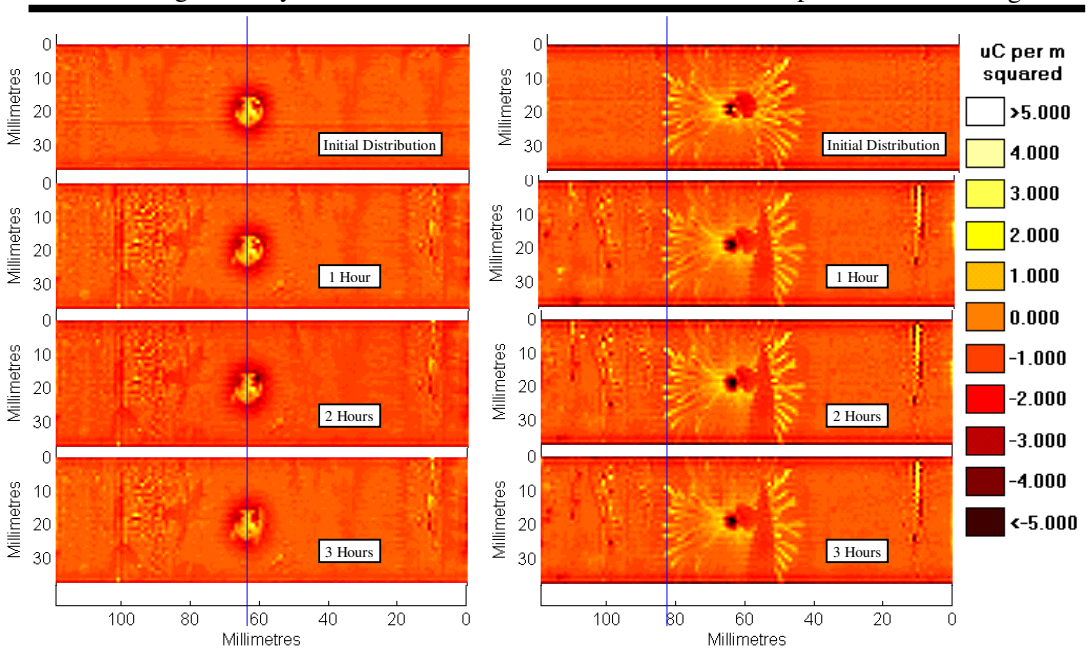

Figure 3.9.6: Surface charge density maps showing the effect a 750kVm^{-1} field has on a negative corona charge distribution.

Figure 3.9.7: Surface charge density maps showing the effect a 750kVm^{-1} field has on a positive corona charge distribution.

The surface charge distributions only changed significantly after the first application of the DC field. The total charge deposited on the surface did not change significantly after the discharge sites around the insulator-electrode junction had deposited a significant charge in the first hour. Figure 3.9.8 shows vertical slices through the middle negative discharge case.

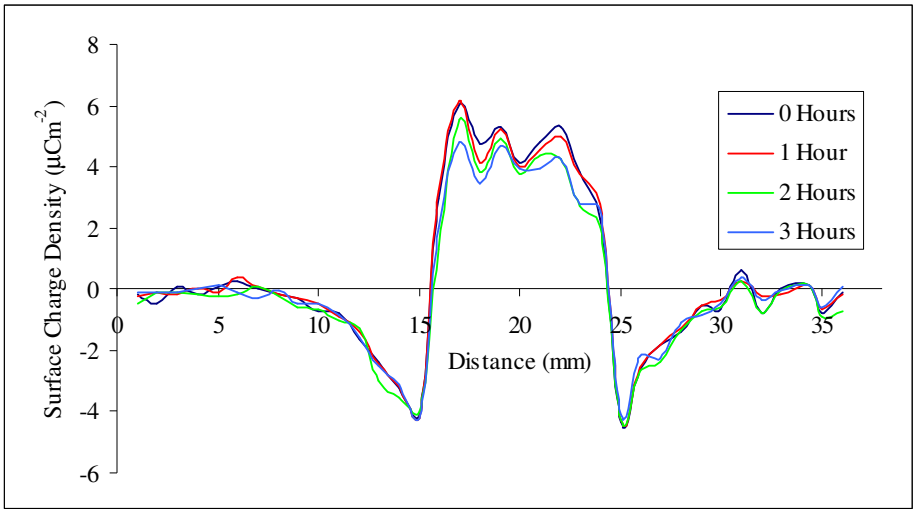

Figure 3.9.8: Vertical slices at 64mm through the surface charge distributions shown in figure 3.9.6.

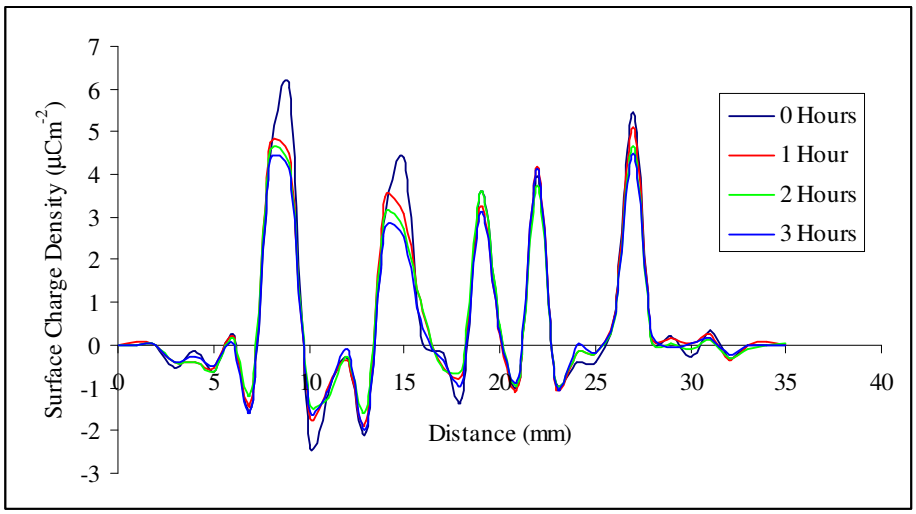

Figure 3.9.9: Vertical slices at 84mm through the surface charge distributions shown in figure 3.9.7.

Figure 3.9.9 shows vertical slices through the left hand side streamer tips of the positive discharge case. In both cases the magnitude of the distribution decayed at a similar rate to that of the zero ambient field experiments. There was no detectable evidence of charge migration across the insulator in the presence of the electric field in either case.

.

3.9.6 Polyethylene Charge Decay

The only other material on which charge decay was studied was polyethylene. The experimental set-up used is shown in figure 3.9.10. Charge was deposited on a neutralised 40mm tall polyethylene insulator by applying ten +26.6kVp impulses to the medium rod in contact 2mm from the top of the surface. The surface was then scanned every 20 minutes for just over 4 hours. Figure 3.9.11 shows some of the charge distributions obtained.

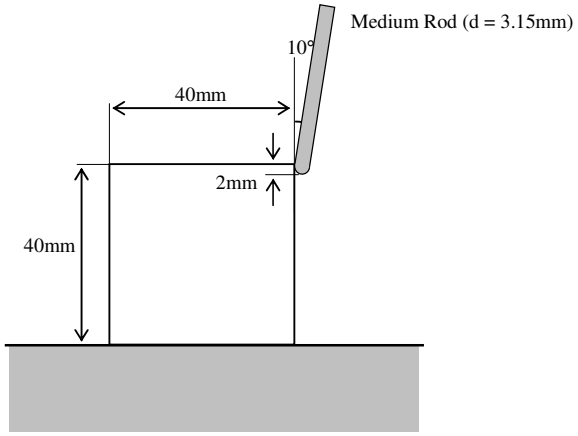

Figure 3.9.10: The apparatus for the polyethylene charge decay experiment.

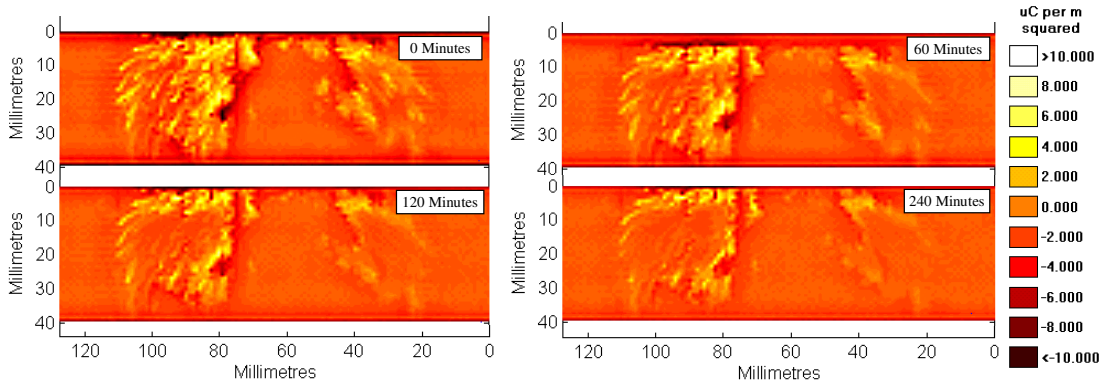

Figure 3.9.11: Surface charge density distributions showing charge decay on polyethylene.

A vertical path through each distribution can be seen at 75mm, this was coincident with a manufacturing defect on the surface.

The charge slowly decayed from the surface in a similar way to PTFE, no charge movement on the surface could be detected. Figure 3.9.12 shows horizontal slices at 20mm through the charge distributions.

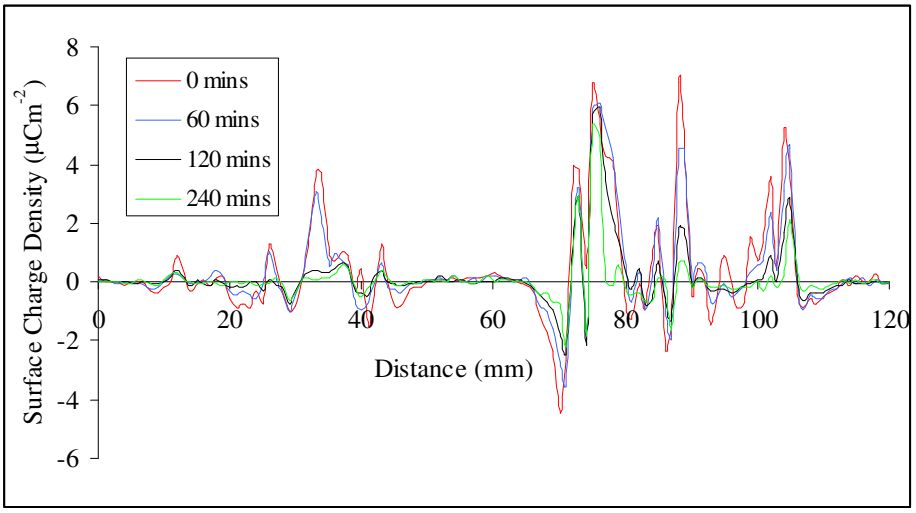

Figure 3.9.12: Horizontal slices through the above charge distributions at 20mm.

It is interesting to note from both the charge distributions and slices through them, that charge from different parts of the insulator decayed at different rates.

Figure 3.9.13 shows how the overall charge decayed away from the insulator.

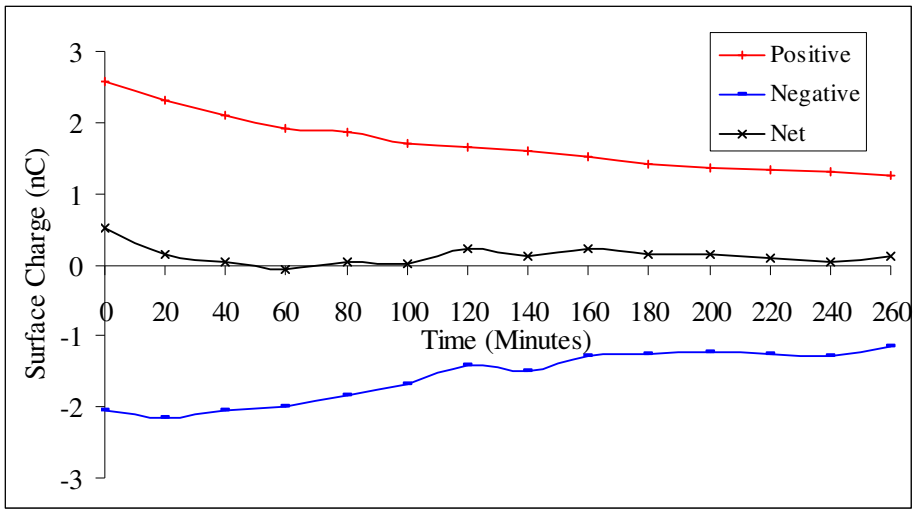

Figure 3.9.13: Surface charge decay from polyethylene.

Polyethylene appeared to have a faster charge decay rate than PTFE. The decay rates for the positive and negative charges appear very similar with a half-life of approximately 4½ hours.

3.10 Contoured Test Objects

3.10.1 Introduction

So far all the experimental work had only employed simple cylindrical insulator test objects. The scanning system was however capable of scanning any number of different shaped test objects. This new technique has opened up vast new areas of possible research far beyond the time available for this particular research project. A few preliminary studies were conducted to evaluate the scanning technique on contoured test objects. This section studies the scanning of one of the most complicated types of geometry that the scanning system could follow: the shed.

3.10.2 The Single Shed Test Object

The single shed was difficult to scan because of the large range of different angular positions that the probe had to move through. Figure 3.10.1 shows the shed geometry and the trajectory that the W-Axis of the scanning platform had to move through to scan the surface. This complicated path had to be very accurately followed to ensure probe tip positional integrity.

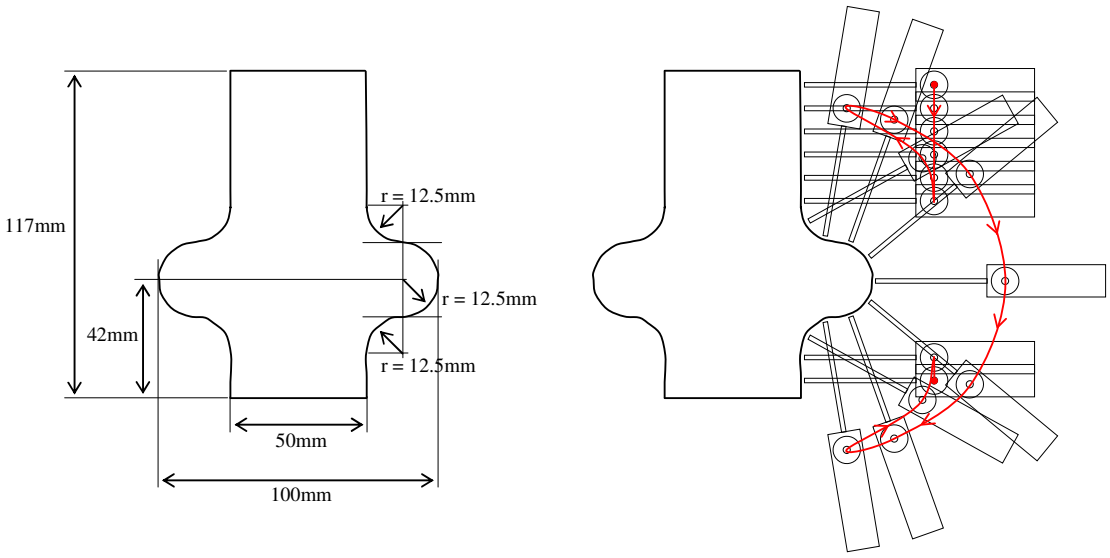

Figure 3.10.1: The single shed test object and the scanning trajectory.

3.10.3 Scanning Problem

The contoured shape of the shed meant that it had quite a large total surface area. To scan the entire surface as a single distribution would have resulted in too large a number of surface elements to be easily solved using the Solver software. Hence the shed surface had to be split into three smaller regions as shown in figure 3.10.2.

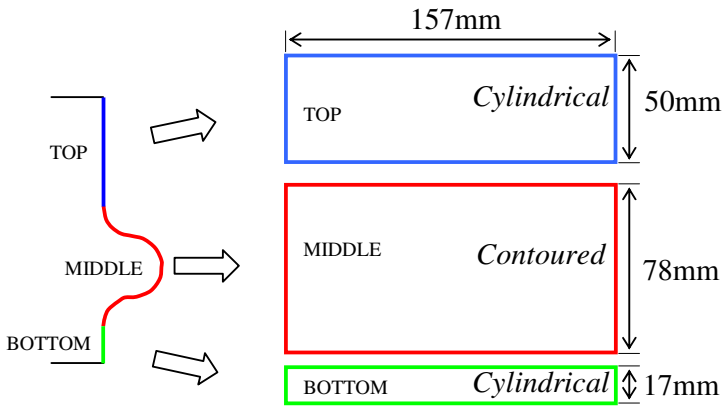

Figure 3.10.2: Division of the shed scanning problem into three sections.

The top and bottom sections of the surface were simple cylinders, leaving only the middle section contoured. The scanning system worked on the principle of equal angular elements; for cylindrical surfaces this led to equal element widths on each layer, for contoured surfaces the element widths changed shape on each layer. The solution software was capable of scaling the Φ-matrix to deal with contoured surfaces however no software was developed to specifically view the surface charge density distributions on contoured surfaces.

3.10.4 Displaying Contoured Surface Charge Distributions

The problem with displaying a contoured surface is that it cannot be simply unrolled on to a flat page as in the case of a cylinder. The usual technique for display such 3D surfaces is to use an orthomorphic projection strategy, such as Mercator's projection for the globe. The problem with projection strategies is that they will always have to distort the surface somehow. Hence the type of projection strategy used needs to be carefully

designed so that the observer can make useful observations from the displayed distribution.

Figure 3.10.3 shows different ways of displaying the middle section of the shed. The surface could be shown as a flat projection. This however distorts the distribution. A better way of displaying the data would be to display it directly onto the actual 3D shape of the surface. This technique is becoming more and more feasible with today's modern fast computers and high level programming languages. Using VRML (Virtual Reality Modelling Language) the whole insulator could be modelled in 3-dimensions and the surface charge density map either wrapped around the surface or plotted directly onto it.

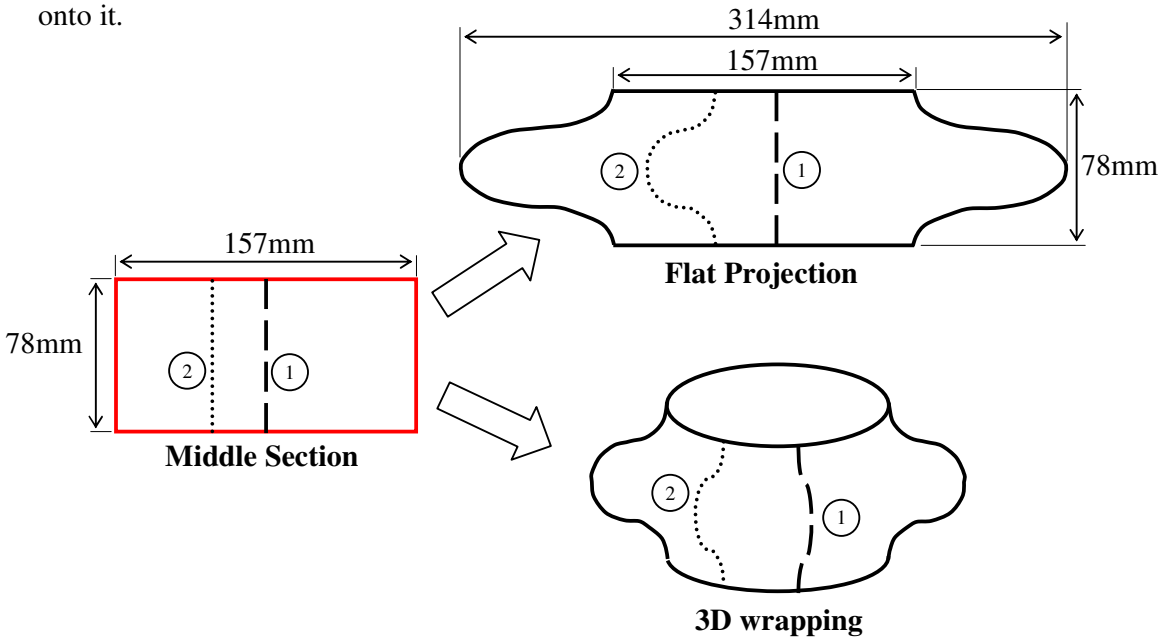

Figure 3.10.3: Problems involved with displaying the contoured middle section accurately. The same two vertical paths are shown in each example.

The contoured surface charge distributions shown in this thesis are displayed in the same way as simple cylindrical ones, as a rectangle. Hence when studying the middle section surface charge distributions one should remember that they should be distorted as shown in figure 3.10.3. However the advantage of displaying the distributions as a rectangle is that vertical paths down the insulator surface correspond to vertical straight lines down the distribution. Whereas if a flat projection is used vertical paths down the insulator correspond to different curved paths down the projection, only path 1, down the centre of the flat projection is a straight line.

3.10.5 Practical Recommendations

Scanning a contoured surface raised a number of points regarding how the scanning system is given the co-ordinates for the shape of the surface. The definition of test object geometry was described in section 2.4.5. Significant positional errors occur if the surface is not defined with a large enough number of test object surface points.

The scanning system calculates the yaw angle of the probe from the two test object surface geometry points on either side of the current layer being scanned, section 2.4.7. For cylindrical test objects only two surface geometry points are required because the probe yaw angle does not change, so the distance between them is simply divided by the number of layers required. For contoured test objects it is recommended that there are *at least* the same number of surface geometry points as there will be layers scanned in. This ensures that a new yaw angle is calculated for each layer.

When the test object geometry has been initially inputted into the scanning system, by whichever technique the user chooses, some of the surface points may need to be moved slightly to make the scanning system follow the contour accurately. This 'fine tuning' is required because of small errors in test object definition and mechanical inaccuracies.

Setting up the system to scan contoured test objects accurately is quite time consuming; more work is required to improve this facility. Once setup the scanning system can repeatedly scan the same test object with reasonable reliability.

3.10.6 Set-up

The electrode configuration was set up as before, with an 80mm gap and the medium rod. The photo-multipliers were positioned as shown in figure 3.10.4. Three different materials were manufactured into the shed design: Carbon filled PTFE, Glazed Porcelain and Un-glazed Porcelain. No charge could be detected on the glazed porcelain specimen, but interestingly some charge was detectable on the unglazed specimen. The experiments described here use only the carbon filled PTFE specimen because it behaved in a similar manner to pure white PTFE. Positive 85kVp impulses were applied to the rod using impulse generator No.2.

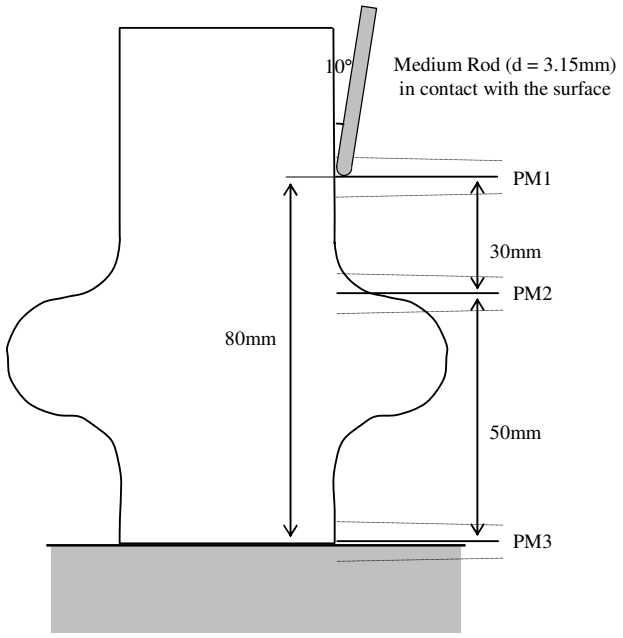

Figure 3.10.4: The electrode set-up for the shed experiments.

The atmospheric conditions in the laboratory were 23.0°C and 750mmHg. The specific humidity was 11.58gm^{-3}.

3.10.7 Results

Initially ten +85kVp impulses were applied to the gap without the insulator present. The gap did not flashover once. An example oscilloscope trace obtained is shown in figure 3.10.5. The neutralised insulator was then positioned in the gap and three +85kVp impulses were applied. The first impulse did not cause the gap to flashover, the second and third did.

The oscilloscope traces for each shot are shown in figures 3.10.6 to 3.10.8. Unfortunately the current signals are quite noisy.

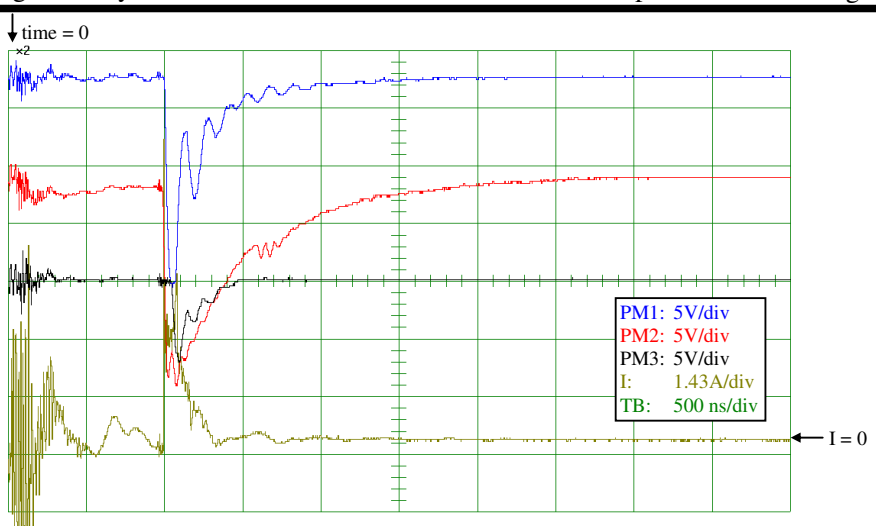

Figure 3.10.5: Example oscilloscope traces for a +68kVp impulse applied to the rod, with *no* insulator present and *no* flashover.

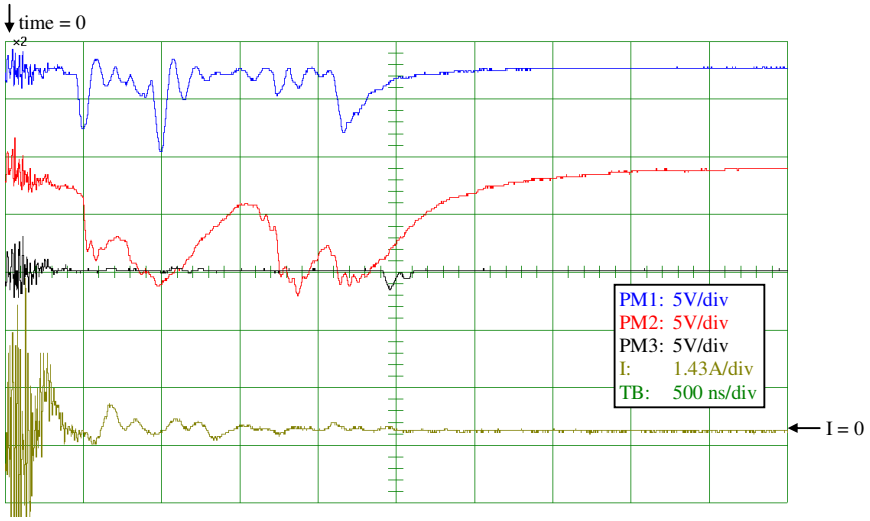

Figure 3.10.6: Oscilloscope traces for the first +68kVp impulse applied to the rod, *with* insulator present and *no* flashover.

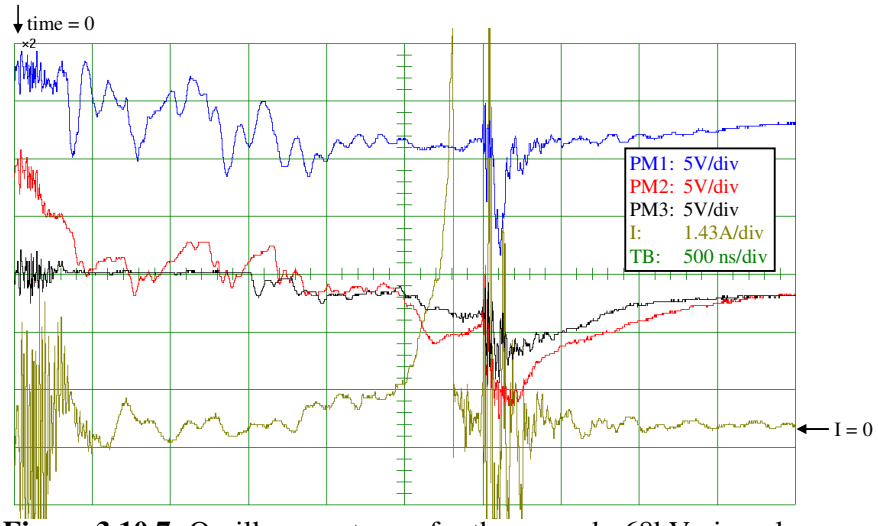

Figure 3.10.7: Oscilloscope traces for the second +68kVp impulse applied to the rod, *with* insulator present and *flashover*.

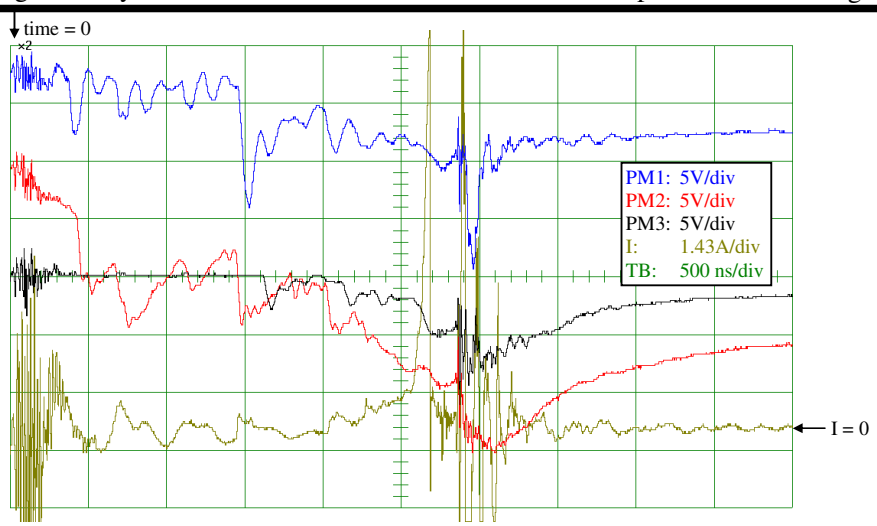

Figure 3.10.8: Oscilloscope traces for the third +68kVp impulse applied to the rod, *with* insulator present and *flashover*.

Two interesting points arise from the oscilloscope traces with the insulator present. Firstly the time from when a discharge was first detected by PM2 just above the shed, to when it appeared at the ground plane was very long.

Secondly a large current pulse was seen just before breakdown in both figures 3.10.7 and 3.10.8.

The surface charge density distributions were only obtained after the first and third shots, they are shown in figures 3.10.9 and 3.10.10. Note that the middle section is contoured and is thus distorted.

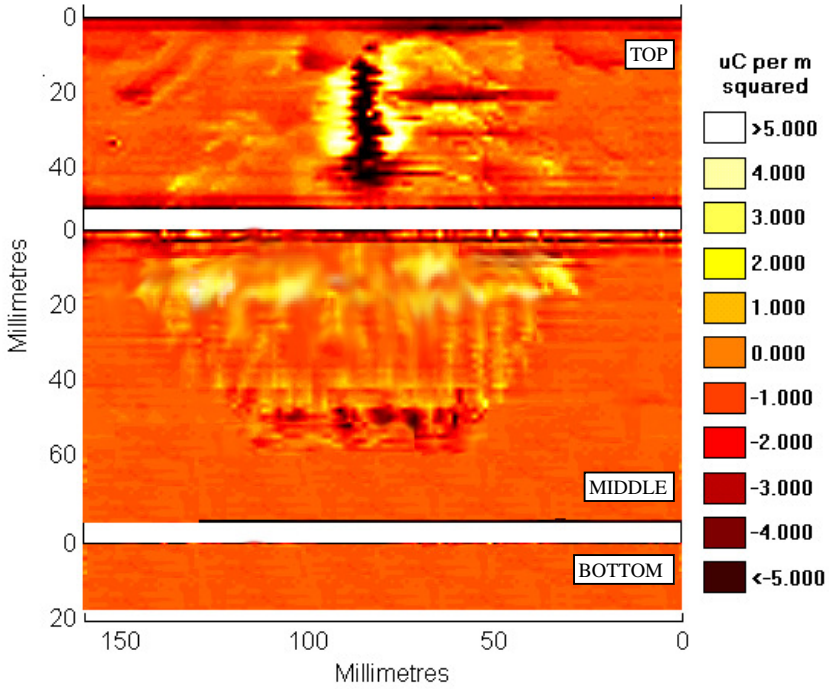

Figure 3.10.9: Surface charge density maps of the shed insulator after a single +85kVp impulse applied to the rod, with no flashover.

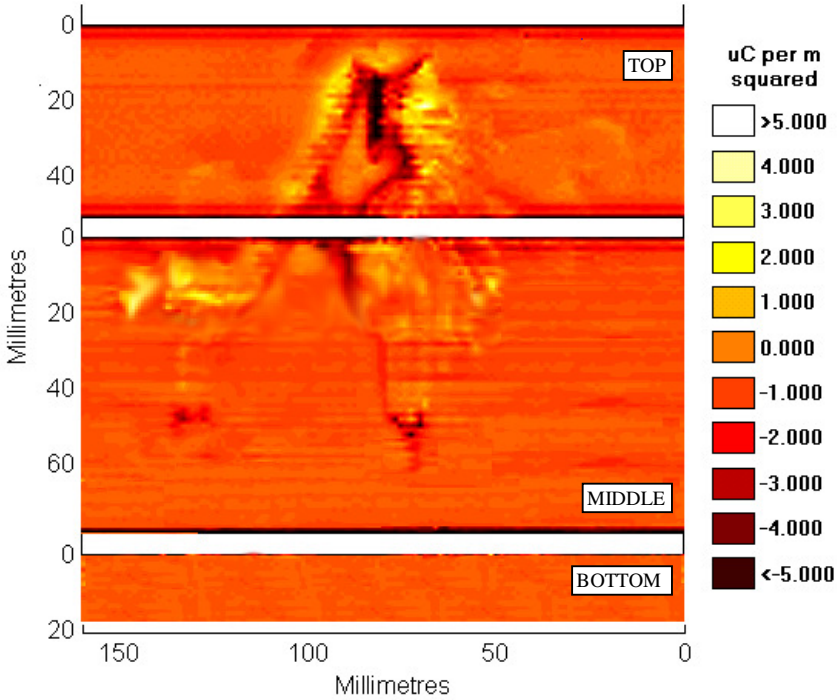

Figure 3.10.10: Surface charge density maps of the shed insulator after a further two +85kVp impulses were applied to the rod, with flashover.

The surface charge density distributions obtained correlate with the previous experiments on cylindrical insulators: a large amount of negative charge directly under the rod and breakdown cuts a neutralised path through the distribution. The most interesting thing about the charge distributions is the point where the charged streamer channels stop as they propagate down the insulator. At a point between 50 and 60mm on the middle section of the surface the streamer channels suddenly change from being positive to negative, then stop. These small negative regions which terminate all the charged channels that propagate that far, appear to be where the streamers left the surface and completed crossing the gap in air. The charge densities observed in these streamer end points were around $-5\mu Cm^{-2}$.

The geometrical significance of this region is shown in figure 3.10.11.

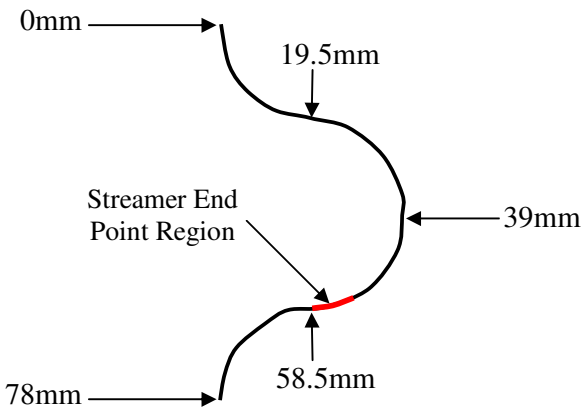

Figure 3.10.11: Points on the contoured middle section of the shed.

The surface charge density maps also indicate that there was a significant positive charge deposited on the topside of the shed.

Chapter 4: SIMULATIONS AND ANALYSIS

4.1 Introduction

4.1.1 Overview

This chapter details the finite element modelling and analysis of the electrostatic probe, the charge on the insulator surface and the electrode geometry. This work was conducted in parallel with the development and experimental work.

Simulations allow a deeper understanding of the electrostatic probe operation and the effect of the Φ-Matrix solution procedure. Using the charge density measurements taken in the experimental work the electric field in the streamer channels was estimated and important observations made.

4.1.2 Electrostatic Field Equations

The initial modelling objective was to obtain the values for the ϕ-functions necessary to calculate surface charge density distributions from probe voltage distributions.

In order to find these values the probe and the insulator surface had to be modelled, this involved solving Poisson's and Gauss' Equations for electric fields. The geometry of the problem could not be reduced to 2-dimensions so a 3-dimensional model was required.

The electric field **E** and electric flux density **D** in the model can be determined from charge densities in volumes and voltages applied to surfaces.

The electric flux density, D is related to the field, E by: $\mathbf{D} = \epsilon\mathbf{E}$

The electric field, E is related to the voltage, V by: $\mathbf{E} = -\nabla V$

The electric flux density, D is related to the volume charge density, ρ by: $\nabla.\mathbf{D} = \rho$

Thus:

$$\nabla.\epsilon\mathbf{E} = \rho$$

Substituting again:

$$-\nabla.\epsilon\nabla V = \rho$$

Developing a computer program to solve the equations to an acceptable level of accuracy in three dimensions would have been too great a task. Instead a commercially available finite-element modelling software package was used. This had the advantage of much greater flexibility and the tools for detailed analysis of the solutions produced.

4.1.3 OPERA 3D

OPERA-3d (**OP**erating environment for **E**lectromagnetic **R**esearch and **A**nalysis) is a pre- and post-processing system for studying electromagnetic field problems. It was written and developed by Vector Fields Inc.

Finite element discretisation forms the basis of the methods used in the analysis program. This technique is widely applicable to the solution of partial differential equations

The system comprises of a suite of programs: A pre-processor provides facilities for the creation of finite element models and definition of material characteristics; An analysis module solves the field equations; and a post-processor provides graphical displays and facilities for the examination of the solution.

4.1.4 Finite Element Modelling

Finite element modelling involves dividing the geometry of the problem into small elements, these elements fit together to form a mesh. The solution potential is then calculated at each node in the mesh. The size of the elements can be reduced by increasing the discretisation of the mesh.

There are several stages in reducing a real problem into a model that can be solved by a computer.

1. *Physical Model:* The specification of the problem in terms of geometry, material properties and sources such as potentials and charges.
2. *Geometric Model:* The reduction of the geometry to relevant active parts of the problem.
3. *Mathematical Model:* The application of the field equations for potentials and boundary conditions taking advantage of any symmetry.
4. *Numerical model:* The discretisation of the geometry and the choice of interpolation functions.
5. *Algebraic Model:* The calculation of the solution potential by solving the derived simultaneous equations for the potential at each node using a matrix technique.

OPERA provides a graphical user interface for the definition and editing of the model, which allows the user to control the degree of discretisation and hence the element size. Two different types of element meshing are possible; tetrahedral or hexahedral, so named because of the element shape produced. Hexahedral meshing provides a more accurate solution, however its is slightly harder to build a complex model with hexahedral rather than tetrahedral elements. Accuracy was important so all models were built using hexahedral meshing.

In regions of importance the element size was reduced to increase the accuracy of the model. The elements were reduced in size until an accuracy of the solution was sufficient.

If processing power was not a factor the entire geometry could be modelled with a very large number of elements. However the processing time required to solve 3-dimensional problems required an optimisation of the number of elements used. Regions of the model of little importance were modelled with large elements.

4.1.5 Modelling Surface Charge

Model

OPERA only allowed volume charges to be defined, so surface charges had to be modelled as very thin volumes. A simple study was undertaken to evaluate the effect of this modelling consideration. Figure 4.1.1 shows the arrangement modelled.

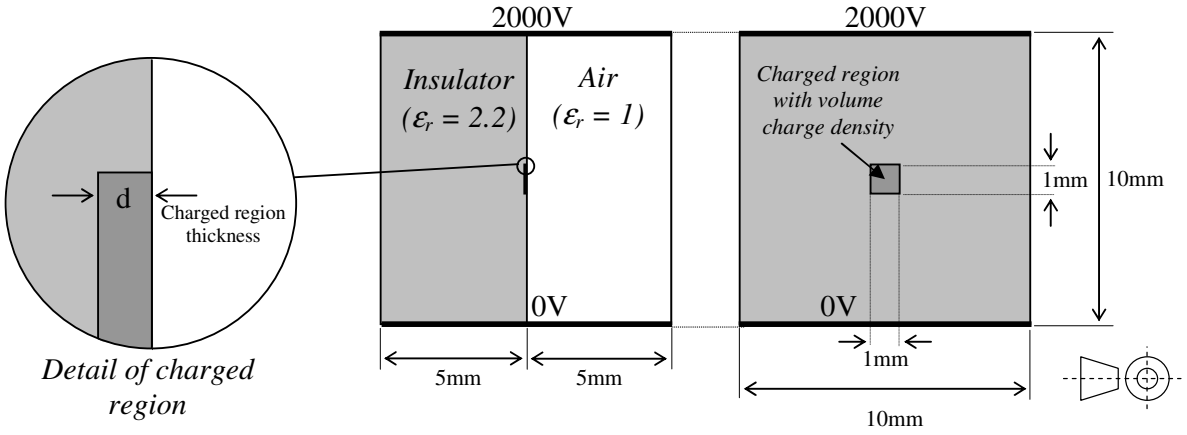

Figure 4.1.1: A simple model to study the effect of charged region thickness.

The arrangement consisted of a 10mm×10mm×5mm insulator with a relative permitivity of 2.2, between two flat 10mm×10mm electrodes. The bottom electrode was set at 0V and the top at 2000V; this gave a field strength of 200kVm^{-1} between them. The choice of this field strength was completely arbitrary and was chosen simply because it was in the range of fields studied during the analysis. The effect of the charged region thickness on the nearby electric field was the important effect being studied.

The insulator only filled half the gap between the electrodes the other half being filled with air. In the centre of the insulator a 1mm×1mm charged region was defined. This region was set into the insulator surface and had a relative permitivity of 2.2, the same as the surrounding insulator material. The surface charge on the exposed face of the charged region was set to be +1μCm^{-2}. The thickness, d in millimetres of this charged region was varied and the electric field strength along two different paths computed.

Calculating Required Volume Charges

The technique of converting surface charge densities to volume charge densities for use in OPERA simply involves working out the amount of charge in the surface area and calculating the volume charge density that contains the same amount of charge. Figure 4.1.2 illustrates this principle.

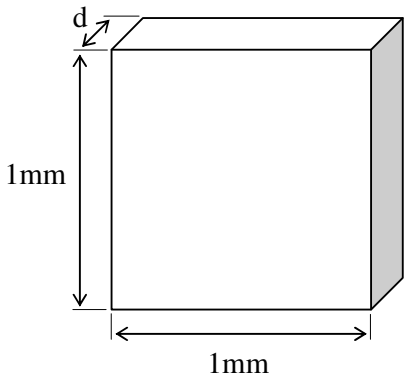

Total Volume = $1\times1\times d = d\ mm^3$

Front face surface area = $1\times1 = 1mm^2 = 1\times10^{-6}\ m^2$

Desired surface charge density = $\sigma\ \mu Cm^{-2}$

Hence total charge on surface = $1\times10^{-6}\times\sigma\times10^{-6} = \sigma\times10^{-12}\ C$

So the volume charge density required = $\frac{\sigma\times10^{-12}}{d}\ Cmm^{-3}$

Figure 4.1.2: Calculation of required volume charge densities from surface charge densities.

Care was required not to confuse the units being used; Surface charge densities were defined in μCm^{-2}. Volume charge densities were defined in Cmm^{-3}, the reason for this is that OPERA operated a per unit system in which the units of length were chosen as millimetres. Millimetres were chosen as the modelling unit because it made the numbers easier to handle when defining the finite element mesh.

Table 4.1.1 shows the five different charged region thickness' modelled and the volume charge densities used to simulate the $+1\mu Cm^{-2}$ charge density on the $1mm^2$ region of the surface.

Charged Region Thickness, d (mm)	Volume Charge Density (Cmm^{-3})
1	$+1\times10^{-12}$
0.1	$+1\times10^{-11}$
0.05	$+2\times10^{-11}$
0.01	$+1\times10^{-10}$
0.001	$+1\times10^{-9}$

Table 4.1.1: The volume charge densities required to simulate a $1\mu Cm^{-2}$ surface charge density distribution on the $1mm^2$ region on the surface for different region thickness'.

Results

The two straight line paths along which the electric fields were calculated are shown in figure 4.1.3. Both paths were 10mm long and went between the two electrodes, the bottom electrode was at 0mm and the top at 10mm. The first path ran along the surface of the insulator directly through the centre of the charged region. The second path ran parallel to this but 1mm away from the surface.

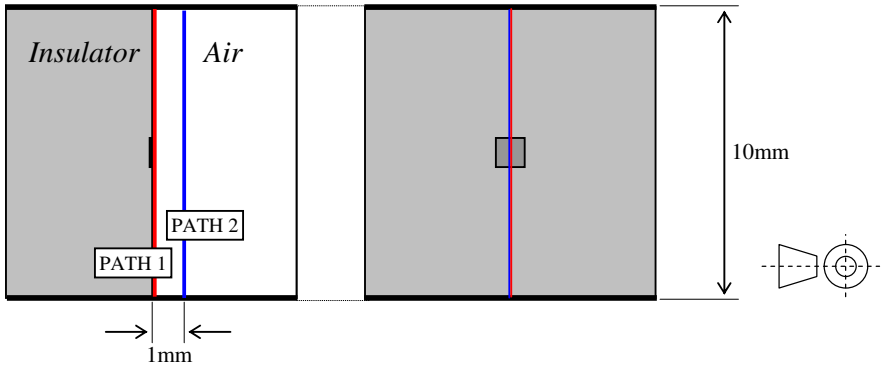

Figure 4.1.3: The two paths through the model along which the electric field strength was calculated.

The electric field strength along the two paths for different region thickness' are shown in figures 4.1.4 and 4.1.4. Note the different field strength axis ranges.

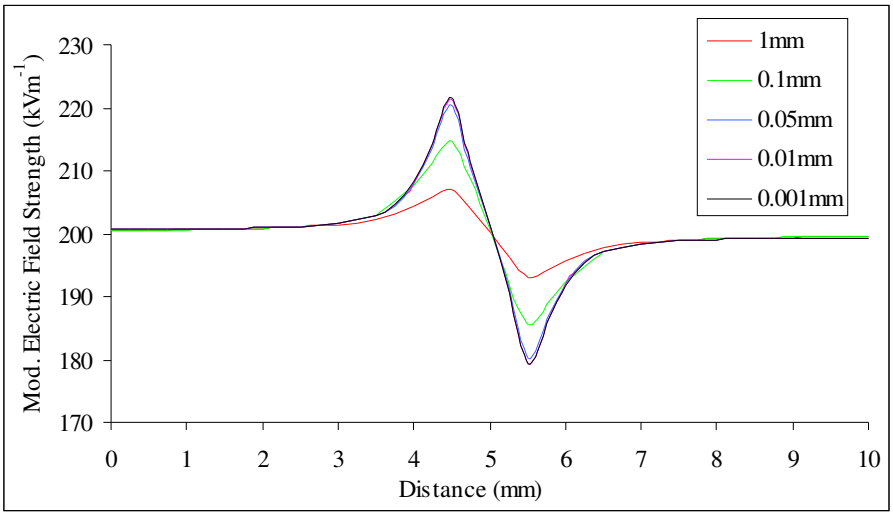

Figure 4.1.4: The electric field strength along path 1 for the five different charged region thickness'.

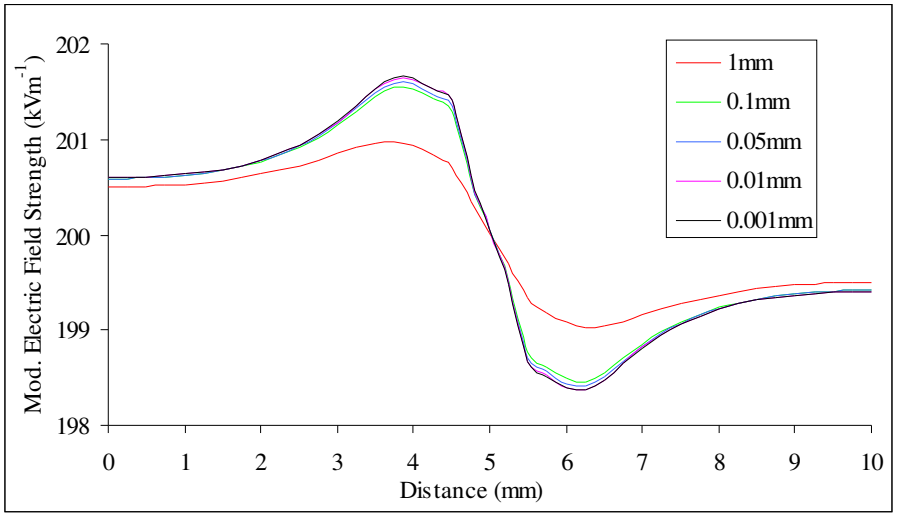

Figure 4.1.5: The electric field strength along path 2 for the five different charged region thickness'.

The first thing to note about the two graphs is that they both tend to a limit as the thickness of the charged region tends to zero. This indicates that the technique of representing surface charge as a very thin volume is valid, which raises the question of what is the actual thickness of the charged region in reality? Physically the deposited surface charge must occupy a volume and hence have a thickness. This thickness will probably be on the molecular scale and involve the surface chemistry.

With the largest element thickness of 1mm the charged region is cube shaped and the electric field strength differs significantly from the asymptotic case. When looking at the field strength along the surface the region thickness needs to be less than 0.05mm to accurately simulate a surface charge density. At 1mm away from the surface the effect of element thickness is less noticeable and the charged region only needs to be less than 0.1mm thick for an accurate simulation.

To ensure accurate results the rest of the simulations involving surface charge used a thickness of 1% of the width of the region. For example, a 1mm×1mm charged region used a thickness of 0.01mm.

4.2 Probe Modelling

4.2.1 Introduction

The main aim of modelling the electrostatic probe was to obtain the values for the ϕ-functions, however it also provided a much deeper understanding of the probe's operation. The beauty of modelling is that it allowed experiments that would be impossible to arrange in real life, such as putting a specific charge density in an exact region on the surface of an insulator.

4.2.2 Model

The ϕ-function was earlier defined as the voltage induced on the probe by a $1\mu Cm^{-2}$ charge density on an element of the surface. The element size was chosen to be $1mm^2$ because this fitted the probe tip geometry very well as is shown in figure 4.2.1. The 1.4mm inner diameter of the outer grounded electrode was set to $\sqrt{2}$ (=1.414mm) in the model so that the element size was exactly $1mm^2$.

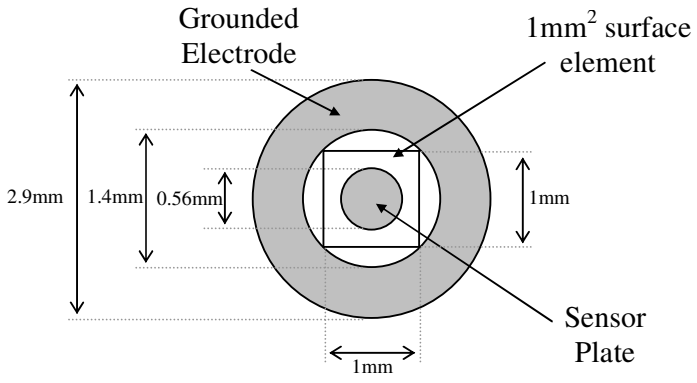

Figure 4.2.1: The probe tip and surface element size.

To obtain the ϕ-functions the probe, the insulator and the surface elements had to be modelled. This allowed surface charges to be applied to different elements at different distances from the probe axis and the voltage induced on the probe found.

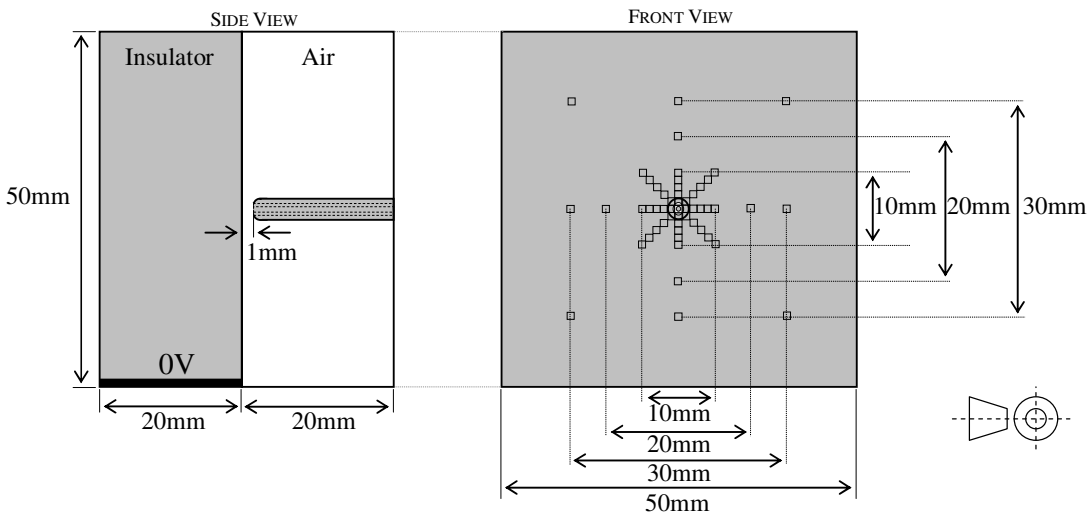

Figure 4.2.2: The model of the probe and insulator surface used to find the probe response ϕ-functions.

To simplify matters the insulator was modelled as flat rather than cylindrical. The error introduced by this assumption was very small because on the scale of the probe the insulator surface was nearly flat. The model used is shown in figure 4.2.2. A 50mm×50mm×20mm portion of the insulator surface was modelled, the bottom of the insulator was set at 0V. This represented the base of the grounded mounting spigot on the scanning platform. The probe was accurately modelled and positioned 1mm away from the surface. The probe was modelled with a rounded grounded outer electrode and a floating inner sensing electrode. The completed finite element mesh is shown in figure 4.2.4.

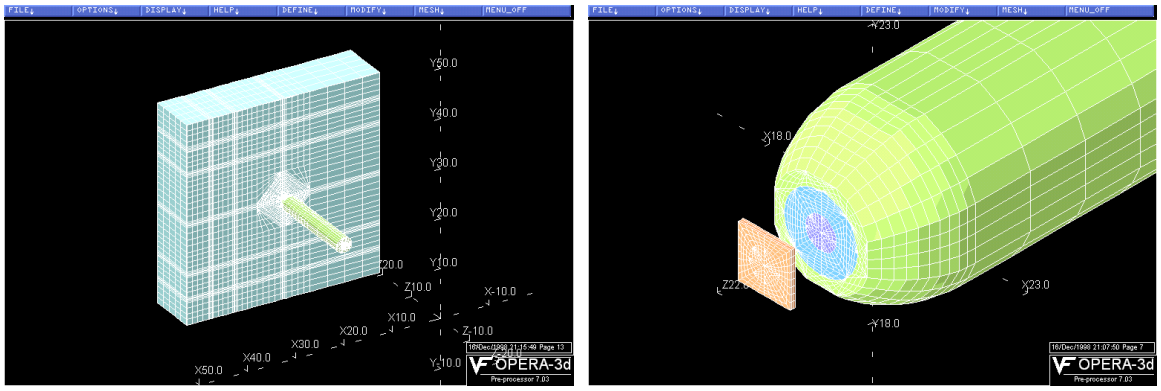

The insulator and probe *Detail of the probe tip and an element of charge*

Figure 4.2.3: The finite element mesh used to model the experimental set-up, the element size is decreased near the probe-tip for greater accuracy.

Not all the surface elements of charge were modelled, for two reasons: firstly the number of simulations required to find the probe voltage for *every* surface element would be immense. Secondly the ϕ-function is relatively well behaved and contains no discontinuities so finding the probe response for every element would be excessive when the missing values could be accurately interpolated. The probe voltage was found for elements directly underneath and at distances of 1, 2, 3, 4, 5, 10 and 15mm from the probe axis in the direction of the four compass points as shown in figure 4.2.2. These probe voltages could then be interpolated into the ϕ_x and ϕ_y functions that combine to form the complete ϕ-function as illustrated in figures 2.5.5 and 2.5.6. To check the accuracy of the interpolation procedure extra probe voltages for elements at 45° angles to the axis were also found. They confirmed the adequacy of the technique very well.

It was also necessary to find ϕ-functions for different layers as the probe moved down the insulator surface towards the grounded bottom of the insulator. Rather than moving the complete probe and surface element arrangement down the insulator towards the grounded plane, the grounded plane can simply be moved up the insulator as is shown in figure 4.2.4.

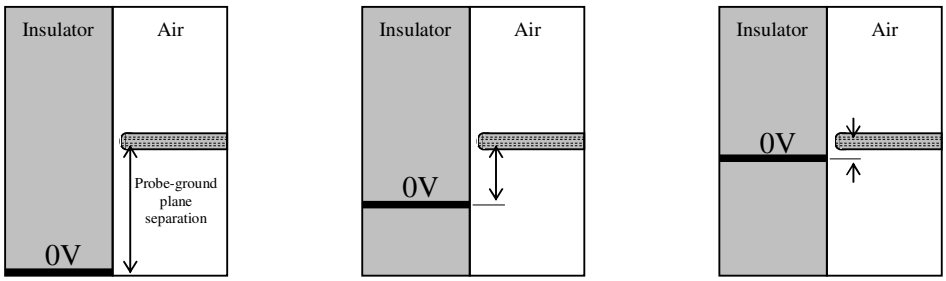

Figure 4.2.4: To model the probe scanning different layers the ground plane was moved up the insulator surface.

The effect of the probe's locality to the ground plane only became significant when in close proximity. This meant that for probe-ground plane separations of 25mm or more the same ϕ-function could be used.

Results

The main aim of the modelling was simply to obtain the probe voltage values. OPERA also allowed a complete analysis of the fields and potentials present in the model. Figure 4.2.5 shows the voltages induced in the insulator by the charged element at different horizontal distances from the probe axis. The presence of the grounded outer probe screen distorts the field produced by the surface charge.

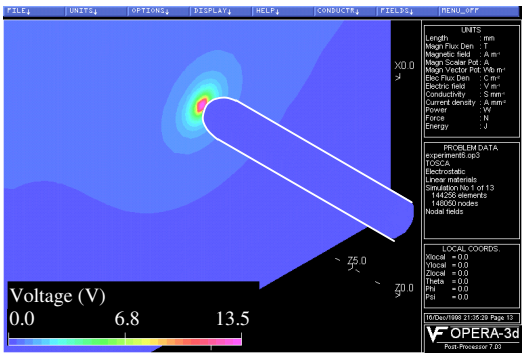

(a) Charged element directly under probe

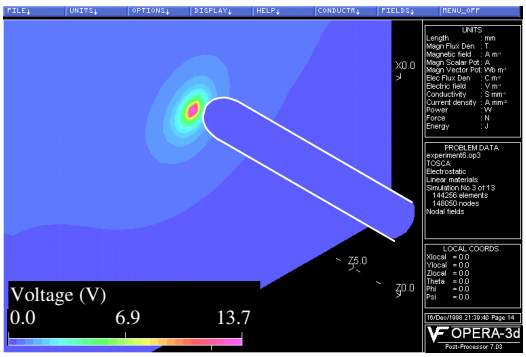

(b) Charged element 1mm sideways

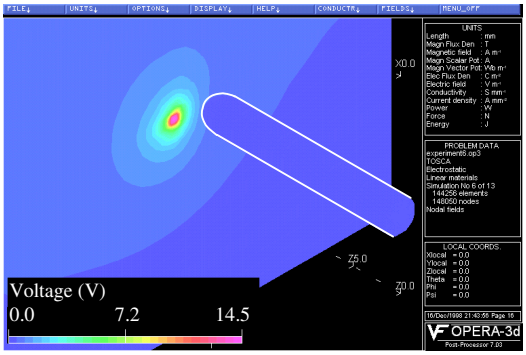

(c) Charged element 3mm sideways

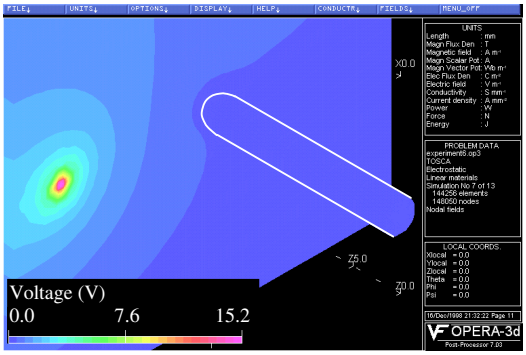

(d) Charged element 15mm sideways

Figure 4.2.5: The voltage distribution produced in the test object by the 1mm^2 element with a 1μCm^{-2} charge.

It is also obvious from the above figures that the potential distribution produced by the charge extends some distance and hence charges away from the probe axis will have an effect of the induced probe voltage.

The voltage induced in the PTFE insulation sleeve between the inner sensing electrode and the outer grounded electrode can also be studied. Figure 4.2.6 shows a cut away view of the probe tip, the depth of penetration of the field produced by the charged element directly under the probe can be seen. This has implications for future design of new electrostatic probes and indicates the minimum depth of the sensor plate required. In this case the depth of the sensor plate is effectively the probe length because the sensor plate is simply the polished end of the inner conductor.

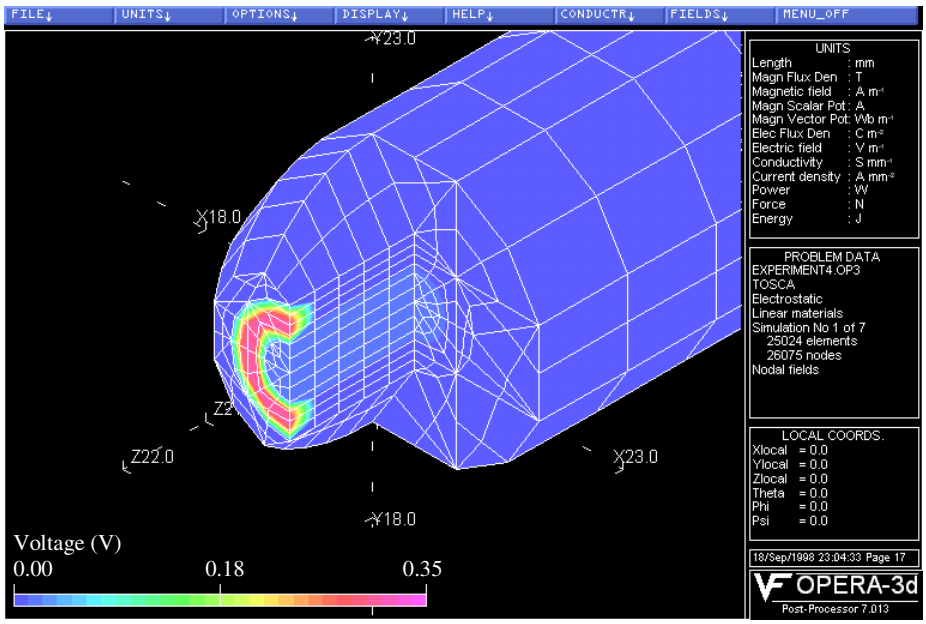

Figure 4.2.6: The voltage distribution induced in the PTFE insulation in the probe, half of the tip has been removed to show the depth of penetration.

The figures on the following page show how the field and voltage induced in the PTFE insulation sleeve around the sensing plate varies as the charged region is moved around the surface. For a $1\mu Cm^{-2}$ charge density on the element the electric field strength in the sleeve did not exceed $5kVm^{-1}$. The highest field strengths occurred not when the charged region was directly under the probe, but when it was directly under the edge of the outer grounded electrode of the probe.

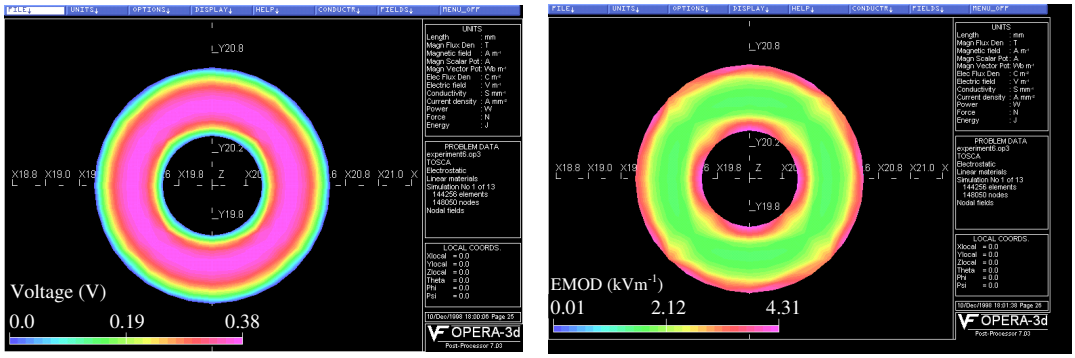

Figure 4.2.7: The voltage and electric field induced in the PTFE insulation in the probe by a 1mm^2, 1μCm^{-2} charge distribution 1mm directly under the probe.

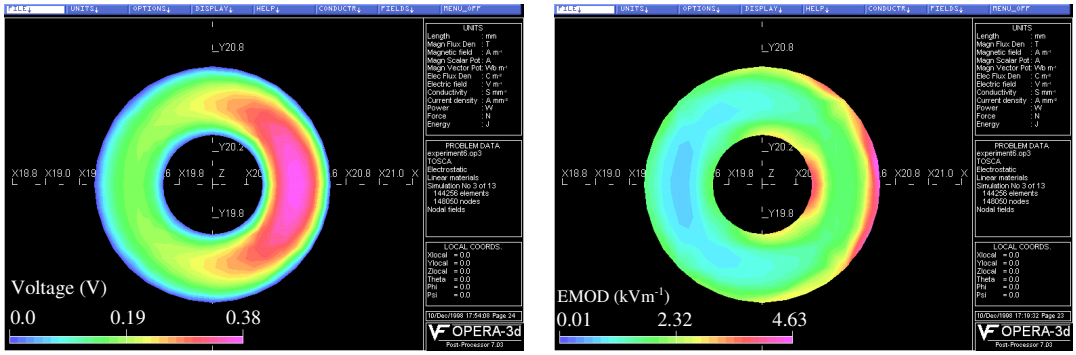

Figure 4.2.8: The voltage and electric field induced in the PTFE insulation in the probe by a 1mm^2, 1μCm^{-2} charge distribution 1mm to the right of the probe axis.

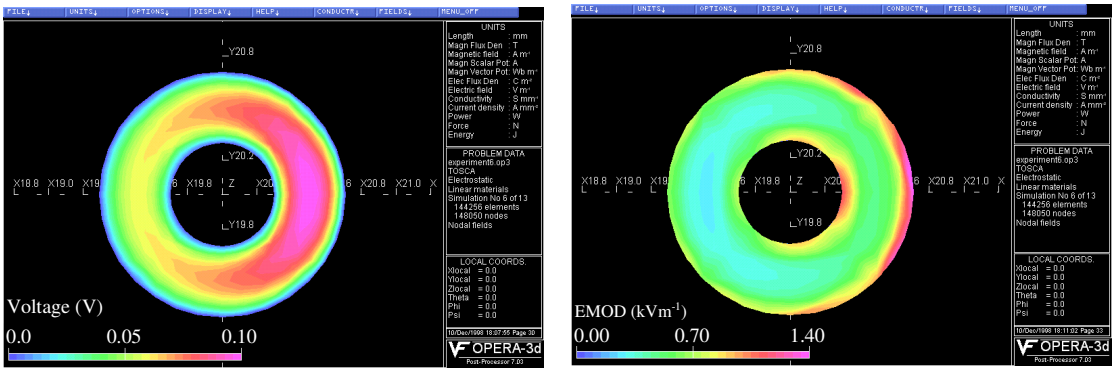

Figure 4.2.9: The voltage and electric field induced in the PTFE insulation in the probe by a 1mm^2, 1μCm^{-2} charge distribution 3mm to the right of the probe axis.

The graphs in figure 4.2.10 show the obtained ϕ-function for the probe 25mm away from the ground plane, with the probe 1mm away from the insulating surface with a relative permitivity of 2.2 (this is the relative permitivity of PTFE). The ϕ_x and ϕ_y functions are shown, these were defined in figure 2.2.5, they combine orthogonally to produce the full ϕ-function otherwise known as the probe response function. The origin of the graphs is the centre of the probe. The ϕ_x-function is symmetrical about the origin this is obvious when considering the symmetry of the problem.

Positive distances on the ϕ_y-function refer to points above the probe axis and negative ones below. This explains why the ϕ_y-function is not symmetrical; elements closer to the ground plane make less contribution than those the same distance above the probe.

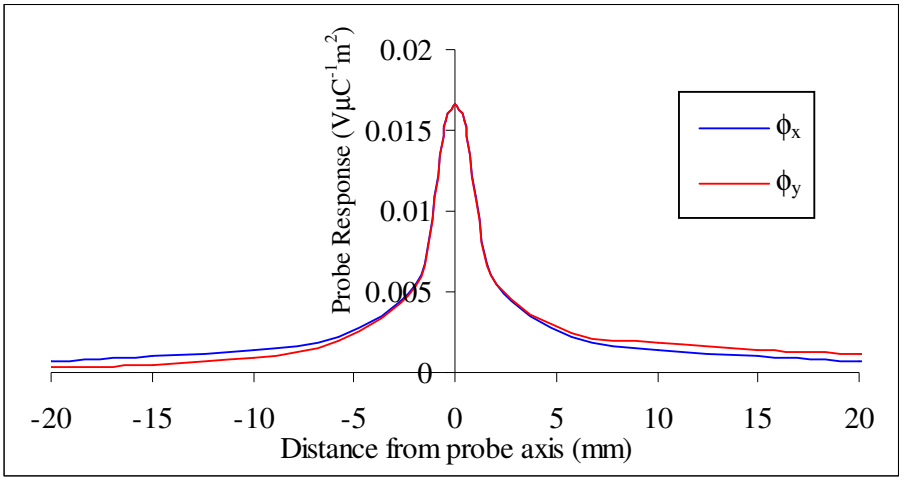

Figure 4.2.10: The ϕ-function for the probe 25mm above the ground plane 1mm away from a surface with a relative permitivity of 2.2.

Figure 4.2.11 shows the probe response function when the probe is only 5mm above the ground plane. The functions value directly under the probe axis is almost exactly the same as for the probe further away from the ground plane though slightly less: 0.01657 as opposed to 0.01664 $V\mu C^{-1}m^2$. However the ϕ_x function reduces to zero more quickly. Horizontally distant charges make a much smaller contribution to the total probe voltage when close to the ground plane.

The ϕ_y function stops at –5mm when it reaches the ground plane.

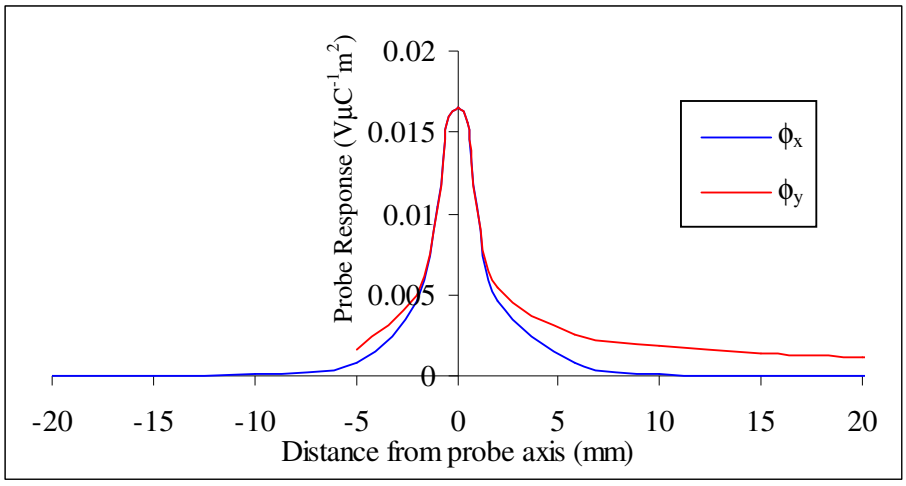

Figure 4.2.11: The ϕ-function for the probe 5mm above the ground plane 1mm away from a surface with a relative permittivity of 2.2.

To study the operation of the probe further, the probe-surface separation was changed to 0.5mm. The ϕ_x function obtained is compared with the 1mm case in Figure 4.2.12. Moving the probe closer to the surface dramatically increases the peak value and makes the overall shape of the function sharper; it effectively increases the resolution of the probe. This effect is discussed further in the next section. The important point is that the probe is sensitive to variations in probe-surface separation, which puts emphasis on the mechanical precision of the scanning system.

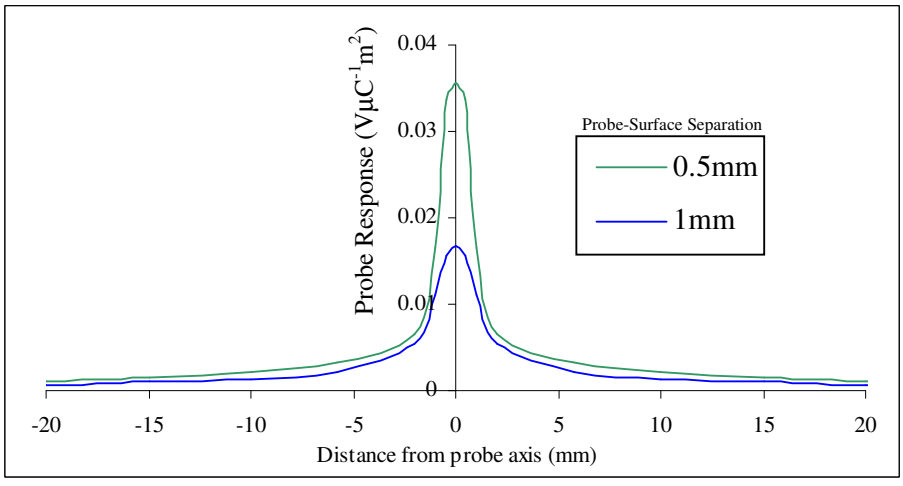

Figure 4.2.12: The ϕ_x-functions for the probe at two different probe-surface separations for insulator with a relative permittivity of 2.2.

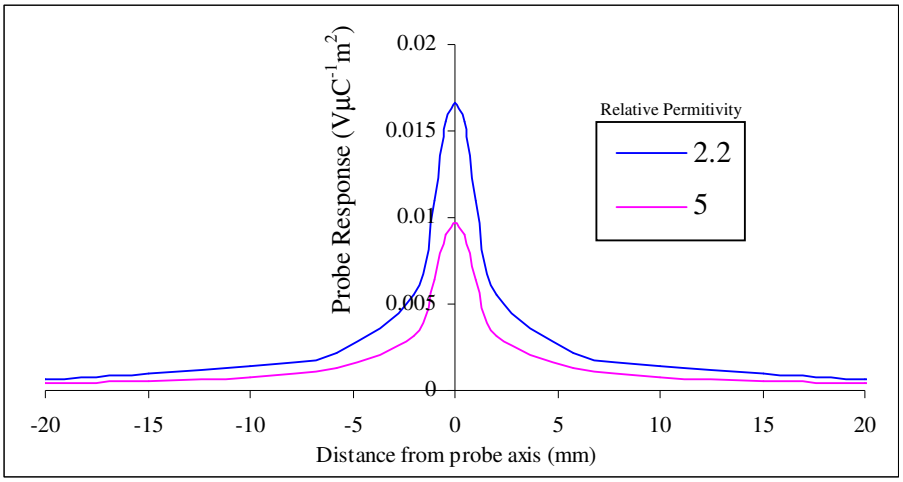

Figure 4.2.13: The ϕ_x-functions for the probe 1mm above the surface for two different material permittivities.

Different insulator materials were scanned so it was also necessary to calculate the ϕ-functions for materials of different permittivities. In general the higher the permittivity the smaller the values in the ϕ-function. Figure 4.2.13 shows two ϕ_x-functions for materials with a relative permittivities of 2.2 and 5.

4.2.3 Probe Calibration

In the earlier chapter on charge measurement the probe response to a calibration test piece was found. The calibration test piece consisted of a metal strip that could be set at a potential. To check the calibration of the whole system a strip on the surface of the modelled insulator the same size as that on the calibration test piece was set at a voltage. The probe voltage calculated was only 1% more than the average of the actual measured values. This put great confidence in the modelling procedure and in the overall reliability of the scanning system.

4.3 Effects of the Φ-Matrix

4.3.1 Introduction

Distribution Appearance

The effectiveness of the scanning technique has been clearly demonstrated in the Experiments Chapter. The measured probe voltage distributions were successfully converted to charge distributions that very closely matched the obtained dust figures. The calculated charge distributions are clearly different in appearance from the probe voltage distributions; a good qualitative observation is that they appear 'sharper' or 'better defined'. The Φ-Matrix solution procedure effectively removes the probe response characteristic, or ϕ-function, from the probe voltage distribution.

The main variable in the solution procedure is the ϕ-function itself. This section studies the effect the shape of the ϕ-function has on the appearance of the calculated charge distribution.

Shape of the ϕ-Function

If the probe only responded to charge directly beneath its axis then the appearance of the probe voltage distribution would be identical to the charge distribution. This is the assumption made in the simple capacitative model of probe operation (Section 1.3.3), where each probe voltage measurement corresponds directly to a charge density measurement. The simple capacitative model of probe operation corresponds to a probe response or ϕ-function that is zero everywhere apart from directly under the probe, as illustrated by the red function in figure 4.3.1(a).

The 'width' of the ϕ-function can be slowly increased from this simple capacitive case, as shown in figure 4.3.1(a), and its effect on the appearance of the derived charge distribution observed.

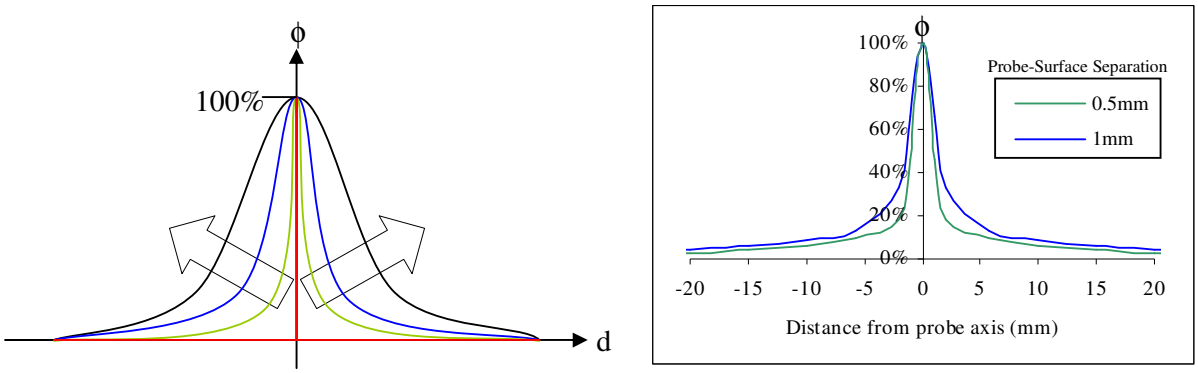

(a) Increasing the width of the ϕ-function corresponds to probes with poorer resolution.

(b) The normalised ϕ-functions for two different probe-surface separations

Figure 4.3.1: Different shaped ϕ-functions correspond to different probe arrangements.

The width of the ϕ-function changes for different probe-surface separations as shown in figure 4.3.1(b). The same probe closer to the surface has a better resolution. The dimensions and construction of the probe and the permittivity of the insulator upon which the charge is measured also affect the width of the ϕ-function. To allow comparison all the ϕ-functions are normalised so that the peak value directly under the probe corresponds to 100%. It is the appearance of the distribution that is under study here not its magnitude. To borrow a term from filter design the width of the ϕ-function can be referred to as its selectivity or Q.

4.3.2 Experiments

Probe Voltage Distribution

To allow the effect of the Φ-Matrix to be studied an example probe voltage distribution was required upon which the calibration procedure was undertaken for different width ϕ-functions. To reduce the length of time to solve the distribution each time a medium sized probe voltage distribution consisting of 40×40 measurements was employed. The probe-surface separation was set at 1mm. The distribution was obtained by applying a negative impulse to the sharp rod above a PTFE insulator specimen. The details of the voltage that caused the distribution are not of importance here.

As was shown in Section 4.2, the exact shape of the ϕ-function does vary slightly as the probe moves closer to the ground plane. This is only really important for the contribution of distant charges close to the ground plane. To avoid this complication and allow a constant shape to the ϕ-functions the distribution was scanned at the top 40 mm of a 100mm tall insulator specimen. The grounding connector for the test object mounting spigot on the scanning platform was also removed. The measurements were thus all far from the ground plane and the same shape ϕ-function could be used throughout each Φ-Matrix. Figure 4.3.3 shows the probe voltage distribution used in these experiments.

Vary ϕ-Function Width

The first experiment was to simply use a set of widening ϕ-functions. Figure 4.3.2 shows the set of ϕ-functions tested. The shape of the functions used was arbitrarily chosen. Each ϕ-function was used to generate a Φ-Matrix, which was then inverted and multiplied by the voltage distribution as usual. The resulting distributions are shown on the next page.

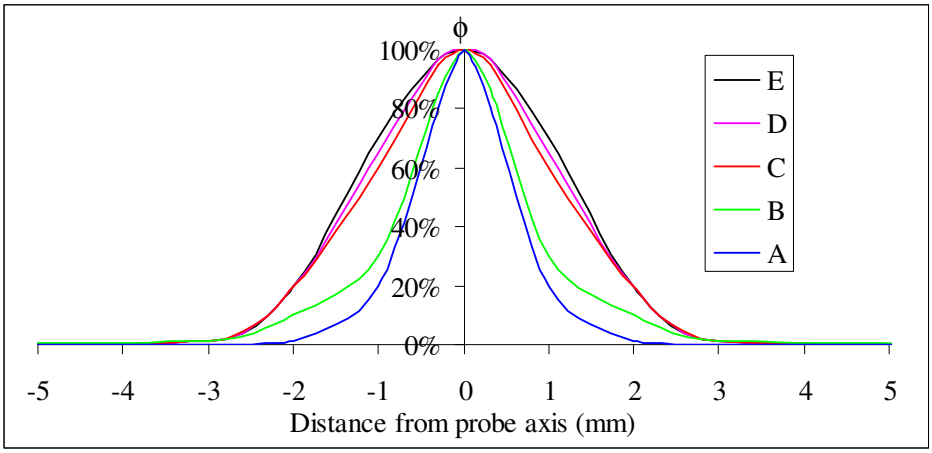

Figure 4.3.2: Graphs showing the first set of slowly increasing width ϕ-functions tested.

The distributions are displayed as 3-dimensional surfaces as opposed to the contour maps used previously, this because they best show the changing shape of the distribution.

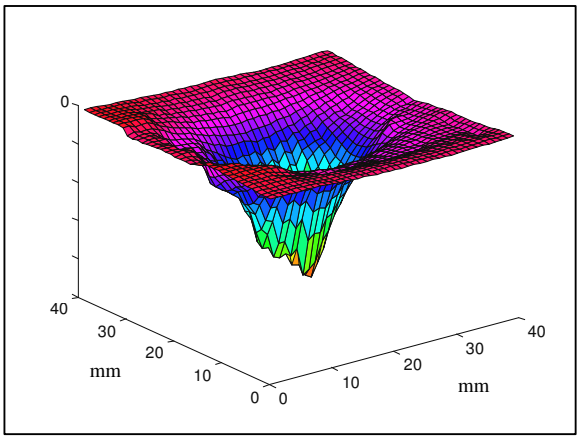

Figure 4.3.3: The shape of the original distribution

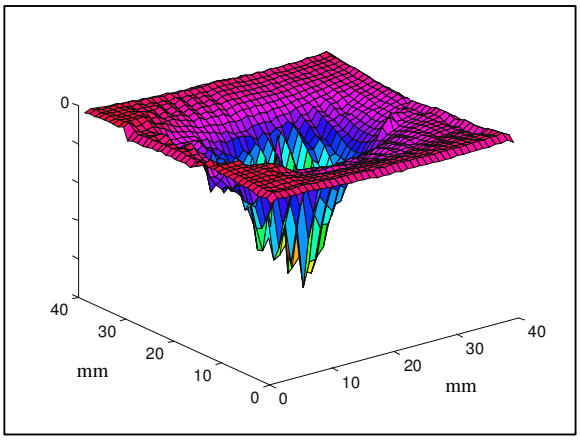

Figure 4.3.4: The distribution created by ϕ-function A.

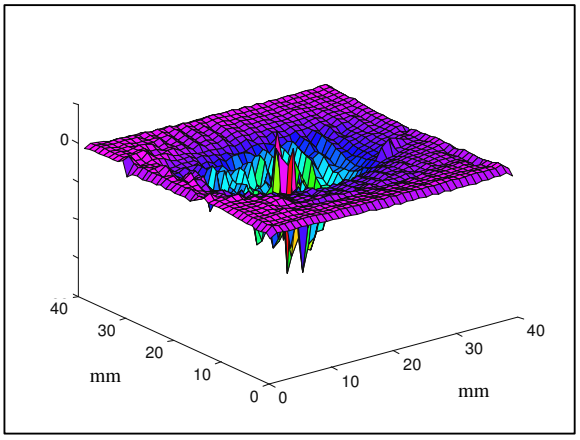

Figure 4.3.5: The distribution created by ϕ-function B.

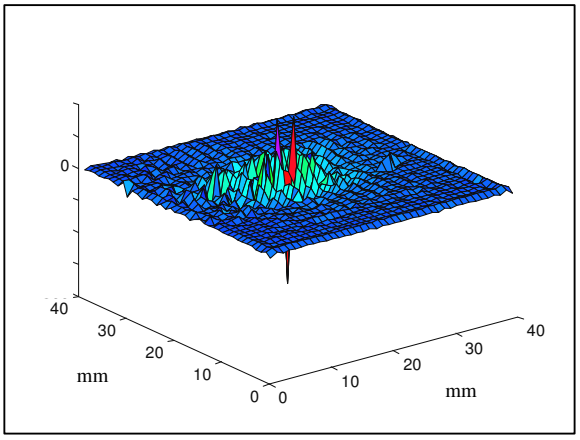

Figure 4.3.6 : The distribution created by ϕ-function C.

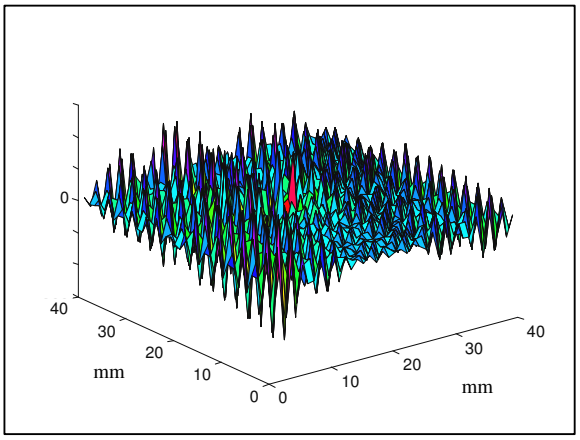

Figure 4.3.7: The distribution created by ϕ-function D.

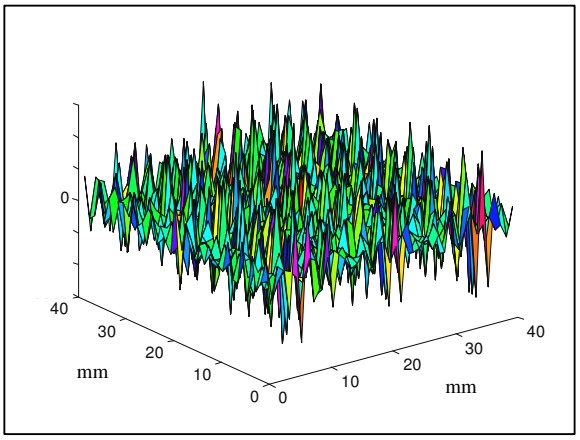

Figure 4.3.8: The distribution created by ϕ-function E.

As the ϕ-function slowly gets wider the shape of the resulting distribution slowly changes, it becomes more localised, local minima and maxima become more defined. This continues until at a specific ϕ-function width, large disturbances begin to appear in the distribution. If the width is increased slightly further these disturbances swamp the distribution and it becomes completely unrecognisable.

Vary ϕ-Function Skirt Height

There is a second factor that defines the shape of a ϕ-function: the rate at which the skirt of the function decays. This corresponds to the contributions from distant charges. The previous test ϕ-functions only varied the width, and they all decayed to zero by 5mm from the probe axis. The actual calculated ϕ-functions take much longer to decay to zero when the probe is some distance from the ground plane. To test the effect of the skirt decay rate the 4 different ϕ-functions shown in figure 4.3.9 were tested. The width of the ϕ-function is based on that for case C in the previous tests. The resulting distributions generated by the ϕ-functions are shown in the figures on the next page.

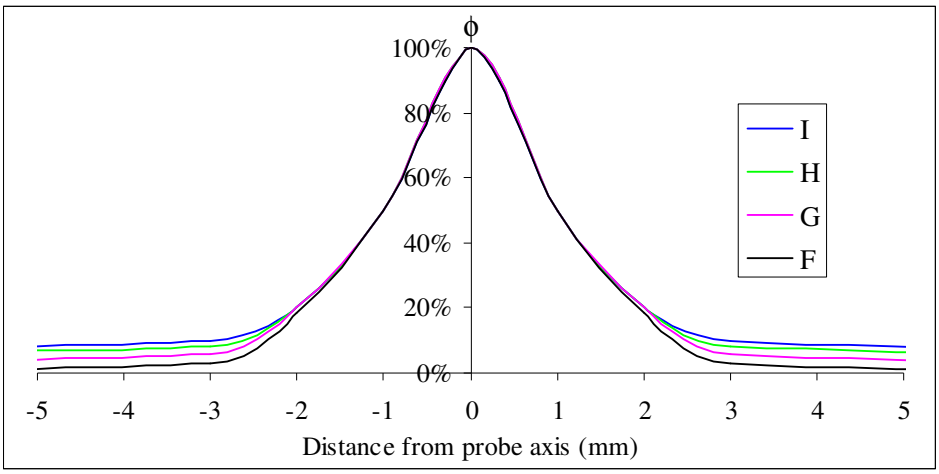

Figure 4.3.9: Graphs showing the second set of ϕ-functions tested with a slowly increasing skirt.

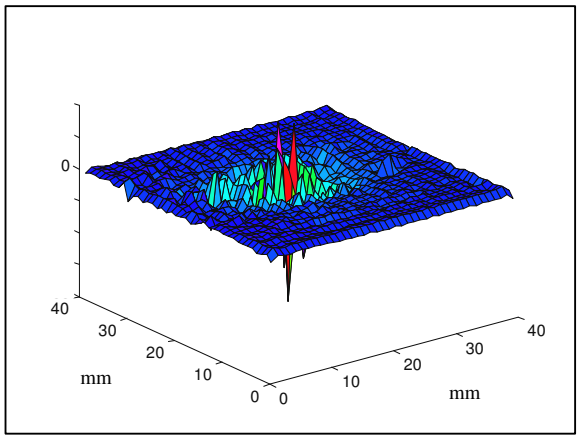

Figure 4.3.10: The distribution created by ϕ-function F.

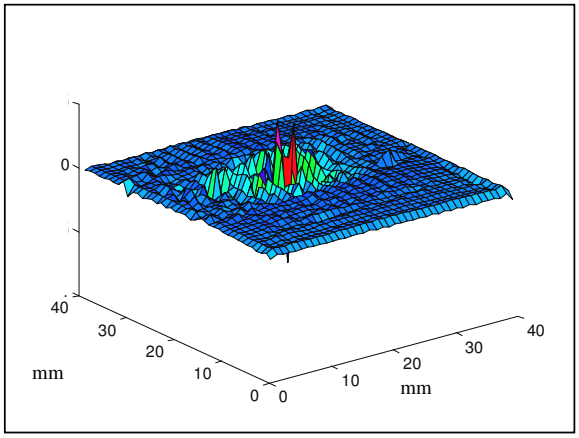

Figure 4.3.11: The distribution created by ϕ-function G.

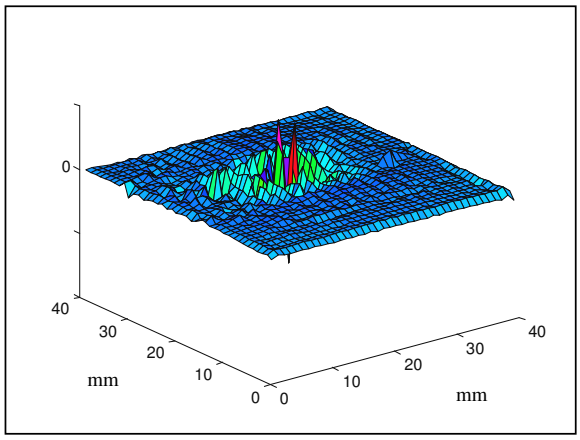

Figure 4.3.12: The distribution created by ϕ-function H.

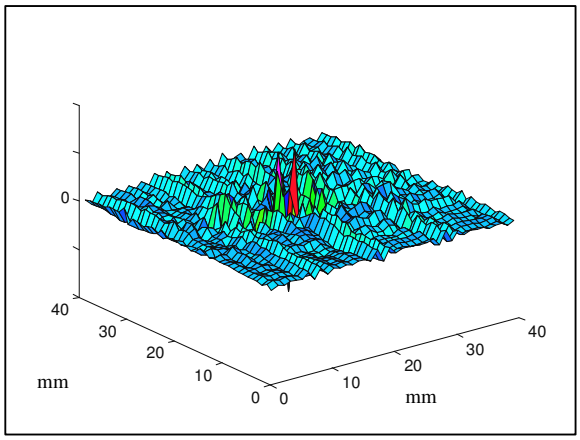

Figure 4.3.13: The distribution created by ϕ-function I.

Changing the level of the skirt caused less violent changes in the generated distributions, however a limit was still reached beyond which the disturbances became significant as is shown in Figure 4.3.13.

The Limiting Case

By first increasing the width of the ϕ-function then increasing the height of the skirt a limiting case can be found beyond which the generated distribution becomes unstable. The limiting case appears to be ϕ-function H. This function is compared with the actual ϕ-function of the probe that first measured the probe voltage distribution in figure 4.3.14.

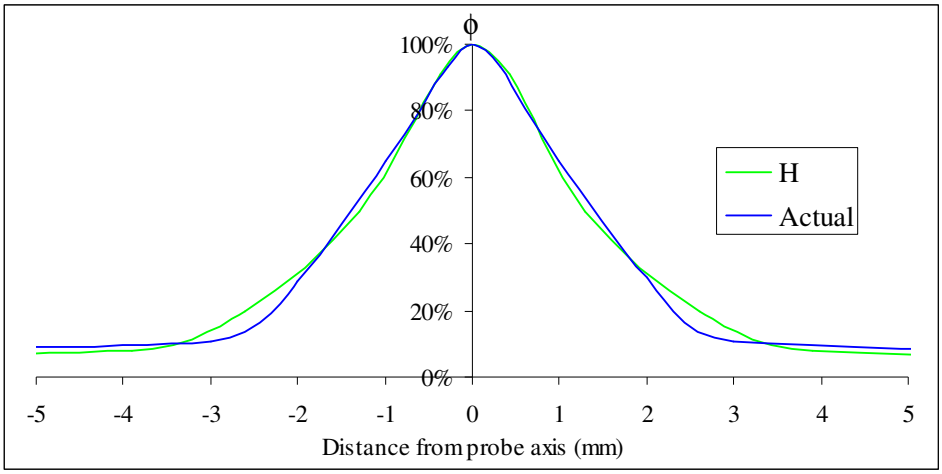

Figure 4.3.14: Comparison between the calculated probe response and the limiting case H found by varying the shape of the ϕ-function.

As was said earlier the Φ-Matrix technique effectively removes the probe response characteristic from the distribution. The results obtained here suggest that the removal of a probe response characteristic that is wider than the response of the probe that actually measured the distribution will cause the distribution to 'blow-up'. Using ϕ-functions beyond the limiting case is effectively like trying to find a charge distribution from a voltage distribution that could never have been produced by a probe of that resolution. The Φ-Matrix technique is the solution of a large number of simultaneous equations, when the distribution 'blows-up' it suggests there is no solution to the equations and the generated distribution descends into chaos.

It is important to remember that the voltage distribution used to test the effect of the varying ϕ-function was measured experimentally and will therefore include experimental error. As the ϕ-function nears its limiting case the solution to the equations will become unstable and the small experimental errors will be amplified. This is seen in small peaks appearing in the distributions near the limiting case. It is also the reason why all the solved charge distributions shown in the previous chapter were displayed as contour maps. When displayed as a 3-dimensional surface the small peaks caused by amplified experimental error made the shape of the distributions harder to see.

4.3.3 Theorem

The similarity between the limiting case and the calculated values is clear and this leads to the proposal of a new theory:

The limiting values of the ϕ-function will resolve a charge distribution from a probe voltage distribution.

If the stated theory holds true, it should be possible to solve a charge distribution without doing a simulation to find all the values for the ϕ-functions. The overall shape of the ϕ-function could be found by obtaining the limiting ϕ-function. The only value then required would be the ϕ(0) measurement for the charge directly under the probe, which would be used to scale the ϕ-function to the correct value.

The probe response is intrinsically part of each measured probe voltage distribution and it should be possible to remove it.

It follows that a program could derive a charge distribution by first simply calculating the ϕ(0) value using a simple capacitive model (this procedure could be easily calibrated using test pieces to estimate the relevant capacitances). Then using successive iterations with Φ-matrices generated using different ϕ-functions, the limiting ϕ-function could be found. Thus this technique not only finds the charge distribution but it also finds the probe response function.

A very large amount of processing power would be required to solve high-resolution distributions in a reasonable time and the iteration procedure would have to be optimal in order to reduce the number of matrix inversions required. If the solution is unstable or the voltage distribution not accurate enough, this may introduce complications or limitations to this technique.

4.4 Electrode Modelling

4.4.1 Introduction

The electrode arrangement was also modelled; this allowed the ambient fields present on the insulator surface to be evaluated.

4.4.2 Model

Figure 4.4.1 shows the electrode arrangement modelled. The symmetry of the problem meant that only half of the geometry needed to be modelled. This reduced the solution time and allowed more elements to be used for greater accuracy. OPERA provided the facilities in post processing to mirror the model and display the whole insulator. The rod-surface separation was set at 0mm, 5mm and 10mm. An insulator with a relative permitivity of 2.2 was used to represent the PTFE insulator specimen. The ground plane at the bottom of the model was set at 0V and the voltage on the rod was set at 1V. This provided the per unit field and voltage distribution.

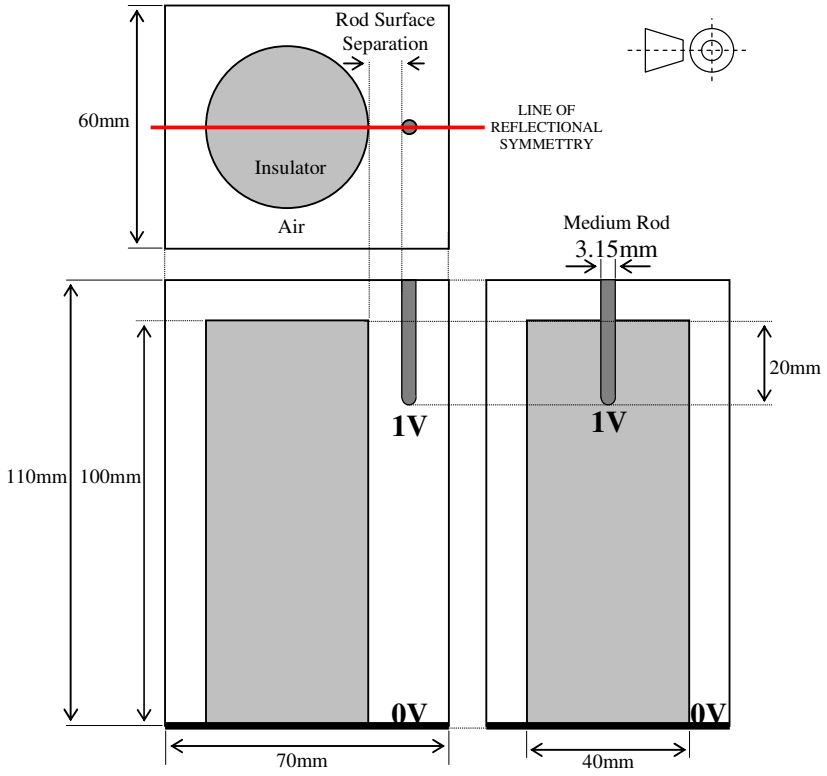

Figure 4.4.1: The model of the electrode arrangement.

4.4.3 Results

The per-unit voltage and field distributions can be used to find the field produced by any voltage applied to the rod. This is achieved by simply multiplying the per-unit field values by the voltage applied to the rod.

Figure 4.4.2 shows the per-unit voltage and field strength distributions for the rod in contact with the insulator. The distributions are shown directly on a 3-D view of the insulator.

Figure 4.4.3 and 4.4.4 show the distributions for rod-surface separations of 5mm and 10mm respectively.

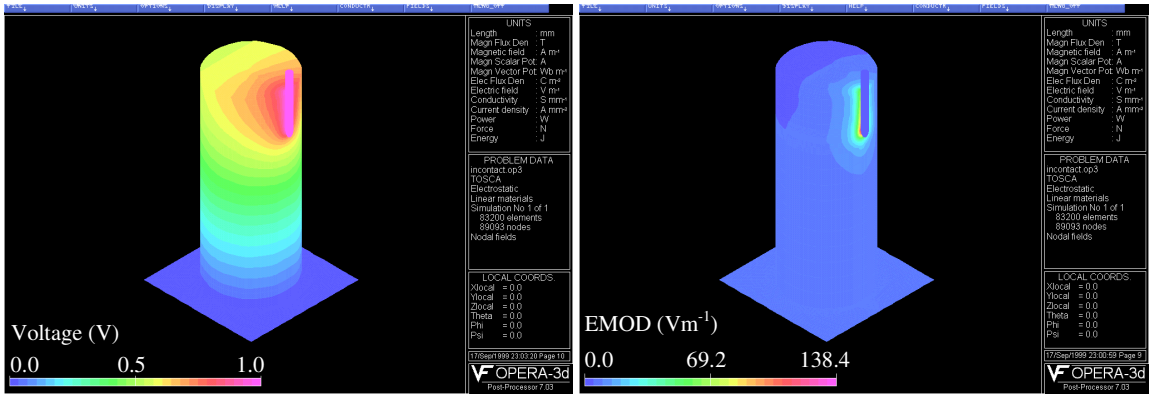

Voltage Distribution *Electric Field Strength*

Figure 4.4.2: The results obtained with the rod in contact with the insulator.

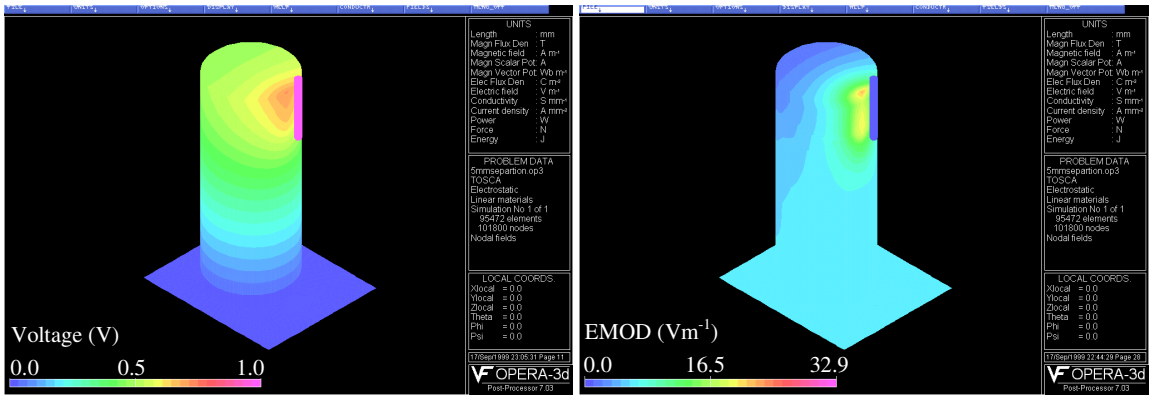

Voltage Distribution *Electric Field Strength*

Figure 4.4.3: The results obtained with the rod 5mm away from the insulator.

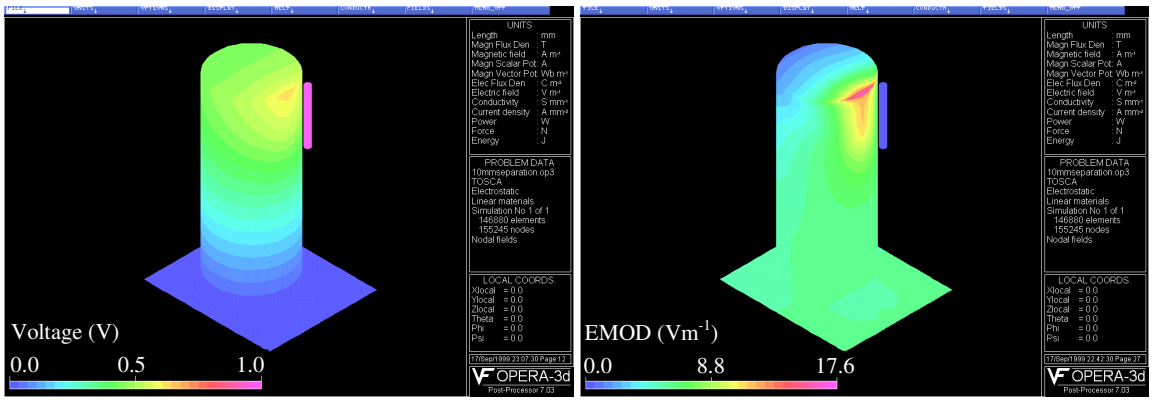

Voltage Distribution *Electric Field Strength*

Figure 4.4.4: The results obtained with the rod 10mm away from the insulator.

The 3-dimensional views of the distributions are only useful for providing a feel for the shape the field present on the insulator surface. To allow accurate comparisons with the charge distributions obtained in the experimental chapter, the field on the insulator surface must be displayed as a contour map.

The figures on the following pages show the per-unit contour maps for voltage and field strength on the insulator surface for three different rod-surface separations. The 5% per-unit voltage contours are shown. Per-unit field strength contours are shown up to $20Vm^{-1}$ in $1Vm^{-1}$ steps. Above this value the field contours become too close together to display clearly.

To best illustrate the field in the region near the probe tip, the field along a path on the insulator surface was found. The fields on a vertical path along the entire height of the insulator nearest the rod are shown in figures 4.4.10 and 4.4.11. These graphs illustrate the maximum fields present on the insulator surface for each rod-surface separation.

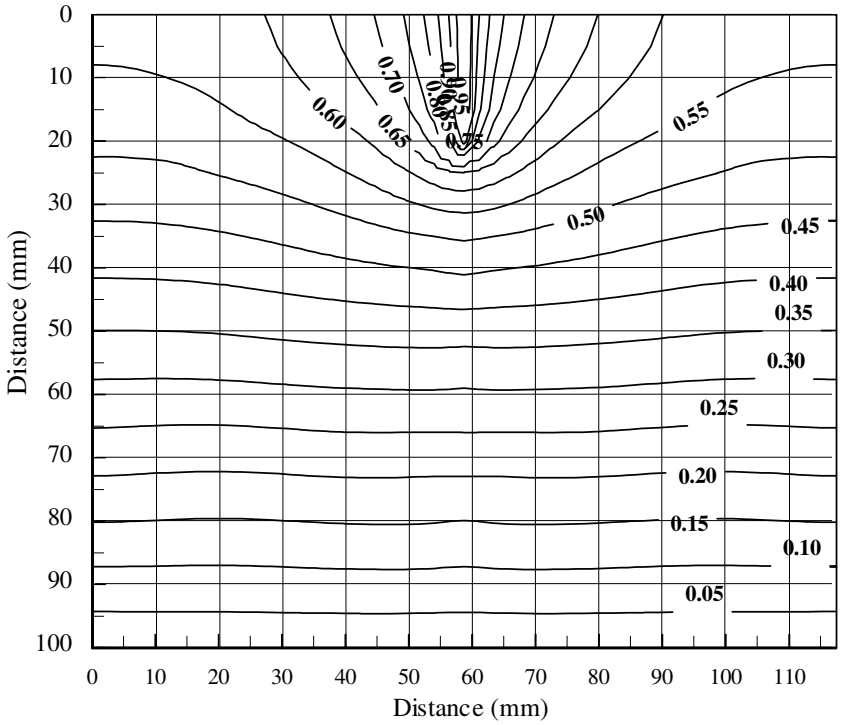

Figure 4.4.5: The per unit voltage distribution on the surface of the insulator for the rod in contact.

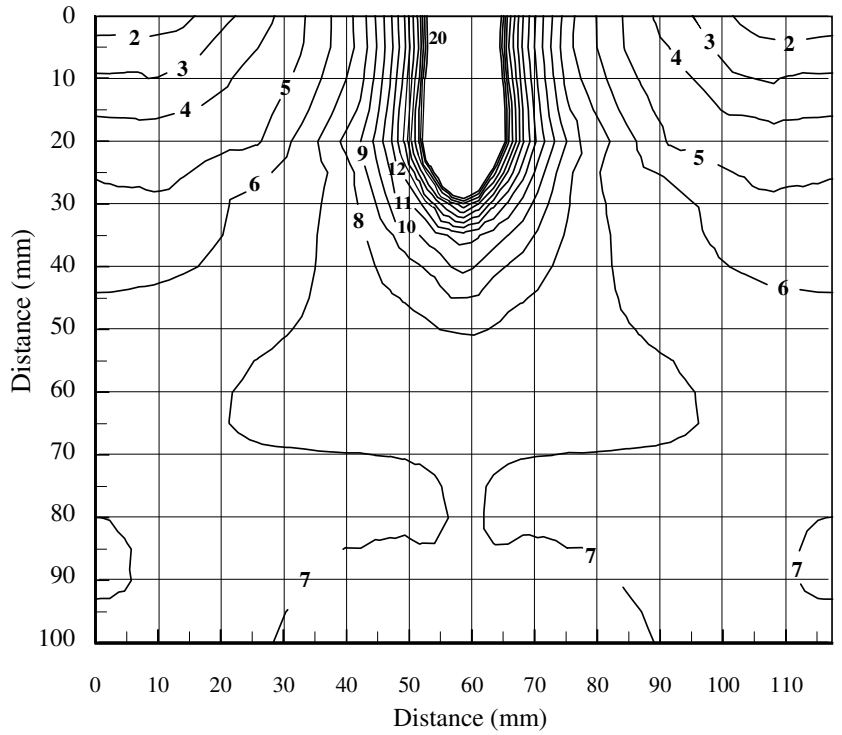

Figure 4.4.6: The per unit field strength on the surface of the insulator for the rod in contact.

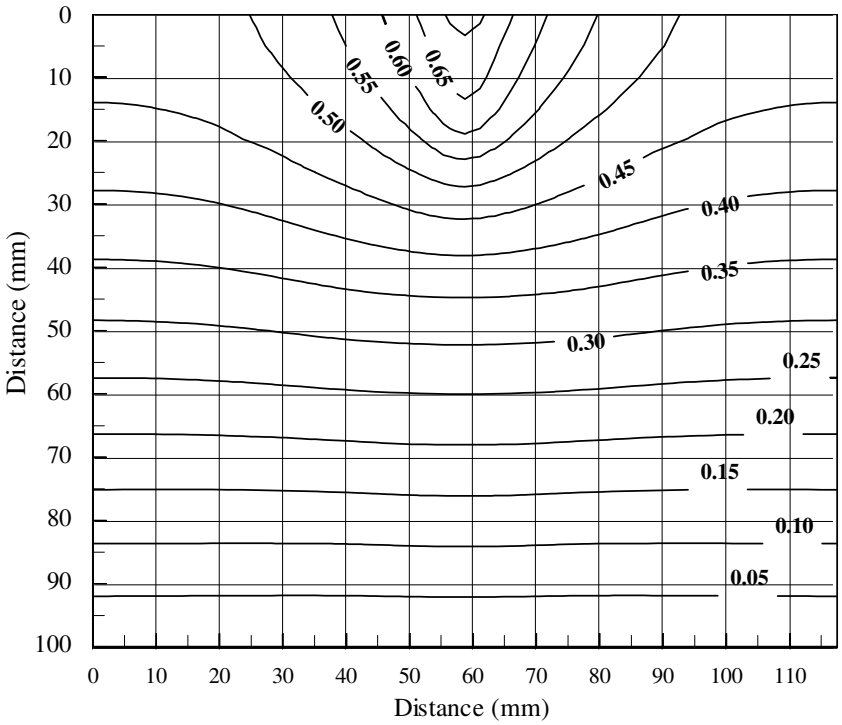

Figure 4.4.7: The per unit voltage distribution on the surface of the insulator for the rod 5mm away.

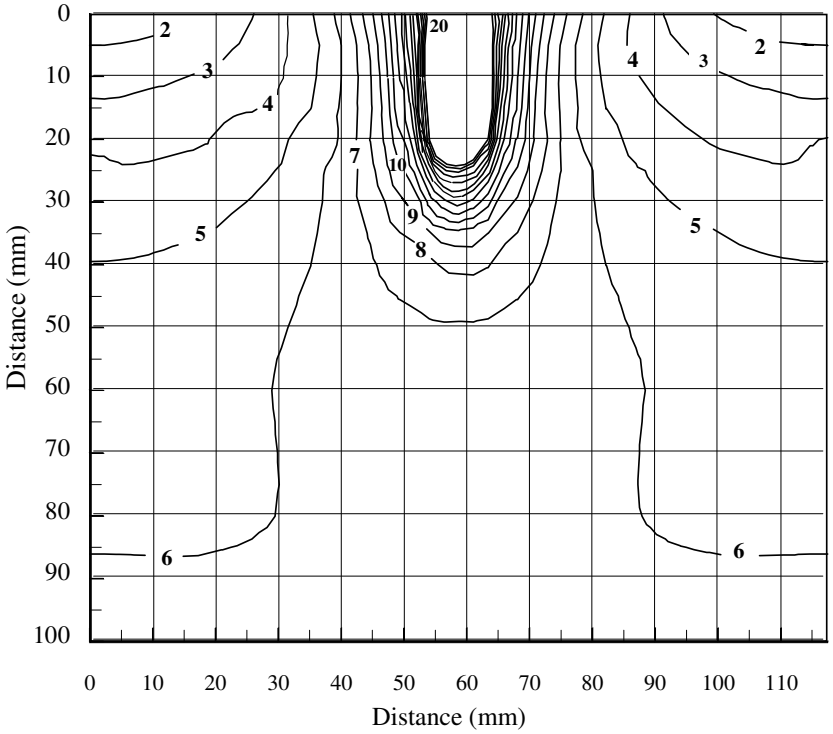

Figure 4.4.6: The per unit field strength on the surface of the insulator for the rod 5mm away.

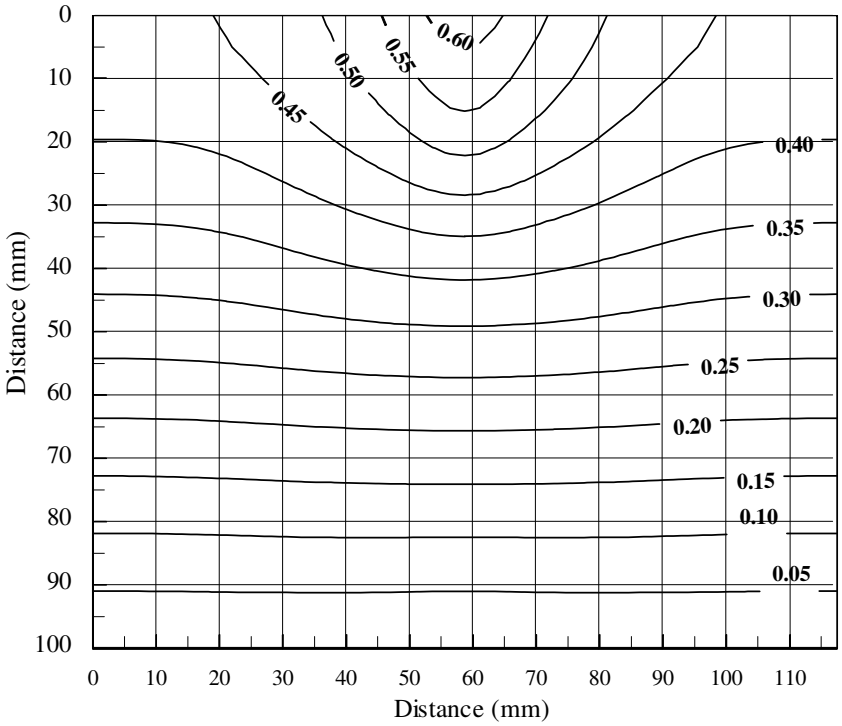

Figure 4.4.8: The per unit voltage distribution on the surface of the insulator for the rod 10mm away.

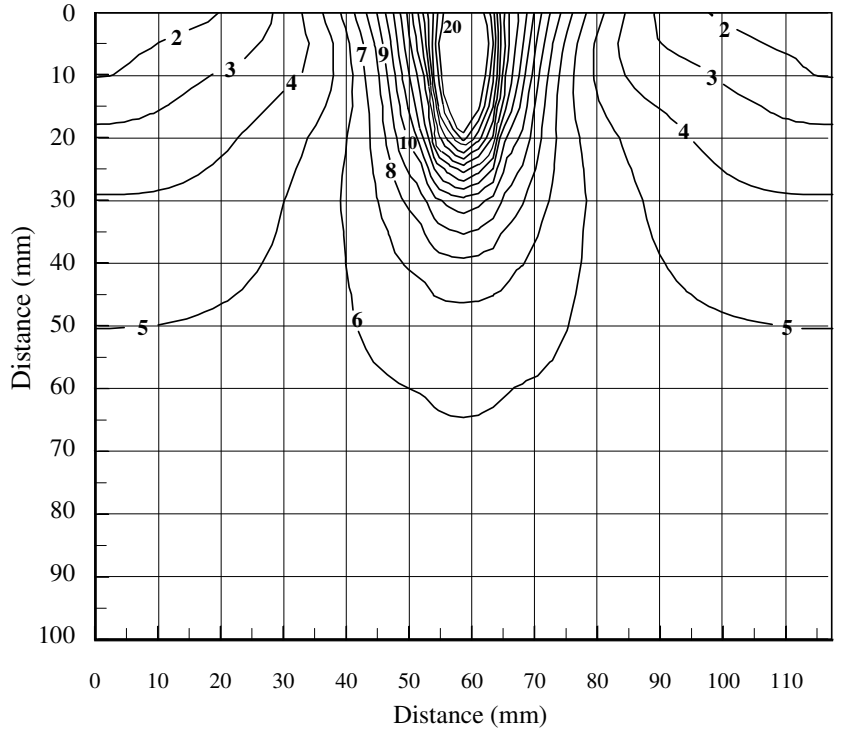

Figure 4.4.9: The per unit field strength on the surface of the insulator for the rod 10mm away.

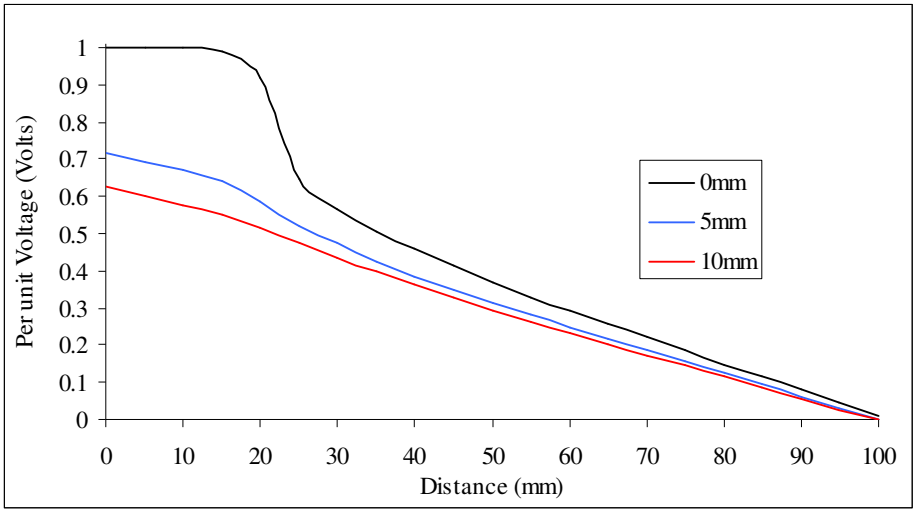

Figure 4.4.10: The per unit voltage distribution on a path running down the insulator surface parallel to the rod, starting at the top. Different rod-surface separations are shown.

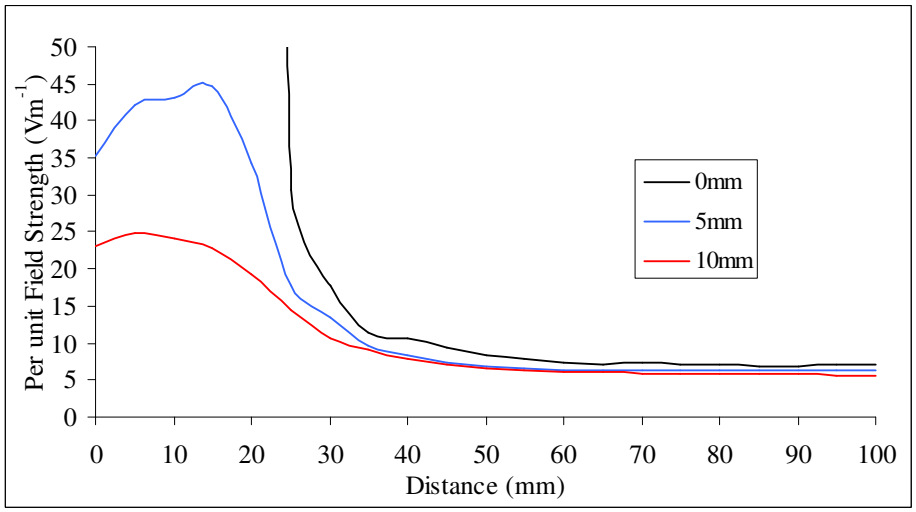

Figure 4.4.11: The per unit field strength on a path running down the insulator surface parallel to the rod, starting at the top. Different rod-surface separations are shown.

When the rod is in contact with the surface the electric field strength near where the tip touches increases rapidly because of the triple-junction created where the rounded probe tip touches the surface. The maximum value that this field reaches depends on the actual size of the triple junction. In a simulation, this triple junction could be made infinitely thin, thus the localised field would tend to infinity. The model employed here used a final triple junction width created where the rod touches the surface of 0.1mm, which produced a maximum per-unit field strength of $366 Vm^{-1}$.

4.5 Surface Charge Modelling

4.5.1 Introduction

The surface charge scanning system developed is unique in that it has provided the first ever data on the surface charge deposited by ***individual*** streamers propagating across a practical insulator arrangement. Previous calibrated systems have either not been of a high enough resolution (Ootera and Nakanishi, 1988) or were on a microscopic scale with small test cells (Iizuka et al, 1997).

This section studies some of the data obtained in conjunction with field studies.

4.5.2 Instantaneous Geometric Field

The field on the surface of the insulator is an important quantity because it is in this region that the streamers interact with the surface. In the previous section the electric field strength on the surface set up by the geometric arrangement of the electrodes was calculated. This is the magnitude of the electric field strength on the surface. The direction of the field can be found from the calculated voltage distribution: the field lines are orthogonal to the lines of equal potential.

The charge density maps can be combined with the calculated geometric field produced by the instantaneous voltage applied to the electrodes at the time of discharge. This provides a view of the ambient field strength in which the streamers propagated. Obviously the actual electric field present at the propagating streamer tips will be greatly enhanced by the charge densities in the streamer head. It also useful to remember what the charge density maps represent: the charge footprint or debris left after a discharge.

Similarly the charge density maps can be combined with the calculated voltage distribution to view the direction of the field on the surface.

Three example distributions are shown for three different rod-surface separations.

Medium Rod In Contact

Figure 4.5.1 shows the charge density distribution produced by a single discharge event. The rod was in contact with the PTFE insulator and the instantaneous voltage applied to

the rod when the discharge occurred was **+12.7kV**. The ambient per unit electric field strength on the surface of the insulator is also shown as contour lines superimposed on the charge density distribution. Thus the ambient field present at different points in the distribution can be found by multiplying the per unit field strength by 12.7×10^3. For example a per unit field strength of 4 corresponds to a field strength of $4\times12.7\times10^3 = 50.8\text{kVm}^{-1}$.

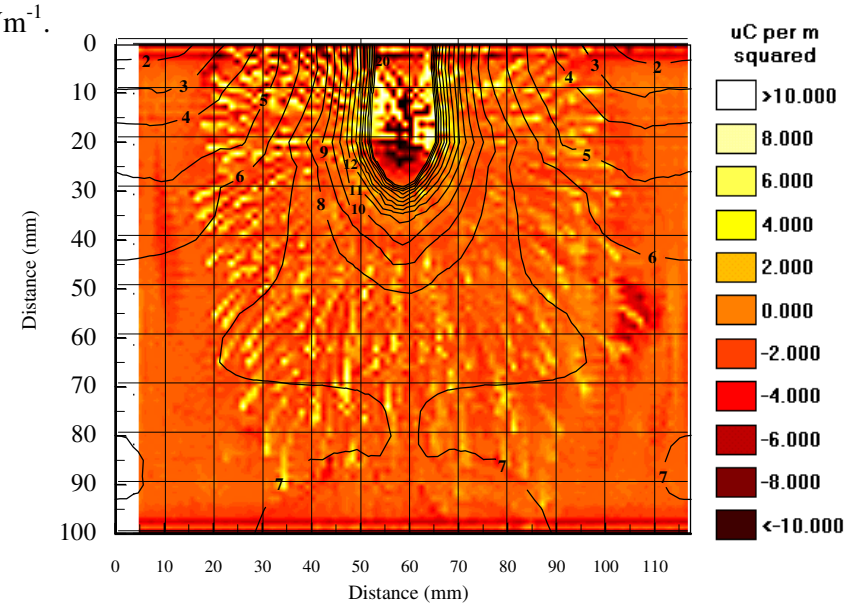

Figure 4.5.1: Combined charge density and per unit ambient field map for a discharge at an instantaneous voltage of +12.7kV with the rod in contact with the insulator.

Figure 4.5.2 shows the same charge density distribution with the calculated surface voltage distribution. The direction of the field is orthogonal to the lines of equipotential.

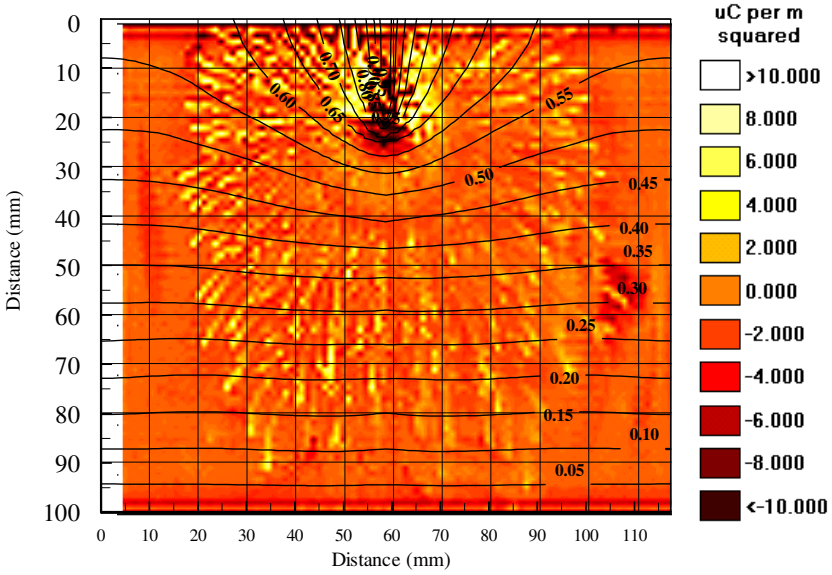

Figure 4.5.2: Combined charge density and per unit voltage distribution for a discharge at an instantaneous voltage of +12.7kV with the rod in contact with the insulator.

Rod 5mm Away

Figure 4.5.3 shows the combined surface charge density and ambient per unit field strength distributions for the rod 5mm away from the surface. The single discharge event occurred at an instantaneous voltage of **+18.3kV**.

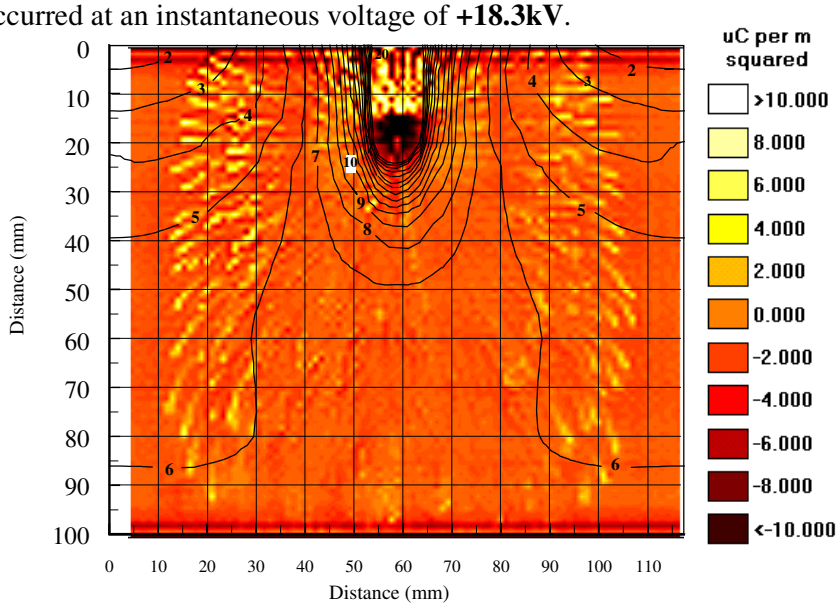

Figure 4.5.3: Combined charge density and per unit ambient field map for a discharge at an instantaneous voltage of +18.3kV with the rod 5mm away from the insulator.

Figure 4.5.4 shows the same charge density distribution with the calculated surface voltage distribution. The direction of the field is orthogonal to the lines of equipotential.

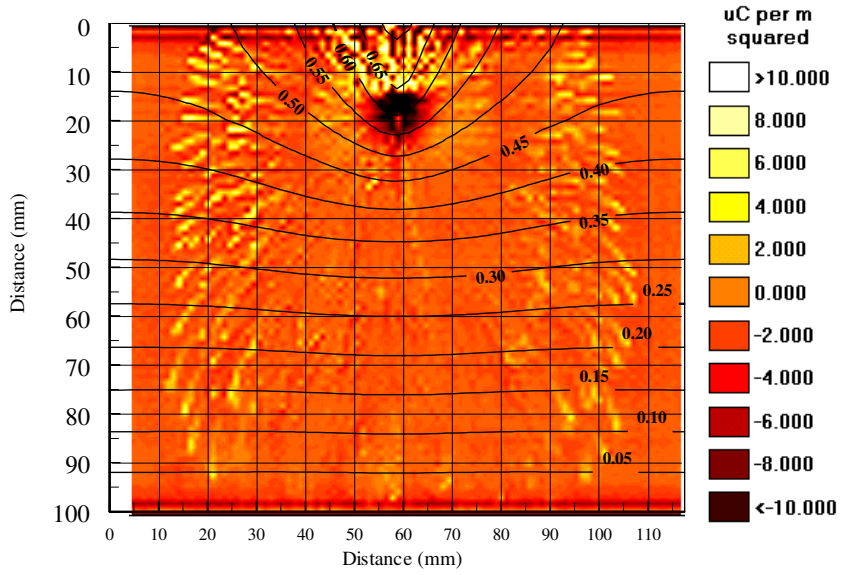

Figure 4.5.4: Combined charge density and per unit voltage distribution for a discharge at an instantaneous voltage of +18.3kV with the rod 5mm away from the insulator.

Rod 10mm Away

Figure 4.5.5 shows the combined surface charge density and ambient per unit field strength distributions for the rod 10mm away from the surface. The single discharge event occurred at an instantaneous voltage of **+29.5kV**.

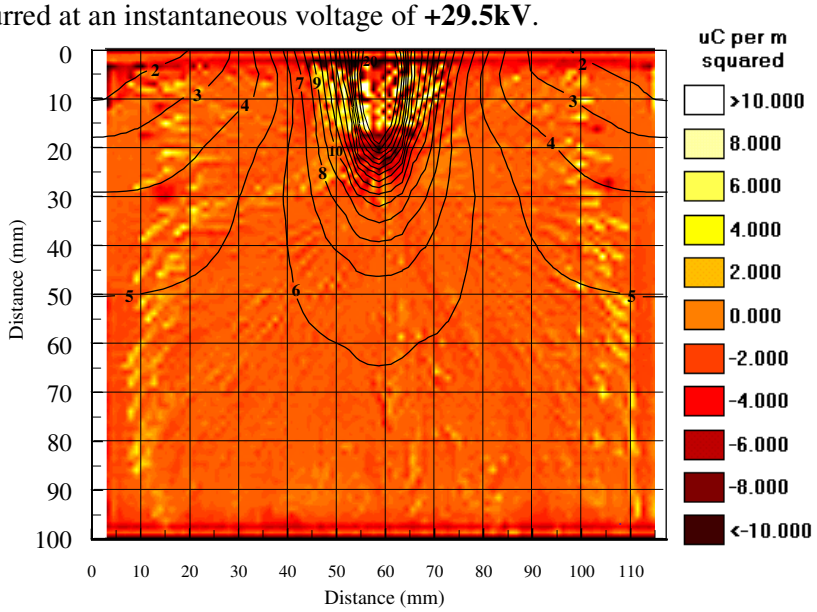

Figure 4.5.5: Combined charge density and per unit ambient field map for a discharge at an instantaneous voltage of +29.5kV with the rod 10mm away from the insulator.

Figure 4.5.6 shows the same charge density distribution with the calculated surface voltage distribution. The direction of the field is orthogonal to the lines of equipotential.

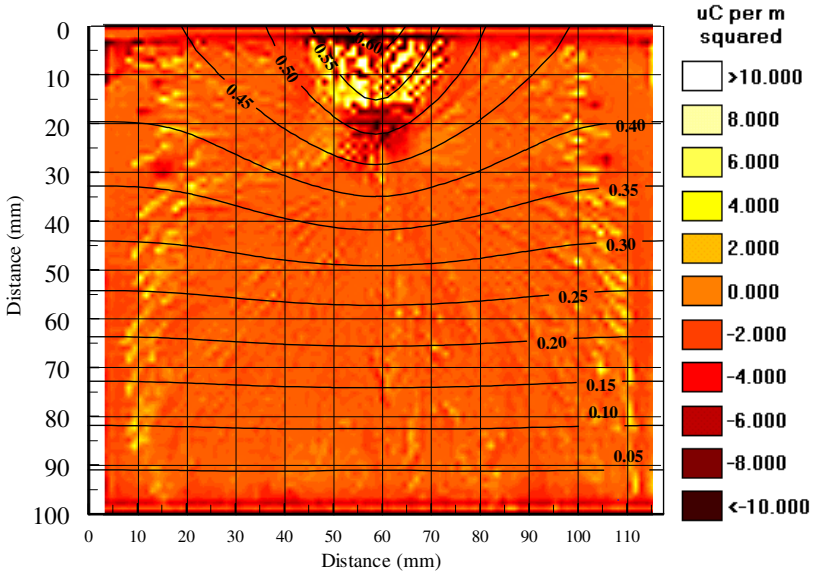

Figure 4.5.6: Combined charge density and per unit voltage distribution for a discharge at an instantaneous voltage of +29.5kV with the rod 10mm away from the insulator.

The distributions produced by the three different rod surface separations show that streamers are capable of propagating across the surface of PTFE in ambient applied fields as low as 50kVm^{-1}.

The distributions also show that in some places on the surface the streamers can actually propagate in almost the same direction as the equipotentials.

These two observations reinforce the significance of the electric field set up by the charge in the streamers themselves. To assess this field the charge in the deposited streamer trails is studied further.

4.5.3 Charge in a Streamer

The charged paths where the streamers stopped propagating are clearly visible around the perimeter of the deposited charge distributions. Using the Viewer software the charge density along these paths can be found.

It is important to remember the limit of resolution of the scanning system when considering these results. The actual width of the charged path will be less than the 1 mm wide surface elements. As a result when a streamer path cuts diagonally across the surface elements the streamer path becomes pixilated as shown in figure 4.5.7. When the viewer software calculates the charge density along a path it interpolates the surrounding values in the distribution using a cubic polynomial to find values for points on the path. The pixilation error manifests itself through the interpolation process as oscillations in the values along the path. The oscillations are caused by contributions to the interpolated values from neighbouring elements with little or no charge.

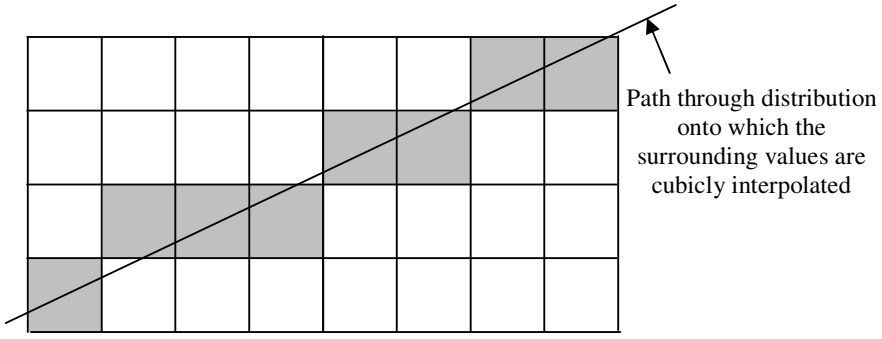

Figure 4.5.7: The limited resolution of the scanning system means that pixilation error introduces oscillations in path values.

Each charge distribution measured contained in the order of 50 streamer tail ends. This meant that every charge distribution could provide a wealth of previously unmeasured information. To illustrate this the charge distribution shown in figure 4.5.1 produced by the rod in contact is studied in further detail. This is a good example of the charge deposited by a typical surface discharge event.

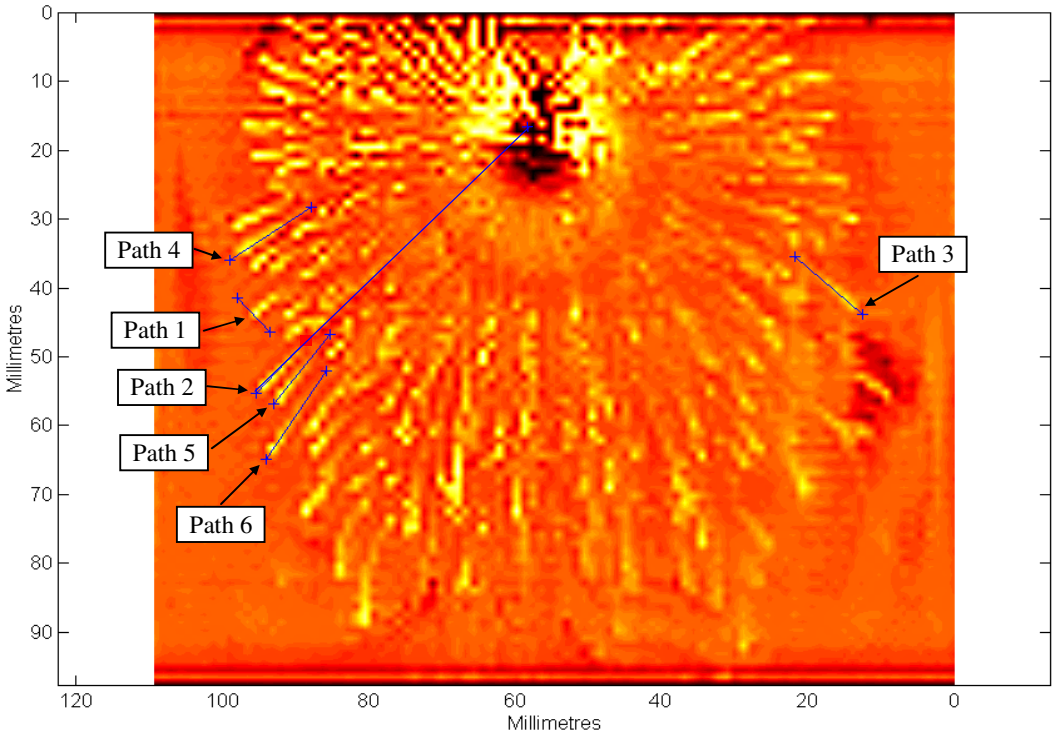

Figure 4.5.8: Charge density map showing the paths along which the surface charge density is calculated.

Figure 4.5.8 shows paths through the charge distribution. Path 1 cuts across the tip of a streamer. Path 2 goes from a streamer tip all the way back to the rod. The other paths show the charge along four streamer tips. Figures 4.5.9 to 4.5.14 show the calculated charge density along each path. Although the curves appear smooth it is important to remember that they were interpolated from points 1mm apart.

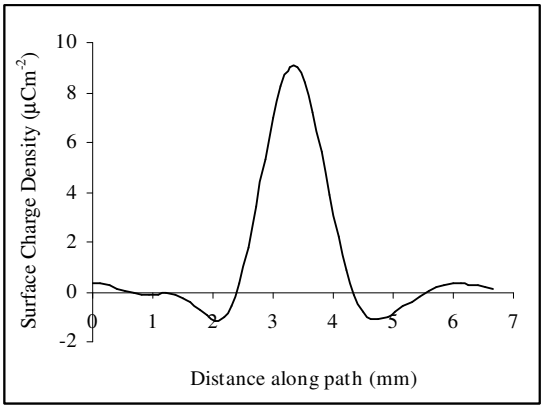

Figure 4.5.9: Charge density along path 1.

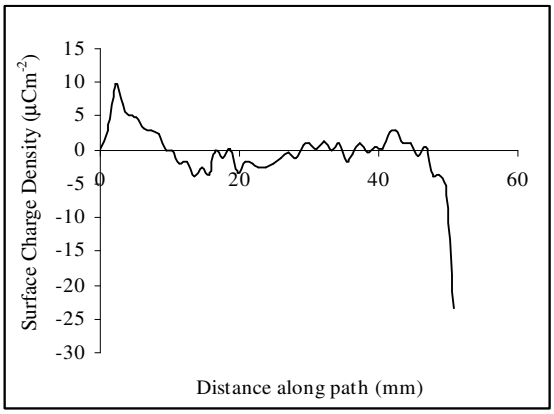

Figure 4.5.10: Charge density along path 2.

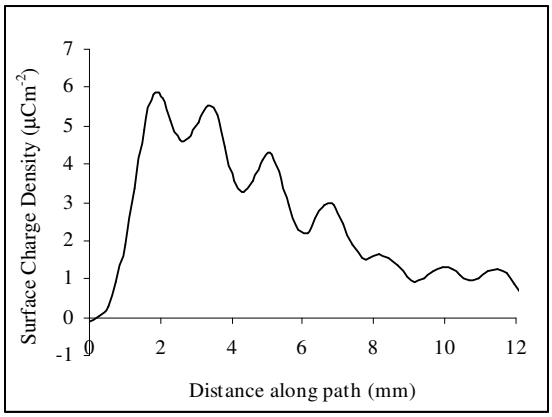

Figure 4.5.11: Charge density along path 3.

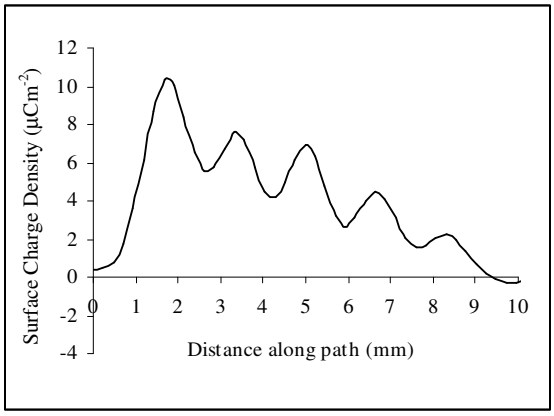

Figure 4.5.12: Charge density along path 4.

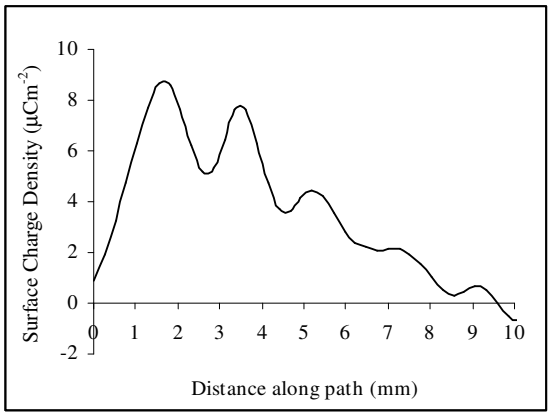

Figure 4.5.13: Charge density along path 5.

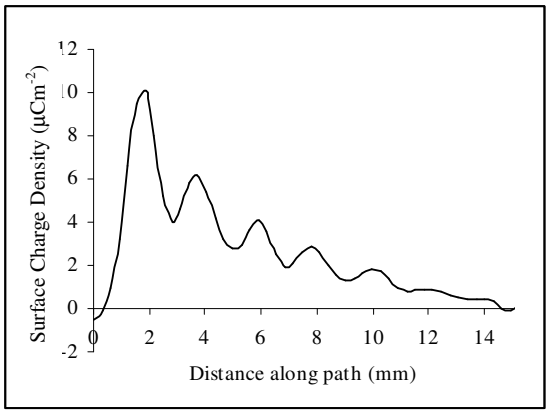

Figure 4.5.14: Charge density along path 6.

Figure 4.5.9 shows a slice through the tip of one of the streamer channels; the charge density peaks at about $+10\mu Cm^{-2}$ at the streamer tip. The width of the channel is the same as or less than the resolution of the probe (≈1mm).

Figure 4.5.10 shows the charge density along a path from a streamer channel tip, back to the rod electrode. The charge density jumps to the peak value then decays to below zero, then it follows a complicated pattern as other streamer channels cross the path. Finally near the rod electrode a large amount of negative charge is present.

This straight-line path may not always be exactly on the streamer trail, the distribution becomes very complicated away from the streamer tips. Only the first 15mm of the path is definitely directly on a streamer trail, beyond this several other streamer trails intersect the path. This high density of streamer channels makes the interpretation of the middle section of the distribution very difficult.

Figures 4.5.11 and 4.5.14 show the charge density along the tips of four different streamer channels. The maximum charge density is at the very tip of the streamer. The charge density rises to its peak value in less than one element width (≈1mm), then decays to half its peak value by about 5mm away from the peak. The interpolation process causes the oscillations.

4.5.4 Analysis of Charge Measurements

Peak Value

The charge density measurements give an indication of the distribution of charge within the discharge at the instant the streamers stopped propagating.

The maximum charge density observed in the streamer tips was $+10\mu Cm^{-2}$. This charge density was distributed over a $1mm^2$ element and so corresponded to a total charge of: $10\times10^{-6} \times 1\times10^{-6} = +10pC$. The exact distribution of charge over the $1mm^2$ element is not known; however it will not be distributed uniformly. The dust figures indicate that the charge is confined in a very thin path. The exact width of this path is unknown but the measurement of +10pC over $1mm^2$ can be used to say that at the streamer tips the charge channel contains 10pC per mm. This is illustrated in figure 4.5.15.

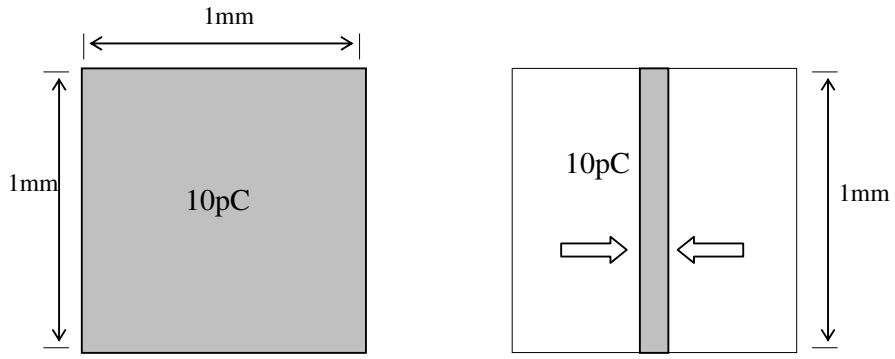

Figure 4.5.15: The measured value of 10pC over 1mm^2 can be also be thought of as 10pC per mm.

Decay Rate

The rate at which the charge density distribution decays along the streamer path can be estimated from the measured charge density distributions. This allows a direct measurement of the overall surface attachment coefficient, A.

Using the equation first derived in the Introduction (section 1.4.3) for charge in a streamer channel:

$q_s = N_o e^{-Ax}$ Where: A is the overall surface attachment coefficient.

The distance along the streamer channel by which the charge has fallen to half:

$$\frac{N_0}{2} = N_o e^{-Ax}$$

and by rearranging:

$$A = \frac{0.7}{x}$$

Experimentally measured half distances range from 3 to 5mm in the cases for PTFE, which gives values for the overall surface attachment coefficient that range from to 140 to 233 m^{-1}.

4.5.5 Modelling Surface Charge Measurements

Charge on an Element

Using the sort of charge densities measured in the experiments the electric field produced by the surface charge can be found. Figure 4.5.16 shows the simple model used: a very thin element of net positive surface charge with a 1mm^2 surface area, positioned on the surface of an insulator between two earthed electrodes. A relative permittivity of 2.2 was used for the insulator.

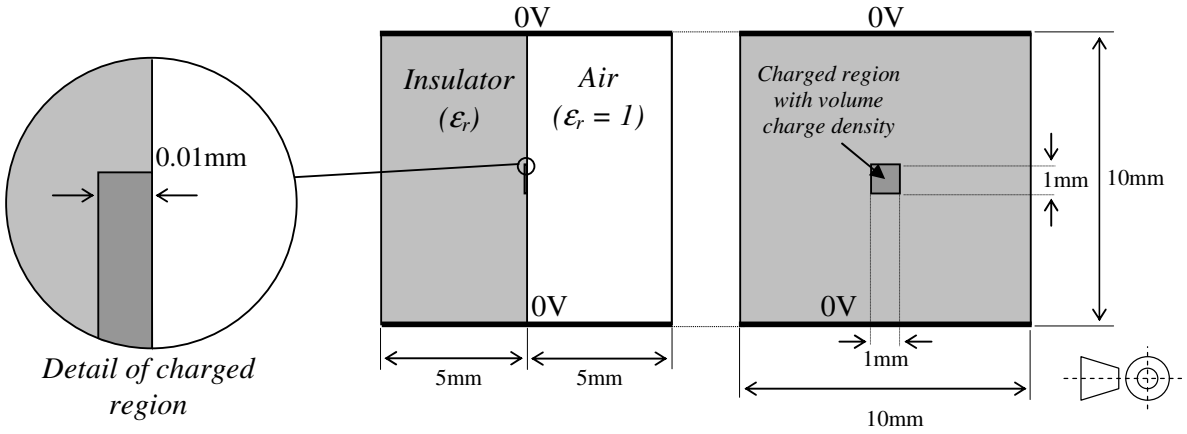

Figure 4.5.16: A simple model to study the field produced by a charged region.

The electric field set up by the uniform region of surface charge is illustrated in figure 4.5.17. The length and direction of the arrows indicate respectively the magnitude and direction of the electric field on the insulator surface. The field arrows point in the direction of the lines of force, they always point away from the positively charged region. The field magnitude is greatest at the very edges of the charged region and dips to a local minimum at its centre.

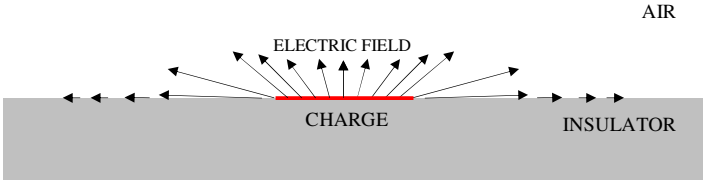

Figure 4.5.17: The electric field on the surface of an insulator set up by a uniform region of surface charge.

The magnitude of the electric field strength through the centre of the charged region along the surface is plotted in figure 4.5.18 for different charge densities. The greatest field strength is clearly visible at the edges of the 1mm wide region.

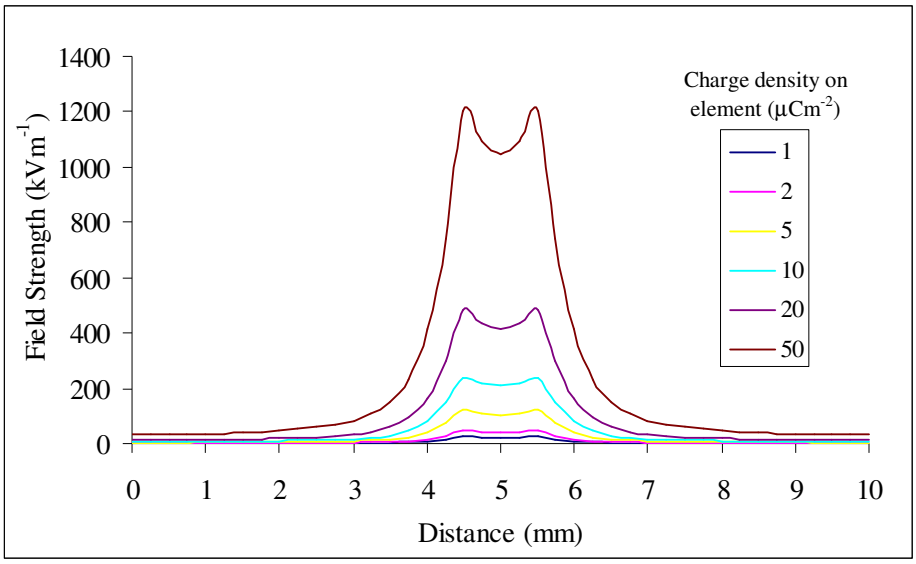

Figure 4.5.18: The magnitude of surface electric field strength along a path through the centre of the charged region.

If the surface charge density measured on a surface element is uniformly distributed across it then the surface electric strengths set up are not very great until relatively high charge densities of 20µCm^{-2} or more are reached.

Charge on a Streamer Channel

The measured value of 10pC or 10µCm^{-2} over 1mm^2 at the tip of the streamer channels will not be uniformly distributed across the 1mm^2, but may be localised along a thin channel 1mm long as indicated earlier.

There is much debate about the exact width of a streamer channel, though it is definitely much smaller than 1mm. The thinner the channel the greater the localised charge density becomes and hence the higher the field strength.

To study the effect streamer channel width has on the localised surface field strength, a portion of streamer channel was modelled with a charge density of 10pC per 1mm length. The streamer channel model was based around the model shown figure 4.5.16.

The 1mm^2 element studied earlier was replaced with a 1mm length of streamer channel as shown in figure 4.5.19. Using different numbers of 10μm wide strips charge density streamer channels of width 20μm to 100μm could be simulated. The element size around the channel was greatly reduced in the model to maintain a high level of accuracy. The channel thickness was also made very small (0.1μm) to accurately represent a surface charge. The channel tips were rounded to minimise geometric enhancement of the electric field at its ends.

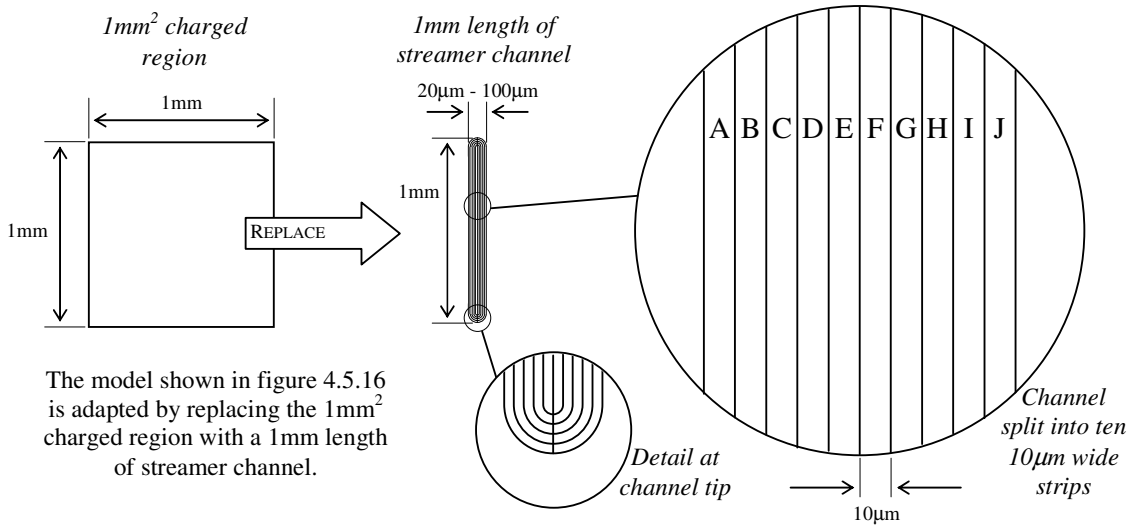

Figure 4.5.19: Detail of the model used to simulate different streamer channel widths.

To maintain a net positive charge of 10pC on the 1mm length of streamer channel the applied surface charge density was increased as the channel width decreased. The values of charge density used are shown in table 4.5.1.

Streamer channel width	Surface Charge Density required to produce 10pC per mm
1 mm	10 μCm^{-2}
100 μm	100 μCm^{-2}
80 μm	125 μCm^{-2}
60 μm	167 μCm^{-2}
40 μm	250 μCm^{-2}
20 μm	500 μCm^{-2}

Table 4.5.1: The uniform charge densities applied to the 1mm length of modelled streamer channel to produce a total positive charge of 10pC for different streamer widths.

One of the limitations of the modelling software was that it only allowed *uniform* charge distributions in each region. The model shown in figure 4.5.19 could overcome this limitation by applying different charge densities to each of the streamer channel strips at once. This allowed simple non-uniform charge distributions to be simulated within the streamer channel.

Charge densities were applied to produce a Gaussian distribution of charge in the streamer channel while maintaining a total charge of 10pC per mm length. This is illustrated in figure 4.5.20.

Region	Charge Density	Area	Charge
A	**16 µCm^{-2}**	1mm×10µm	160 fC
B	**44 µCm^{-2}**	1mm×10µm	44 fC
C	**92 µCm^{-2}**	1mm×10µm	92 fC
D	**152 µCm^{-2}**	1mm×10µm	152 fC
E	**196 µCm^{-2}**	1mm×10µm	196 fC
F	**196 µCm^{-2}**	1mm×10µm	196 fC
G	**152 µCm^{-2}**	1mm×10µm	152 fC
H	**92 µCm^{-2}**	1mm×10µm	92 fC
I	**44 µCm^{-2}**	1mm×10µm	44 fC
J	**16 µCm^{-2}**	1mm×10µm	16 fC
		TOTAL =	10pC

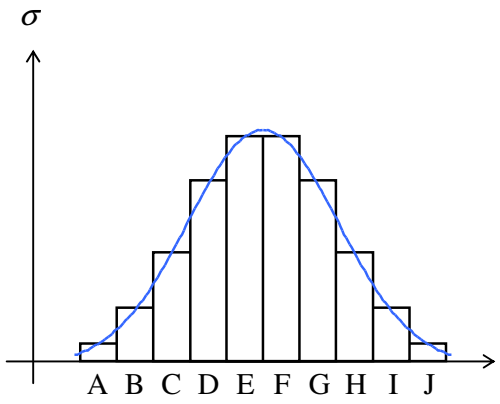

Figure 4.5.20: The uniform charge densities applied to each of the streamer channel strips to produce a Discrete-Gaussian distribution of charge with a net charge of 10pC per mm.

The charge density appeared normally distributed through a cross section of the channel. This is a much more realistic model of a streamer channel. In practice a streamer will not deposit charge in a region with exact boundaries.

Figure 4.5.21 gives a view of the fields calculated for three different streamer channel cross-sections. The first two cases have completely uniform charge distributions within 20µm and 100µm width channels. The third case is the Discrete-Gaussian distribution. All three cases contain 10pC of charge per millimetre length.

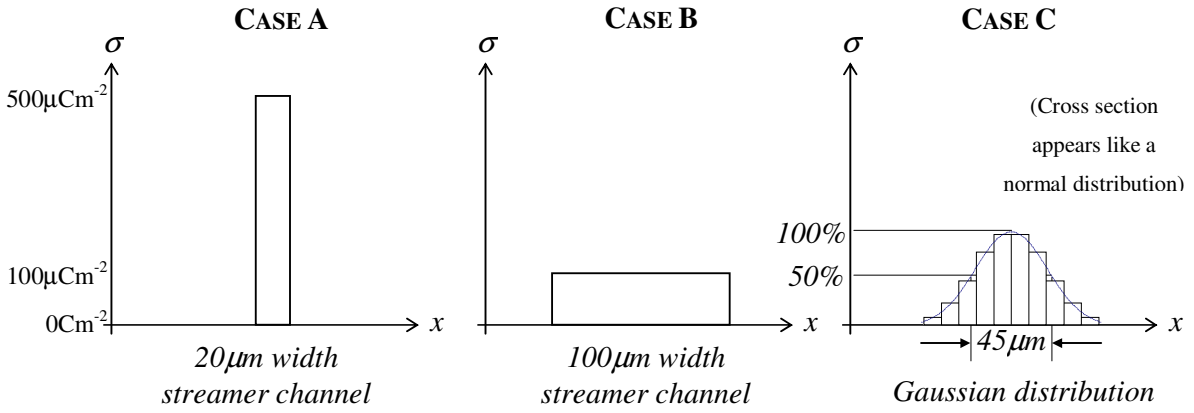

(a) Charge density distribution through cross sections of the modelled streamer channels.

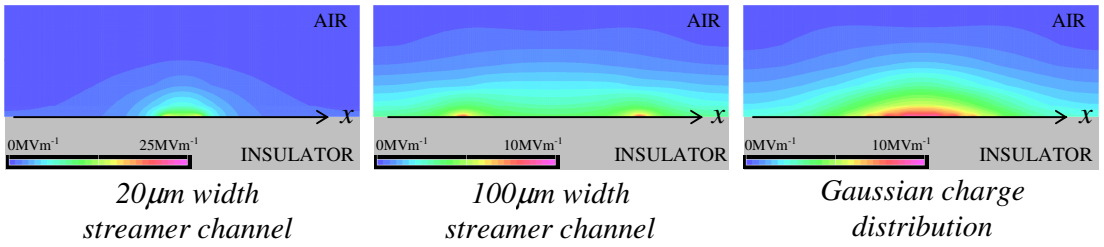

(b) Cross sections through the model showing the electric field in air set up by the surface charge.

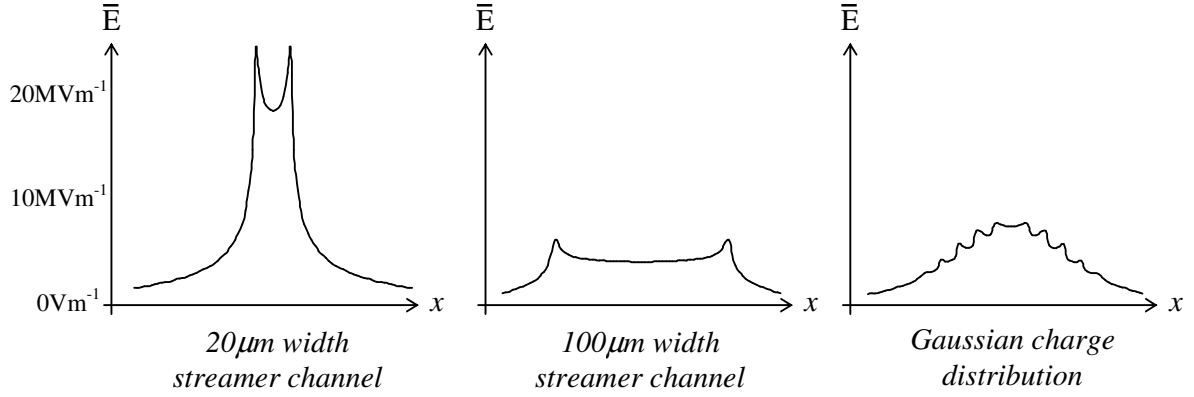

(c) The surface electric field strengths through the modelled streamer channel.

Figure 4.5.21: The measured value of 10pC of charge per 1mm can result in different electric field strengths depending on how the charge is distributed within the surface element.

Figure 4.5.21(b) shows the electric field in air produced by the modelled streamer channel. The field strength is strongest at the edges of the uniform distribution cases, but for the Gaussian distribution the field is strongest at the centre. Figure 4.5.21(c) shows the magnitude of the electric field strength along the surface. For the Gaussian distribution local maxima and minima can be seen at the boundaries of the nested regions. If a truly continuous variation of charge density could be modelled within the streamer channel then these perturbations would disappear.

Figure 4.5.22 shows the resultant surface electric field through the centre of the streamer channel for all the different channel widths modelled. The thin streamer channels produce very high electric fields. For 10pC over a 1mm×20µm region, fields of over 20MVm^{-1} are present. This is clearly an unfeasible situation because the distribution would blow itself apart or cause further ionisation, in either case the streamer channel would not be stable.

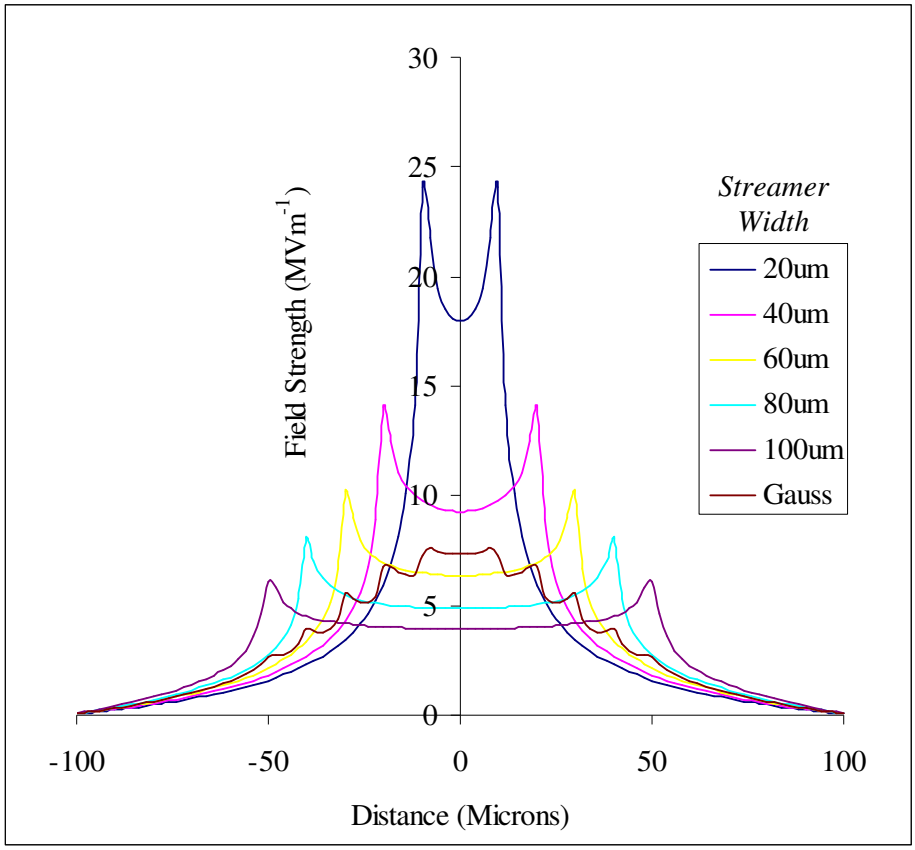

Figure 4.5.22: Magnitude of surface electric field strength on surface across the streamer channel for different streamer widths.

Figure 4.5.22 also shows the field produced by the Gaussian distribution of charge. The maximum field strength is found at the centre of this distribution; not at the edges as with the uniform distribution cases. The Gaussian distribution is probably the more natural distribution because discrete boundaries at the edges of the channel cause large field enhancements. Nature always acts to equalise large differentials.

The peak value of the Gaussian distribution corresponds approximately to the field at the centre of a 50µm diameter streamer channel with discrete boundaries. Hence the Gaussian distribution modelled can be said to have an effective diameter of approximately 50µm. This is very close to the 45µm half width of the Gaussian charge distribution itself (see figure 4.5.21(a) CASE C). These two values may in fact be the same; the difference caused by the discretisation of the distribution.

If this is true then the magnitude of the field strength at the centre of a uniform distribution can be used as the maximum value of an equivalent Gaussian distribution.

The magnitude of the surface electric field strength on the central axis of the uniform distribution streamer channels is plotted against streamer width in figure 4.5.23.

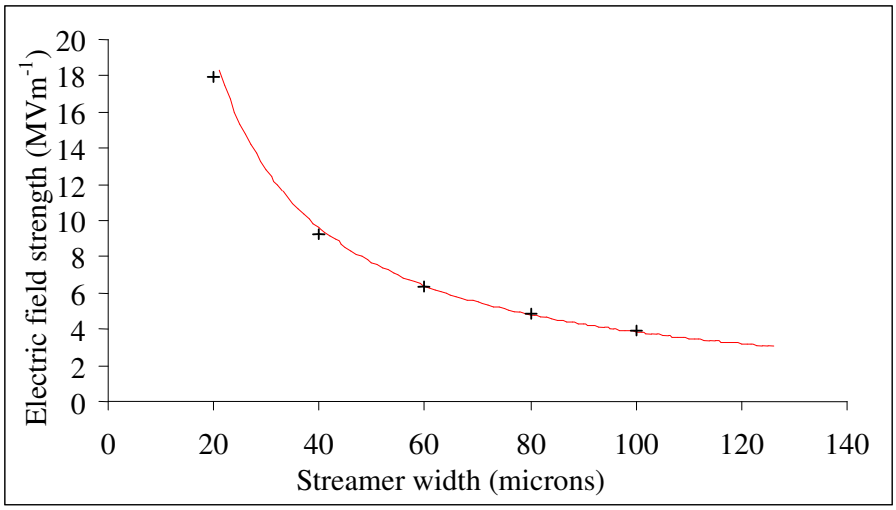

Figure 4.5.23: Electric field strength on surface across the streamer channel for different streamer widths.

The values of surface electric field strength follow very closely the red curve shown in figure 4.5.23. The best fit equation for the curve was E = 384/w, where E is the electric field strength with units of MVm^{-1} and w is the streamer width with units of µm.

Substituting a value of $3MVm^{-1}$ for the field strength that causes ionisation in air into the equation gives a minimum streamer channel width of about 130µm.

Chapter 5: DISCUSSION

5.1 Introduction

This penultimate chapter provides a summary and discussion of the work conducted. The first section covers charge measurement and the Scanning System. Then follows a section entitled Single Discharge Experiments, this covers work done with the three different rods for positive single discharge events. The rest of the practical experiments are covered in the next section entitled Additional Experiments. The finial discussion section covers the Simulations and Analysis chapter.

5.2 Charge Measurement

5.2.1 Charge Detection

Various techniques are available for the detection of surface charge ranging from dust figures to electro-optical measurements. These were assessed and the electrostatic probe chosen because it was simple to construct and a full analysis of its operation could be undertaken on commercially available electrostatic field solvers. The electrostatic probe provides a clean, non-contact and quantitative charge measurement technique.

5.2.2 Calibration Technique (Section 2.2)

The voltage signal from the electrostatic probe has to be converted into charge density measurements on the surface. Using a simple one-to-one relationship, each probe voltage value can be converted directly to a surface charge density measurement by simple scaling. However this simple multiplication yields unsatisfactory results if the selectivity of the probe is poor.

The Φ-Matrix technique has been developed to obtain an accurate surface charge distribution from a set of probe voltage measurements irrespective of the probe selectivity. The technique used here is an adaptation of Pedersen's λ-function (Pedersen, 1987). He related the *Poissonian charge* induced on the probe to the surface charge density, whereas the Φ-Matrix technique relates the *voltage* induced on the probe to the surface charge density. The technique involves removing the probe's voltage response characteristic, or ϕ-function from the voltage measurements. This is achieved by solving a large number of simultaneous equations, the coefficients of which are ϕ-function values calculated using 3-Dimensional finite element modelling software. The matrix inversion technique is then used to solve the simultaneous equations. The number of simultaneous equations and hence the size of the matrix is determined by the number of probe voltage measurements.

5.2.3 Scanning System Hardware (Section 2.3)

The scanning system hardware consists of the electrostatic probe itself and the mechanism required to move it accurately over the surface of the insulator under test and record its signal.

The mechanism controlling the movement of the probe was designed to be flexible and allow many different insulator geometries to be studied. This is a major advance over the previous scanning systems of many other researchers (D.K.Davies, 1967; Connolly, 1984; Abdul-Hussain and Cornick, 1987; Vasconcelos, 1994; Al-Bawy and Farish, 1991; Bier et al 1991; Davidson and Bailey, 1999) that were designed for specific insulator geometries only. To scan contoured axi-symmetric geometries the probe movement has to have 4 degrees of freedom. The probe movements are actuated using stepper motors, chosen for their positional accuracy and their open-loop control capabilities. Limit switches allow accurate reference positions to be specified.

The probe signal is buffered using a very high input impedance op-amp and fed into a computer for recording. The signal recorded from a calibration test piece compared very favourably with finite element modelling calculations. This simultaneously vindicates the probe measurements and the modelling technique used to find the ϕ-function values,

which in turn puts great faith in the Φ-Matrix technique and the derived surface charge densities.

The charge density resolution of the scanning system is limited by the noise in the system. This resolution was found experimentally by scanning a grounded conducting surface. The calculated charge distribution obtained was random with peak values of about ±0.05μC. This noise sets the lower limit of the charge densities measurable by the scanning system.

The greatest measurable surface charge density is restricted purely by breakdown to the probe. As the grounded probe screen nears a highly charged surface very high electric fields can occur between the two and there is a risk of breakdown to the probe. Very high charge densities can be scanned by moving the probe further away from the surface; however this results in reduced spatial resolution. The greatest surface charge densities that can easily be measured are in the order of $50\mu Cm^{-2}$ over $1mm^2$ regions.

5.2.4 Scanning System Control Software (Section 2.4)

Vitally important to the surface charge measurement apparatus is the control software that automates the entire process. The software performs a number of complicated tasks: generating clock and control signals for the stepper motors; being aware of the test insulator's geometry; manoeuvring the probe accurately over the insulator surface without colliding with it; controlling and monitoring the operation of the probe itself.

As the program accurately moves the probe over the surface it also has to record the probe voltage signal. A file format was developed that contained all the probe voltage measurements and all the parameters used in the scanning process. This file format greatly simplifies the storage of large numbers of probe voltage measurements. The data is stored in a very efficient manner so that the thousands of measurements that make up a high-resolution surface can be stored in a single file of only a few kB. These surface data files are automatically filed for the user in a library directory structure. This storage technique is fundamental to making the scanning system easy-to-use with each scanned surface appearing as a single object. To make the program intuitive to use a menu system is employed. Graphical displays make the complicated process of scanning a surface very simple and straightforward.

5.2.5 Solver Software (section 2.5)

The surface data files containing all the probe voltage measurements for each scan then have to be converted into surface charge density measurements. This is achieved by implementing the Φ-Matrix calibration procedure on a large computer. The entire calibration procedure is automated to a point where the user only has to provide the surface data files generated by the Scanning Control Software, and then type 'Solve'. The software automatically generates the required ϕ-functions from a text file containing key points, it then uses these ϕ-functions to generate the Φ-Matrix. This facility allows the effect of changing the shape of the ϕ-function to be investigated simply by altering the values of the key points.

The amount of computer memory and time available is the limiting factor in the size of the surface charge distributions that can be solved. A surface charge distribution with a resolution of approximately 100×100 measurements is the upper limit at the moment, taking approximately 24 hours to calculate. Almost all of this time is spent inverting the matrix. There are much quicker ways of solving simultaneous equations however the matrix inversion technique allows an explicit solution to be found and hence large numbers of charge distributions measured on the same insulator can be solved at once.

Moores Law states that the speed of computers doubles approximately every 18 months. Figure 5.2.1 shows what Moores Law predicts the time to invert the Φ-Matrix in the future will be. This increase in speed could also be employed to solve higher resolution charge distributions.

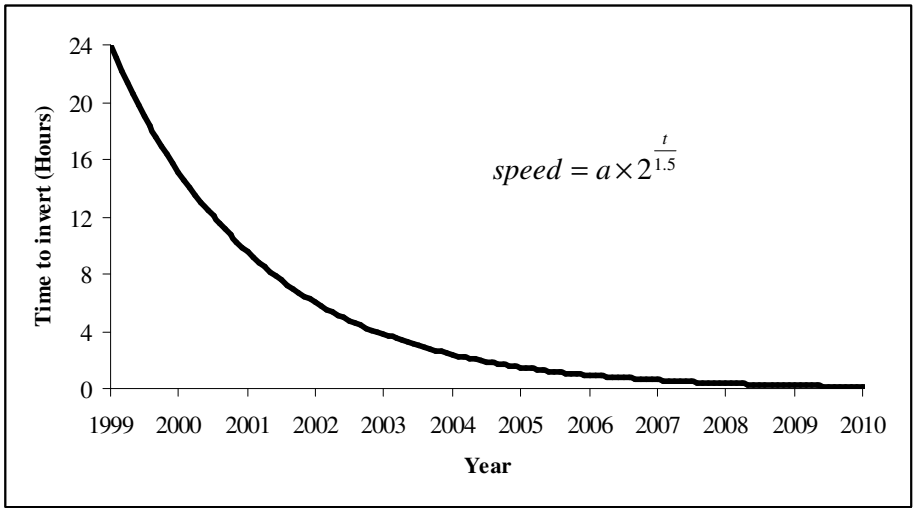

Figure 5.2.1: The predicted time to invert a matrix to solve a 100×100 distribution.

5.2.6 Viewer Software (Section 2.6)

Having obtained a charge density distribution consisting of anything up to 100,000 values the next problem is how to analyse, interpret and display the data. Once solved the charge distributions can be viewed using software specially written in Matlab for a Windows GUI.

Several options are available in the viewer software.

A 3-dimensional surface graph provides a view of the magnitudes present in the distribution. However it is very hard to ascertain the exact position and overall distribution of charge on the surface. This is caused by the very localised nature of the surface charge deposited by the discharge. The distribution appears very 'spiky' when viewed as a 3D-surface.

A contour map provides an excellent view of the positions of regions of charge in the distribution and provides an idea of the magnitude present in each area. To allow an exact view of the charge density values present, a slice or path can be shown as a simple line graph. The complexity of the distributions means that a slice or path through the distribution on its own is almost meaningless. A contour map is required with any slices or paths shown to put them in context.

Streamers rarely propagate straight down or across the insulator surface, so the ability to plot the charge density along any path, in any direction is an essential quality for any software used to view high-resolution surface charge density distributions. It is also important to be able to calculate the net charge in any region of the surface.

5.2.7 Scanning System Comments

The scanning system was developed to be used as a piece of laboratory measurement equipment. It is flexible, versatile and most important, easy to use. The suite of specially written software hides the complex task of measuring, calculating and analysing surface charge density distributions from the user.

The very close agreement between the measured and simulated probe voltages for the calibration test piece combined with the similarity between the measured surface charge density distributions and the corresponding dust figures, give great confidence in the results obtained.

Prior to the development of the scanning system, dust figures were the only way of getting a detailed view of the charge distribution on the surface of a practical insulator. The dust figure still provides the best possible spatial resolution, but it has a number of drawbacks. It is not quantitative; it is very messy; it is final (meaning once the dust figure has been obtained no further test voltages can be applied to the insulator specimen without first thoroughly cleaning it). The scanning technique in comparison is a quantitative, clean and non-contact measurement technique.

The scanning system can detect charge densities in the range of 0.1 to about $50\mu Cm^{-2}$ on $1mm^2$ elements of the surface. The total measured charge on the insulator surface is in the order of a few nano-coulombs of positive and negative charge. The net charge on the surface is often close to zero. This emphasises the inadequacy of low-resolution measurements of surface charge density that would simply show that there is very little charge on the surface. Very localised regions of charge density would be averaged out by low-resolution net surface charge measurements.

Previous researchers have employed the electrostatic probe principle for charge measurement D.K. Davies being the first in 1967.

Many such as Abdul-Hussain and Cornick, 1987 and Davidson and Bailey, 1999 have employed high-resolution techniques without calibration; they are justified in doing this because their measurements use thin insulating samples on a grounded back plane, this way each probe measurement is converted one-to-one to a charge density measurement. However, Al-Bawy and Farish, 1991 used the same principle without calibration for thick specimens with poor results.

Takuma et al, 1998 in a recent review paper conclude that a multi-point calibration technique aided by numerical field calculations is the only way to obtain accurate charge density measurements for thick insulating specimens.

Rerup and McAllister, 1996 use Pedersen's λ-function (similar to the ϕ-function used here) but do not use a 3D field solver to find the probe's response function which leads to inaccuracies as shown in a discussion paper (Wintle et al, 1997). Other researchers run into problems with inaccurate calculation of the probe response function such as Sudhakar and Srivastava, 1987 who neglect the presence of the probe itself in their calculations.

Ootera and Nakanishi, 1988 developed a scanning system for GIS cone spacers but achieved poor spatial resolution because of the size of their probe and discretisation of their surface.
None of the scanning systems mentioned above is as versatile as the one described here, they are all tied to specific insulator geometries.

The Solver software that implements the surface charge density calculation needs to know the exact shape of the ϕ-function for every probe position on the surface. It obtains these values by quadratic interpolation of key values from a text file. This is an essential feature of the solver software because it allows the investigator full control over what is effectively a four dimensional function. The effect of ground plane proximity can thus be fully implemented into the solution procedure.

The main advance is the spatial resolution obtainable using calibrated probe measurements. Previously all researchers have only been able to solve distributions with a relatively small number of large surface elements (such as Ootera and Nakanishi, 1988). The exponential increase in computing power in the late 20th century combined with a well designed and implemented data-handling strategy has allowed this achievement.
The scanning system has made the practical research conducted in this research project possible. Without this well designed system the measurement of high-resolution surface charge distributions would be impossibly arduous.

The scanning system has facilitated a number of unique studies:

1. The evaluation of different methods of neutralising surface charge.
2. The effect of multiple discharges on the build-up of surface charge.
3. The surface charge present in paths deposited by individual streamers.
4. An accurate quantitative macroscopic view of the overall surface charge distribution.

5.3 Single Discharge Experiments

5.3.1 Apparatus (Section 3.2)

Introduction

The aim of these experiments is to collect as much information as possible about individual discharge events. In many high voltage studies, observations are made through the use of gross statistics and averaging of the measured quantities. This technique is excellent for finding general trends however fine detail can often be lost through the averaging process. A detailed study allows a deeper insight into the nature of discharges. The experiments conducted here record as many measureands as possible for each discharge event, this allows measureands to be plotted against each other and trends observed.

The experiments are also used to evaluate the scanning technique in a practical laboratory situation.

Electrodes

The rod-plane gap is used because it produces a simple streamer discharge, is commonly used as a reference gap, can be modelled easily, and has a single, isolated, non-uniform field region. Previous researchers such as Gallimberti et al, 1991 have also employed the rod plane gap in studying insulator flashover.

The rod-plane facilitates the study of streamers propagating in a diverging field, a situation that often occurs in the flashover of high voltage plant.

HV Generation

A positive impulse voltage is applied to the rod to provide a single controllable positive discharge event. A 4/62μs impulse wave-shape is chosen because it produces a single easily measurable discharge event. Impulse generators provide a convenient method of generating such impulses.

Measurement Equipment

Three photo-Multipliers are used to observe the single dimensional spatial propagation of the streamers. Photomultipliers provide a measurement electrically isolated from the main high voltage test circuit. This reduces interference problems. The use of three photomultipliers provides two different velocity measurements for each discharge.

A resistive current shunt on the low voltage side is used to measure current and hence injected charge in the gap. These 4 signals are recorded for each discharge using a fast storage oscilloscope.

Insulator Test Objects

PTFE is mainly studied, this is because of its excellent ability to hold surface charge and its common place usage in modern HV plant. Simple cylindrical insulator specimens are studied although a later experiment involves the use of contoured insulators. As with any new measurement technique it is important to first prove the technique with simple insulator geometries before progressing onto more complex ones.

Different reported surface discharging techniques are evaluated using the scanning system to measure residual surface charge. A technique (Gallimberti, 1991) involving stroking the surface with a grounded copper brush actually deposits more charge that it removes.

A quick and effective technique for neutralising insulator surfaces has been developed consisting simply of swathing the insulator in paper soaked in ethanol. After using this neutralising technique no charge can be detected by the scanning system.

This technique proved invaluable during the course of the experiments by allowing quick neutralisation of the insulator surface. Washing and drying techniques would have been to time consuming and require a large number of identical insulator specimens.

5.3.2 Blunt Rod - Initial Experiments (Section 3.3)

Introduction

The initial experiments are designed to evaluate the effectiveness of the scanning system and to provide the starting point of the investigation. To provide a reference, the characteristics of the air gap alone is first investigated

Air

Impulses are applied to the blunt rod with a number of different peak impulse voltages. A single discharge event occurred at each impulse voltage.

The time to discharge can be used to calculate the instantaneous voltage on the rod. In excess of 100 individual discharge events are studied in detail.

Several basic trends can be observed:

- Discharges occurring at higher instantaneous voltages generally have greater peak currents and initial velocities of propagation than those at lower voltages.
- Discharge velocity and peak current are strongly related; higher peak currents are associated with higher velocities.
- Discharges with higher peak currents inject more charge into the gap.

The results suggest that at higher instantaneous voltages, and hence peak currents, the discharge mechanism begins to change. This is readily visible in the shape of the current waveform with a widening of the current pulse (figure 3.3.9). The changing shape of the current pulse suggests that a second discharge initiation site on the rod begins to operate at the higher voltages and hence peak currents.

The blunt rod has a small hole drilled in the end directly up the central axis, it is presumably the edges of this hole that provide the first lower voltage discharge site. The second, higher voltage, discharge initiation site is the outer radius of the rod tip itself. The interaction between these two discharge sites on the same rod could offer an explanation for the strange behaviour documented in table 3.3.1, where between 40 and 50kVp the number of discharges observed reduces. When the second site reaches its discharge voltage it may mask the activity of the first by producing additional space charge.

Insulator

Charge Distributions

A PTFE insulator specimen is placed in the gap. Impulses are applied and recorded as before, but prior to each impulse the insulator surface is neutralised. Deposited surface charge is measured using the scanning system and a dust figure taken of the distribution. The dust figures and surface charge density distributions reveal the fine detail in the discharge. These two measurements provide two different indications of the charge footprint left after a discharge. Figure 5.3.1 shows an example charge distribution and dust figure obtained from a +36kVp impulse.

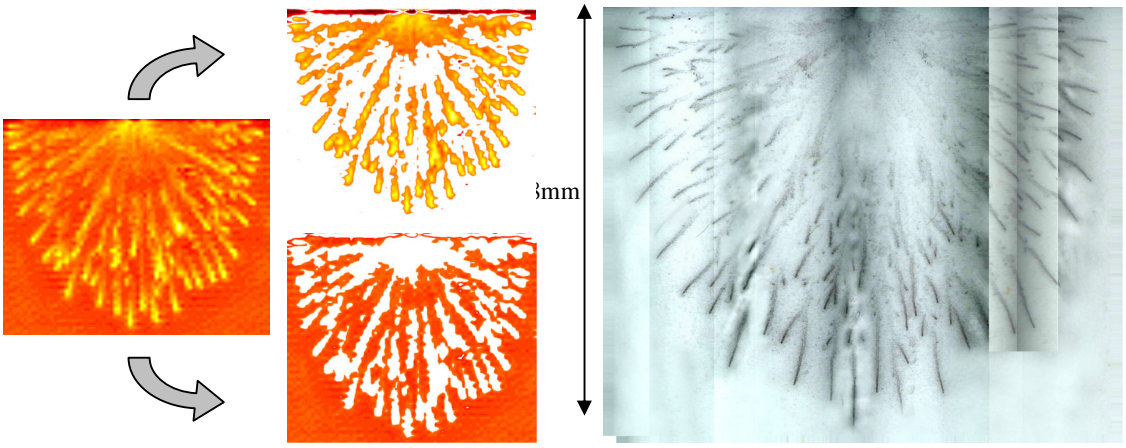

a) Split measured charge distribution into charged and non-charged regions.

b) Dust figure.

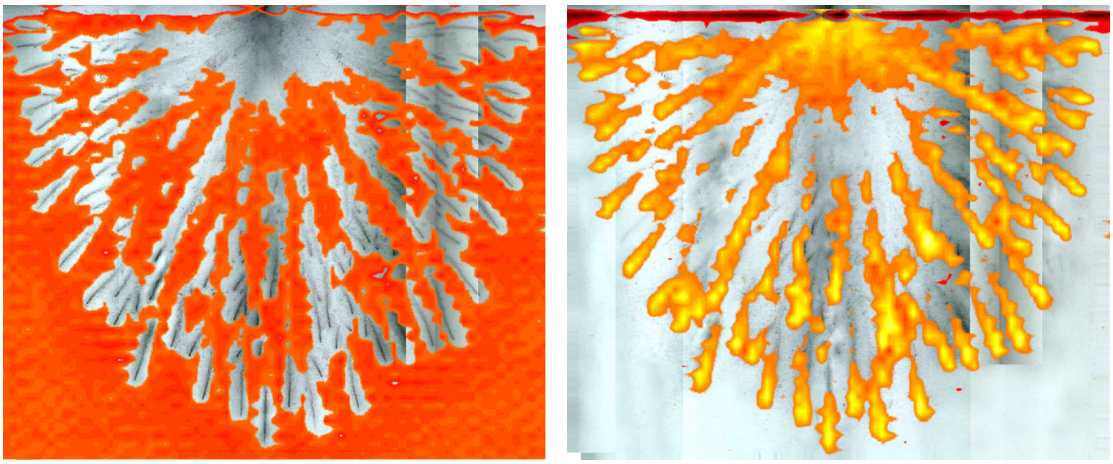

c) Combined dust figure and non-charged region.

d) Combined dust figure and charged region.

Figure 5.3.1: Close inspection of a charge distribution and corresponding dust figure.

The dust figures and calculated surface charge distributions are very similar in appearance. The charge paths left by individual streamer channels can be clearly seen in both techniques. This vindicates the resolution and operation of the scanning system.

Figure 5.3.1 raises a number of interesting points.

The discharge is comprised of a large number of streamers of which over 50 have left clearly recognisable paths in both the dust figure and measured charge distribution. The question is, how much of the discharge occurs in air and how much along the surface? Photographic evidence by previous researchers (Ghaffar, 1994) suggests that discharges in the presence of insulators propagate very close to the insulator surface.

Charge is not uniformly distributed along the streamer channels but is at a maximum at the streamer tips where the streamers stopped propagating. The distribution of charge in a streamer tip is studied in detail later in the analysis section.

The streamer channels themselves do not appear to form a continuous path back to the rod. This observation is very interesting when considering the autograph pictures of Nasser, 1968 shown in figure 5.3.2.

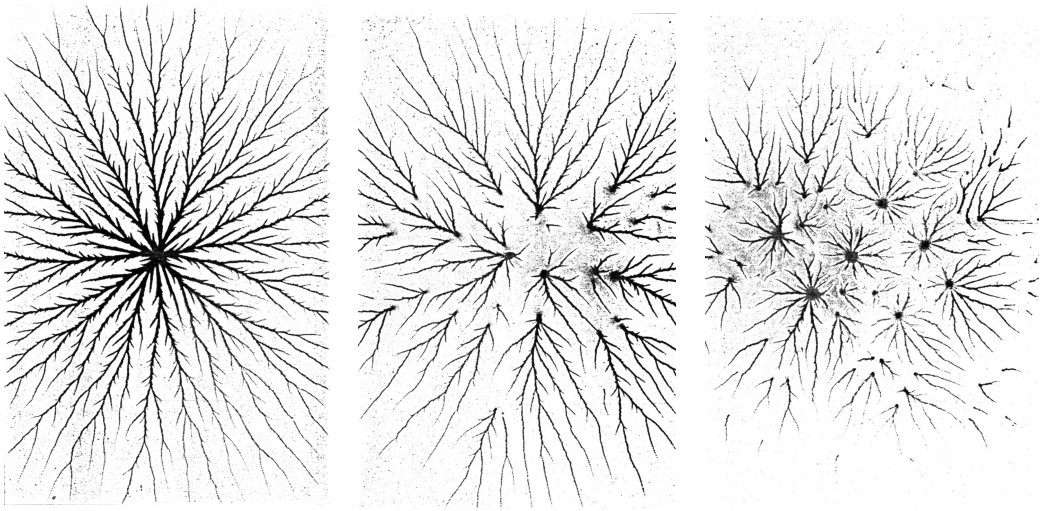

(a) 0mm separation *(b) 10mm separation* *(c) 20mm separation*

Figure 5.3.2: Autographs showing streamer phenomena produced by a +30kV pulse at an increasing separation from a rod electrode.

The autograph pictures are produced by applying a high voltage to a rod at different distances above a photographic film above a grounded plane. When the rod is touching

the surface all streamers form continuous paths back to the rod. As the rod is moved away from the surface streamers form in air then impinge on the surface and spread out in continuous paths from their impact points.

The autographs differ from the surface charge density measurements in a several ways. Firstly the autograph technique can be only used to study the propagation of streamers across photographic materials. Secondly and more fundamentally, the autograph is an integrated record of the photon activity during the complete discharge whereas the charge density measurements show the discharge charge footprint when it stopped propagating.

So although the autographs show the discharges propagate from the point they impinge on the surface in a continuous path, the charge density distributions indicate that the charge may not be deposited in a continuous path.

The charge density in the streamer channels is greatest at the very tips where they stopped propagating. This could explain why low resolution or uncalibrated charge measurements of similar surface discharges by previous researchers (Abdul-Hussain and Cornick, 1987; Vasconcelos, 1994) could only see a distribution of charge resembling a volcano in appearance. In such measurements the streamer channels around the outside of the distribution cannot be resolved individually and hence appear as the continuous ‘rim’ of the volcano distribution. The cause of the central ‘crater’ in the volcano distributions is possibly because fewer streamers propagate in the centre. This behaviour is illustrated in figure 5.3.2(b) where streamers impinge on the surface away from the centre, which implies a charge and potential minimum in the centre.

In figure 5.3.1 individual streamer channels can be easily resolved at the edges of the distribution, however nearer the centre of the distribution individual streamer channels become harder to see in both the charge density map and the dust figure. This is either because less charge is left in this region or there are equal and opposite amounts of both polarities of charge in this region. For the latter to be true the charge would have to be deposited with a very fine distribution beyond the resolution of both measurement techniques. The resolution of the dust figure is limited by the dust particle size, which for the photocopier toner used is in the order of microns.

So the arrangement of charge in the centre of the measured distribution is either less than at its edges or there are equal and opposite amounts of charge with a distribution containing features in the order of microns.

Comparisons with Air

In air peak currents can reach up to 7A at 40kV instantaneous applied voltage whereas with the insulator present the peak current was only 1.6A at 40kV (figure 3.3.19). The currents in air alone are scattered over a large range; this is caused by the two different discharge initiation sites on the rod. Peak currents are very much reduced by the presence of insulator, but it is important to note that even with the insulator present, the peak current-instantaneous voltage characteristics are within the range obtained in air without the insulator present.

When plotted against peak current the results contain less scatter. For a given peak discharge current the streamers have a faster initial peak velocity with the insulator present.

Several other interesting observations can be made:

- In the presence of the insulator the discharge current waveform becomes much sharper. This can be seen by comparing the current signals in figure 3.3.9 with 3.3.10 to 3.3.18. It is also clearly illustrated in figure 3.3.22 where the area under the current wave shape (injected charge) is smaller with the insulator present.
- The distance at which the discharge stops propagating increases with instantaneous voltage and peak current.
- Streamers that propagate further across the insulator surface leave more negative net surface charge on the surface as a whole.

5.3.3 Sharp Rod (Section 3.4)

Introduction

At higher applied voltages the results suggest that the blunt rod is capable of supporting more than one discharge site. The two main pieces of evidence for this are: the data points, although scattered, are grouped around two regions, and the changing shape of the discharge current waveform. The central hole drilled in the rod axis is presumably the site of the first discharge site.

Hence the blunt is inadequate for the length of rod-plane gap used. To ensure a single discharge is initiated from one point a much sharper rod is utilised for the next set of experiments.

Set-up

The initial experiments indicate that a highly charged region of insulator surface occurs directly under the rod tip. This region is suspected to be of importance because of its locality to the discharge initiation site. To allow its further study the main rod-plane gap separation is reduced to 80mm; thus moving the rod tip to a point 20mm below the top of the insulator, to facilitate the full scanning of this region.

The rod is also mounted at a slight angle to the vertical; this provides a single point of contact with the insulator, thus reducing the likelihood of multiple discharge sites.

Another feature suspected to be important is the rod-surface separation. By simple argument, as the rod surface separation tends to infinity, the gap characteristics should tend to the air gap case. A few trial rod-surface separations are employed and the effect of repeated discharges is studied by scanning the insulator after each shot.

Air

When plotted against instantaneous voltage the results show much less scatter than for the blunt rod case. This indicates that the sharp a rod produces a more repeatable discharge.

The results obtained follow similar trends to the blunt rod case with good agreement between the currents and velocities as a function of instantaneous voltage. The relationship between injected charge and peak current is also close for both rod types. This agreement gives confidence that although the instantaneous voltages and currents are less than with the blunt rod, the behaviour of the current is much the same. The shape factor (Injected Charge/Peak Current) is also the same for both rods.

Insulator

Charge Distributions

The overall shape and structure of the surface charge distribution deposited by a positive discharge can be clearly seen in the measured charge distributions as shown in figure 5.3.3. Directly under the rod a highly negatively charged region is always produced. This is surrounded by a region of positive charge which in turn is surrounded by a horseshoe region containing a lightly charged region. Between this region and the perimeter of the charge distribution many streamer paths are visible. The streamer paths reduce in number towards the perimeter of the distribution. At the very perimeter of the distribution the charge deposited by streamer tips as they finished propagating is clearly visible.

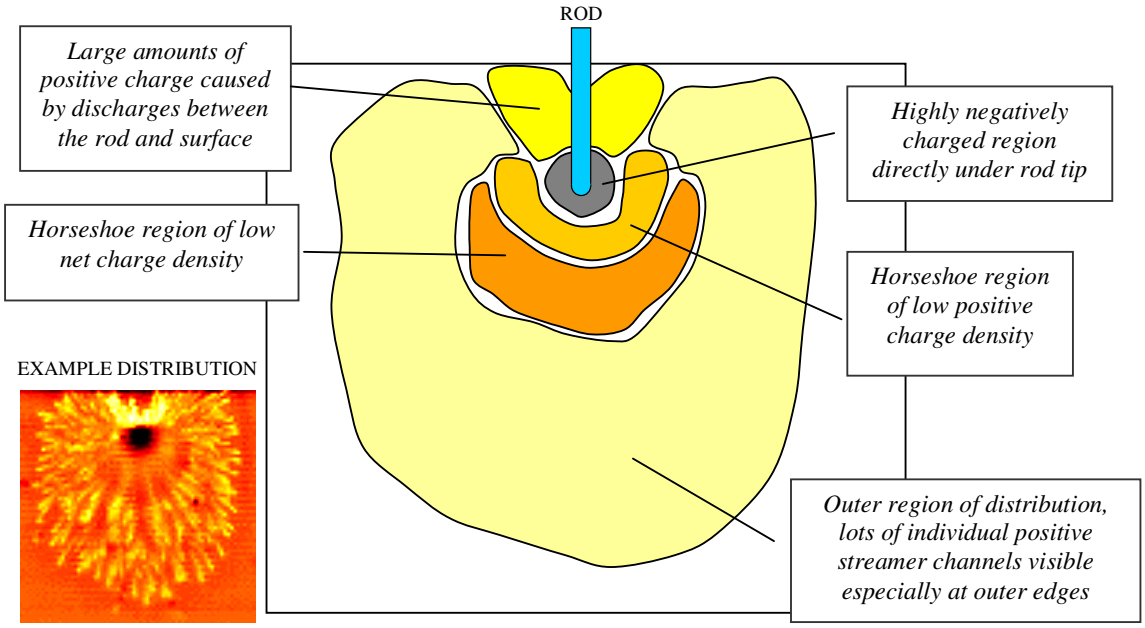

Figure 5.3.3: The distinctive regions in a surface charge distribution left by a single positive discharge on PTFE.

After each impulse was applied the surface was scanned; this allows a picture to be built up of the effect multiple discharges have on a surface charge distribution. Each new discharge alters the distribution slightly. After about three impulses the net amount of surface charge stabilised and further discharges served only to redistribute the surface charge.

Sharp Rod Problems

The major disadvantage of the sharp rod is that it has a much lower corona inception voltage because of the field enhancement around the sharp tip. The presence of the insulator in the gap further reduces the inception voltage by introducing a triple junction field enhancement. The result of this low inception voltage is that the discharge always occurs very early in the applied impulse voltage wave. The discharge current signal is often lost in the noise at the start of the impulse caused by the generator firing. This is obviously not desirable for a detailed study.

To delay the discharge the impulse voltage applied is reduced but the discharges still occur too early to be free of noise. In a last attempt to get a clean current signal the rod is moved 1mm away from the surface to reduce the effect of the triple junction. This causes the discharge to occur at a higher instantaneous voltage and hence delays the discharge enough to be relatively free of noise.

To obtain more data the rod-surface separation is increased to 2mm and another two impulses of the same voltage applied. The surface charge distributions obtained are very similar to the 1mm rod-surface separation case.

Comparison with Air

The limited number of results with the insulator present means only simple comparisons can be made with the sharp rod air-gap characteristics. For a given instantaneous voltage applied to the sharp rod, peak currents are higher with the insulator present than in air alone, this can be seen in figure 3.4.23. This is a difference with the blunt rod case; the high field around the sharper tip is probably a factor.

5.3.4 Medium Rod (Section 3.5)

Introduction

The sharp rod produces a reliable discharge initiation site at the cost of a very low corona inception voltage. A third rod size, in-between the previous two, with a diameter of 3.15mm, is used for the rest of the experiments. The medium rod is found to produce a reliable measurable discharge even when in contact with the insulator.

Set-up

The experiments are designed to study the effect of multiple discharges and the effect of the proximity of the rod to the insulator.

Twenty impulses are applied, each discharge is fully recorded and the insulator surface scanned after the 1st, 2nd, 3rd, 4th, 5th, 10th and 20th shot.

This process is repeated for rod-surface separations of 0mm, 5mm, 10mm and in air. The insulator surface is neutralised for each new rod-surface separation.

Comparison of Air Results With Other Rods

The air gap characteristics for the three different rod diameters can now be compared. When plotted against instantaneous voltage the current and initial velocity data from each of the rods are distributed in three different trend regions (figures 3.5.2 and 3.5.3). The data for the medium rod and sharp rod are in two separate clearly defined regions, whereas for the blunt rod there is a lot of scatter.

Compared to the medium rod the currents and initial velocities are much lower for the sharper rod. This is obviously because for a given instantaneous voltage on the rod the electric field around the tip depends on rod diameter. The highly localised field around the sharp rod causes discharges to be initiated at lower voltages and hence propagate into a quickly reducing field resulting in lower velocities and lower currents.

The blunt rod data is almost bounded by the two regions defined by the medium and sharp rods and interestingly most of the data is distributed towards the edges. This emphasises that two distinct discharge points were operating on the blunt rod caused by the small hole drilled in its end. It is presumably the edges of this hole that provide the lower corona inception voltage discharge site and hence some characteristics resembling

the sharp rod. The blunt rod can actually be thought of as a composite rod offering several corona inception voltages and discharge initiation sites.

When initial discharge velocity is plotted against peak discharge current for all the rods (figure 3.5.4), the results all fall into the same trend region, though obviously the sharp rod results are mainly distributed towards the lower current end of the trend region. This appears to show that no matter what the rod diameter, initial velocity and peak current are linked. This is interesting because the velocity is dependent on field, which is locally defined by the rod diameter. The initial velocity is measured over the first 35mm of propagation from the rod, this means that the local field enhancement around the tip must only have a small effect on the streamers velocity as they start propagating.

When injected charge is plotted against peak discharge current the data for low currents fall into one trend region (figure 3.5.5). For peak currents of above 2A two distinct trend regions appear: one for the blunt rod and one medium rod. The medium rod trend is a linear continuation from the low current trend and it is the blunt rod characteristics that deviate. This again corresponds to the changing the shape of the discharge current waveform observed for the blunt rod at higher instantaneous voltages and onset of the second discharge on the blunt rod.

Insulator

Effect of Multiple Discharges

With an initially neutralised surface, the first discharge sets up an initial surface charge distribution. This initial distribution affects the second discharge. For the cases with the rod in contact and 5mm from the insulator, the second discharge always has a much smaller peak current than the first (figure 3.5.25 and 3.5.26). The measured surface charge distributions allow us to see what actually happens for the first time; the second discharge occupies the central region of low surface charge density set up by the initial discharge (figures 3.5.8 and 3.5.14). Further discharges add to the surface charge distribution but after about three discharges the total net surface charge does not greatly change. Additional discharges merely serve to redistribute the surface charge distribution.

Effect of Rod Surface Separation on Deposited Surface Charge

As the rod-surface separation is increased the appearance of the surface charge distributions change:

- The streamers propagate further around the insulator.
- The region directly beneath the rod becomes less negatively charged.
- The central region of low surface charge density enlarges.
- Less net surface charge is deposited.

When the rod is in direct contact with the insulator the triple junction effect produces very high localised field strengths and hence lowers the corona inception voltage. This causes the discharge to occur earlier in the applied impulse voltage and in general to have a lower peak current and velocity. This is an important point, because it is the conditions present in the main gap when the discharge starts propagating that largely determine its peak current, velocity and propagation distance around the insulator and along its length.

As the rod surface separation increases the streamers propagate almost all the way round the insulator. The field in which these streamers propagate is discussed further in the Simulations and Analysis section.

Comparison of Different Rod Surface Separations

When discharge velocity is plotted against peak current (figures 3.5.35 and 3.5.36) an interesting trend can be observed. For a particular peak current the *overall* gap velocity is independent of the presence of the insulator, however in the presence of the insulator the *initial* velocity reaches its maximum velocity when the rod is at a distance of 10mm from the surface. This is a very interesting result and may involve the high fields that exist around the rod, that lead to increased photo-ionisation on the surface in the region near the rod.

The photographic work of Ghaffar, 1994 showed that even in uniform fields discharges tended to move towards surfaces from distances as great as 50mm. The presence of the insulator distorts the electric field towards the insulator slightly when propagating as shown in figure 1.4.1.

Effect of Rod Surface Separation on Discharge Current Waveform

The shape of the discharge current waveform is affected by the presence of the insulator. The current decays much faster when the rod is in close proximity to the insulator. This is best illustrated in figure 3.5.34 where injected charge is plotted against peak current. The data points fall clearly into different regions, the overall gradient of each region (referred to as shape factor earlier) can be clearly seen to increase with rod-surface separation, this corresponds to the widening of the current pulse.

Within the time resolution obtainable there is no measurable difference in the rise time of the discharge current waveform. The rise time for all the discharges in the presence of the insulator or otherwise is about 6ns. The oscilloscope used sampled each channel every 2ns so the front time can at best be stated as 6 ±2ns.

5.3.5 The Single Discharge Event

Introduction

It is important to try to understand what comprises a single discharge. The voltage on the rod rises with the applied impulse until the localised field around the rod tip reaches a critical level and a free electron is available to initiate the discharge.

The discharge starts from the rod and propagates in the diverging geometric field as a wave of ionisation. The basic processes involved in the propagation of discharges were first described in Section 1.4.2.

Measurement Observations

The charge measurements indicate that the corona discharge is an agglomeration of individual streamers. It is these streamers that make up the wave of ionisation.

The photo multiplier signals provide information about the spatial propagation of the discharge. The measured current signal shows the current flowing in the external circuit. The externally measured current wave shape can be integrated to find the total charge injected into the gap. The externally measured current is comprised of two components: Displacement current and Electron current.

Figure 5.3.4 illustrates the part these two components play in the discharge itself. The displacement current results from the wave of ionisation that propagates and creates equal numbers of free electrons and positive ions by successive avalanches.

The Electron current corresponds to these free electrons being swept towards the rod. Some of these electrons will be attached to neutral molecules to create negative ions. On the time scales involved the positive and negative ions will remain largely stationary.

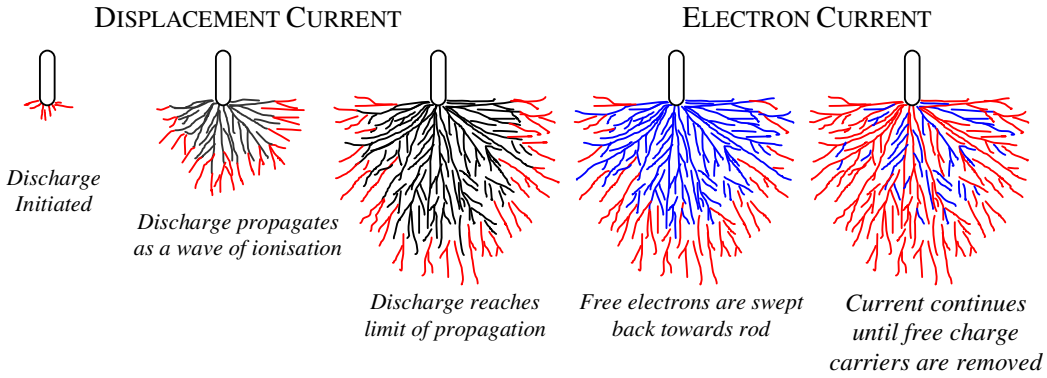

Figure 5.3.4: The development of a discharge and an illustration of the two components that make up the discharge current measured in the external circuit.

Figure 5.3.5 shows typical oscilloscope traces obtained during experimentation with the insulator present and without it, in air alone. The discharge starts at t_1, is detected by the mid-gap photomultiplier at t_2 and is detected at the ground plane at t_3. It is clear from the photomultiplier signals in both cases that the external current pulse has decayed almost to zero by the time the discharge is detected by the ground plane photomultiplier.

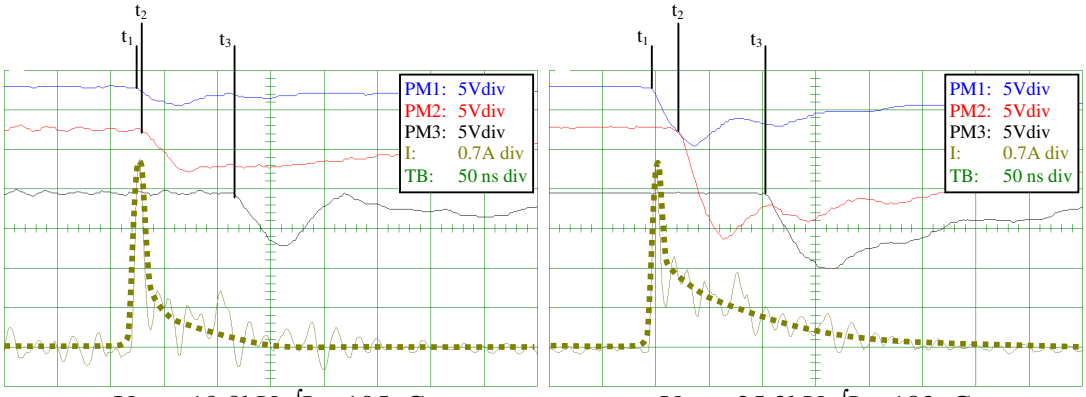

V_{inst} =19.8kV $\int I$ = 105nC

(a) Medium Rod with insulator

V_{inst} =25.3kV $\int I$ = 183nC

(b) Medium Rod in air alone

Figure 5.3.5: Close inspection of the external discharge current waveforms and photomultiplier signals.

Current Measurement Problems

The current signals contain large amounts of oscillations introduced by reflections within the measurement system. These oscillations were not caused by interference, this was proved by shorting the 70Ω current shunt, shown in figure 3.2.22. Many attempts were made (such as changing earthing configurations, cable lengths, terminations etc.) during the course of the research to reduce these oscillations but to no avail. As such care should be taken when interpreting peak currents and rise times; however relative comparisons are still valid.

Current Interpretation Problems

A number of difficulties arise when attempting to interpret the external discharge current signal and its relation to discharge propagation. In a uniform field it might be expected that the maximum external discharge current should occur at the limit of discharge propagation. However it is clear from figure 5.3.5 that the peak of the discharge current waveform occurs at some time when the discharge is between the rod and the mid-gap photomultiplier (35mm below the rod tip).

In order to calculate external discharge current a model of propagation is required, the problem is that any model introduces assumptions and simplifications. The displacement current could, for example, be modelled as an expanding shell of charge representing the positive space charge in the streamer tips. The propagation velocity could be found from the local applied field strength and hence the external displacement current could be calculated from the rate of creation of charge. Using such a model it is possible to show that in a rapidly diverging field the displacement current can reach a maximum when the discharge has not propagated very far into the gap

.

However this model assumes that in the early stages of propagation displacement current dominates, it also assumes a distribution of charge within the propagating shell, and the relationship between discharge velocity and applied field strength.

Fundamentally the displacement current model assumes that all the lines of force from the positive space charge terminate on the plane. This is not true, an indeterminate

proportion will terminate on the electrons in the replicating avalanches ahead of the discharge.

These points illustrate that interpretation of the external discharge current waveform is not trivial.

5.3.6 Single Discharge Experiments –Comments

- Peak Current vs. Instantaneous Voltage – Blunt and Medium rod show common max values up to 4A. Sharp rod currents are lower. Above 4A a second discharge site starts on the blunt rod, this changes the shape of the discharge current waveform.

- Initial Velocity vs. Peak Current – Good agreement between all three rods up to 18×10^5 ms^{-1} at 4A. With all rods, velocity is higher with surface present than in air alone.

- Injected Charge vs. Peak current – Larger for blunt rod on account of additional discharge site. In general charge injected was less than for air, but note that deionisation is more rapid.

- Less injected charge with surface discharges, this is possibly due to faster de-ionisation.

- Smaller inception voltages with rod in contact with surface, but not when separated.

- Measurements indicate that the peak of the external discharge current occurs soon after the discharge has started propagating for the rod plane gap.

5.4 Additional Experiments

5.4.1 Introduction

This section contains the discussion on the rest of the laboratory experiments conducted. These experiments are not as comprehensive as the single discharge experiments but are just as important because every measurement with the scanning system is a new discovery.

The experiments cover:

- Flashover
- Negative Impulse, DC and AC
- Materials other than pure white PTFE
- Charge Decay
- Surface Condition
- Contoured Test Objects

5.4.2 Flashover (Section 3.6)

Introduction

Thus far only pre-breakdown discharges have been observed, this experiment studies the effect of flashover on deposited surface charge. The voltage applied to the rod is increased to +85kVp and the rod-plane gap separation is kept at 8cm. The same pure white PTFE specimen as before is used.

Results

To make a comparison, impulses are first applied to the gap without the insulator present. Twenty +85kVp impulses are applied without once flashing over the gap.

The initially cleaned and neutralised insulator is then positioned in the gap with the rod in contact with the surface. The first applied impulse does not cause flashover, however every following impulse does. The presence of the insulator introduces a triple junction effect that significantly lowers the flashover voltage.

Two different types of clearly observable flashover paths are present: along the surface or away from the surface. The different flashover paths do not have recognisably different photomultiplier and current signals, however only flashovers along the surface cause permanent carbonised track marks on the insulator surface.

The oscilloscope traces and charge distributions are shown in figures 3.6.3 to 3.6.11. It is interesting to note that from the third impulse onwards (the first after the first flashover), the photo-multiplier at the ground plane records no light until the final build-up towards breakdown begins. Whereas the first two photo-multipliers looking at the rod and 35mm below its tip, record light almost continuously from the first streamer burst until breakdown; a period of well over a microsecond in most cases. This suggests continuous discharge activity near the rod until breakdown.

The onset of breakdown is heralded by a continuous burst of light observed by all three photomultipliers. This suggests that a large burst of streamers grows from the continuous discharge activity near the rod.

Charge Distributions

The first impulse applied to the initially uncharged insulator sets up a charge distribution that covers almost the entire surface. The distribution is basically an enlargement of that described in figure 5.3.3. The horseshoe of low net surface charge density extends to the ground plane with only a few streamer channel tips visible at the sides. The inner ring of low positive charge is larger as is the region of negative charge directly under the rod, which appears to contain also small highly localised regions of positive charge.

The effect of flashover on the surface charge distribution is to cut a neutralised swathe through it. It has long been reported that a flashover neutralises surface charge, and to the resolution obtainable by the scanning system this appears to be true. A small charged region remains directly under the rod, though significantly less total charge remains on the surface.

The thin arc channel contains roughly equal numbers of positive and negative charge carriers. The arc is maintained until the capacitors in the impulse generator are

discharged, at which point the arc collapses, diffuses and deposits equal numbers of positive and negative charges on the surface. The charge recombines and leaves the surface with a neutral net charge.

It is interesting that not all the surface charge is neutralised and the neutralised region has clear distinct boundaries, bordered by a thin region of negative charge. This is surprising because of the width of the neutralised region involved: over half of the circumference of the insulator. The cylindrical shape of the test object may have something to do with the clear boundaries but it is definitely not the only cause. The neutralised region becomes wider near the ground plane and often meanders down the insulator with gently curving boundaries as shown in figures 3.6.5 and 3.6.6.

It is also interesting to note that no difference can be found between charge distributions whether the flashover is along or away from the surface.

This suggests the process of the arc collapsing, diffusing and interacting with the PTFE surface has a distinct boundary and operates over a large region greater than 20mm from the arc channel itself.

Increasing Rod-Surface Separation

The experiment is repeated with the rod-surface separation increased to 5mm (figures 3.6.15 and 3.6.16). Again the gap does not flash over until the second impulse is applied. The flashover again neutralises a large swathe across the surface, however this time there is no charge left on the surface directly under the rod. Finally the rod-surface separation is increased to 10mm and the gap does not flashover (figure 3.6.18). Hence the presence of the insulator and its triple junction enhances the field near the rod and causes flashover.

5.4.3 Negative Impulse, DC and AC (Section 3.7)

Introduction

The work so far has concentrated on positive discharge events, but this is only one of many different types of high voltage discharge. It is important to observe surface charging by discharges produced by a number of different test voltages.

Negative Impulses

Negative impulses of the same wave shape as used in the positive impulse experiments (4/50μs wave approx.) were applied to the same insulator electrode set-up as used before with the rod in contact with an initially neutralised insulator.

The surface charge distributions deposited on the insulator shown in figures 3.7.2 to 3.7.5, are very complicated and localised in nature. A clear horseshoe shaped boundary around the edge of the distribution is visible. Inside the horseshoe there is a complex pattern of positively charged channels interspersed with localised regions of negative charge. Charge densities of up to $20\mu Cm^{-2}$ of both polarities are observed in the distribution.

A negative discharge from a point is a very complicated phenomenon and even less is known about it especially when interacting with a surface. Electrons are accelerated into a diverging field, and each affects the others by its self-field in a complicated way.

In the distribution shown in figure 3.7.2 a charged channel is created beyond the localised region, this could be a precursor to breakdown, possibly some sort of leader formation.

The distributions are too complicated and contain detail beyond the resolution of the scanning system to give anything but a qualitative analysis of the results.

Direct Voltage

Using exactly the same test gap set-up, DC voltages were applied to the rod for one minute. At low voltages only very localised charge was deposited around the tip of the rod. For voltages where an audible corona was present a general charging of the surface occurred. The charged regions are localised around barely visible manufacturing defects on the surface and charge of both polarities is present. The same is true for both positive

and negative applied DC voltages. This may have important consequences for the manufacturing of high voltage insulators, especially in DC applications.

Alternating Voltages

Again using the same set-up, 50Hz alternating voltages were applied to the rod for one minute then abruptly switched off. Two test voltages of 15 and 30kVrms are used. In both cases the surface discharge pattern observed (figures 3.7.11 and 3.7.12) are very similar to the single positive discharge events, with streamer channel paths visible around the edge of the distribution. For the higher test voltage the surface discharge pattern is significantly larger and more charge is deposited. It should be noted that at 15kV the rod might not produce discharges on the negative half cycle.

At 30kV the rod is assumed to be producing positive and negative corona discharges on alternate half cycles. The work done on multiple discharges in this thesis only covers same-polarity discharges and indicates that each discharge produces a new distribution of charge within its region of propagation. Negative discharges do not propagate as far for a given voltage and so should not reach the positive streamer channel paths visible around the edge of the distribution. It is also important to note that it is not known whether the test voltage was removed during the positive or negative half cycle.

For comparison the experiment was repeated at 30kV but the voltage was reduced slowly to zero over about 10 seconds. The deposited charge distribution (figure 3.7.13) is much smaller than when the test voltage is abruptly removed. The distribution obtained appears to be created by a small positive discharge.

This phenomenon can be explained as follows: as the voltage is slowly lowered the rod continues to produce smaller and smaller discharges, until the corona extinction voltage is reached at which point no further corona activity occurs and the surface is left with the charge distribution generated by the last discharge. The fact that the last discharge appears to have been a positive one follows because negative corona inception and extinction voltages are greater than positive ones for the same electrode configuration. Thus as the voltage is lowered the rod stops producing discharges on the negative half cycle before the positive half cycle, as shown in figure 3.7.14.

5.4.4 Other Materials (Section 3.8)

Introduction

All the work so far has studied surface charge on pure white PTFE. Its excellent ability to hold surface charge make it an ideal test object for the development of the scanning system and starting point for the investigation. PTFE is also commonly used in many high voltage applications including circuit breaker nozzles.

Various other materials are investigated to a limited extent to put the PTFE measurements into perspective. Only specimens half the height of those used previously are available so the rod plane gap had to be reduced to 40mm.

Air and PTFE

The properties of the shorter gap were briefly studied in air and with a 40mm tall PTFE specimen. Impulse voltages of peak magnitude +26.6kV are applied to the rod. Without the insulator present the photomultipliers indicate the discharge just crosses the gap (figure 3.8.2). With the PTFE insulator present the triple junction effect causes the discharges to occur at a much lower voltage and the mid-gap and ground plane photomultipliers did not detect a signal. However several distinct small discharge events did occur with each application of the impulse voltage as visible from the current signal and the photomultiplier looking directly at the rod tip (figure 3.8.4).

Two other types of PTFE were tested; Molybdenum disulphide doped and carbonised. They exhibited similar charging patterns and discharge characteristics to pure white PTFE.

Polyethylene

An initially neutralised polyethylene test object of the same size was positioned in the gap and ten +26.6kV impulses applied to the rod. The current and photomultiplier traces appear very similar to the PTFE case: several distinct small discharges that are only detected by the first photomultiplier. The surface charge distributions show positive streamer channels similar to those obtained on PTFE. Some of the streamer channels

almost bridge the entire gap. This is further evidence that the absence of a photomultiplier signal does not necessarily indicate the absence of discharge activity.
In a similar way to PTFE the total amount of surface charge deposited on the insulator surface begins to level out after about three discharges, and manufacturing defects on the surface affected the shape of the charge distributions.

Other Materials

Other materials were studied only to a very limited extent. Some surface charge was detected on epoxy resin, unglazed porcelain, glass, fibreglass. No surface charge was detected on nylon or glazed porcelain.
The absence of surface charge can mean one of three things: either the material does not attach surface charge; or it does but only very slightly and the scanning system cannot detect it; or it does but the surface charge decays away before the scanning system can measure it.

5.4.5 Charge Decay and Surface Condition (Section 3.9)

Introduction

When charge is detected it is found to stay on the surface for a substantial length of time. The condition of the surface plays an important part in the decay of charge from the insulator's surface. A dirty, greasy or track-marked surface will lose charge quicker than a clean one. To allow repeatable experiments to be made, all the insulator specimens were thoroughly cleaned using ethanol to remove any greasy surface residue.
Manufacturing marks on the surface of the insulator cause charged regions to appear when the surface is subjected to high fields or corona discharge activity. The manufacturing marks are barely visible to the naked eye but because they are effectively

small distortions in the surface they cause localised enhancements in the applied electric field. This effect is observed for all insulating materials on which surface charge can be detected. This has important implications for industrial applications where very high tolerances for surface smoothness may improve insulator performance.

Ignoring the complications caused by the macroscopic condition of the surface, the basic mechanisms available for surface charge decay are as follows:

a) Ions from bulk material attracted by charge to surface
b) Atmospheric ions reaching surface to neutralise
c) Ions of both polarity combining on surface
d) Combination between the sharply defined regions of positive and negative charge
e) Surface mobility of charge

Natural PTFE Decay

Starting from an initial charge distribution on clean PTFE the total amount of surface charge decreases slowly with a half-life of about eight days. Slices through the charge distribution (figure 3.9.3) show that the charge density in each region of the insulator surface decays slowly with time. There is no significant evidence for the charge spreading out over the insulator surface; hence surface mobility under its own field must be negligible. Davidson and Bailey, 1999 made the same observation in measurements on thin polyethylene sheets against a grounded back plane.

Stressed PTFE Charge Decay

To provide an idea of the surface mobility of charge under an imposed electric field, the decay of surface charge from PTFE is studied under a uniform electric field.

In the Single Discharge Experiments the voltage remains on the rod for a short time after the discharge has occurred. The effect this field has on the deposited surface charge distributions after the discharge has finished propagating is of interest when

analysing the charge distributions. The study of surface charge under D.C. stress also has important significance where insulation is used in D.C. applications.

First the effect of electric field on an initially neutralised insulator is evaluated. Two plane electrodes are used to apply a uniform field of $750kVm^{-1}$ for 1 hour to a PTFE specimen. Significant charge densities of around $\pm 5\mu Cm^{-2}$ were measured on the insulator surface (figure 3.9.5). The charge is mainly concentrated around small manufacturing defects on the surface. Triple junctions created by manufacturing defects near the electrodes are apparently the source of the discharge activity that produces the surface charge.

Then two different initial charge distributions (one generated by negative corona figure 3.9.6, and the other by positive figure 3.9.7) are subjected to the same uniform field for 3 hours and the surface scanned every hour. Additional charge is deposited by the triple junctions and manufacturing defects but this does not increase significantly after the first hour. There is no detectable evidence of charge migration from the original distributions across the insulator in the presence of the electric field in either case.
This leads to the conclusion that the surface mobility of the charge is low even under high field stresses. Hence the charge distributions will not have been effected by the voltage remaining on the rod after the discharge, and will give an accurate representation of the charge deposited when the discharge finished propagating.

Polyethylene Charge Decay

Polyethylene is the only other material on which charge decay is studied. Natural charge decay was found to have a half-life of approximately 4 hours. Close studies of the charge distributions indicate that in some regions charge decays faster than in others. A possible explanation is macroscopic differences in the surface.

5.4.6 Contoured Test Objects (Section 3.10)

Introduction

So far all the experimental work has employed simple cylindrical insulator test objects. The scanning system is capable of scanning a vast number of different shaped test objects. Time restrictions meant that a full study into the effect of insulator profile on surface charging could not be undertaken. The single shed is the most complicated geometry the scanning system can handle and is chosen for a brief study.

Scanning Problem

To scan the shed geometry the probe must move through a large range of different angular positions (figure 3.10.1). This tests the positional accuracy of the stepper motors.

The contoured shape of the test object means that it has a very large surface area. To reduce the size of the Φ-Matrix used in the inversion the surface is split into three regions. Each of these regions can be scanned and solved separately.

A number of options are open when trying to the display the contoured surface charge distributions because of the problem with unrolling the distributions to be shown on a flat page.

Results

The contoured insulator specimen made of carbonised PTFE is positioned in an 80mm rod plane gap and +85kVp impulses applied to the rod. The applied voltage is high enough to cause flashover.

A lot of discharge activity is present near the rod however the photomultiplier signals (figure 3.10.6) indicate that in some cases it takes a long time before streamers reach the ground plane. The shed obviously has some sort of delaying action

Streamer channels can be seen in the surface charge distributions (figure 3.10.9), and in flashover cases (3.10.10) a neutralised path is cut through the charge distribution consistent with those observed previously on cylindrical insulators.

The streamer channels appear to stop on the underside of shed, indicating that the streamers left the surface and continued to travel in air at this point. The top of the shed

has a net positive charge and the bottom of the shed has a net negative charge. The negative charge on the underside of the shed appears to be concentrated at points where the streamers left the surface. This has similarities with the region directly under the rod, which is also negatively charged.

Unfortunately these initial experiments ask more questions than they answer, and there is much more work to be done here.

5.4.7 Additional Experiments- Comments

- Flashover cuts a wide neutralised path through surface charge distributions with clearly defined boundaries.

- The absence of a photomultiplier signal does not necessarily indicate the absence of discharge activity.

- Surface charge is found around manufacturing defects on the surface.

- Manufacturing defects combined with triple junction effects can creat sources of discharge initiation sites.

- Surface charge can remain on clean PTFE for days.

- The surface mobility of the charge is low even under high field stresses.

- Different materials have different decay rates.

- Not all insulator materials exhibit surface charging.

5.5 Simulations and Analysis

5.5.1 Introduction

Modelling the probe and the surface charge allows a much deeper understanding of the experimental work. The main tool is 3-Dimensional finite element modelling software. Rerup et al, 1996 used 2-Dimensional approximations to find solutions, however finding the probe's response function is clearly a three-dimensional problem. Values obtained from a 2-Dimensional model will at best be approximations.

The accuracy of the values obtained depend upon the validity and discretisation of the model. The validity of the model depends on how accurately it represents the object being modelled, i.e. dimensions, permitivities, simplifications.

The discretisation of the model is how small the elements in the finite element mesh are. The model is a solution of Poisson's and Gauss' Equations for electric fields so smaller elements produce a closer approximation to the solution. Very small elements are used where high accuracy is required.

5.5.2 Probe Modelling (Section 4.2)

Model

The initial aim of modelling the probe is to find its response or ϕ-function; this is the voltage induced on the probe by a unit charge at every position on the surface. The Solver software only requires key points in the probe's response function, so it is not necessary to model every individual element of charge on the surface. This greatly reduces the time taken to find the probe's response function.

Results

Modelling the entire surface and probe arrangement allows a much deeper insight into the operation of the electrostatic probe. The field produced by an element of surface charge extends some distance from its perimeter; as the grounded outer screen of the probe approaches it distorts this field (figure 4.2.5). This complex relationship operating over a distance emphasises the inadequacy of the simple capacitive calibration

technique and proves that only a 3-dimensional solution will yield accurate results. It also shows that the presence of the probe cannot be neglected as Sudhakar and Srivastava, 1987 did in their calculations.

The field in air between the element of surface charge and the probe reaches a maximum when the grounded outer screen and not the sensor plate itself is directly above the element. It is this field that limits the closeness of the probes approach to the surface before the surface charge flashes over to it.

The field distribution within the probe's insulation itself is also studied (figure 4.2.6) and observations made such as the depth of field penetration into the insulation which have implications for future probe design.

The main limitation of a 2-dimensional model of the probe as discussed by Wintle et al, 1997 is boundary problems. With the 3-dimensional model however it is easy to study what happens when the probe nears a ground plane at the edge of an insulator: distant charges make a smaller contribution to the total probe voltage. It is necessary to take this into account to maintain the accuracy of the calculated surface charge distribution.

Increasing the probe-surface separation greatly reduces contributions from charge directly beneath the probe, whereas charge some distance from the probe still contributes a similar amount (figure 4.2.12).

The effect of increasing insulator material permitivity is to scale down the probe response function; charges effectively induce smaller voltages on the probe. Further studies into the exact nature of this scaling would allow an automated system to calculate the required probe response function. A "standard" probe response function could be transformed for different insulator permittivities.

Accuracy

The calibration test piece is modelled by setting a strip of the surface to a voltage; this simulates a metal strip on the surface. The calculated and measured values differ by only 1%. This puts great confidence in the accuracy of the model and the values measured by the probe.

The model is used to calculate the probe response function, which is used in the Φ-Matrix calibration technique. The interaction of the accuracy of the calculated values

and measured values during this technique is complex, however with a starting error of only 1% in both quantities the overall accuracy of the system should still be reliable.

5.5.3 Effects of the Φ-Matrix (Section 4.3)

Introduction

The surface charge distributions and the probe voltage distributions differ dramatically in appearance. The probe voltage measurements are the combination of the probe response function and the surface charge distribution. The matrix technique effectively removes or de-convolutes the probe response function from the probe voltage distribution. In this section the effect of removing different shaped probe response functions from a measured probe voltage distribution is studied.

Experiments

The probe response functions were all normalised to the same peak value. The width or Q (see figure 4.3.1) of the probe response function is related to the probe's effective resolution.

A probe response function that is zero everywhere apart from directly under the probe (equivalent to the simple capacitive model) will produce a charge distribution that looks exactly like the voltage distribution from which it was derived (figure 4.3.3).

The probe response function is progressively widened and the resulting distribution becomes more localised (figures 4.3.4 to 4.3.6) until at certain critical width large chaotic values swamp the derived distribution (figures 4.3.7 and 4.3.8). By altering the shape of the probe response function slightly the limiting case can be found beyond which the calculated distribution descends into chaos.

Theory

The limiting case probe response function is very close to the calculated probe response function of the actual probe that first measured the voltage distribution. On the basis of this observation it is proposed that for a given voltage distribution the limiting case

probe response function is the actual probe response function of the probe that measured the voltage distribution.
Thus it should be possible to derive a charge distribution from the probe voltage distribution without doing the probe modelling required to find the probe response function. The voltage distribution does after all contain characteristics from both the charge distribution and the probe response function.

The calibration procedure is effectively the solution of a large number of simultaneous equations. The charge distribution is the unique solution for a given voltage distribution and probe response. The limiting case occurs when a probe response function wider than the probe response function that actually measured it is removed. This is effectively like trying to find a charge distribution from a voltage distribution that could never have been produced by probe of that resolution.

It is not possible to find the exact limiting case because small errors in the voltage distribution are amplified as the limit is approached. This will limit the accuracy of using this technique to remove probe response functions from a probe voltage distribution.
This accuracy may be improved if a 'mean' limiting case is found from a large number of different probe voltage distributions measured with the same probe. However for high-resolution charge distributions the task of finding numerous limiting cases each requiring several iterations of the Φ-Matrix procedure would be colossal and beyond the realms of any near computing power (see figure 5.2.1).

5.5.4 Electrode Modelling (Section 4.4)

Model

The rod-plane gap electrode arrangement is modelled to allow the evaluation of the ambient field in which streamers propagate. The field on the insulator surface is of interest for different rod-surface separations; this will allow the single discharge experiments with the medium rod to be analysed further. A 3-Dimensional model is essential because the geometry cannot be reduced to a 2-Dimensional problem; however

the line of reflectional symmetry can be exploited (figure 4.4.1) to halve the size of the model and hence halve number of calculations required. The solution obtained is obviously scalable so a per-unit voltage is applied to the rod.

Triple Junction

The triple junction effect was first described in the Introduction chapter. When the rod is in contact with the surface a triple junction is set up as the rounded tip of the rod touches the surface. The electric field strength rises rapidly at this point; the maximum value of the field depends on the actual dimensions of triple junction.

This shows a limitation of the modelling technique; the triple junction could be modelled as infinitely thin, in which case the localised field strength would tend to infinity. Practically this is obviously not the case so an assumption must be made as to the final thickness of the triple junction. The model employed here uses an arbitrary final triple junction width of 0.1mm. This is the final distance between the rounded rod tip and the insulator; the rod tip curves asymptotically to meet the surface, when it is 0.1mm away from the surface the rod is stepped-out to make contact. This is a necessary simplification to the model. For the electrode arrangement modelled a 0.1mm final width triple junction produces a maximum per-unit surface field strength of $366Vm^{-1}$. When compared with a maximum per-unit surface field strength of only $45Vm^{-1}$ when the rod is 5mm away from the surface, the importance of triple junction field enhancement in lowering the corona inception voltage is obvious.

5.5.5 Surface Charge Modelling and Analysis (Section 4.5)

Instantaneous Geometric Field

It is essential to compare the measured charge distributions with the calculated applied surface electric field strengths. The applied electric field strength is calculated from the instantaneous voltage applied to the rod at the moment of discharge. The measured charge distributions are combined with the calculated field strengths for comparison. It should be noted that in the practical experiments the rod is positioned at a small angle to the horizontal to provide a “single” point of contact on the insulator surface, whereas

the fields are calculated with the rod vertical to simplify the modelling process. This means that the field strength directly under the rod will be lower than those calculated. Surface field strengths away from the rod will not be effected by this difference.

It is obvious from all the results that the streamers are capable of propagating not only in very low field strengths (≈50kVm^{-1}) but also almost orthogonal to the applied geometric field. Where the applied geometric field is lowest (near the top of the insulator away from the rod) the streamers deviate the most from the direction of the applied lines of force (see figures 4.5.1 to 4.5.6).

This result emphasises the importance of the self-field produced by the streamers themselves. The streamers propagate under a combination of the applied electric field and the field at the streamer tips. This self-field also plays a significant role in causing each of the streamers to repel each other and hence the discharge to spread out.

As the rod-surface separation is increased the inception voltage is increased because of the reducing triple junction effect. This leads to the discharge occurring at higher instantaneous voltages and the discharge propagating in higher ambient fields. The streamers propagate further around the surface when the rod-surface separation is increased. So although the self field plays a dominant role in streamer propagation, the ambient field strength in which the streamers propagate also plays in important part. It is a combination of the two that determine propagation distance.

Analysis of Charge Measurements

Streamer Paths

Upon close analysis of the charge measurements (figures 4.5.8 to 4.5.14) it is obvious that the charge density in the streamer paths around the perimeter of the distribution are greatest at the tips and decay towards the rod. These are snapshots of the charge deposited by the streamers just as they stop propagating. It is interesting that only the last 10 to 20mm of each streamer path is visible, beyond this the streamer paths fade out and are lost in the horseshoe region of low net surface charge density (see figure 5.3.4 for the generic anatomy of a surface charge density distribution for a single positive discharge event on PTFE). This is partly a limitation of the resolution of the charge measurement technique because the streamer channels become too close together to

resolve individually. The actual width of a single streamer path will be smaller than the 1mm limit of resolution of the scanning system.

Maximum Streamer Path Charge Density

It is interesting to note that in all charge distributions studied from the single discharge experiments the maximum charge density at individual streamer path tips is about $10\mu Cm^{-2}$. This equates to 10pC of charge in the last millimetre of the streamer.

The streamer itself is comprised of the number of avalanche heads. A figure often quoted for the number of charge carriers in a single avalanche head is 10^8. This equates to a charge of approximately $10^8 \times 1.6 \times 10^{-19}$ = 16pC. This value compares very favourably with the charge measured on the surface.

The last millimetre of streamer presumably contains several avalanche heads. If each avalanche head is approximately 100μm in diameter there will be 10 heads or approximately 160pC of charge of each polarity available to deposit on the surface. So a measured value of 10pC means that only a 1/16th of the available charge is deposited on the surface.

It should also be noted that the value of 10pC is an average over the last millimetre of streamer path. The charge in the streamer path decays rapidly, so the last millimetre will actually contain charge densities higher and lower than the $10\mu Cm^{-2}$ measured.

Streamer Path Charge Density Decay

The rate at which the charge density decays along streamer paths can be estimated from the charge distributions. This allows a direct measurement of the *overall* surface attachment coefficient as first defined in section 1.4.3. Previous researchers such as Gallimberti et al, 1991 employed an indirect method involving a similar propagation model and discharge current data to calculate the surface enhanced attachment coefficient. The problems of interpreting external discharge current were discussed briefly in section 5.3.5.

Gallimberti estimates the surface enhanced attachment coefficient for PVC as between 10 and $15cm^{-1}$.

As was stated in the Introduction Chapter, the surface enhanced attachment coefficient is the surface attachment coefficient plus the attachment coefficient for the surrounding air. If the attachment coefficient for the surrounding air is the same as for air with no insulator present then the surface attachment coefficient can be calculated by subtracting the air value from the enhanced one. From Gallimberti's results this gives values between 4 and 8cm^{-1}. The surface discharge is the interaction between the surface and the surrounding air, so it is possible that air near the surface of the insulator behaves differently from air away from the insulator and so the simple subtraction is invalid.

The values measured in this thesis for the *overall* surface attachment coefficient for PTFE range between 1.4 and 2.3 cm^{-1}. This is in the same order of magnitude as Gallimberti's results for surface enhanced attachments on PVC. The values should be expected to be different for a number of reasons: they are obtained using different types of measurement, on different materials, and the overall surface attachment coefficient takes into account processes occurring after propagation has ceased. It may be possible to use the overall surface attachment coefficient to test future theories on overall discharge behaviour.

Modelling Surface Charge Measurements

The electric field produced by the surface charge, its self-field, or space charge field as it is sometimes referred to, is obviously of importance in surface discharges. Finite element modelling using the charge densities measured in the experiments allows a quantitative study into these field strengths.

A 1mm^2 surface element (figure 4.5.16) has uniform charge densities applied and the field on the surface calculated. The field strengths are greatest at the edges of the element; the field is lower in the centre of the element due to the screening effect of the surrounding charge. A perfectly uniform distribution over a 1mm^2 element is obviously not a naturally occurring distribution of charge.

It is clear that an individual streamer will deposit charge in a thin path. The next step is to investigate the effect the width of the charged path has on the electric field strength. The measured peak streamer tip charge density of 10μCm^{-2} or 10$pCmm^{-1}$ is applied to the thin charged path and its width varied from 20 to 100μm. The surface field strengths

produced are in the order of MVm^{-1} (figure 4.5.22). It clear that very thin paths cannot possibly hold this amount of charge; the self-field produced is too great, the distribution would blow itself apart.

Assuming the maximum field allowable in a distribution is $3MVm^{-1}$ this gives a minimum charged path width of about 130μm (figure 4.5.23).

This value of 130μm is exceptionally close to previous researchers (Mikropoulos, 1998) estimates of streamer diameter which range from 25 to 125μm. It is important to remember that 130μm is an estimation of *charged path width*, which is different from actual *streamer diameter*. It should also be noted that the 25 to 125μm estimate is for air.

It is interesting that 130μm is slightly larger than the upper estimates for streamer diameter. A possible explanation for this is that the streamer has a wide range of influence as it propagates. Another interesting explanation is that the streamer deposits a large amount of charge which then expands under its own field into a wider path.

Either way it appears that the limiting factor in the deposition of surface charge is the field produced by the charge itself. This perhaps provides an explanation as to why only a fraction of the total charge in the streamer itself is deposited on the surface.

Charge is deposited on the surface until an equilibrium is reached when the field due to the deposited charge density is equal to the field that is driving the charge towards the surface. The surface charges up on account of the thermal energy of the ions and electrons in the streamer and equilibrium will be reached when the repulsive field would impart to the ions a force equal to that which they have by virtue of thermal motion.

Rather than a uniform distribution of charge within the streamer channel a Gaussian distribution is probably a more natural distribution. It will approximate the assumed ion density in the head of the streamer in air. When a Gaussian charge distribution is applied to the modelled streamer path it has the effect of smoothing the overall field and removing the maxima at the channel's outer edges. For a charge distribution with a Gaussian cross section the greatest field strength occurs at its centre; this is a more natural distribution of charge, where the greatest charge density coincides with the

greatest electric field strength. It also corresponds to the likely distribution of charged particles in the streamer in air

The peak value of the modelled Gaussian distribution corresponds approximately to the field at the centre of a 50μm diameter uniform charge density streamer channel. This is very close to the 45μm half width of the Gaussian charge distribution itself (see figure 4.5.21(a) CASE C). Hence it can be said that the 130μm limit for the charged path width is also the maximum half width if the charge is distributed with Gaussian cross-section.

5.5.6 Simulations and Analysis – Comments

- An accurate 3D model is essential when calculating the probe response function.

- A voltage distribution contains a combination of the surface charge density distribution and the probe response function it may be possible to separate the two in an iterative manner in the future.

- The triple junction effect creates very high, localised field strengths when the rod is in contact with the insulator.

- The electrode modelling field studies show that the self-field produced by the streamers themselves is obviously of great importance when streamers propagate.

- The scanning system allows a direct measurement of the overall surface attachment coefficient.

- The field studies combined with the charge measurements show that the self-field produced by the charged path is obviously of great importance as charge is deposited, and is probably the limiting factor in the deposition of charge.

Chapter 6: CONCLUSIONS

6.1 Overview

A new experimental technique has been developed and evaluated that has allowed a quantitative study of the surface charge deposited on practical insulator specimens. Charge density distributions have never before been quantitatively measured to the resolutions obtained here on practical insulator specimens.

The measurement system has allowed many unique experiments, such as the effect repeated discharges have on the surface charge distribution. It is also capable of resolving the charge deposited by individual streamers. These experimental measurements have been applied to models and have revealed that the self-field is an important limiting factor in the deposition of charge on the surface.

6.2 Charge Measurement

The Scanning System provides an advance in instrumentation because of a combination of qualities:

- High Spatial Resolution Measurement
- Works on thick and Practical Insulator Specimens
- Multi-point Calibration Technique
- Accurate 3D solution of probe response function
- Capable of scanning different and contoured insulator geometries
- Easy to use

Previous scanning systems have had one or two of these qualities but not all of them. The scanning systems strength is that it is a complete tool for measuring, calculating and analysing surface charge density distributions.

When studying surface charge, high-resolution measurements are essential because of the complex and detailed nature of the deposited charge. Low spatial resolution measurements are only useful in determining total net surface charge and general regions of high and low net charge density.

The very close agreement between the measured and modelled probe voltages for the calibration test piece combined with the similarity between the measured surface charge density distributions and the corresponding dust figures, give great confidence in the results obtained. The scanning system can detect charge densities in the range of 0.1 to about $50\mu Cm^{-2}$ on $1mm^2$ elements of the surface.

The scanning system is flexible and capable of measuring surface charge distributions on many different insulator sizes and even on contoured insulators by scaling the probe response functions (ϕ-functions) accordingly.

The probe voltage to surface charge density conversion technique (Φ-Matrix technique) was developed for this project and has been fully researched to allow deeper insights into the technique. It may be possible to find a surface charge distribution from a probe voltage distribution without first knowing the exact probe response function as discussed in section 5.5.3.

6.3 Experiments

Several Conclusions can be drawn from the experimental work:

When an insulator is introduced into an electrode arrangement and touches the electrodes a triple junction will be created. The triple junction effect greatly lowers the discharge inception voltages by distorting the ambient electric field, causing localised field enhancement. Hence the discharge is initiated in a lower ambient field, which is directly related to the voltage on the rod electrode.

Discharges propagate faster in the presence of a PTFE insulator. Initial velocities in high fields near the rod show the greatest increase in velocity and the insulator continues to have an effect when the rod is 10mm away from the surface.

High negative surface charge densities occur on a PTFE insulator surface directly under the HV electrode when positive streamers propagate from it.

After 3 to 5 discharges the amount of surface charge deposited reaches a limit. Further discharges merely serve to alter the distribution of surface charge. This is true for all materials studied.

Surface charge from streamer corona is deposited in a very localised manner; it is not diffusely spread. Any theories involving surface discharges should take this into account.

The field produced by surface charge deposited by streamers can be very high. It may be high enough to affect the propagation of further streamers and the deposition of further surface charge.

Small manufacturing defects can cause and affect surface charge distributions. Measurements have shown that in high fields manufacturing defects at triple junctions are the source of discharge activity. Also in the presence discharge activity small surface imperfections anywhere on the surface will accumulate surface charge.

Flashover neutralises PTFE surface charge over a large region with clear boundaries. Measurements have shown that charge is neutralised over a region of up to 40mm either side of the arc channel. Further work is needed to explain the mechanisms that result in such a wide neutralised region with clearly defined boundaries.

Surface charge can remain on clean PTFE for days. No movement or re-dispersal of surface charge could be detected. Greasy or heavily track marked insulators loose charge much quicker than clean ones. Different decay rates are observed for different materials and not all materials exhibit surface charging.

The self-field of the streamers themselves plays an important part in their propagation. Streamers have been observed propagating in very low ambient applied fields and in a direction almost orthogonal to the applied field.

The scanning system is capable of resolving individual streamer channels and allows a direct measurement of overall surface attachment coefficient for streamers after they have stopped propagating.

Measured values show the maximum surface charge deposited in the last mm of a streamer channel on PTFE is 10pC. This is of the same order of magnitude as the accepted value of 16pC (10^8 electrons) in an avalanche-head.

The self-field produced by the charged streamer path is probably the limiting factor in the deposition of charge. Using this assumption with the measured and calculated values in this thesis, the limiting half-width of a streamer channel is found to be 130μm.

6.4 In Summary

The scanning system has quantified the fine detail in streamer discharges in practical situations and revealed that localised surface charge can produce very high fields. It is clear that we do not fully understand surface discharges. High spatial resolution measurement of surface charge distributions is essential in furthering our knowledge of the way discharges interact with insulating surfaces.

Surface charge will continue to be a problem for manufacturers using modern synthetic materials. Surface charge can easily set up very high fields in complicated distributions that will affect discharges in a number of ways. Surface charge is the cause of the increased variability and occasional unpredictability of breakdown in the presence of an insulating surface.

6.5 Future Work

The Scanning System has opened up many different routes for research and there are numerous studies that could be undertaken using the scanning system:

- Contoured insulators – The effect of geometry on deposited surface charge
- Detailed Study of Other Materials
- Negative Surface Discharges
- Improve the resolution of the probe - build a smaller probe.
- Volume Charges – Preliminary studies indicate that the multi-point scanning and calibration technique could be adapted to calculate volume charge distributions within insulators.

In addition the current measurement technique should be improved by the use of a high bandwidth optical link for isolation of the measurement system from high voltages and sources of noise.

Appendix A: The effect of Offset

The only measurement that contains significant errors is the probe voltage offset. There are various contributing factors; the probe buffer circuit's response to being grounded, the probe drift between grounding and first measurement, and the electrical work done in moving the sensor plate from ground through the field created by the surface charge to the first measurement position.

The probe voltage offset error is constant and present for all the voltage measurements in a surface. The effect of offset on the Φ-Matrix calibration procedure can be assessed by considering a simple 3×3 matrix multiplication:

Take an arbitrary matrix and a vector of 3 voltage readings V_1, V_2, V_3 which can be multiplied together to produce a resultant vector:
First assume no voltage offset error:

$$\begin{bmatrix} a & b & c \\ d & e & f \\ g & h & i \end{bmatrix}\begin{bmatrix} V_1 \\ V_2 \\ V_3 \end{bmatrix} = \begin{bmatrix} aV_1 + bV_2 + cV_3 \\ dV_1 + eV_2 + fV_3 \\ gV_1 + hV_2 + iV_3 \end{bmatrix}$$

Then assume a voltage offset error of k:

$$\begin{bmatrix} a & b & c \\ d & e & f \\ g & h & i \end{bmatrix}\begin{bmatrix} V_1 + k \\ V_2 + k \\ V_3 + k \end{bmatrix} = \begin{bmatrix} a(V_1 + k) + b(V_2 + k) + c(V_3 + k) \\ d(V_1 + k) + e(V_2 + k) + f(V_3 + k) \\ g(V_1 + k) + h(V_2 + k) + i(V_3 + k) \end{bmatrix}$$

$$= \begin{bmatrix} aV_1 + bV_2 + cV_3 \\ dV_1 + eV_2 + fV_3 \\ gV_1 + hV_2 + iV_3 \end{bmatrix} + \begin{bmatrix} k(a + b + c) \\ k(d + e + f) \\ k(g + h + i) \end{bmatrix}$$

$$= \begin{bmatrix} a & b & c \\ d & e & f \\ g & h & i \end{bmatrix}\begin{bmatrix} V_1 \\ V_2 \\ V_3 \end{bmatrix} + \begin{bmatrix} k(a + b + c) \\ k(d + e + f) \\ k(g + h + i) \end{bmatrix}$$

So by adding a constant value k, to the voltage vector the resultant vector is added to by k times a vector made up of the sums of the rows in the matrix.

If the sums of all the rows in the matrix were the same then offset errors in the voltage would be translated into a simple offset in the resultant vector.

However if the sums of the rows are different then a more complicated translation takes place.

To see how this result affects the calibration procedure the sums in the Φ-Matrix need to be found. In the Φ-Matrix case the columns are summed not the rows, this is simply because the matrix multiplication involved is $\overline{\sigma} = \overline{V}\Phi^{-1}$ not $\overline{\sigma} = \Phi^{-1}\overline{V}$ as shown in the example. (The latter version was shown as an example simply because it fitted on the page better.) The vector containing the column sums of the inverted Φ-Matrix is defined as $\overline{\mathrm{CS}(\Phi^{-1})}$. The effect of the unknown probe voltage offset *k*, can thus be equated as:

$$(\overline{V} + k)\Phi^{-1} = \overline{\sigma} + k \times \overline{\mathrm{CS}(\Phi^{-1})}$$

Where $(\overline{V} + k)$ is the probe voltage vector with *k* added to each of its values.

This equation means that the charge distribution can be extracted from a probe voltage distribution even if the probe voltage offset is unknown.

To understand how this works the properties of the inverted Φ-Matrix column sum vector require investigation.

This vector can easily be calculated during the Φ-Matrix calibration procedure, but explain its appearance one must refer to the composition of the Φ-Matrix itself.

Each column of the Φ-Matrix contains all the values of the ϕ-function for each probe position. So each value in the column sum vector of the Φ-Matrix is the sum of all the ϕ-function values for each probe position.

The sum of all ϕ-function values can be thought of as the volume under the ϕ-function if the per-unit elements are used. This volume remains largely constant, and it is only as the probe approaches a grounded object that the ϕ-function becomes distorted and hence its volume slightly altered. So the values in the column sum vector of the Φ-Matrix should be mostly the same. However a second complication affects this similarity.

The question of what to do with the ϕ-function as the probe nears the edges of the surface causes this complication. This can best be explained using the idea of edge wrapping. Figure A.1 illustrates the four basic approaches to edge wrapping.

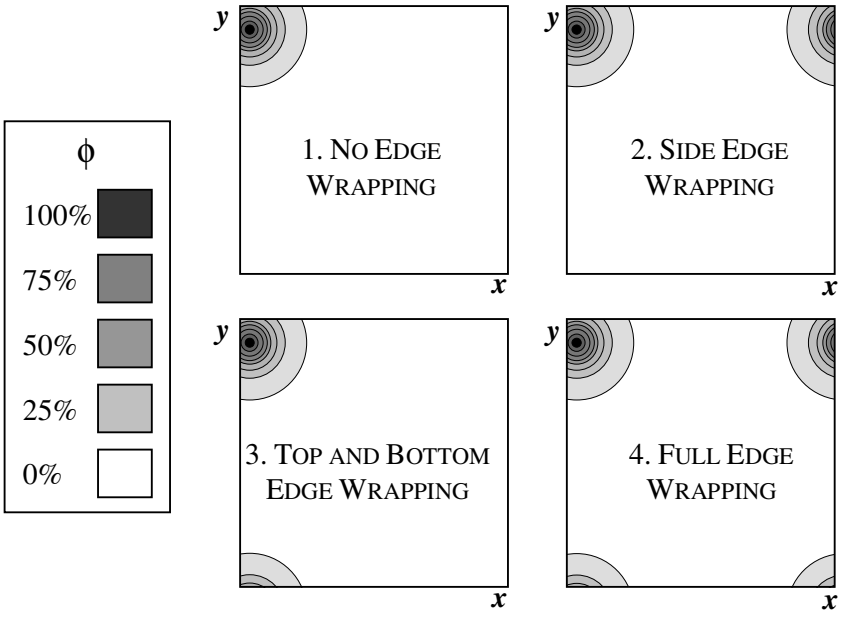

Figure A.1: The ϕ-function for the probe near the top left corner of the surface for different types of edge wrapping.

The first edge wrapping technique is no edge wrapping. This leads to the volume under the ϕ-function decreasing as the probe nears the any of the edges of the defined surface. This technique is used when the surface is used when only a portion of the surface is scanned.

The second type of edge wrapping, the technique employed in the solution of all the distributions in this thesis is side edge wrapping. This technique is used when the entirety of a cylindrical surface is scanned so the extreme left and right of the distribution is the same place. The volume under the ϕ-function only decreases significantly when the probe nears the top and bottom of the distribution.

The third type of edge wrapping is effectively the same as the second, but wraps the top and bottom instead.

Full edge wrapping removes any major variations in the volume under the ϕ-function, but does not represent a realistic surface.

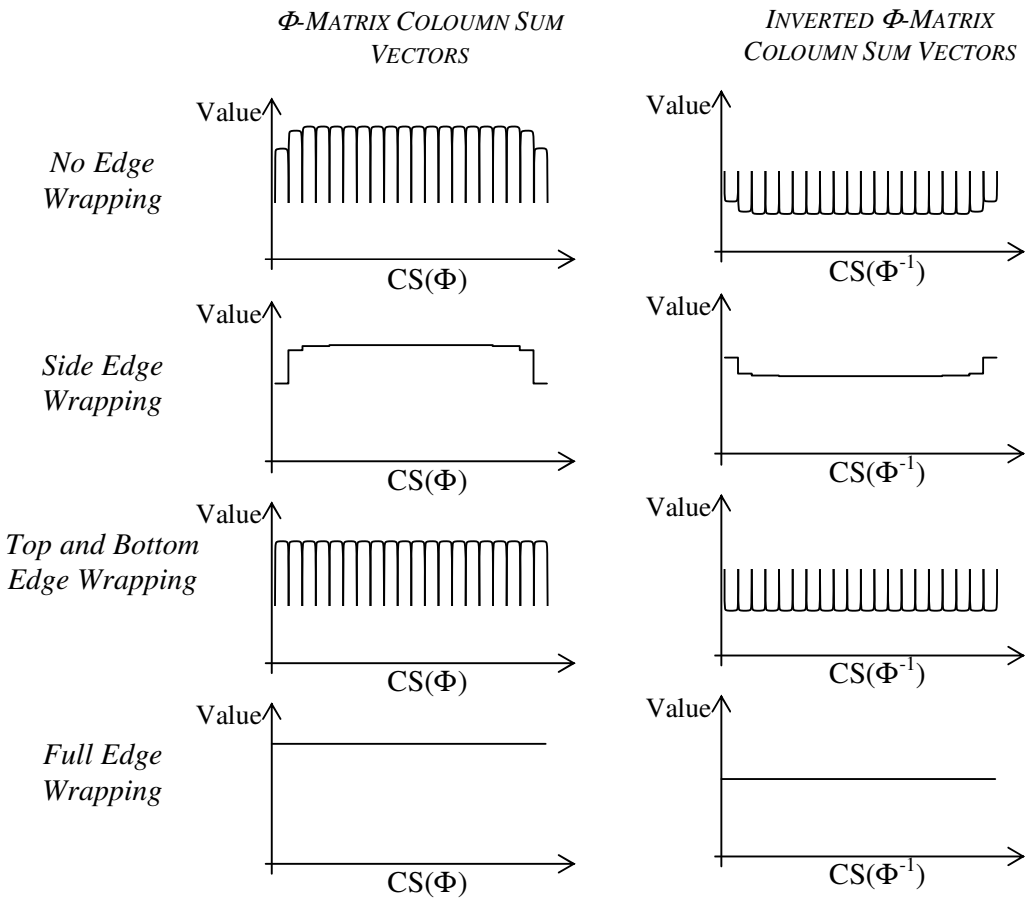

Figure A.2: The column sum vector for the Φ-Matrix and its inverse for different types of edge wrapping.

Figure A.2 illustrates what the values in the column sum vectors actually look like for the Φ-Matrix with different types of edge wrapping. The example shown represents a 20×20 surface division. To understand its structure it is important to remember that the surface is converted to a vector simply by stacking each of the layers on top of each other.

With no edge wrapping the sum drops every time the probe nears the edges, this is visible as the repeated dips, and the lower values at the ends.

With side edge wrapping the sum is the same for all values on each layer. Only the layers near the top and the bottom of the surface have reduced sums.

With top and bottom wrapping the sum drops each time the probe nears the edges but is the same for the top and bottom.

With full edge wrapping the sum remains the same, although there could be a very small change (<2%) if the probe nears a ground plane because of the changing shape of the ϕ-function. Though this is a localised phenomenon, the ϕ-functions only change shape significantly when in close proximity to a ground plane.

The column sum vector for the respective inverted Φ-Matrices are also shown, they follow a similar pattern.

When a multiple of the inverted matrix column sum vector is added to a surface its effect is to offset the surface by a constant amount except at the edges. The regular dips in the column sum vector cause the edges of the surface to curl up.

If no edge wrapping has been employed in the generation of the original Φ-Matrix then any error in the probe offset voltage will cause all of the edges of the resulting charge density distribution to curl up.

If side edge wrapping has been employed then only the top and bottom edges of the resulting distribution will curl up. Similarly if top and bottom edge wrapping is employed then only the side edges will curl up.

If full edge wrapping is employed then none of the edges curl up; the distribution is merely offset by a constant amount.

All the charge distributions shown in this thesis were calculated using a Φ-Matrix constructed using edge wrapping. As a result the errors in probe offset voltage manifest themselves as top and bottom edge curling. This can be seen in any of the charge distributions as thin horizontal black lines at the very top and bottom of the distributions. The effect is localised around the top and bottom of the distributions with only the first few rows of elements seriously affected.

The rest of the surface is offset by a constant amount and this offset can be easily removed by simply setting regions where no surface charge is present to zero. This was the technique employed throughout this thesis.

The limitation of this technique is that the surface being scanned must have a region that can confidently be said to have no net surface charge. In most cases this is no problem; streamers do not propagate over the entire surface, and regions of zero net charge density stand out because of their uniformity. Exactly uniform regions of charge that extend in all directions for several elements widths have not been observed, so it is

usually obvious which parts of the distribution have no net charge. A utility for picking out the regions of zero charge density and offsetting the distribution accordingly is included in the Viewer Software.

The problem can arise when the entire scanned surface is densely covered in streamer channels, then it becomes difficult to remove the unknown offset from the calculated charge distribution.

To solve this problem the Φ-Matrix calibration procedure requires a final improvement, which unfortunately was not implemented before the end of the work for this thesis.

The column sum vector for the inverted Φ-Matrix could easily be calculated and stored during the calibration procedure. Then k times the column sum vector could be subtracted from the calculated charge distribution, this would provide the exact surface charge distribution with no edge distortions. The following equation illustrates this.

$$\overline{\sigma} = (\overline{V} + k)\Phi^{-1} - k \times \overline{\mathrm{CS}(\Phi^{-1})}$$

The exact value of k is obviously unknown, however it could easily be found by simply varying it until the edge distortions disappear in the resulting charge distribution.

This technique could either be applied manually or a suitable algorithm written to remove the uniform and easy to spot edge distortions.

Appendix B: Stepper Motor Procedures

SetupMotor procedure

Function: Sets the stepping parameters for a motor

Declaration: **SetupMotor** (MotorID; Steps, Period,Direction, Size)

Remarks: **SetupMotor** sets the step timing for the motor selected by **MotorID**. **Steps** specifies the required number of steps. **Period** selects the period of a step in milliseconds, the direction of motion is set by **Direction** and **Size** selects the stepping size. **SetupMotor** will wait for the motor to stop before modifying the step timing.

Constants: The following constants are defined for the **MotorID** parameter:

Xaxis = 0	Yaxis = 1
Zaxis = 2	Waxis = 4

The following constants are defined for the **Direction** parameter:

CW = 0	{Clockwise rotation}
CCW = 1	{Anti-Clockwise rotation}

The following constants are defined for the **Size** parameter:

Half = 0	{Half step}
Full = 1	{Full step}

Restrictions: The **Steps** and **Period** parameters should both be positive (or zero) and be a whole number. An invalid value of any parameter will result in the procedure exiting without modifying the motor setup.

StartMotor Procedure

Function: Starts a stepper motor.

Declaration: **StartMotor** (MotorID)

Remarks: The motor selected by **MotorID** is stepped as defined by previous call to **SetupMotor** for that motor. This procedure has no effect if the motor is already in motion or being driven against either end-stop.

Constants: The following constants are defined for the **MotorID** parameter:

Xaxis = 0	Yaxis = 1
Zaxis = 2	Waxis = 4

Restriction: An invalid value for **MotorID** will result in the procedure exiting.

StopMotor Procedure

Function: Stops a stepper motor

Declaration: **StopMotor** (MotorID)

Remarks: The motor selected by **MotorID** is stopped. This procedure has no effect if the motor is already stationary.

Constants: The following constants are defined for the **MotorID** parameter:

Xaxis = 0 Yaxis = 1

Zaxis = 2 Yaxis = 4

Restriction: An invalid value for **MotorID** will result in the procedure exiting.

GetMotorStatus Procedure

Function: Get status information for a motor

Declaration: **GetsMotorStatus** (MotorID, Steps, Period, Direction, Size, Limiting)

Remarks: **GetMotorStatus** determines the current status for the motor selected by **MotorID**. **Period**, **Direction** and **Size** are the parameters set by the last call to **SetupMotor** for the selected motor. Steps is the remaining number of steps (0 indicates that the motor is stationary) and Limiting indicates if, and on which end-stop, the motor is limiting.

Constants: The following constants are defined for the **MotorID** parameter:

Xaxis = 0 Yaxis = 1

Zaxis = 2 Yaxis = 4

The following constants are defined for the **Direction** parameter:

CW = 0 {Clockwise rotation}

CCW = {Anti-Clockwise rotation}

The following constants are defined for the **Size** parameter:

Half = 0 {Half step}

Full = 1 {Full step}

The following constants are defined for the **Limiting** parameter:

NOTLIMIT = -1 {Not limiting}

CW = 0 {Clockwise end-stop}

CCW = 1 {Counter-clockwise end-stop}

Restriction: An invalid value for **MotorID** will result in the procedure exiting.

MotorRunning Function

Function: Tests if a motor is running.

Declaration: **MotorRunning** (MotorID)

Result type: Boolean

Remarks: **MotorRunning** returns true if the motor selected by **MotorID** is running and false otherwise.

Constants: The following constants are defined for the **MotorID** parameter:

Xaxis = 0 Yaxis = 1

Zaxis = 2 Yaxis = 4

Restriction: An invalid value for **MotorID** will result in the procedure exiting.

MotorLimiting Function

Function: Tests if a motor is limiting on an end-stop.

Declaration: **MotorLimiting** (MotorID)

Result type: Boolean

Remarks: **MotorLimiting** returns true if the motor selected by **MotorID** is limiting on an end-stop and false otherwise.

Constants: The following constants are defined for the **MotorID** parameter:

Xaxis = 0 Yaxis = 1

Zaxis = 2 Waxis = 4

Restriction: An invalid value for **MotorID** will result in the procedure exiting.

GroundProbe Function

Function: Grounds the probe using a relay.

Declaration: **GroundProbe** (ProbeGroundStatus)

Remarks: The probe will remain in the state set until the next call to **GroundProbe**.

Constants: The following constants are defined for the **ProbeGroundStatus** parameter:

Grounded = 1

NotGrounded = 0

Restriction: An invalid value for **ProbeGroundStatus** will result in the procedure exiting.

PowerProbe Function

Function: Turns the power to the probe buffer circuit on and off.

Declaration: **PowerProbe** (ProbePowerStatus)

Remarks: The probe power will remain in the state set until the next call to **PowerProbe**.

Constants: The following constants are defined for the **ProbePowerStatus** parameter:

On = 1

Off = 0

Restriction: An invalid value for **ProbePowerStatus** will result in the procedure exiting.

Appendix C: IOP Electrostatics 1999: Proceedings of the 10th International Conference, Cambridge 28-31 March 1999

A System For Obtaining High Resolution Macroscopic Surface Charge Density Distributions On Contoured Axi-Symmetric Insulator Specimens

D C Faircloth and N L Allen

Department of Electrical and Electronic Engineering, UMIST, UK

Abstract. This paper describes the method of operation of a system for measuring high-resolution surface charge density maps on practical insulator specimens using an electrostatic probe. Apparatus is described that can scan the electrostatic probe over the surface of the insulator and record the probe signal. The process of obtaining a charge density map from the probe signal measurements is explained. An example charge distribution is shown.

1. Introduction

Atmospheric air provides the basic insulation for many practical high voltage installations such as transmission lines, switchgear etc. However, the high voltage conductor in any such system must be mechanically supported, and the only practical solution is to use solid insulation. This introduces an insulating surface between the high voltage conductor and ground. An insulator's surface is intrinsically the weakest part of the solid-gas insulation system. Thus, physical knowledge of the insulating properties of solid insulation surfaces is very important. A major factor which influences surface discharges is the charge deposited on the surface of the solid insulation. This has led to the development of the surface charge scanning apparatus described in this paper. The apparatus is capable of measuring high-resolution charge density maps on all or part of almost any contoured axi-symmetric insulator specimen.

2. Surface Charge Density Measurement

2.1. *Electrostatic Probe*

The electrostatic probe principle [1] is used, where charge on the surface induces a voltage on the centre conductor of a coaxial probe positioned above the surface. The outer conductor is grounded and the voltage induced on the centre conductor is measured via a very high input impedance ($>10^{15}\Omega$) op-amp. The outer diameter of the probe is 2.9mm and the diameter of centre conductor is 0.6mm. A multi-point measuring technique is employed, where the probe voltage is recorded at many points above the insulator surface.

2.2. *Calibration Problem*

The probe voltage measurements must be converted into surface charge density measurements. Early investigators [1] used a simple capacitive method in which each value was linearly related to a charge density. This technique yields limited accuracy and makes no account for the probe's response to neighbouring charges on the surface. In recent years techniques have evolved to model the probe response to distant charges [2]. The technique used here is an adaptation of Pedersen's λ-function [3]. He related the Poisionian charge (q) induced on the probe to the surface charge density (σ) on a surface element: $q = \lambda\sigma$.

The technique employed here relates contribution to the total probe voltage (v) directly to the surface charge density (σ) on a surface element: $v = \phi\sigma$, where ϕ is the constant of proportionality measured in $Cm^{-2}V^{-1}$. Each element has a different associated ϕ-value depending on its distance from the probe. The total probe voltage (V) is the sum of the contributions from all the elements of surface charge: $V = \Sigma v = \Sigma\phi\sigma$. For the probe in one particular position the ϕ-values for all the elements on the surface make up the probe response function. The probe has a different response function for each voltage measurement position.

2.3 *The Φ-Matrix Technique*

The surface area is divided into elements as shown in figure 1. The elements do not have to be square and there does not have to be an equal number of horizontal and vertical divisions.

The probe voltage in position (i,j) is given by:

$$v_{ij} = \sum_{n_y}^{y=1}\left[\sum_{n_x}^{x=1}\phi_{ij}(xy)\,\sigma_{xy}\right]$$

where, $\phi_{ij}(xy)$ is the value of the probe's response function to charge at position (x,y) for the probe at position (i,j) and, σ_{xy} is the surface charge density on the surface element at position (x,y). This is a first order function of the $n_x n_y$ surface charge densities.

There are $n_x n_y$ probe voltage measurements in total and each of these voltages is a function of $n_x n_y$ surface charge densities. The problem is reduced to the solution of $n_x n_y$ simultaneous equations, which is solved using the matrix inversion technique.

The measured probe voltages and the unknown charge densities are grouped to two vectors $\overline{V}$ and $\overline{\sigma}$. They are related by the matrix equation: $\overline{V} = \overline{\sigma}\,\Phi$

where, Φ is a matrix containing all the ϕ-function values that are coefficients of the simultaneous equations. Hence the unknown charge density's can be found from: $\overline{\sigma} = \overline{V}\,\Phi^{-1}$

Surface is divided into $n_x \times n_y$ elements numbered from the top left corner

Specific surface elements can be identified using the variables *(x,y)*

The element which the probe is directly above is identified using the variables *(i,j)*

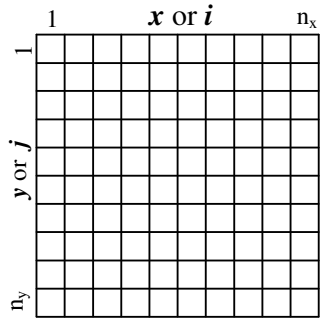

Figure 1: The division of the surface

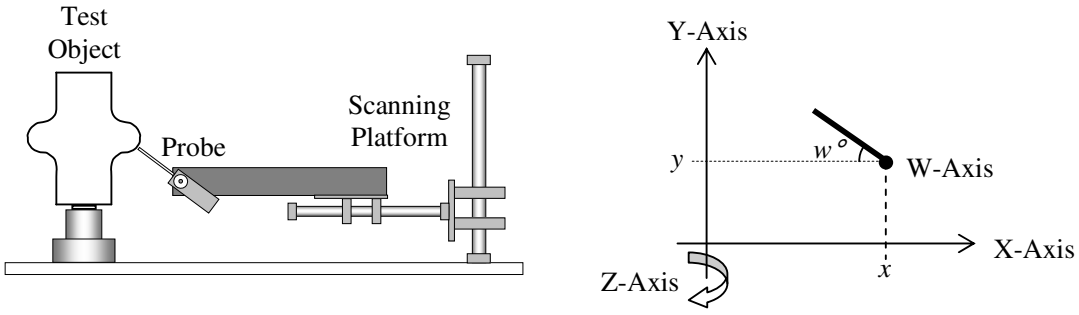

Figure 2: The scanning apparatus and the four axes that define the position of the probe above the surface.

3. The Scanning Apparatus

The probe is positioned using 4-stepper motors, as shown in figure2. The scanning platform was designed and constructed at UMIST. A computer controls the whole scanning system using specially written software. The contour of the test object can be entered into the computer manually or the system can measure the shape of the test object automatically using a spring-loaded sensor. The computer then calculates the probe positions to scan the surface. The probe must be kept perpendicular to, and a constant distance from, the surface. The surface is divided up into measurement points at which the probe voltage is recorded.

The surface is scanned in layers by rotating the test object. After each rotation the probe moves to the start position of the next layer until the whole surface has been scanned.

As the probe moves over the surface the probe voltage is measured at each point and stored in a file on the computer. All the settings for the scanning system are also stored in the same file; this allows the user to recall measurement parameters at a later date. The software has the facility to graphically display the scanned in voltage measurements and monitor each layer as it is scanned in. The scanning system has been developed as a versatile, easy to use piece of equipment with many useful facilities to help the user.

4. Implementing The Calibration Technique

The probe's response functions are found using a 3-D electrostatic field solver, key values are found, then a computer generates the Φ-matrix by quadraticaly interpolating any missing ϕ-values.

The matrix is inverted in Matlab running under UNIX on a Fujitsu AP3000. The solution of the charge distributions is automated using script files; files generated by the scanning system are read in, the required Φ-matrix is automatically generated and the charge distributions are solved and saved, all without any user intervention.

The solution time increases with the resolution of the surface. As the number of surface divisions increases so does the size of the matrix required to solve the charge distribution. The amount of computer memory required increases as n^4 where n is the 1-dimensional division of the surface (i.e. a surface is divided into n × n elements). For example a surface scanned to a 100×100 resolution requires a 10,000×10,000 Φ-matrix which needs 800MB of RAM and takes just under 24 hours to solve. The amount of RAM required increases very quickly with resolution; for a 150×150 surface division 4GB of RAM is required.

5. Example Surface Scans

To demonstrate the resolution of the system, a scan is made of the corona produced by a single -10kV 1.2/50μs impulse applied to a point electrode 1mm above the surface of a cylindrical PTFE insulator specimen. The effect of calibration using the Φ-Matrix technique is clearly visible by the differences between figures 3 and 4. After the surface was scanned a dust figure was obtained (figure 6) using black photocopier toner which adheres to positive charge. The dust figure compares favourably with the charge density contour map (figure 5).

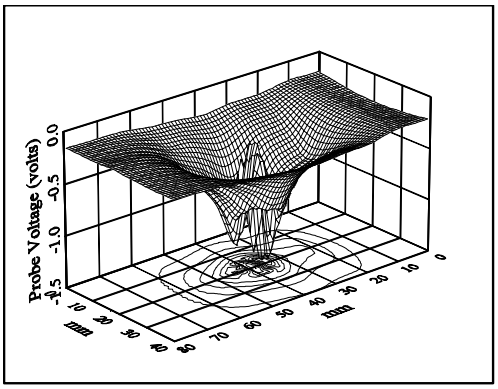

Figure 3: The measured probe voltage

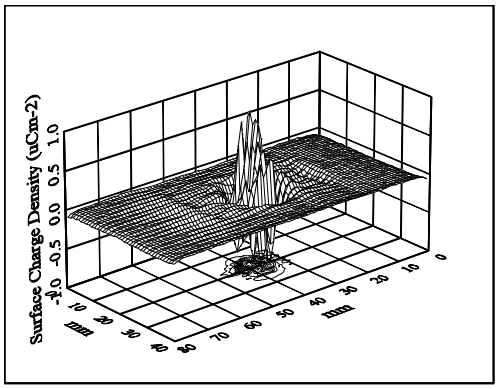

Figure 4: The calibrated surface charge density

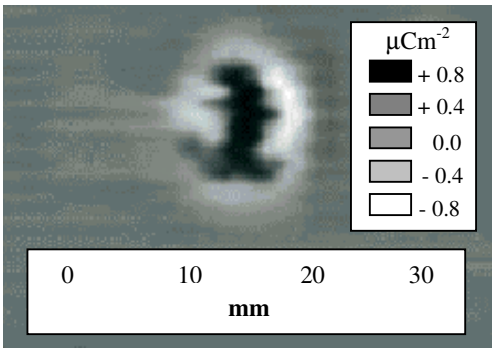

Figure 5: Surface charge contour map

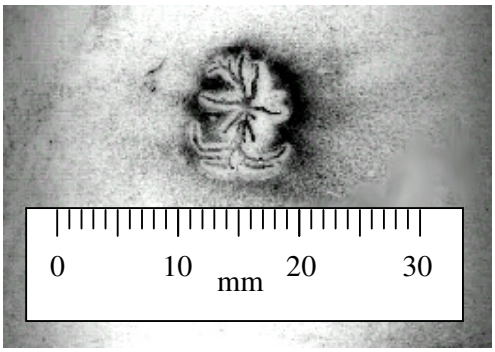

Figure 6: Dust figure obtained after surface had been scanned.

6. References

[1] D.K. DAVIES, "The Examination of the Electrical Properties of Insulators by Surface Charge Measurement", Journal of Scientific Instrumentation, Vol. 44, pp. 521-524, 1967.

[2] T.O. Rerup, et al, "Using the λ Function to Evaluate Probe Measurements of Charged Dielectric
Surfaces", IEEE Trans. Dielectrics EI, Vol. 3, pp. 770-777, 1996.

[3] A. Pedersen, 'On the Electrostatics of Probe Measurements of Surface Charge Densities', Gaseous Dielectrics V, Pergamon Press, pp. 235-240, 1987.

References

ABDUL-HUSSAIN, M.A. and CORNICK, K.J. : "Charge Storage on Insulation Surfaces in Air under Unidirectional Impulse Conditions", IEE Proceedings, Vol. 134, Pt A. No. 9, pp 731-740, November 1987.

AL-BAWY, I. and FARISH, O : "Charge Deposition on an Insulating Spacer Under Impulse-Voltage Conditions", IEE Proceedings, Vol. 138, Pt A. No. 3, pp. 145-152, May 1991.

ALLEN, N.L. and GHAFFAR, A. : "Propagation of Positive Streamers over Insulating Surfaces in Air", IEEE Conference on Electrical Insulation and Dielectric Phenomena, pp. 447-450, October 1995.

ALLEN, N.L., "The propagation of Positive Streamers in Air and at Air/Insulator Surfaces", Phenomena in Ionised Gases XXII, American Institute of Physics Conference Proceedings 363, pp. 247-256, 1995.

BIER, S., GUTHEIL, B. and WIEβ, P. : "Measurement System for Determination of Surface Charge Distributions on Dielectrics", 7th International Symposium on High Voltage Engineering, pp 139-142, August 1991.

CHUBB, J. : " Experience with Electrostatic Fieldmeter Instruments with No Earthing of the Rotating Chopper", Institute of Physics, Electrostatics 1999 Conference Proceedings, pp. 443-446, March 1999.

CONNOLLY, P. : "Surface Charging and Flashover on Insulators", PhD Thesis, University of Strathclyde, 1984.

DAVIES, D.K. : "The Examination of the Electrical Properties of Insulators by Surface Charge Measurement", Journal of Scientific Instrumentation, Vol. 44, pp. 521-524, 1967.

DAVIDSON, J. L. and BAILEY, A. G.: "Surface Charge Distribution Mapping of Insulating Materials", Institute of Physics, Electrostatics 1999 Conference Proceedings, pp. 439-442, March 1999.

FAIRCLOTH, D.C. and ALLEN, N.L. :"A System for Obtaining High Resolution Macroscopic Surface Charge Density Distributions on Contoured Axi-Symmetric Insulator Specimens", Institute of Physics, Electrostatics 1999 Conference Proceedings, pp. 451-454, March 1999.

GALLAGHER, T.J. et al: 'High Voltage-Measurement, Testing and Design', Wiley 1984

GALLIMBERTI, I., MARCHESI, G. and NIEMEYER, L.: "Streamer Corona at an Insulating Surface", 7th International Symposium on High Voltage Engineering, pp 47-50, August 1991.

GHAFFAR, A. : "The effect of Temperature on Streamer Propagation in Air and along Insulating Surfaces", PhD Thesis, University of Leeds, 1994.

IIZUKA, K., YONGCHANG ZHU and TAKADA, T.: "Dynamic Observation of Surface Charge Distribution by Electro-Optic Pockels Effect Technique" Proceedings of the SPIE- The International Society for Optical Engineering, Vol. 2873, pp 37-40, 1997.

MAHAJAN, S.M. and SUDARSHAN, T.S.: "Measurement of the Space Charge Field in Transformer Oil Using its Kerr Effect", IEEE Trans. on Dielectrics and Electrical Insulation, Vol. 1, No. 1, pp. 63-70, 1994.

MEEK, J.M. and CRAGGS, J.D.: "Electrical Breakdown of Gases", Oxford Clarendon Press, 1953.

MIKROPOULOS, P.N. : Private Correspondence, UMIST, 1998.

NASSER, E.: "Spark Breakdown in Air at a Positive Point", IEEE Spectrum, pp 127-134, November 1968.

OOTERA, H. and NAKANISHI, K.: "Analytical Method for Evaluating Surface Charge Distribution on a Dielectric from Capacitive Probe Measurement – Application to a Cone-Type Spacer in ±500kV DC-GIS" IEEE Transactions on Power Delivery, Vol. 3, No. 1, pp. 165-172, January 1988.

PEDERSEN, A., : "On the Electrostatics of Probe Measurements of Surface Charge Densities", Gaseous Dielectrics V, NewYork: Pergamon Press, pp.235-240, 1987.

RERUP, T.O., CRICHTON, G.C. and McALLISTER, I.W. :"Response of an Electrostatic Probe for a Right Cylindrical Spacer", Annual Report Conference on Electrical Insulation and Dielectric Phenomena, pp 167-176, October 1994.

RERUP, T.O., CRICHTON, G.C. and McALLISTER, I.W. :"Using the λ Function to Evaluate Probe Measurements of Charged Dielectric Surfaces", IEEE Transactions on Dielectrics and Electrical Insulation, Vol.3 No. 4, pp. 770-777, August 1996.

SONE, M., TORIGAMA, K. and TORIGAMA, Y.: Applied Physical Letters, 24, 115, 1974.

SUDHAKAR, C. E. and SRIVASTAVA, K. D. : "Electric Field Computation from Probe Measurements of Charge on Spacers Subjected to Impulse Voltages", 5th International Symposium on High Voltage Engineering, Braunschweig, Germany, paper 33.14, 1987.

TAKUMA,T.,YASHIMA, M. and KAWAMOTO, T. : ”Principle of Surface Charge Measurement for Thick Insulating Specimens”, IEEE Transactions on Dielectrics and Electrical Insulation, Vol.5 No. 4, pp. 497-504, August 1998.

TOWNSEND, J.S. : ”The theory of Ionisation of Gases by Collision”, Constable, London, 1910.

VASCONCELOS, F.H. : “Insulator Charging and Decay Generated by Impulse Voltages on Polymers in SF_6 Medium”, PhD Thesis, UMIST, 1994.

WINTLE, H.J., RERUP, T.O., CRICHTON, G.C. and McALLISTER, I.W.: ”Discussion-Using the λ Function to Evaluate Probe Measurements of Charged Dielectric Surfaces”, IEEE Transactions on Dielectrics and Electrical Insulation, Vol.4 No .4, pp. 470-473, August 1997.

ZHU, Y., TAKADA, T. and TU, D.: “Discharge Behaviour Observed by Pockels Effect Surface Charge Distribution Measurement”, pp. 484-487.